

## REPORT DOCUMENTATION PAGE

Public reporting burden for this collection of information is estimated to average 1 hour per response, including the preparation, collection, and maintenance of the data needed, and completing and reviewing the collection of information. Send comments, including suggestions for reducing this burden, to Washington Headquarters Services, Directorate for Information Operations and Budget, Paperwork Reduction Project (0704-0188), 1204, Arlington, VA 22202-4302, and to the Office of Management and Budget, Paperwork Reduction Project (0704-0188).

1. AGENCY USE ONLY (Leave Blank)		2. REPORT DATE December, 1994	3. REPORT TYPE AND DATES COVERED Final
4. TITLE AND SUBTITLE USAF Summer Research Program - 1994 Graduate Student Research Program Final Reports, Volume 8, Phillips Laboratory			5. FUNDING NUMBERS
6. AUTHORS Gary Moore			
7. PERFORMING ORGANIZATION NAME(S) AND ADDRESS(ES) Research and Development Labs, Culver City, CA			8. PERFORMING ORGANIZATION REPORT NUMBER
9. SPONSORING/MONITORING AGENCY NAME(S) AND ADDRESS(ES) AFOSR/NI 4040 Fairfax Dr, Suite 500 Arlington, VA 22203-1613			10. SPONSORING/MONITORING AGENCY REPORT NUMBER
11. SUPPLEMENTARY NOTES Contract Number: F49620-93-C-0063			
12a. DISTRIBUTION AVAILABILITY STATEMENT Approved for Public Release			12b. DISTRIBUTION CODE
13. ABSTRACT (Maximum 200 words) The United States Air Force Graduate Student Research Program (USAF-GSRP) is designed to introduce university, college, and technical institute graduate students to Air Force research. This is accomplished by the graduate students being selected on a nationally advertised competitive basis during the summer intersession period to perform research at Air Force Research Laboratory Technical Directorates and Air Force Air Logistics Centers. Each participant provided a report of their research, and these reports are consolidated into this annual report.			
14. SUBJECT TERMS AIR FORCE RESEARCH, AIR FORCE, ENGINEERING, LABORATORIES, REPORTS, SUMMER, UNIVERSITIES			15. NUMBER OF PAGES
			16. PRICE CODE
17. SECURITY CLASSIFICATION OF REPORT Unclassified	18. SECURITY CLASSIFICATION OF THIS PAGE Unclassified	19. SECURITY CLASSIFICATION OF ABSTRACT Unclassified	20. LIMITATION OF ABSTRACT UL



March 5, 1999

Lilla Mae Davis,

The following pages are unavailable because of bindery problems. In 1994 the publishing company we used had problems with the bindery.

Volume 5A page 4-5 missing.

Volume 5B page 34-6 missing.

Volume 5B page 58-14 side of page cut-off.

Volume 8 page 15-4 missing.

Johnetta Thompson  
Program Administrator

UNITED STATES AIR FORCE  
SUMMER RESEARCH PROGRAM -- 1994  
GRADUATE STUDENT RESEARCH PROGRAM FINAL REPORTS

VOLUME 8  
PHILLIPS LABORATORY

RESEARCH & DEVELOPMENT LABORATORIES  
5800 Uplander Way  
Culver City, CA 90230-6608

Program Director, RDL  
Gary Moore

Program Manager, AFOSR  
Major David Hart

Program Manager, RDL  
Scott Licoscos

Program Administrator, RDL  
Gwendolyn Smith

Program Administrator  
Johnetta Thompson

Submitted to:

AIR FORCE OFFICE OF SCIENTIFIC RESEARCH  
Bolling Air Force Base  
Washington, D.C.  
December 1994

19981204 044

DTIC QUALITY INSPECTED

## PREFACE

Reports in this volume are numbered consecutively beginning with number 1. Each report is paginated with the report number followed by consecutive page numbers, e.g., 1-1, 1-2, 1-3; 2-1, 2-2, 2-3.

This document is one of a set of 16 volumes describing the 1994 AFOSR Summer Research Program. The following volumes comprise the set:

<u>VOLUME</u>	<u>TITLE</u>
1	Program Management Report <i>Summer Faculty Research Program (SFRP) Reports</i>
2A & 2B	Armstrong Laboratory
3A & 3B	Phillips Laboratory
4	Rome Laboratory
5A & 5B	Wright Laboratory
6	Arnold Engineering Development Center, Frank J. Seiler Research Laboratory, and Wilford Hall Medical Center <i>Graduate Student Research Program (GSRP) Reports</i>
7	Armstrong Laboratory
8	Phillips Laboratory
9	Rome Laboratory
10	Wright Laboratory
11	Arnold Engineering Development Center, Frank J. Seiler Research Laboratory, and Wilford Hall Medical Center <i>High School Apprenticeship Program (HSAP) Reports</i>
12A & 12B	Armstrong Laboratory
13	Phillips Laboratory
14	Rome Laboratory
15A&15B	Wright Laboratory
16	Arnold Engineering Development Center

**GSRP FINAL REPORT TABLE OF CONTENTS****i-xiv**

<b>1. INTRODUCTION</b>	<b>1</b>
<b>2. PARTICIPATION IN THE SUMMER RESEARCH PROGRAM</b>	<b>2</b>
<b>3. RECRUITING AND SELECTION</b>	<b>3</b>
<b>4. SITE VISITS</b>	<b>4</b>
<b>5. HBCU/MI PARTICIPATION</b>	<b>4</b>
<b>6. SRP FUNDING SOURCES</b>	<b>5</b>
<b>7. COMPENSATION FOR PARTICIPANTS</b>	<b>5</b>
<b>8. CONTENTS OF THE 1994 REPORT</b>	<b>6</b>

**APPENDICIES:**

<b>A. PROGRAM STATISTICAL SUMMARY</b>	<b>A-1</b>
<b>B. SRP EVALUATION RESPONSES</b>	<b>B-1</b>

**GSRP FINAL REPORTS**

**SRP Final Report Table of Contents**

<b>Author</b>	<b>University/Institution Report Title</b>	<b>Armstrong Laboratory Directorate</b>	<b>Vol-Page</b>
MS Jennifer M Ball	Wright State University , Dayton, , OH Relation Between Detection and Intelligibility in	AL/CFBA	7- 1
MR. Richard G Best	Southwest Missouri State Univ. , Springfield, , MO The Effects of Socialization on Vocational Aspirat	AL/HRMJ	7- 2
MR. Daniel A Brown	Grand Canyon University , Phoenix, , AZ Toward Modeling Higher Level Control Systems: Inc	AL/HRAU	7- 3
MS. Susan T Chitwood	Bowling Green State University , Bowling Green, , OH Further Explorations in Epistemological Space	AL/CFHP	7- 4
John E Cisneros	California State University , Los Angeles , CA Aurally Directed Search: A Comparison Between Syn	AL/CFBA	7- 5
Candace E Clary	Duke University , Durham , NC Intra-Ocular Laser Surgical Probe (ILSP) for Vitre	AL/OEO	7- 6
Robert M Colbert	Villanova University , Villanova , PA Finite Element Modeling of Manikin Necks for the A	AL/CFBV	7- 7
MR. Mark C Delgado	University of Georgia , Athens, , GA Determination of the Oxidative Redox Capacity of A	AL/EQC	7- 8
MR. Steven J Essler	North Dakota State University , Fargo, , ND Estimation of Four Arterial Vascular Parameters fo	AL/AOCIY	7- 9
Lawrence R Gottlob	Arizona State University , Tempe , AZ Accuracy Curves in a Location-Cuing Paradigm for V	AL/HRAT	7- 10
MS. Jennifer L Greenis	Michigan State University , East Lansing, , MI ITS Evaluation: A Review of the Past and Recommen	AL/HRTE	7- 11

**SRP Final Report Table of Contents**

<b>Author</b>	<b>University/Institution Report Title</b>	<b>Armstrong Laboratory Directorate</b>	<b>Vol-Page</b>
MS. Patricia M Harn	University of Washington , Seattle , WA Testing R-Wise: Reading and Writing in a Supporti	AL/HRTI	7- 12
Jason E Hill	University of Scranton , Scranton , PA Rapid Bacterial DNA Fingerprinting by the Polymer	AL/AOEL	7- 13
Mr. Rod J Hughes	Oregon Health Sciences University , Portland , OR Melatonin, Body Temperature and Sleep in Humans:	AL/CFTO	7- 14
Mr Roman G Longoria	Rice University , Houston , TX The Measurement of Work Experience: Issues and Im	AL/HRTE	7- 15
Uyen A Luong	Trinity University , San Antonio, , TX Millimeter Wave-Induced Hypertension Does Not Invo	AL/OER	7- 16
MR. Scott A Macbeth	University of Dayton , Dayton, , OH Using Electronic Brainstroming Tools to Visually	AL/HRG	7- 17
MR. Nicholas F Muto	University of Scranton , Scranton, , PA Rapid Bacterial DNA Fingerprinting by the Polymera	AL/AOEL	7- 18
Kevin P Nau	Kent State University , Kent , OH Proposal for the Establishment of a Comprehensive	AL/CFTF	7- 19
MR. Eric O Riise	Cal State Univ/Chico , Chico, , CA A Study of Interaction in Distance Learning	ALL/HRT	7- 20
Ms Heather E Roberts	Virginia Tech , Blacksburg , VA Gender and Racial Equity of the Air Force Officer	AL/HRMM	7- 21
MR. Dale F Rucker	West Virginia University , Morgantown, , WV Improved Numerical Modeling of Groundwater Flow an	AL\EQC	7- 23

**SRP Final Report Table of Contents**

<b>Author</b>	<b>University/Institution Report Title</b>	<b>Armstrong Laboratory Directorate</b>	<b>Vol-Page</b>
Arthur M Ryan	Wright State University , Dayton , OH The Workload Assessment Monitor: Progress Towards	AL/CFHP	7- 24
Mark J Schroeder	North Dakota State University , Fargo , ND Arterial Elastance in the Maximization of External	AL/AOCY	7- 25
MS. Katherine M Specht	Ohio State University , Columbus., OH Tactile Perception in a Virtual Environment	AL/CFBA	7- 26
MR. Joseph M Stauffer	University of Iowa , Iowa City , IA Predicting Pilot Training Success with Logistic or	AL/HRMA	7- 27
DR. Scott G Stavrou	University of Central Arkansas , Conway., AR Analysis of the Absorption and Metabolism of Trich	AL/OET	7- 28
MS. Virginia K Stromquist	Michigan Technological Inst. , Houghton, , MI Solid Phase Microextraction as a Method for Quanti	AL/EQC	7- 29
MR. Eric S Wieser	Trinity University , San Antonio, , TX Millimeter Wave-Induced Hypotension Does Not Invol	AL/OER	7- 30
MR. Gregory S Zinkel	Georgia Institute Technology , Atlanta., GA A Study of the Use Predictive Modeling for Dynamic	AL/AO	7- 31

**SRP Final Report Table of Contents**

<b>Author</b>	<b>University/Institution Report Title</b>	<b>Phillips Laboratory Directorate</b>	<b>Vol-Page</b>
<b>MR. William W Brocklehurst</b>	University of Cincinnati , Cincinnati , OH Effect of Dissolved Gases on the Discharge Coeffic	PL/RKFA	8- 1
<b>MR. Stephen E Clarke</b>	Utah State University , Logan , UT REPORT NOT AVAILABLE AT PRESS TIME	PL/VTRP	8- 2
<b>Peyman Ensaf</b>	University of Denver , Denver , CO Influence of Model Complexity and Aeroelastic Cont	PL/WSA	8- 3
<b>MR. Frank S Gulczinski</b>	University of Michigan , Ann Arbor, , MI Interior Spectroscopic Investigation of Plasma Com	PL/RKCO	8- 4
<b>MR. Derik C Herpfer</b>	University of Cincinnati , Cincinnati , OH Drop Sizing of a Like-Impinging Element Injector I	PL/RKFA	8- 5
<b>MR. Phillip N Hutton</b>	Old Dominion University , Norfolk, , VA Effectiveness of Thermionic Heat Pipe Module	PL/VTPN	8- 6
<b>MR. Robert J Leiweke</b>	Ohio State University , Columbus , OH A Single Temperature/Material Ablation Algorithm f	PL/WSP	8- 7
<b>MR. John I Lipp</b>	Michigan Technological Univ , Houghton , MI Estimation of Tilts Extended Images in the Presenc	PL/LIAE	8- 8
<b>MR. Stephen A Luker</b>	University of Alabama , Tuscaloosa , AL Determining Cloud Coverages for Input to Thermal C	PL/GPAA	8- 9
<b>MR. Daniel T Moriarty</b>	MIT , Cambridge , MA Laboratory Experiments with the Versatile Toroidal	PL/GPSG	8- 10
<b>MR. Tim C Newell</b>	University of North Texas , Denton , TX Synchronization Using Control Chaotic Diode Resona	PL/LIDN	8- 11

**SRP Final Report Table of Contents**

<b>Author</b>	<b>University/Institution Report Title</b>	<b>Phillips Laboratory Directorate</b>	<b>Vol-Page</b>
Jeffrey W Nicholson	University of New Mexico , Albuquerque , NM Relaxation Processes in Gain Switched Iodine Laser	PL/LIDB	8- 12
MR. Sean R Olin	Boston University , Boston, , MA An Investigation of Flight Characteristics of the	PL/SX	8- 13
MS. Janet M Petroski	Cal State Univ/Northridge , Northridge , CA Thermoluminescence of Simple Species in Solid Mole	PL/RKFE	8- 14
MR. Aaron J Ridley	University of Michigan , Ann Arbor, , MI The Dynamic Convection Reversal Boundary	PL/GPIA	8- 15
MR. Richard M Salasovich	University of Cincinnati , Cincinnati , OH Fabrication and Mechanical Testing of Mixed-Matrix	PL/VTSC	8- 16
MR. Kevin L Scales	University of New Mexico , Albuquerque , NM A Study of Numerical Methods in Atmospheric Light P	PL/LIMI	8- 17
Greg T Sharp	University of New Mexico , Albuquerque , NM Further Studies of High Temperature Cs-Ba Tachotron	PL/WSP	8- 18
MR. Joseph M Sorci	Massachusetts Inst. Technology , Cambridge, , MA A Study of Low Frequency Weak Turbulence in a Hollow	PL/GPID	8- 19
Jonathan Stohs	University of New Mexico , Albuquerque , NM Radiation Exposure of Photonic Devices	PL/VTET	8- 20
MR. Jose Suarez	Florida Inst. of Technology , Patrick AFB, , FL Meteoroid & Orbital Debris Collision Hazard Analysis	PL/WSC	8- 21
MR. Tony F von Sadovszky	University of Nevada, Reno , Reno, , NV PICLL: A Portable Parallel 3D PIC Code Implementation	PL/WSP	8- 22

**SRP Final Report Table of Contents**

<u>Author</u>	<u>University/Institution Report Title</u>	<u>Rome Laboratory Directorate</u>	<u>Vol-Page</u>
MR. John C Bertot	Syracuse University , Syracuse, , NY Transferring Technology Via the Internet	RL/XPP	9- 1
MR. Jerry M Couretas	University of Arizona , Tucson, , AZ Analysis of Extraction and Aggregation Techniques	RL/IRDO	9- 2
MR. Frederick L Crabbe	Univ California/Los Angeles , Los Angeles, , CA Using Self-Organization to Develop Vector Represen	RL/IRDO	9- 3
MS. Julie Hsu	Louisiana State University , Baton Rouge, , LA An Assignment Based Approach to Parallel-Machine S	RL/C3CA	9- 4
Andrew J Laffely	Univ. of Maine , Orono , ME Automatic Extraction of Drainage Network from Di	RL/IRRP	9- 5
MR. Daniel K Lee	Southern Illinois University , Carbondale , IL Mutual Coupling Effect of Square Microstrip Patch	RL/ERA	9- 6
Slawomir J Marcinkowski	Syracuse University , Syracuse , NY Transferring Technology Via the Internet	RL/XPP	9- 7
MR. Sean S O'Keefe	Cornell University , Ithaca, , NY Integration of Optoelectronic Devices with Microwa	RL/OCBP	9- 8
MR Robert L Popp	University of Connecticut , Storrs , CT Multisensor-Multitarget Data Fusion Using an S-Dim	RL/OCTM	9- 9
MR. Steven J Pratt	Syracuse University , Syracuse, , NY Analysis and Comparison of the Performance/Life Co	RL/C3AB	9- 10
Francis X Reichmeyer	Syracuse University , Syracuse , NY Local Area ATM Network Interfaces	RL/C3AB	9- 11

**SRP Final Report Table of Contents**

<b>Author</b>	<b>University/Institution Report Title</b>	<b>Rome Laboratory Directorate</b>	<b>Vol-Page</b>
<b>MR. David H Sackett</b>	<b>Rochester Institute of Technol , Rochester , NY Self-Sustained Pulsation and High Speed Optical Ne</b>	<b>RL/OCPA</b>	<b>9- 12</b>
<b>ME. Paul E Shames</b>	<b>Univiersity of Cal/San Diego , San Diego, , CA A Study of High Speed Polarization Rotators for Us</b>	<b>RL/IRAP</b>	<b>9- 13</b>
<b>Terrence W Towe</b>	<b>Univ of Arkansas-Fayetteville , Fayetteville , AR REPORT NOT AVAILABLE AT PRESS TIME</b>	<b>RL/ERX</b>	<b>9- 14</b>
<b>Okechukwu C Ugweje</b>	<b>Florida Atlantic University , Boca Raton, , FL A Program Plan for Transmitting High-Data-Rate ATM</b>	<b>RL/C3BA</b>	<b>9- 15</b>
<b>MR. Martin A Villarica</b>	<b>Syracuse University , Syracuse, , NY A Study of the Application of Fractals and Kineti</b>	<b>RL/ERDR</b>	<b>9- 16</b>
<b>Stanley J Wenndt</b>	<b>Colorado State University , Fort Collins , CO An Investigation of Cepstrum Based Speaker Identif</b>	<b>RL/IRAA</b>	<b>9- 17</b>

**SRP Final Report Table of Contents**

<b>Author</b>	<b>University/Institution Report Title</b>	<b>Wright Laboratory Directorate</b>	<b>Vol-Page</b>
<b>MS. Terri L Alexander</b>	University of Central Florida , Orlando, , FL Design of Spectroscopic Material-Characterization	WL/MNGS	10- 1
<b>MR. Joseph L Binford, III</b>	University of Dayton , Dayton, , OH Thermal Stability Apparatus Design and Error Analy	WL/MLPO	10- 2
<b>MR Jonathan A Bishop</b>	University of Oklahoma , Norman, , OK Influence of Model Complexity and Aeroelastic Cons	WL/FIBR	10- 3
<b>MR. Steven P Burns</b>	Purdue University , West Lafayette, , IN The Use of Pressure Sensitive Paints on Rotating M	WL/POTF	10- 4
<b>MR. Lance H Carter</b>	University of Texas/Austin , Austin , TX Gain-Scheduled Bank-to-Turn Autopilot Design Using	WL/MNAG	10- 5
<b>MR. Peng Chen</b>	University of North Texas , Denton , TX Synthesis & Characterization of Lanthanum Phosphat	WL/MLLM	10- 6
<b>MS. Lora A Cintavay</b>	University of Cincinnati , Cincinnati , OH Processing and Characterization of Nonlinear Optic	WL/MLBP	10- 7
<b>MR. William K Cope</b>	University of Illinois/Urbana , Urbana, , IL Assessment of Gasp for the Simulation of Scramjet	WL/POPT	10- 8
<b>Mike J Cutbirth</b>	Oklahoma State University , Stillwater , OK A Study of the Heat Transfer for the High Flux Hea	WL/POOS	10- 9
<b>Craig M Files</b>	University of Idaho , Moscow , ID Using a Search Heuristic in an NP-Complete Problem	WL/AART-	10- 10
<b>MR Edward M Friel</b>	University of Dayton , Dayton , OH Direction Finding in the Presence of a Near Field	WL/AARM	10- 11

**SRP Final Report Table of Contents**

<b>Author</b>	<b>University/Institution Report Title</b>	<b>Wright Laboratory Directorate</b>	<b>Vol-Page</b>
MR. Keith D Grinstead	Purdue University , West Lafayette, , IN Obtaininng the Correction Factors for Two-Photon I	WL/POSF	10- 12
MR. Jason J Hugenroth	Louisiana State University , Baton Rouge, , LA A Research Plan for Evaluating Wave Gun as a Low-L	WL/MNAA	10- 13
MR. Andrew Kager	University of Central Florida , Orlando, , FL A Numerical Study of the Effect of Base and Collec	WL/ELRA	10- 14
MR. John C Lewis	University of Kentucky , Lexington , KY A Theory for the Testing of Materials Under Combin	WL/MNM	10- 15
MR. Kenneth P Luke	Wright State University , Dayton, , OH Three-Dimensional Modeling Using a Calibrated Came	WL/AARF-	10- 16
John D Mai	Univ of Calif-Los Angeles , Los Angeles , CA Preliminary Characterization and Calibration of Mi	WL/FIME	10- 17
MR. Mark A Manzardo	Univ of Alabama-Huntsville , Huntsville , AL High Speed Imaging Infrared Polarimetry	WL/MNGS	10- 18
MR. David B Maring	University of FloridaFL , Gainesville, , FL Fabrication and White-Light Characterization of An	WL/MNG	10- 19
MR. Joseph R Miramonti	University of Missouri/Columbi , Columbia, a , MO Scanning Image Alegbra Networks for Vehicle Identi	WL/MNGA	10- 20
MS. Jennifer S Naylor	Auburn University , Auburn, , AL Automation Control Issues in the Development of an	WL/MNAG	10- 21
MR. Ned F O'Brien	University of Dayton , Dayton, , OH A Study of RF Fiber Optic Communication Link Techn	WL/AAAI-	10- 22

**SRP Final Report Table of Contents**

<b>Author</b>	<b>University/Institution Report Title</b>	<b>Wright Laboratory Directorate</b>	<b>Vol-Page</b>
<b>MR. Tae W Park</b>	Univ of Illinois/Chicago , Chicago, , IL A Numerical Study of DropleVortx Interactions in a	WL/POSF	10- 23
<b>MS Margaret F Pinnell</b>	University of Dayton , Dayton , OH A Parametric Study of the Factors Affecting the Op	WL/MLBM	10- 24
<b>MR. Seth M Pinsky</b>	Oregon Grad Inst. Sci & Tech , Portland, , OR S-Parameter Measurements on a GaAsFET Variable-Gai	WL/ELM	10- 25
<b>MR. David A Ress</b>	Tennessee Technological Univ , Cookeville, , TN Modifications To The Thinker Discovery System	WL/MLIM	10- 26
<b>Mohammed A Samad</b>	University of New Orleans , New Orleans , LA A Study of Delamination Damage and Energy Exchange	WL/FIVS	10- 27
<b>MR. Robert W Slater III</b>	University of Cincinnati , Cincinnati , OH Low-Velocity Impact of Moisture-Conditioned Lamina	WL/FIBE	10- 28
<b>Ed P Socci</b>	University of Virginia , Charlottesville , VA X-ray Diffraction Study of Siloxane/Cholestrol Bas	WL/MLPO	10- 29
<b>MR. Edward A Thompson</b>	University of Cincinnati , Cincinnati, , OH Annealed Fuzzy Control for a Self-Tuning Piezoelect	WL/FIBG	10- 30
<b>MR. Brent A Veltkamp</b>	Michigan State University , East Lansing, , MI Pixel Plane Design for SIMD Graphic Processor	WL/ELED	10- 31
<b>MR. Christopher C Vogt</b>	University of Cal San Diego , San Diego, , CA The Combinatorics of Function Decomposition and Ap	WL/AART-	10- 32
<b>MR. Ralph J Volino</b>	University of Minnesota , Minneapolis, , MN Documentation of Boundary Layer Characteristics fo	WL/POTT	10- 33

SRP Final Report Table of Contents

<u>Author</u>	<u>University/Institution</u>	<u>Wright Laboratory</u>	<u>Vol-Page</u>
	<u>Report Title</u>	<u>Directorate</u>	
MR. Jeffrey A Walrath	University of Cincinnati , Cincinnati, , OH Integration of Champ Firm Macro Library with DSS	WL/AAAT-	10- 34

**SRP Final Report Table of Contents**

<b>Author</b>	<b>University/Institution Report Title</b>	<b>Arnold Engineering Development Center Directorate</b>	<b>Vol-Page</b>
<b>MR. William A Alford</b>	Univ. Tennessee Space Inst. , Tullahoma, , TN Design of Testing and Debugging Software for C31 N	Sverdrup	11- 1
<b>MR. Brian C DeAngelis</b>	University of Illinois/Urbana- , Urbana , IL Performance and Validation Studies of the Kiva-II	SVERDRU	11- 2
<b>MR. Harold D Helsley</b>	Univ Tennessee Space Inst , Tullahoma, , TN Development of a Monitor for a Multi-Processor Net	Sverdrup	11- 3
<b>MR. Christopher W Humphres</b>	University of Alabama , Tuscaloosa, , AL Parallelization of Chimera Utilizing PVM	Calspan	11- 4
<b>MR. Curtis S Mashburn</b>	University of Tennessee Space , Tullahoma, , TN Prediction of the Performance of a 7-Stage Axial-F	Sverdrup	11- 5
<b>MR. William S Meredith</b>	Univ of Tennessee Sp. Inst. , Tullhoma, , TN REPORT NOT AVAILABLE AT PRESS TIME	Calspan	11- 6
<b>MR. Michael S Moore</b>	Vanderbilt University , Nashville , TN A Model Based Real Time Image Processing System	SVERDRU	11- 7
<b>MR David T Pratt</b>	Univ of Tennessee Space Inst , Tullahoma , TN Analysis and Comparison of the Performance/Life Co	Sverdrup	11- 8
<b>MR. David B Underhill</b>	Univ of Tenn Space Inst , Tullahoma , TN Application of Vorticity Confinement to a Delta Wi	Calspan	11- 9

**SRP Final Report Table of Contents**

<b>Author</b>	<b>University/Institution Report Title</b>	<b>Frank J Seiler Research Laboratory Directorate</b>	<b>Vol-Page</b>
MR. Christian S Bahn	Colorado School of Mines , Golden, , CO A Theoretical Study of Lithium and Molten Salt Gra	FJSRL/NC	11- 10
MR. Antonio M Ferreira	Memphis State University , Memphis, , TN Theoretical Investigations of the NLO Properties o	FJSRL/NC	11- 11
MS Joan Fuller	University of Alabama , Tuscaloosa , AL Investigations of Carbon Materials in Alkali Metal	FJSRL/CD	11- 12

**SRP Final Report Table of Contents**

<b>Author</b>	<b>University/Institution</b>	<b>Wilford Hall Medical Center</b>	<b>Vol-Page</b>
	<b>Report Title</b>	<b>Directorate</b>	
MR Ramachandra P Tummala	University of Miami , Coral Gables , FL Effects of Temperature on Various Hematological P	WHMC/RD	11- 13

## **INTRODUCTION**

The Summer Research Program (SRP), sponsored by the Air Force Office of Scientific Research (AFOSR), offers paid opportunities for university faculty, graduate students, and high school students to conduct research in U.S. Air Force research laboratories nationwide during the summer.

Introduced by AFOSR in 1978, this innovative program is based on the concept of teaming academic researchers with Air Force scientists in the same disciplines using laboratory facilities and equipment not often available at associates' institutions.

AFOSR also offers its research associates an opportunity, under the Summer Research Extension Program (SREP), to continue their AFOSR-sponsored research at their home institutions through the award of research grants. In 1994 the maximum amount of each grant was increased from \$20,000 to \$25,000, and the number of AFOSR-sponsored grants decreased from 75 to 60. A separate annual report is compiled on the SREP.

The Summer Faculty Research Program (SFRP) is open annually to approximately 150 faculty members with at least two years of teaching and/or research experience in accredited U.S. colleges, universities, or technical institutions. SFRP associates must be either U.S. citizens or permanent residents.

The Graduate Student Research Program (GSRP) is open annually to approximately 100 graduate students holding a bachelor's or a master's degree; GSRP associates must be U.S. citizens enrolled full time at an accredited institution.

The High School Apprentice Program (HSAP) annually selects about 125 high school students located within a twenty mile commuting distance of participating Air Force laboratories.

The numbers of projected summer research participants in each of the three categories are usually increased through direct sponsorship by participating laboratories.

AFOSR's SRP has well served its objectives of building critical links between Air Force research laboratories and the academic community, opening avenues of communications and forging new research relationships between Air Force and academic technical experts in areas of national interest; and strengthening the nation's efforts to sustain careers in science and engineering. The success of the SRP can be gauged from its growth from inception (see Table 1) and from the favorable responses the 1994 participants expressed in end-of-tour SRP evaluations (Appendix B).

AFOSR contracts for administration of the SRP by civilian contractors. The contract was first awarded to Research & Development Laboratories (RDL) in September 1990. After completion of the 1990 contract, RDL won the recompetition for the basic year and four 1-year options.

## 2. PARTICIPATION IN THE SUMMER RESEARCH PROGRAM

The SRP began with faculty associates in 1979; graduate students were added in 1982 and high school students in 1986. The following table shows the number of associates in the program each year.

Table 1: SRP Participation, by Year

YEAR	Number of Participants			TOTAL
	SFRP	GSRP	HSAP	
1979	70			70
1980	87			87
1981	87			87
1982	91	17		108
1983	101	53		154
1984	152	84		236
1985	154	92		246
1986	158	100	42	300
1987	159	101	73	333
1988	153	107	101	361
1989	168	102	103	373
1990	165	121	132	418
1991	170	142	132	444
1992	185	121	159	464
1993	187	117	136	440
1994	192	117	133	442

Beginning in 1993, due to budget cuts, some of the laboratories weren't able to afford to fund as many associates as in previous years; in one case a laboratory did not fund any additional associates. However, the table shows that, overall, the number of participating associates increased this year because two laboratories funded more associates than they had in previous years.

### **3. RECRUITING AND SELECTION**

The SRP is conducted on a nationally advertised and competitive-selection basis. The advertising for faculty and graduate students consisted primarily of the mailing of 8,000 44-page SRP brochures to chairpersons of departments relevant to AFOSR research and to administrators of grants in accredited universities, colleges, and technical institutions. Historically Black Colleges and Universities (HBCUs) and Minority Institutions (MIs) were included. Brochures also went to all participating USAF laboratories, the previous year's participants, and numerous (over 600 annually) individual requesters.

Due to a delay in awarding the new contract, RDL was not able to place advertisements in any of the following publications in which the SRP is normally advertised: *Black Issues in Higher Education*, *Chemical & Engineering News*, *IEEE Spectrum* and *Physics Today*.

High school applicants can participate only in laboratories located no more than 20 miles from their residence. Tailored brochures on the HSAP were sent to the head counselors of 180 high schools in the vicinity of participating laboratories, with instructions for publicizing the program in their schools. High school students selected to serve at Wright Laboratory's Armament Directorate (Eglin Air Force Base, Florida) serve eleven weeks as opposed to the eight weeks normally worked by high school students at all other participating laboratories.

Each SFRP or GSRP applicant is given a first, second, and third choice of laboratory. High school students who have more than one laboratory or directorate near their homes are also given first, second, and third choices.

Laboratories make their selections and prioritize their nominees. AFOSR then determines the number to be funded at each laboratory and approves laboratories' selections.

Subsequently, laboratories use their own funds to sponsor additional candidates. Some selectees do not accept the appointment, so alternate candidates are chosen. This multi-step selection procedure results in some candidates being notified of their acceptance after scheduled deadlines. The total applicants and participants for 1994 are shown in this table.

Table 2: 1994 Applicants and Participants

PARTICIPANT CATEGORY	TOTAL APPLICANTS	SELECTEES	DECLINING SELECTEES
SFRP (HBCU/MI)	600 (90)	192 (16)	30 (7)
GSRP (HBCU/MI)	322 (11)	117 (6)	11 (0)
HSAP	562	133	14
<b>TOTAL</b>	<b>1484</b>	<b>442</b>	<b>55</b>

### **4. SITE VISITS**

During June and July of 1994, representatives of both AFOSR/NI and RDL visited each participating laboratory to provide briefings, answer questions, and resolve problems for both laboratory personnel and participants. The objective was to ensure that the SRP would be as constructive as possible for all participants. Both SRP participants and RDL representatives found these visits beneficial. At many of the laboratories, this was the only opportunity for all participants to meet at one time to share their experiences and exchange ideas.

## **5. HISTORICALLY BLACK COLLEGES AND UNIVERSITIES AND MINORITY INSTITUTIONS (HBCU/MIs)**

In previous years, an RDL program representative visited from seven to ten different HBCU/MIs to promote interest in the SRP among the faculty and graduate students. Due to the late contract award date (January 1994) no time was available to visit HBCU/MIs this past year.

In addition to RDL's special recruiting efforts, AFOSR attempts each year to obtain additional funding or use leftover funding from cancellations the past year to fund HBCU/MI associates. This year, seven HBCU/MI SFRPs declined after they were selected. The following table records HBCU/MI participation in this program.

Table 3: SRP HBCU/MI Participation, by Year

YEAR	SFRP		GSRP	
	Applicants	Participants	Applicants	Participants
1985	76	23	15	11
1986	70	18	20	10
1987	82	32	32	10
1988	53	17	23	14
1989	39	15	13	4
1990	43	14	17	3
1991	42	13	8	5
1992	70	13	9	5
1993	60	13	6	2
1994	90	16	11	6

## **6. SRP FUNDING SOURCES**

Funding sources for the 1994 SRP were the AFOSR-provided slots for the basic contract and laboratory funds. Funding sources by category for the 1994 SRP selected participants are shown here.

Table 4: 1994 SRP Associate Funding

FUNDING CATEGORY	SFRP	GSRP	HSAP
AFOSR Basic Allocation Funds	150	98 <sup>*1</sup>	121 <sup>*2</sup>
USAF Laboratory Funds	37	19	12
HBCU/MI By AFOSR (Using Procured Addn'l Funds)	5	0	0
<b>TOTAL</b>	<b>192</b>	<b>117</b>	<b>133</b>

\*1 - 100 were selected, but two canceled too late to be replaced.

\*2 - 125 were selected, but four canceled too late to be replaced.

## **7. COMPENSATION FOR PARTICIPANTS**

Compensation for SRP participants, per five-day work week, is shown in this table.

Table 5: 1994 SRP Associate Compensation

PARTICIPANT CATEGORY	1991	1992	1993	1994
Faculty Members	\$690	\$718	\$740	\$740
Graduate Student (Master's Degree)	\$425	\$442	\$455	\$455
Graduate Student (Bachelor's Degree)	\$365	\$380	\$391	\$391
High School Student (First Year)	\$200	\$200	\$200	\$200
High School Student (Subsequent Years)	\$240	\$240	\$240	\$240

The program also offered associates whose homes were more than 50 miles from the laboratory an expense allowance (seven days per week) of \$50/day for faculty and \$37/day for graduate students. Transportation to the laboratory at the beginning of their tour and back to their home destinations at the end was also reimbursed for these participants. Of the combined SFRP and GSRP associates, 58% (178 out of 309) claimed travel reimbursements at an average round-trip cost of \$860.

Faculty members were encouraged to visit their laboratories before their summer tour began. All costs of these orientation visits were reimbursed. Forty-one percent (78 out of 192) of faculty associates took orientation trips at an average cost of \$498. Many faculty associates noted on their evaluation forms that due to the late notice of acceptance into the 1994 SRP (caused by the late award in January 1994 of the contract) there wasn't enough time to attend an orientation visit prior to their tour start date. In 1993, 58 % of SFRP associates took orientation visits at an average cost of \$685.

Program participants submitted biweekly vouchers countersigned by their laboratory research focal point, and RDL issued paychecks so as to arrive in associates' hands two weeks later.

HSAP program participants were considered actual RDL employees, and their respective state and federal income tax and Social Security were withheld from their paychecks. By the nature of their independent research, SFRP and GSRP program participants were considered to be consultants or independent contractors. As such, SFRP and GSRP associates were responsible for their own income taxes, Social Security, and insurance.

## 8. CONTENTS OF THE 1994 REPORT

The complete set of reports for the 1994 SRP includes this program management report augmented by fifteen volumes of final research reports by the 1994 associates as indicated below:

Table 6: 1994 SRP Final Report Volume Assignments

LABORATORY	VOLUME		
	SFRP	GSRP	HSAP
Armstrong	2	7	12
Phillips	3	8	13
Rome	4	9	14
Wright	5A, 5B	10	15
AEDC, FJSRL, WHMC	6	11	16

AEDC = Arnold Engineering Development Center  
FJSRL = Frank J. Seiler Research Laboratory  
WHMC = Wilford Hall Medical Center

## **APPENDIX A – PROGRAM STATISTICAL SUMMARY**

### **A. Colleges/Universities Represented**

Selected SFRP and GSRP associates represent 158 different colleges, universities, and institutions.

### **B. States Represented**

SFRP -Applicants came from 46 states plus Washington D.C. and Puerto Rico. Selectees represent 40 states.

GSRP - Applicants came from 46 states and Puerto Rico. Selectees represent 34 states.

HSAP - Applicants came from fifteen states. Selectees represent ten states.

### **C. Academic Disciplines Represented**

The academic disciplines of the combined 192 SFRP associates are as follows:

Electrical Engineering	22.4%
Mechanical Engineering	14.0%
Physics: General, Nuclear & Plasma	12.2%
Chemistry & Chemical Engineering	11.2%
Mathematics & Statistics	8.1%
Psychology	7.0%
Computer Science	6.4%
Aerospace & Aeronautical Engineering	4.8%
Engineering Science	2.7%
Biology & Inorganic Chemistry	2.2%
Physics: Electro-Optics & Photonics	2.2%
Communication	1.6%
Industrial & Civil Engineering	1.6%
Physiology	1.1%
Polymer Science	1.1%
Education	0.5%
Pharmaceutics	0.5%
Veterinary Medicine	0.5%
<hr/> TOTAL	100%

Table A-1. Total Participants

Number of Participants	
SFRP	192
GSRP	117
HSAP	133
TOTAL	442

Table A-2. Degrees Represented

Degrees Represented			
	SFRP	GSRP	TOTAL
Doctoral	189	0	189
Master's	3	47	50
Bachelor's	0	70	70
TOTAL	192	117	309

Table A-3. SFRP Academic Titles

Academic Titles	
Assistant Professor	74
Associate Professor	63
Professor	44
Instructor	5
Chairman	1
Visiting Professor	1
Visiting Assoc. Prof.	1
Research Associate	3
TOTAL	192

Table A-4. Source of Learning About SRP

SOURCE	SFRP		GSRP	
	Applicants	Selectees	Applicants	Selectees
Applied/participated in prior years	26%	37%	10%	13%
	19%	17%	12%	12%
	32%	18%	19%	12%
	15%	24%	9%	12%
	--	--	39%	43%
	8%	4%	11%	8%
TOTAL	100%	100%	100%	100%

Table A-5. Ethnic Background of Applicants and Selectees

	SFRP		GSRP		HSAP	
	Applicants	Selectees	Applicants	Selectees	Applicants	Selectees
American Indian or Native Alaskan	0.2%	0%	1%	0%	0.4%	0%
Asian/Pacific Islander	30%	20%	6%	8%	7%	10%
Black	4%	1.5%	3%	3%	7%	2%
Hispanic	3%	1.9%	4%	4.5%	11%	8%
Caucasian	51%	63%	77%	77%	70%	75%
Preferred not to answer	12%	14%	9%	7%	4%	5%
TOTAL	100%	100%	100%	100%	99%	100%

Table A-6. Percentages of Selectees receiving their 1st, 2nd, or 3rd Choices of Directorate

	1st Choice	2nd Choice	3rd Choice	Other Than Their Choice
SFRP	70%	7%	3%	20%
GSRP	76%	2%	2%	20%

## **APPENDIX B -- SRP EVALUATION RESPONSES**

### **1. OVERVIEW**

Evaluations were completed and returned to RDL by four groups at the completion of the SRP. The number of respondents in each group is shown below.

Table B-1. Total SRP Evaluations Received

Evaluation Group	Responses
SFRP & GSRPs	275
HSAPs	116
USAF Laboratory Focal Points	109
USAF Laboratory HSAP Mentors	54

All groups indicate near-unanimous enthusiasm for the SRP experience.

Typical comments from 1994 SRP associates are:

"[The SRP was an] excellent opportunity to work in state-of-the-art facility with top-notch people."

"[The SRP experience] enabled exposure to interesting scientific application problems; enhancement of knowledge and insight into 'real-world' problems."

"[The SRP] was a great opportunity for resourceful and independent faculty [members] from small colleges to obtain research credentials."

"The laboratory personnel I worked with are tremendous, both personally and scientifically. I cannot emphasize how wonderful they are."

"The one-on-one relationship with my mentor and the hands on research experience improved [my] understanding of physics in addition to improving my library research skills. Very valuable for [both] college and career!"

Typical comments from laboratory focal points and mentors are:

"This program [AFOSR - SFRP] has been a 'God Send' for us. Ties established with summer faculty have proven invaluable."

"Program was excellent from our perspective. So much was accomplished that new options became viable "

"This program managed to get around most of the red tape and 'BS' associated with most Air Force programs. Good Job!"

"Great program for high school students to be introduced to the research environment. Highly educational for others [at laboratory]."

"This is an excellent program to introduce students to technology and give them a feel for [science/engineering] career fields. I view any return benefit to the government to be 'icing on the cake' and have usually benefitted."

The summarized recommendations for program improvement from both associates and laboratory personnel are listed below (Note: basically the same as in previous years.)

- A. Better preparation on the labs' part prior to associates' arrival (i.e., office space, computer assets, clearly defined scope of work).
- B. Laboratory sponsor seminar presentations of work conducted by associates, and/or organized social functions for associates to collectively meet and share SRP experiences.
- C. Laboratory focal points collectively suggest more AFOSR allocated associate positions, so that more people may share in the experience.
- D. Associates collectively suggest higher stipends for SRP associates.
- E. Both HSAP Air Force laboratory mentors and associates would like the summer tour extended from the current 8 weeks to either 10 or 11 weeks; the groups state it takes 4-6 weeks just to get high school students up-to-speed on what's going on at laboratory. (Note: this same argument was used to raise the faculty and graduate student participation time a few years ago.)

## 2. 1994 USAF LABORATORY FOCAL POINT (LFP) EVALUATION RESPONSES

The summarized results listed below are from the 109 LFP evaluations received.

1. LFP evaluations received and associate preferences:

Table B-2. Air Force LFP Evaluation Responses (By Type)

Lab	Evals Recv'd	How Many Associates Would You Prefer To Get ? (% Response)											
		SFRP				GSRP (w/Univ Professor)				GSRP (w/o Univ Professor)			
		0	1	2	3+	0	1	2	3+	0	1	2	3+
AEDC	10	30	50	0	20	50	40	0	10	40	60	0	0
AL	44	34	50	6	9	54	34	12	0	56	31	12	0
FJSRL	3	33	33	33	0	67	33	0	0	33	67	0	0
PL	14	28	43	28	0	57	21	21	0	71	28	0	0
RL	3	33	67	0	0	67	0	33	0	100	0	0	0
WHMC	1	0	0	100	0	0	100	0	0	0	100	0	0
WL	46	15	61	24	0	56	30	13	0	76	17	6	0
Total	121	25%	43%	27%	4%	50%	37%	11%	1%	54%	43%	3%	0%

**LFP Evaluation Summary.** The summarized responses, by laboratory, are listed on the following page. LFPs were asked to rate the following questions on a scale from 1 (below average) to 5 (above average).

2. LFPs involved in SRP associate application evaluation process:
  - a. Time available for evaluation of applications:
  - b. Adequacy of applications for selection process:
3. Value of orientation trips:
4. Length of research tour:
5. a. Benefits of associate's work to laboratory:  
b. Benefits of associate's work to Air Force:
6. a. Enhancement of research qualifications for LFP and staff:  
b. Enhancement of research qualifications for SFRP associate:  
c. Enhancement of research qualifications for GSRP associate:
7. a. Enhancement of knowledge for LFP and staff:  
b. Enhancement of knowledge for SFRP associate:  
c. Enhancement of knowledge for GSRP associate:
8. Value of Air Force and university links:
9. Potential for future collaboration:
10. a. Your working relationship with SFRP:  
b. Your working relationship with GSRP:
11. Expenditure of your time worthwhile:

(Continued on next page)

- 12. Quality of program literature for associate:
- 13. a. Quality of RDL's communications with you:
  - b. Quality of RDL's communications with associates:
- 14. Overall assessment of SRP:

Laboratory Focal Point Responses to above questions

	<i>AEDC</i>	<i>AL</i>	<i>FJSRL</i>	<i>PL</i>	<i>RL</i>	<i>WHMC</i>	<i>WL</i>
<i># Evals Recv'd</i>	10	32	3	14	3	1	46
<i>Question #</i>							
2	90 %	62 %	100 %	64 %	100 %	100 %	83 %
2a	<b>3.5</b>	<b>3.5</b>	4.7	4.4	4.0	4.0	<b>3.7</b>
2b	4.0	3.8	4.0	4.3	4.3	4.0	3.9
3	4.2	3.6	4.3	3.8	4.7	4.0	4.0
4	3.8	3.9	4.0	4.2	4.3	NO ENTRY	4.0
5a	4.1	4.4	4.7	4.9	4.3	3.0	4.6
5b	4.0	4.2	4.7	4.7	4.3	3.0	4.5
6a	<b>3.6</b>	4.1	<b>3.7</b>	4.5	4.3	<b>3.0</b>	4.1
6b	3.6	4.0	4.0	4.4	4.7	3.0	4.2
6c	3.3	4.2	4.0	4.5	4.5	3.0	4.2
7a	3.9	4.3	4.0	4.6	4.0	3.0	4.2
7b	4.1	4.3	4.3	4.6	4.7	3.0	4.3
7c	3.3	4.1	4.5	4.5	4.5	5.0	4.3
8	4.2	4.3	5.0	4.9	4.3	5.0	4.7
9	3.8	4.1	4.7	5.0	4.7	5.0	4.6
10a	4.6	4.5	5.0	4.9	4.7	5.0	4.7
10b	4.3	4.2	5.0	4.3	5.0	5.0	4.5
11	4.1	4.5	4.3	4.9	4.7	4.0	4.4
12	4.1	3.9	4.0	4.4	4.7	3.0	4.1
13a	<b>3.8</b>	<b>2.9</b>	4.0	4.0	4.7	<b>3.0</b>	<b>3.6</b>
13b	<b>3.8</b>	<b>2.9</b>	4.0	4.3	4.7	<b>3.0</b>	<b>3.8</b>
14	4.5	4.4	5.0	4.9	4.7	4.0	4.5

### **3. 1994 SFRP & GSRP EVALUATION RESPONSES**

The summarized results listed below are from the 275 SFRP/GSRP evaluations received.

Associates were asked to rate the following questions on a scale from 1 (below average) to 5 (above average)

- |  |          |
|--|----------|
| 1. The match between the laboratories research and your field: | 4.6      |
| 2. Your working relationship with your LFP:                    | 4.8      |
| 3. Enhancement of your academic qualifications:                | 4.4      |
| 4. Enhancement of your research qualifications:                | 4.5      |
| 5. Lab readiness for you: LFP, task, plan:                     | 4.3      |
| 6. Lab readiness for you: equipment, supplies, facilities:     | 4.1      |
| 7. Lab resources:  | 4.3      |
| 8. Lab research and administrative support:                    | 4.5      |
| 9. Adequacy of brochure and associate handbook:                | 4.3      |
| 10. RDL communications with you:                               | 4.3      |
| 11. Overall payment procedures:                                | 3.8      |
| 12. Overall assessment of the SRP:                             | 4.7      |
| 13.     a. Would you apply again?                              | Yes: 85% |
| b. Will you continue this or related research?                 | Yes: 95% |
| 14. Was length of your tour satisfactory?                      | Yes: 86% |
| 15. Percentage of associates who engaged in:                   |          |
| a. Seminar presentation:                                       | 52%      |
| b. Technical meetings:   | 32%      |
| c. Social functions:   | 03%      |
| d. Other   | 01%      |

16. Percentage of associates who experienced difficulties in:

- |                     |     |
|---------------------|-----|
| a. Finding housing: | 12% |
| b. Check Cashing:   | 03% |

17. Where did you stay during your SRP tour?

- |                      |     |
|----------------------|-----|
| a. At Home:          | 20% |
| b. With Friend:      | 06% |
| c. On Local Economy: | 47% |
| d. Base Quarters:    | 10% |

**THIS SECTION FACULTY ONLY:**

18. Were graduate students working with you? Yes: 23%

19. Would you bring graduate students next year? Yes: 56%

20. Value of orientation visit:

- |                 |     |
|-----------------|-----|
| Essential:      | 29% |
| Convenient:     | 20% |
| Not Worth Cost: | 01% |
| Not Used:       | 34% |

**THIS SECTION GRADUATE STUDENTS ONLY:**

21. Who did you work with:

- |                       |     |
|-----------------------|-----|
| University Professor: | 18% |
| Laboratory Scientist: | 54% |

#### **4. 1994 USAF LABORATORY HSAP MENTOR EVALUATION RESPONSES**

The summarized results listed below are from the 54 mentor evaluations received.

1. Mentor apprentice preferences:

Table B-3. Air Force Mentor Responses

Laboratory	# Evals Recv'd	How Many Apprentices Would You Prefer To Get ?				
		HSAP Apprentices Preferred	0	1	2	3+
AEDC	6		0	100	0	0
AL	17		29	47	6	18
PL	9		22	78	0	0
RL	4		25	75	0	0
WL	18		22	55	17	6
Total	54		20%	71%	5%	5%

Mentors were asked to rate the following questions on a scale from 1 (below average) to 5 (above average)

2. Mentors involved in SRP apprentice application evaluation process:
  - a. Time available for evaluation of applications:
  - b. Adequacy of applications for selection process:
3. Laboratory's preparation for apprentice:
4. Mentor's preparation for apprentice:
5. Length of research tour:
6. Benefits of apprentice's work to U.S. Air force:
7. Enhancement of academic qualifications for apprentice:
8. Enhancement of research skills for apprentice:
9. Value of U.S. Air Force/high school links:
10. Mentor's working relationship with apprentice:
11. Expenditure of mentor's time worthwhile:
12. Quality of program literature for apprentice:
13.
  - a. Quality of RDL's communications with mentors:
  - b. Quality of RDL's communication with apprentices:
14. Overall assessment of SRP:

	<i>AEDC</i>	<i>AL</i>	<i>PL</i>	<i>RL</i>	<i>WL</i>
<i># Evals Recv'd</i>	<b>6</b>	<b>17</b>	<b>9</b>	<b>4</b>	<b>18</b>
<i>Question #</i>					
<b>2</b>	100 %	76 %	56 %	75 %	61 %
<b>2a</b>	4.2	4.0	<b>3.1</b>	<b>3.7</b>	<b>3.5</b>
<b>2b</b>	4.0	4.5	4.0	4.0	3.8
<b>3</b>	4.3	<b>3.8</b>	<b>3.9</b>	<b>3.8</b>	<b>3.8</b>
<b>4</b>	4.5	<b>3.7</b>	<b>3.4</b>	4.2	<b>3.9</b>
<b>5</b>	<b>3.5</b>	4.1	<b>3.1</b>	<b>3.7</b>	<b>3.6</b>
<b>6</b>	4.3	3.9	4.0	4.0	4.2
<b>7</b>	4.0	4.4	4.3	4.2	3.9
<b>8</b>	4.7	4.4	4.4	4.2	4.0
<b>9</b>	4.7	4.2	3.7	4.5	4.0
<b>10</b>	4.7	4.5	4.4	4.5	4.2
<b>11</b>	4.8	4.3	4.0	4.5	4.1
<b>12</b>	4.2	4.1	4.1	4.8	3.4
<b>13a</b>	<b>3.5</b>	<b>3.9</b>	<b>3.7</b>	4.0	<b>3.1</b>
<b>13b</b>	4.0	4.1	3.4	4.0	3.5
<b>14</b>	4.3	4.5	3.8	4.5	4.1

## **5. 1994 HSAP EVALUATION RESPONSES**

The summarized results listed below are from the 116 HSAP evaluations received.

HSAP apprentices were asked to rate the following questions on a scale from 1 (below average) to 5 (above average)

- |   |          |
|---|----------|
| 1. Match of lab research to you interest:                                       | 3.9      |
| 2. Apprentices working relationship with their mentor and other lab scientists: | 4.6      |
| 3. Enhancement of your academic qualifications:                                 | 4.4      |
| 4. Enhancement of your research qualifications:                                 | 4.1      |
| 5. Lab readiness for you: mentor, task, work plan                               | 3.7      |
| 6. Lab readiness for you: equipment supplies facilities                         | 4.3      |
| 7. Lab resources: availability  | 4.3      |
| 8. Lab research and administrative support:                                     | 4.4      |
| 9. Adequacy of RDL's apprentice handbook and administrative materials:          | 4.0      |
| 10. Responsiveness of RDL's communications:                                     | 3.5      |
| 11. Overall payment procedures:   | 3.3      |
| 12. Overall assessment of SRP value to you:                                     | 4.5      |
| 13. Would you apply again next year?  | Yes: 88% |
| 14. Was length of SRP tour satisfactory?  | Yes: 78% |
| 15. Percentages of apprentices who engaged in:                                  |          |
| a. Seminar presentation:  | 48%      |
| b. Technical meetings:  | 23%      |
| c. Social functions:  | 18%      |

**Effect of Dissolved Gases on the Discharge Coefficient in a Single-Orifice Injector**

**William W. Brocklehurst**

**Graduate Student**

**Department of Aerospace Engineering and Engineering Mechanics**

**University of Cincinnati**

**Mail Location #70**

**Cincinnati, OH 45221**

**Final Report for:**

**Summer Graduate Student Research Program**

**Phillips Laboratory**

**Sponsored by:**

**Air Force Office of Scientific Research**

**Bolling Air Force Base, DC**

**and**

**Phillips Laboratory**

**September 1994**

## **Effect of Dissolved Gases on the Discharge Coefficient in a Single-Orifice Injector**

William W. Brocklehurst

Graduate Student

Department of Aerospace Engineering and Engineering Mechanics

University of Cincinnati

### **Abstract**

The effect of dissolved gases on the discharge coefficient in a single-orifice injector was studied. The high pressure cold flow chamber at USAF Phillips Laboratory was used to accumulate the experimental data. Discharge coefficients were measured for injector  $\Delta P$ 's of 0 to 100 psi and a variety of system configurations. Experimental results show that the orifice discharge coefficient has a dependence on the dissolved gas concentration in the working fluid (demineralized water in this case). As the dissolved gas concentration increases, the orifice discharge coefficient also increases. The effect is greater at lower orifice flow rates and seems to have no effect when the flow is cavitating at the higher  $\Delta P$ 's. The orifice discharge coefficient was found to be very dependent on the dissolved gas concentration in the working fluid.

## **Effect of Dissolved Gases on the Discharge Coefficient in a Single-Orifice Injector**

**William W. Brocklehurst**

### **Introduction**

The cold flow facility at the USAF Phillips Laboratory was developed to directly study the effect of injector design and flow conditions on spray field characteristics. This data can be used to help predict stability, mixing, chamber wall compatibility, combustion efficiency, injector pressure drop, and drop sizes. The 21" diameter chamber is rated to 2000 psi and is equip with sapphire optical access windows, a variable height injector housing assembly, and a 27 tube (1/4" dia.) mechanical patternizer rake. The facility operates at pressures up to 2000 psig which are comparable to actual booster-sized, high pressure combustion chambers and is the highest reported pressure capability for such a test facility.<sup>1</sup>

The results of recent orifice flow testing at Phillips Laboratory have shown a 'divergence' in the discharge coefficient data. The discharge coefficient was increasing as the orifice  $\Delta P$  was lowered. The error can be as high as 10% in the lower  $\Delta P$  range. This effect was also noticed as the manifold cross flow rate increased.

It was believed that gases dissolved in the working fluid (water) were a factor contributing to this divergence as they came out of solution. The effect of dissolved gases was to be measured and documented to assure accurate and comparable flow data in the future.

### **Apparatus**

The orifice plate used has a diameter of 0.0784 inches and an L/D of approximately 5. The water supply system is capable of delivering up to 15 GPM with a tank pressure of around 2200 psi. Figure 1 shows a schematic of the manifold design.

The manifold is a cross flow channel type. When the orifice plate is installed in the manifold, a channel 0.26" by 0.24" is formed. Water is then passed through the channel, and consequently some water passes down through the orifice. By recording the flow rate at the entrance and exit of the cross flow channel, simple subtraction gives the flow rate down through the orifice. A static pressure tap,  $P_1$  is located directly over the orifice along the top of the cross flow channel. A differential pressure transducer connected to  $P_1$  and a chamber pressure tap,  $P_c$  directly measures the  $\Delta P$  across the orifice. A flow regulator downstream of the cross flow channel is used to hold the desired  $P_1$ . When testing over a range

of  $\Delta P$ 's, the procedure is to hold  $P_1$  constant and increase  $P_c$  to produce different  $\Delta P$ 's. Figure 2 shows the location of the  $P_1$  pressure tap in relation to the orifice.

The manifold is used to produce three very different flow conditions: cross flow, zero cross flow, and dead-head. In the cross flow configuration, flow enters the channel ( $Q_{in}$ ) and exits through the orifice ( $Q_{orifice}$ ) and channel exit ( $Q_{out}$ ). The flow rate through the orifice is then given by:  $Q_{orifice} = Q_{in} - Q_{out}$ . In the zero cross flow configuration, the channel exit is blocked and flow entering the channel exits only through the orifice giving:  $Q_{orifice} = Q_{in}$ . In the dead-head configuration, flow enters through both ends of the channel and leaves only through the orifice giving:  $Q_{orifice} = Q_{in} + Q_{out}$ . Figure 1 also shows the three manifold configurations.

### Methodology

In order to qualitatively and quantitatively measure the effect of dissolved gases on the orifice discharge coefficient, the dissolved gas concentration in the fluid supply tank is controlled and measured. Four tank treatments are used: degassed, baseline, saturated at atmosphere, and saturated at 100 psi.

A 1/2 HP Kinney Vacuum Pump is attached to the supply tank to prepare for the degassed run. The empty water tank is evacuated to 4 psia and then filled halfway through a generic Delvan spray nozzle while holding the vacuum. The half-full tank then remains under vacuum for 2 hours before being brought up to pressure and run. The tank is only filled halfway to produce the largest possible surface area for the vacuum to work on. The spray nozzle also increases the surface area while filling to greatly increase the outgassing rate of the water. By flowing immediately after pressurizing the tank, the  $GN_2$  used to pressurize is not given sufficient time to diffuse into the supply water and hence invalidate the run. To safeguard the flow system and transducers, the supply tank is never run dry while flowing through the system thereby ensuring that the water directly in contact with the  $GN_2$  never passes through the orifice. Dissolved gas measurements before, after, and during runs show no significant change in dissolved gas concentration. Dissolved oxygen concentration in the degassed tank runs are usually around 2 PPM.

To prepare the tank for a baseline run, the tank is completely filled as usual. The demineralized water is supplied by a 6000 gal. tank-truck outside of the facility. Due to extreme temperature variations outside at Edwards AFB, the dissolved oxygen content in the tank-truck can vary from 5 PPM to 8 PPM during the day. The tests are run shortly after filling the tank to avoid natural outgassing. It was found that if a full tank is allowed to sit over a period little more than one day, the tank (inside of the flow facility) will naturally outgass to about 1.5 PPM. Again, dissolved gas measurements are recorded before, after, and during each run.

A saturated condition is prepared by bubbling compressed air through the supply tank overnight to ensure saturation at atmospheric pressure. A filter is placed on the air line to prevent tank water contamination. Again, the tests are run soon after pressurizing and the dissolved oxygen measurements are around 8.5 PPM.

To fully evaluate the effect of dissolved gases, a 'worst-case' scenario is run. Compressed air is bubbled through the tank much like the saturated case but the water supply tank is kept at 100 psig. Dissolved oxygen measurements from 11 PPM to 13 PPM are common. The milky appearance of the supply water is also a good indication that there is a sufficient gas concentration in the tank.

### Dissolved Gas Measurements

Evacuating and bubbling air through the supply tank significantly changes the dissolved gas concentration in the tank water. Though no direct measurement of the gas concentration is needed for a qualitative analysis, a concentration measurement is helpful both in a quantitative analysis and in ensuring that sufficient change in gas concentration is achieved.

Since the flow system is pressurized with GN<sub>2</sub>, it was originally desired to saturate the tank with the same. However, a commercial dissolved N<sub>2</sub> meter is not readily available and partial pressure measurements are somewhat tedious. A commercial dissolved O<sub>2</sub> meter is readily available and very easy to operate. By measuring the dissolved O<sub>2</sub> content in the supply water, a quantitative comparison between tank treatments can readily be achieved. The total dissolved gas (air) concentration can also be calculated accurately from the O<sub>2</sub> content.

A Cole-Parmer Model 5946-55 Oxygen Meter is used to measure the dissolved oxygen concentration in the aqueous solution. The oxygen meter provides a digital readout of sample temperature (0° to 50°C) and dissolved oxygen content (0 to 19.99 mg/L ± 0.1 mg/L). The oxygen meter probe consists of two electrodes separated by an electrolyte solution. An oxygen permeable membrane separates the electrodes and solution from the sample. When a voltage is passed through the electrodes, thereby reducing the amount of oxygen that has passed through the membrane, the resulting current is linearly proportional to the dissolved oxygen content.

The meter is calibrated to display milligrams of dissolved oxygen per liter of water. To convert from mg/L to PPM, one simply needs to divide by the specific gravity of the sample. However, for 0° to 30°C temperature ranges, the difference between PPM and mg/L is less than 0.5% in fresh water and less than 5% in most sea water.<sup>3</sup> Therefore, the reading on the meter (mg O<sub>2</sub>/L H<sub>2</sub>O) is taken to be the dissolved oxygen content in PPM.

The oxygen meter has proven to be a good indicator of tank treatment accuracy. For the degassed cases, dissolved oxygen concentrations of 2.0 to 3.7 PPM were obtained. The baseline cases ran from 5.2 to 7.5 PPM. Saturating at atmospheric pressure (13.2 psia @ Edwards AFB) gave 8.5 PPM of dissolved oxygen and 11 PPM at 100 psig saturation.

Water samples are taken from a drain line at the bottom of the supply tank next to the exit water line. Dissolved gas measurements are made quickly to avoid natural outgassing effects. By using the separate drain line, samples can be taken from the tank even while it was under pressure.

### Discharge Coefficient Calculations

Before evaluating the effect of dissolved gases on the orifice discharge coefficient is it useful to discuss the discharge coefficient calculations. If an orifice is supplied by an infinite reservoir or situated directly in a moving flow, the discharge coefficient,  $C_d$  is defined as the ratio between the actual mass flow rate and the theoretical mass flow rate. The theoretical mass flow rate is calculated from the orifice  $\Delta P$  using Bernoulli's equation.

$$C_d = (\rho Q_{act}) / (\rho A V_b)$$

where:

- $\rho$  = fluid density
- = function of temperature
- $Q_{act}$  = actual measured volumetric flow rate
- =  $Q_{off}$
- $A$  = orifice area
- =  $3.1145 \text{ mm}^2$
- $V_b$  = theoretical (Bernoulli) velocity
- =  $\sqrt{2\Delta P/\rho}$

When introducing relatively large amounts of dissolved gas into the fluid, changes in  $Q_{act}$  and  $\rho$  must be examined. In the worst-case scenario (13 PPM O<sub>2</sub>) the change in fluid density is less than 0.01% and can safely be ignored. Effects of temperature on the water density are taken into account by the system's software both in the actual and theoretical mass flow rate calculations. The fluid density can therefore be canceled out in the  $C_d$  calculation.

The effect of dissolved gases on the flow meter readings, specifically in the flowmeter turbines, was also addressed. It was thought that the dissolved gases were coming out of solution in the flowmeter turbines (inductance pick-up type) and producing an error in the measured flow rate. Three series of test were done to verify the flow meter readings over their operating range. Flow rates from 0.5 to 6.0 GPM were physically collected, measured, and compared to the flow meter readings for dissolved O<sub>2</sub> tank concentrations of 1.5, 4.6, and 13.0 PPM. No bias with dissolved gas concentration was found and all of the flow meter readings were within 3% of the collected flow. A 3% difference is very acceptable when

considering operator error in measuring the sample time and mass. All in all, a 1% accuracy is easily achieved for flow rates under 6 GPM. It was therefore determined that the flow meter readings were accurate and that density change due to the dissolved gases was negligible. These tests were also helpful in validating the flow meter calibrations.

The  $\Delta P$  measurement across the orifice was also investigated. The flow control program for the cold flow chamber directly reads the orifice  $\Delta P$  from a differential pressure transducer connected to pressure taps above the orifice in the cross flow channel,  $P_1$ , and in the pressure chamber,  $P_c$ .  $P_c$  is also directly measured through another transducer tapped into the pressure chamber.  $P_1$  is then calculated by the system control software from  $P_c$  and  $\Delta P$  so that a downstream regulator can be used to adjust the orifice  $\Delta P$ . It should be noted that  $P_1$  is a static pressure measurement above the orifice and not the total pressure in the cross flow channel. The project engineers working on the cold flow chamber felt that  $C_d$  should be calculated from the pressure that the orifice actually sees. When flow is passing over the orifice, the orifice will only see the static pressure present in the channel. When angled orifice plates are used it is planned to use a geometric correction factor to place  $P_1$  somewhere between the cross flow channel total and static pressure. It is also worthwhile to mention that at an inlet flow rate of 3.0 GPM, the dynamic pressure of the flow in the cross flow channel is only about 1.5% of the static pressure. The repeatability of runs and consistent procedure also allow one to say that the observed dissolved gas effects are real and not simply an error in the calculation procedure.

## Results

Several tests were run to evaluate the effect of dissolved gases on the orifice discharge coefficient. In presenting the data, the orifice  $C_d$  is plotted versus  $P_{cav}$ .  $P_{cav}$  is a parameter used at Phillips Laboratory in the analysis of orifice hydraulics.  $P_{cav}$  is simply  $(P_1 - P_{vap})/(P_1 - P_c)$ , where  $P_{vap}$  is the vapor pressure of the fluid as a function of temperature. At 25°C, the vapor pressure of water is only 0.46 psia. Due to the relatively low value of  $P_{vap}$ ,  $P_{cav}$  is essentially the ratio  $P_1/\Delta P$ . Therefore, on the following figures, an increasing value of  $P_{cav}$  represents a lowering of the orifice  $\Delta P$  and consequently a lower orifice flow rate.

Another important point to note is the gradual decrease in mass flow rate through the system as  $P_{cav}$  increases. This is a problem in the fluid supply system. As the water tank is emptied, more GN<sub>2</sub> is required to keep the same flow rate going into the cross flow channel. Though most of the system is automated, the supply tank pressure and flow rate is still controlled by manual regulators. If the supply pressure or fluid throttling valve are adjusted during the run, large spikes in the  $C_d$  curve will occur. It was decided that a slight reduction in flow rate over the runs was preferable to invalid data. A computer controlled flow regulator is already in-house and will be installed on the water supply line in the near

future. This will allow for much more accurate system flow rate control. The mass flow rate reduction with increasing  $P_{cav}$  in the zero cross flow and dead-head configurations is to be expected however. In these configurations, all of the flow entering the manifold is exiting through the orifice and will therefore decrease as the orifice  $\Delta P$  is lowered. On all of the following figures the entrance manifold velocity,  $V_e$  is documented for the beginning and end of the run. The flow rate usually decreases to about 90% by the end of the runs around a  $P_{cav}$  of 10 for the cross flow configuration. This effect is most noticeable at the lower cross flow rates.

The gradual decrease in flow rate during a cross flow run also results in an increase in  $P_1$ . It was originally thought (after excluding density and flow meter errors) that dissolved gases may have been coming out of solution by the  $P_1$  pressure tap and affecting its reading thereby producing an error in the  $C_d$  calculations. Unfortunately, since  $P_1$  is already changing throughout the run no conclusion can be made about dissolved gas effects on the  $P_1$  reading. Installing the computer controlled flow regulator should stabilize the incoming flow rate and  $P_1$  thereby enabling an evaluation of dissolved gases on the  $P_1$  reading.

Figure 3 shows the orifice discharge coefficient variation due only to the difference in dissolved gas concentration. The five runs were performed at the same cross flow velocity. Seeing as how all five of the runs are identical except for dissolved gas concentration, one can conclude that at higher dissolved gas concentrations, the orifice discharge coefficient is higher.

Figure 4 shows the  $C_d$  variation at the zero cross flow configuration. The same trend is observed as in Figure 3. Figure 5 shows  $C_d$  variation at the dead-head configuration. Once again the dissolved gas effect is the same as in previous figures. It is interesting to note that at the lower dissolved gas concentrations, the  $C_d$  curve becomes fairly constant (as is expected) in the non-cavitating region. This is yet another indication that dissolved gases are affecting the orifice  $C_d$ . Table 1 shows the percent difference in  $C_d$  caused by dissolved gases for the three configurations.

Configuration	$P_{cav}$	Concentration range (dissolved oxygen)	% difference in $C_d$
3 GPM cross flow	2.0	2.0 - 11.0 PPM	1.97
	4.0		4.01
	8.0		6.18
Zero cross flow ( $Q_{orf} = 1.1$ GPM)	2.0	2.0 - 11.0 PPM	1.85
	4.0		3.19
	8.0		5.55
Dead-head ( $Q_{orf} = 1.1$ GPM)	2.0	3.7 - 6.5 PPM	0.50
	4.0		1.25
	8.0		2.93

Table 1: Effect of dissolved gases on orifice discharge coefficient

Surprisingly, dissolved gases seem to have no effect on the orifice discharge coefficient in the cavitated region below a  $P_{cav}$  of 2.0. In the cavitated region, no effect of dissolved gas or cross flow velocity is observed. However, manifold configuration does have a significant effect.

Figure 5 shows an extreme change in  $C_d$  for the dead-head configuration around  $P_{cav} = 1.9$ . This phenomena is known as 'hydraulic flip'. In the cavitated region, the flow is not attached to the orifice wall until a  $P_{cav}$  of 1.9 when it reattaches, or hydraulically flips. This is accompanied by an immediate increase in discharge coefficient. Data points were taken at 2 psi increments for all of the Figures. There are no data points between the cavitated and non-cavitated regions in the dead-head runs meaning that the hydraulic flip occurs at a distinct orifice  $\Delta P \approx 63$  psi. This phenomena has been observed consistently in the past at Phillips Laboratory while flowing with the dead-head configuration.

Figures 3 and 4 show a more gradual transition to the non-cavitated region for the cross flow and zero cross flow configurations. Though the zero cross flow configuration has a somewhat sharper transition, both are relatively smooth compared to the dead-head configuration. The flow enters the non-cavitated regime at a  $P_{cav}$  of 1.9 as in the dead-head case.

Figures 6, 7, and 8 illustrate the differences caused by changing the manifold cross flow rate. Figure 6 is simply a superposition of Figures 7 and 8. Figure 7 shows the variation of  $C_d$  with cross flow velocity at degassed conditions and is an excellent indicator of cross flow rate dependency. This dependency on cross flow rate has been observed in the past at Phillips Laboratory. The divergence of the orifice  $C_d$  is therefore dependent on dissolved gas concentration and cross flow velocity. The  $C_d$  divergence in the zero cross flow and dead-head cases seems to be due only to dissolved gas concentration.

Figures 6, 7, and 8 also show data fluctuations at the higher cross flow rates making a percent difference calculation rather unhelpful. This problem did not occur in past runs at Phillips Laboratory. Significant plumbing changes have been made to the system since the last time  $C_d$  curves were measured. These changes include the addition of a number of 90° and 180° turns in the flow system piping. Perhaps the computer controlled flow regulator will solve this problem of erratic readings at high cross flow rates.

However, calculating the divergence in Figure 7 between the cross flows of 9.4 m/sec and 4.7 m/sec gives differences comparable in magnitude to those caused by dissolved gases. At  $P_{cav}$ 's of 2.0, 4.0, and 8.0 the differences in  $C_d$  are 1.04 %, 2.16 %, and 5.95 % respectively. Apparently the orifice  $C_d$  is equally dependent upon dissolved gas concentration and cross flow velocity.

### Conclusions and Remarks

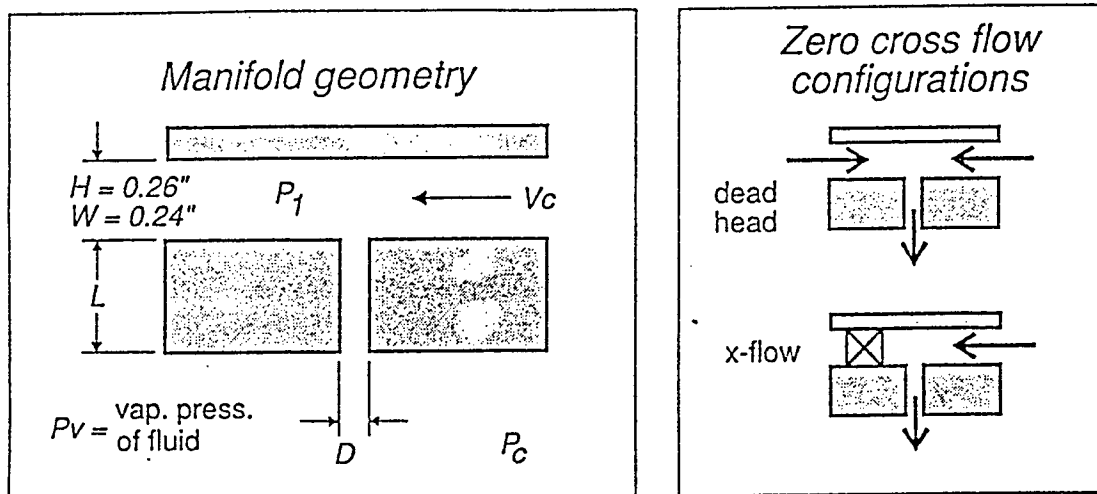
A definite correlation between  $C_d$  divergence and dissolved gas concentration was found. It is thought that dissolved gases coming out in the orifice account for this dependency. It is recommended that the dissolved gas concentration in the reservoir be measured before flowing the system for an experiment. Dissolved oxygen concentrations between 5.5 and 7.5 PPM are recommended to ensure data accuracy. This should pose no significant problem since most baseline conditions fall in this range. By keeping the gas concentration fairly constant the dissolved gas effect on the experimental data can be eliminated.

A  $C_d$  dependence on cross flow velocity was observed. This further reinforces the data taken previously at Phillips Laboratory. Though dissolved gas differences tend to augment the effect, they are not the cause. This is an ongoing investigation in the cold flow chamber facility. Additional pressure taps to better measure the orifice  $\Delta P$ , better flow rate control, and more in-depth data analysis will allow a more complete investigation of cross flow effects.

It is now believed that dissolved gas effects can be accounted for and no further investigation is needed. The data analysis can now be concentrated on the effects of cross flow velocity and manifold geometry. This project has been successful in eliminating the dissolved gas concentration parameter from the data analysis and presentation.

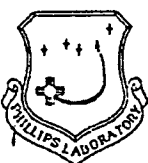


# NOMENCLATURE



Test methodology: Hold  $P_1$  constant and slowly increase  $P_c$ .

Figure 1: Manifold geometry and nomenclature



## ORIFICE HYDRAULICS TEST ARTICLE

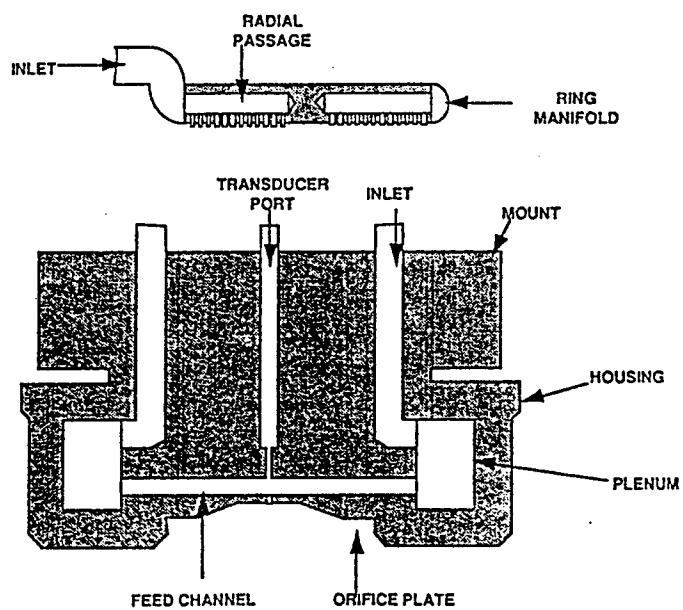


Figure 2: Orifice geometry and cross flow channel pressure tap

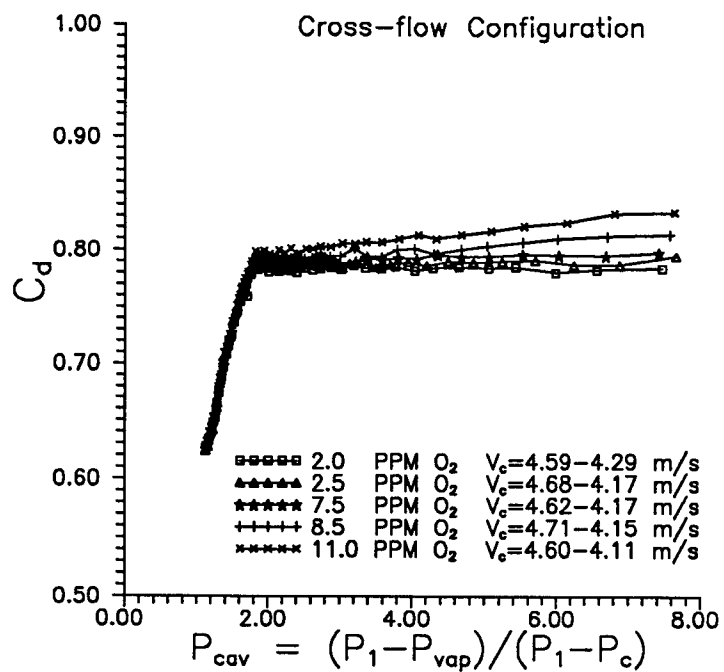


Figure 3: Dissolved gas effect at a single cross-flow velocity

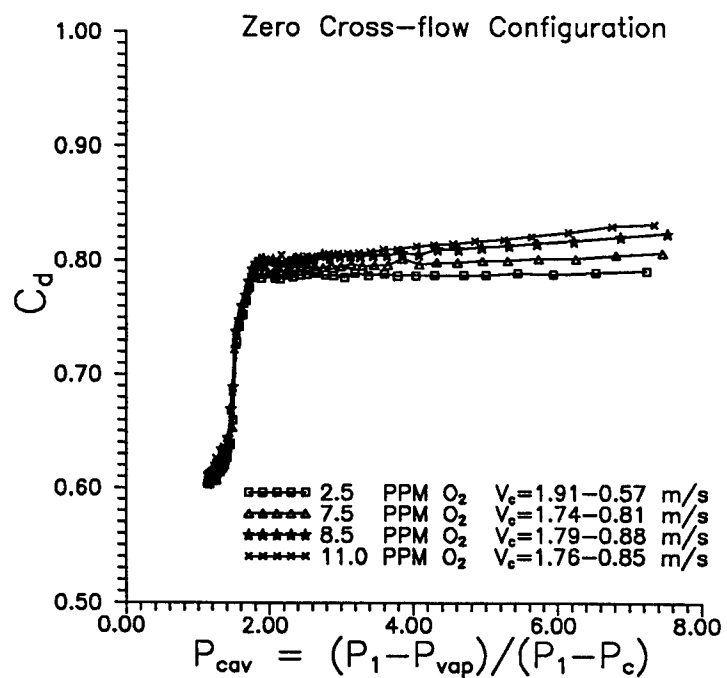


Figure 4: Dissolved gas effect at a single zero cross-flow

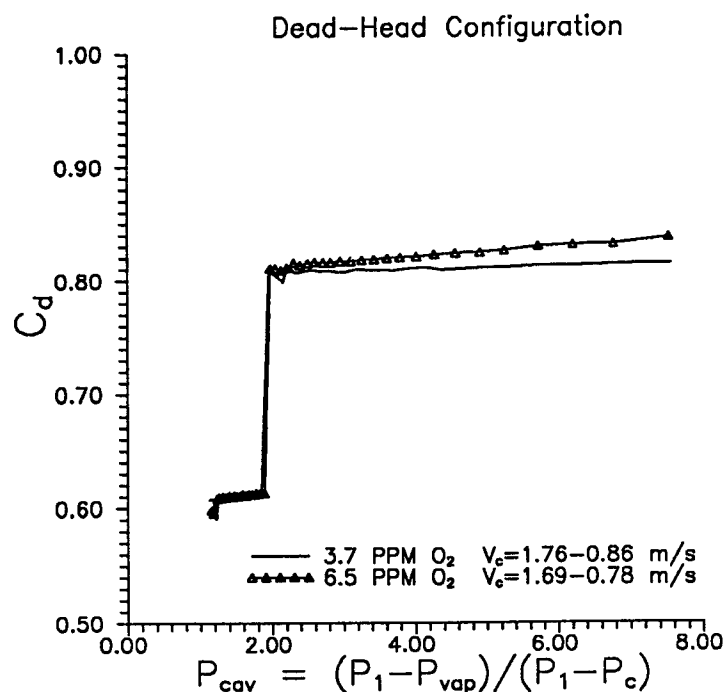


Figure 5: Dissolved gas effect at a single dead-head

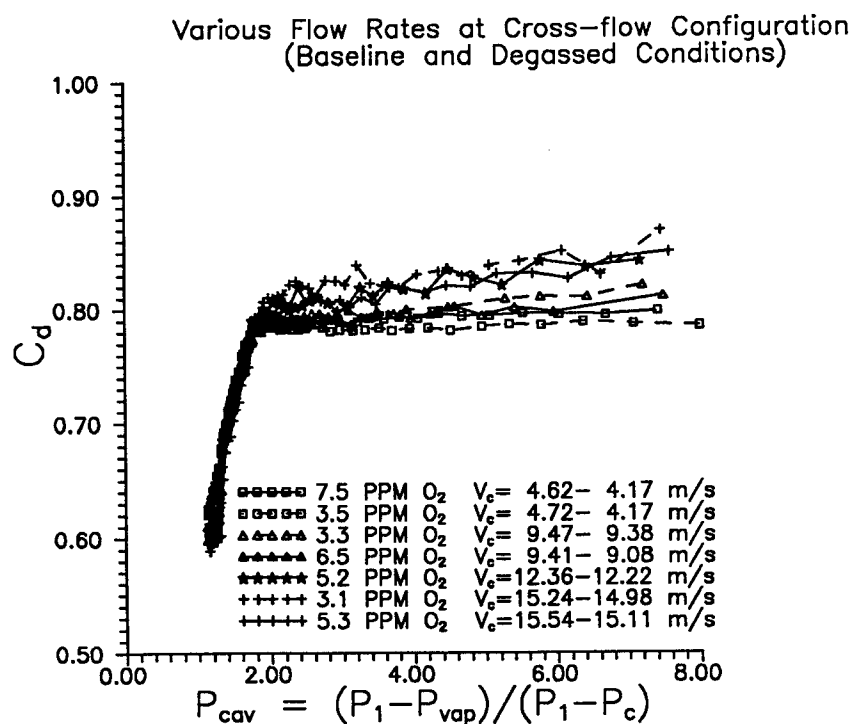


Figure 6: Effect of dissolved gas and cross-flow velocity

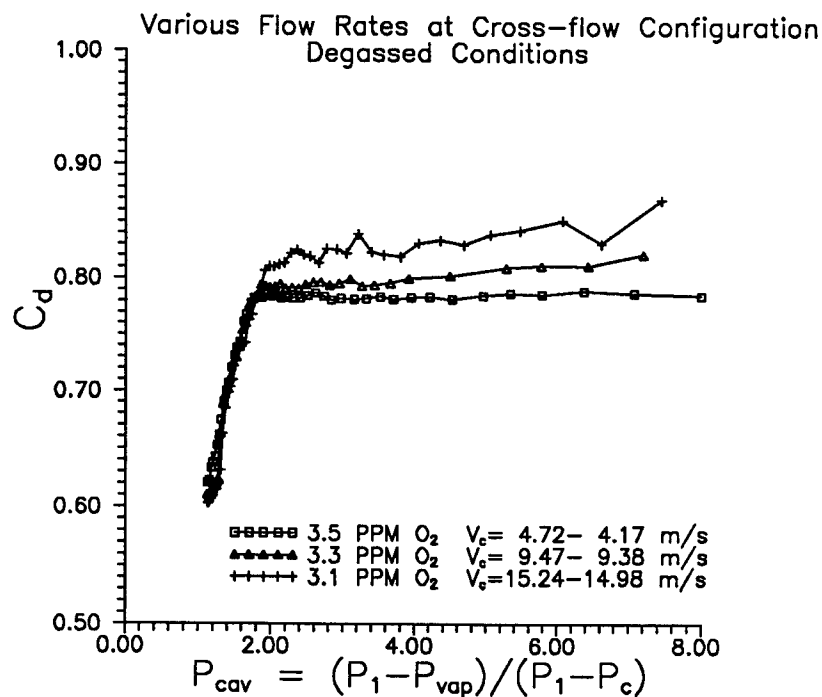


Figure 7: Cross-flow velocity effect at degassed conditions

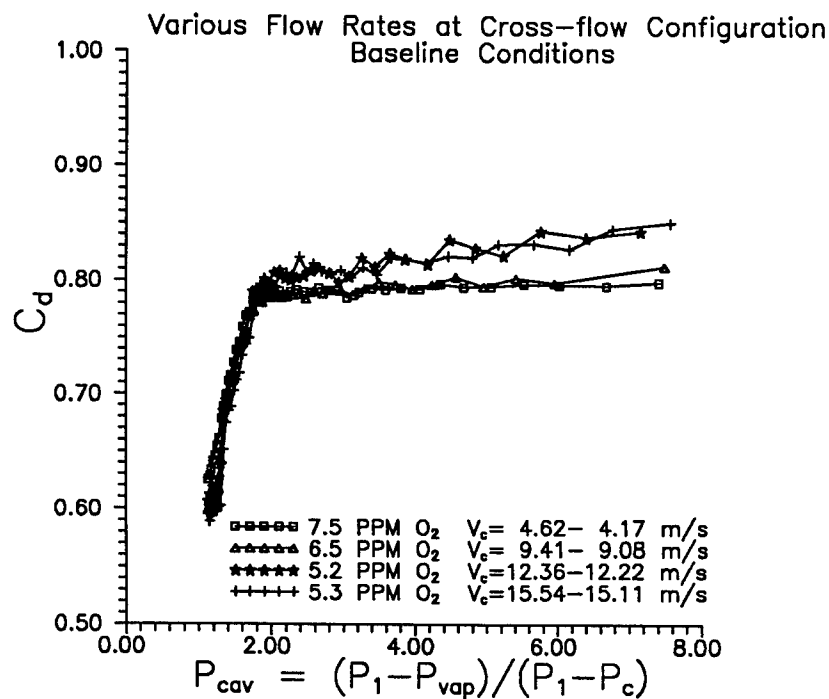


Figure 8: Cross-flow velocity effect at baseline conditions

### Acknowledgments

The author would personally like to thank William Grissom, Karen Olson, and Douglas Talley for their suggestions, help, and encouragement with the test scheduling, instrumentation, and data analysis. I would also like to thank George Miller, Mark Horn, and Ronald Rickel for system modifications, consultations on the facility capabilities, and assisting in the actual test runs.

### References

1. Farmer, Karen O.; Grissom, William M. ; Miller, George "High Pressure Flow Facility for Study of Injector Design Impacts on Spray Characteristics" 6th Annual Conference on Liquid Atomization and Spray Systems, Worcester, MA, May 17-19, 1993.
2. Olson, K.M.; Pelletier, M.E.; Grissom, W.M.; Talley, D.G. "High Pressure Injector Characterization Experiments: Orifice Hydraulics Results" 1993 JANNAF Propulsion Meeting & 30th JANNAF Combustion Subcommittee Meeting, Monterey, CA, November 15-19, 1993.
3. CRC "*Handbook of Chemistry and Physics*", 69th Ed., 1988-1989.
4. Fogg, P.G.T.; Gerrard, W. "*Solubility of Gases in Liquids*", John Wiley and Sons, New York, NY, 1991.
5. Lange "*Handbook of Chemistry*", 10th Ed., McGraw-Hill Book Company, New York, NY, 1967.
6. Hitchman, Michael L. "*Measurement of Dissolved Oxygen*", John Wiley and Sons, New York, NY, 1978.

**ANALYSIS TO DETERMINE THE QUALITY  
FACTOR OF A COMPLEX CAVITY**

Ronald R. DeLyser  
Assistant Professor of Electrical Engineering  
Department of Engineering

Peyman Ensaf  
Graduate Student  
Department of Engineering

University of Denver  
2390 S. York Street  
Denver, CO 80208-0177

Final Report for:  
Summer Faculty Research Program  
Phillips Laboratory

Sponsored by:  
Air Force Office of Scientific Research  
Bolling Air Force Base, Washington, D.C.

September, 1994

ANALYSIS TO DETERMINE THE QUALITY  
FACTOR OF A COMPLEX CAVITY

Ronald R. DeLyser  
Assistant Professor of Electrical Engineering  
Peyman Ensaf  
Graduate Student  
Department of Engineering  
University of Denver

Abstract

The low frequency, preliminary analysis of a simplified model of a space craft sensor has been accomplished using CARLOS-3D™ (Code for Analysis of Radiators on Lossy Surfaces), a general purpose computer code using the Method of Moments (MoM.) Resonances of a cavity region have been identified by determining the cavity quality factor (Q) as a function of frequency. The Q is proportional to the total energy stored in the cavity and inversely proportional to the power lost from the cavity due to lossy materials and apertures. Even though this measure does not give an exact value for power density at a specific point in the system, it does give an indication of the representative power levels one will find in a similar system. An analysis approach for the high frequency range includes using GEMACS (General Electromagnetic Model for the Analysis of Complex Systems) which incorporates the geometrical theory of diffraction, MoM, and the finite difference method for multiple region problems. A comparison of the two methods (CARLOS-3D™ and GEMACS) at an intermediate frequency (~3 GHz) is proposed.

ANALYSIS TO DETERMINE THE QUALITY  
FACTOR OF A COMPLEX CAVITY

Ronald R. DeLyser and Peyman Ensaf

Introduction

Determining the effects of high power microwaves (HPM) to satellite systems and subsystems is one of the missions of the Phillips Laboratory Satellite Assessment Center (SAC). HPM tests can not always be performed on these systems so that analytical techniques are necessary. One such analytical technique has been proposed [1] for the analysis of large complex cavities.<sup>1</sup> However, when the systems are not large, numerical techniques have to be used. When analyzing a single system or subsystem, it can be considered large at high frequencies and not large at the lower frequencies. One therefore has to use different analytical procedures depending on the frequency of interest.

We were tasked with analyzing a simplified model of a typical sensor over a frequency range of several hundred MHz to tens of GHz. Figure 1 shows a skeleton drawing of the model generated by GAUGE (Graphical Aids for Users of GEMACS) [2] which is discussed below. The model of the sensor consists of a lower mirror assembly, and an upper cavity region.

The ultimate goal of any analysis would be to find the power density incident on a particular part in the cavity. However, due to non-uniformity in the manufacturing process or changes in the internal configuration which accompanies field modifications or maintenance, all such sensors will not be alike. Therefore, any analysis of a specific system would be futile. So what should our calculated quantity be? We decided on the quality factor ( $Q$ ) of the upper cavity region. As discussed in detail below,  $Q$  is proportional to the total energy stored in the cavity

---

<sup>1</sup> "Large" is to be taken in the sense that the dimensions of the cavity or object is large when compared to the wavelength of the radiation.

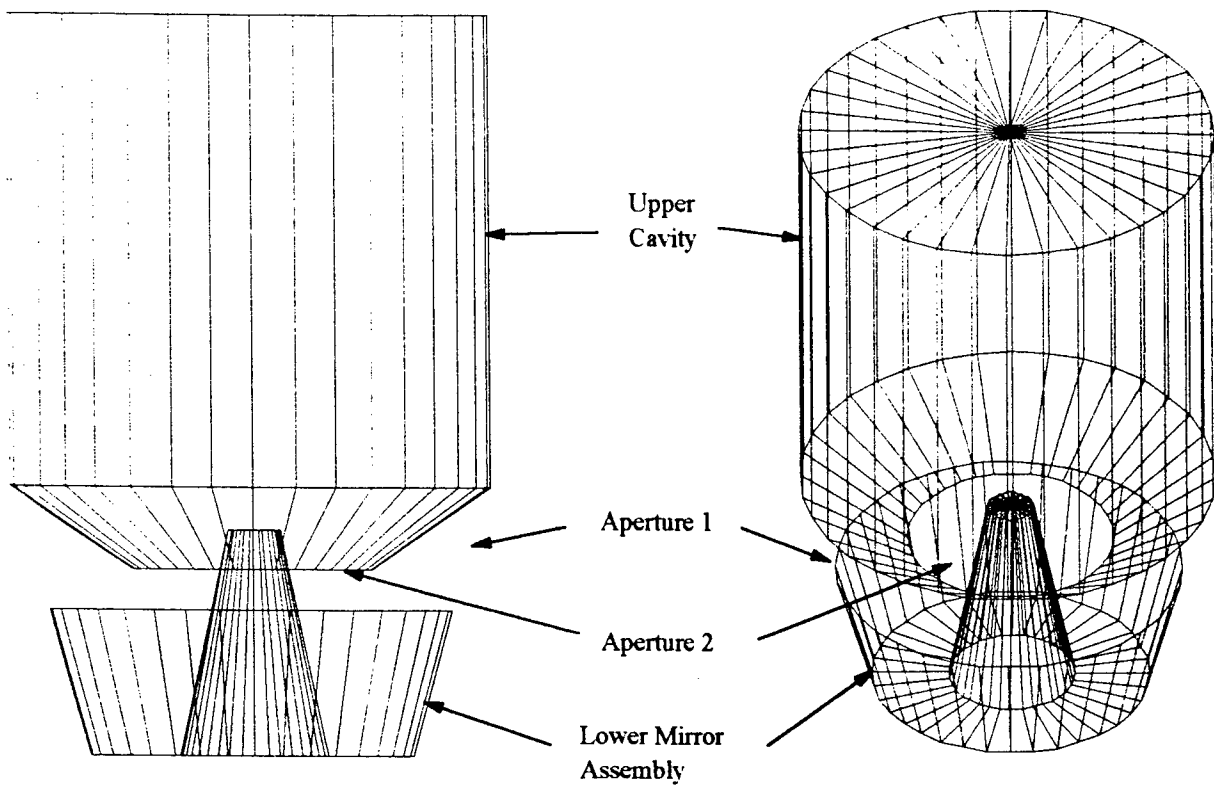


Figure 1. The symplified model of the sensor.

and inversely proportional to the power lost from the cavity due to lossy materials and apertures. Even though this measure does not give an exact value for power density at a specific point in the system, it does give an indication of the representative power levels one will find in a similar system.

#### The Software

The programs available at the SAC which are appropriate for this project are CARLOS-3D™ (Code for Analysis of Radiators on Lossy Surfaces) [3], a general purpose computer code using the Method of Moments (MoM) and GEMACS (General Electromagnetic Model for the Analysis of Complex Systems) [4], which solves electromagnetic radiation and scattering problems using MoM and Geometrical Theory of Diffraction (GTD) for exterior analysis, and a Finite Difference (FD) formulation for solution of interior problems.

## CARLOS-3D™

The CARLOS-3D™ software utilized in this project implements the method of moments (MoM) solution for fully arbitrary three-dimensional complex scatterers. These solutions are obtained for perfectly electrically conducting (PEC) bodies as well as fully or partially penetrable ones. The electromagnetic scattering formulation used in this software (hence in this project) is based on surface integral equations (SIE) spanning the entire external surface of the body and the internal boundaries between penetrable and PEC regions. The analysis and software are extended to boundaries (or surfaces) which may be characterized by resistive or magnetic sheets as well as impedance boundary conditions.

CARLOS-3D™ operates on a triangularly-faceted body that may be composed of the following types of surfaces:

- (1) Conducting (PEC)
- (2) Conducting/Penetrable
- (3) Multi-Region Penetrable
- (4) Resistive Boundary Condition (RBC)
- (5) Magnetically Conducting Boundary Condition (MBC)
- (6) Impedance Boundary Condition (IBC)
- (7) Global or Local RBC and IBC

CARLOS-3D™ implements the MoM solutions for a variety of SIE formulations associated with the classes of 3-D geometries described above. A combined-field formulation is available to overcome the ill-conditioning with the electric and magnetic field integral equations (EFIE and MFIE) for closed conducting bodies at internal resonances.

The following options are available in this code:

- (1) EFIE/PMCHW (after Poggio, Miller, Chu, Harrington, and Wu) formulation for coated conductors (symmetric system matrix)
- (2) EFIE, MFIE and CFIE (Combined Field Integral Equation) on closed conductors
- (3) PMCHW on dielectric boundaries

(4) CFIE for combination of open/closed geometries

The analysis and the implementing software permits the following specific options to be considered for the foregoing classes of 3-D problems:

- (1) Mono- and bistatic scattering,
- (2) far field calculation,
- (3) body symmetry option to minimize storage and execution time,
- (4) automatic modeling of junctions where two or more surfaces intersect,
- (5) infinitesimally thin conducting, resistive, and magnetic surfaces,
- (6) surface current computation,
- (7) infinite ground plane, adjacent to or intersecting the body,
- (8) analytical green's function evaluation using singularity extraction,
- (9) near field calculations,
- (10) radar cross-section,

Specifics of the use of CARLOS-3D<sup>TM</sup> for this project

For penetrable bodies the boundary conditions are generally complicated and depend on geometry and material composition. Integral formulations of Maxwell's equations provide an attractive formulation for these problems, since the necessary boundary conditions are easily incorporated. The resulting equations can then be solved by the Method of Moments technique.

The EFIE and MFIE exhibit an internal resonance phenomenon that is due to the non-uniqueness of the solution in these integral equations at and near the resonance frequencies of the interior problem [5]. These non-unique solutions arise from the fact that the resonant frequency can be achieved in the absence of an excitation source. Therefore, at these particular frequencies, the EFIE and MFIE formulations can lead to non-physical, spurious results. The CFIE remedies this non-uniqueness in results by adding a supplementary integral to eliminate spurious

solutions. In this method it is recognized that at interior resonance frequencies an electric current on the surface that produces no tangential electric field on the surface can exist. This is overcome by placing both an electric current  $J_s$  and a magnetic current  $M_s$  on the surface  $S$ . In this case the combined field integral equation can be written as [5],

$$\hat{n} \times [E^i + E^s(J_s, M_s)] = 0 \quad (1)$$

where  $E^s(J_s, M_s)$  denotes the electric field  $E^s$  radiated by the sources  $J_s$  and  $M_s$ , and  $\hat{n}$  is the unit vector. The CFIE formulation results in a well-posed problem and provides robust solutions at resonances. Therefore in accordance with this approach, a set of calculations will be conducted using the EFIE technique in parallel with a set conducted using the CFIE at these particular internal resonances. Hence, the results obtained from both approaches will be compared and any discrepancies will be acknowledged.

#### Application of Mathematica to the problem.

CARLOS-3D™ requires an input file in which one or more geometrical data files are incorporated. The input file along with the geometrical data files need to be prepared in accordance with the CARLOS-3D™ code. This consists of a descriptive title line followed by the frequency of operation, number of dielectric regions (if any) and then the name of each data file under study along with indications of whether a particular data file represents a perfect electric conductor or a dielectric and also whether it's a closed or an open structure. CARLOS-3D™ recognizes a few different data files such as

- (1) ACAD-facet
- (2) AGM
- (3) IGES

Of many different interfaces compatible with CARLOS-3D™, the one available at the Satellite Assessment Center was Mathematica [6]. Mathematica is not necessarily the best user interface software (this will be discussed below), however, it has some features that made it unique. Mathematica enables the user to write a program generating input data files that incorporate triangular surfaces along with nodal values that describe each triangular surface and also identifies the X, Y, Z coordinates accordingly, providing compatibility with the CARLOS-3D™ code. In order

to generate these structures, Mathematica uses functions such as Surface Of Revolution and Parametric Plot3D. A particularly useful feature in Mathematica is its ability to create a complicated structure by generating sub-structures and ultimately joining each of those together, forming the desired composite structure. In generating the structure of the sensor, it was necessary to keep in mind that the body of each structure must be segmented into a number of cells in which each cell side is taken to be at most one-tenth of the operating wavelength. Therefore, using Mathematica the appropriate number of segmentations was calculated and implemented for each operating frequency range (wavelength).

#### Calculation Of The Quality Factor (Q)

Once the geometry of the sensor was fully generated using the above techniques, the appropriate data files were formed into a compatible input file. At lower frequencies below internal resonances, namely 0.6 GHz-1.6 GHz, the input files dictated the EFIE technique. The next step was to create a grid of points in the interior of the upper cavity of the sensor for the calculation of the near fields. A rectangular grid was chosen.

In general the fields inside the chamber are nonuniform. However, in this analysis, uniformity was assumed for individual cubic cells of 1.5 cm ( $< 0.1\lambda$ ) in each dimension. These grid points (a total of 963) were prescribed in the input file to CARLOS-3D™ for near-field calculations. Ultimately, CARLOS-3D™ calculated the near fields and the Z-directed power at each declared grid point. The power calculations of interest were those into and out of the inlet to the upper chamber of the model. CARLOS-3D™ provides the X,Y,Z components of the fields at each grid point. Knowing these field values, the electric and magnetic energy at each point are calculated using [2]

$$e = \frac{1}{4} \iiint \epsilon |E|^2 dx dy dz \quad (2)$$

$$m = \frac{1}{4} \iiint \mu |H|^2 dx dy dz \quad (3)$$

The integrals in equations (2) and (3) are quite trivial to solve. Since it is assumed that the fields within each cell are constant, the E and the H terms along with the corresponding material properties can be brought out of the integrals leaving only a volume integral with respect to the dimensions of the cell. Keeping in mind that the dimensions of each cell are 1.5 cm on each side, equations (2) and (3) become

$$\epsilon = \frac{1}{4} \epsilon |E|^2 (.015m)^3 \quad (4)$$

$$m = \frac{1}{4} \mu |H|^2 (.015m)^3 \quad (5)$$

Equations (4) and (5) correspond to the electric and magnetic energy for one cell. Now, the same calculations for each cell corresponding to each grid point must be done and then sum the total for both electric and magnetic energies and the sum of their total would be the total energy for each of the  $\theta$  and  $\phi$  polarizations. The chosen incidence angles were  $\theta$  and  $\phi$  at  $90^\circ$  and  $0^\circ$  respectively (figure 1). Once the fields are calculated, the power [2] going out from the chamber can also be calculated, using the Poynting theorem. Hence, power is calculated using

$$\vec{P} = \iint (\vec{E} \times \vec{H}^*) \cdot d\vec{s} \quad (6)$$

Since the outgoing power is in the negative Z- direction, we can calculate the power using

$$\vec{P} = - \iint [ (\hat{\alpha}_x E_x + \hat{\alpha}_y E_y + \hat{\alpha}_z E_z) \times (\hat{\alpha}_x H_x + \hat{\alpha}_y H_y + \hat{\alpha}_z H_z) ] \cdot dx dy \cdot \hat{\alpha}_z \quad (7)$$

$$\vec{P} = - \iint [ \hat{\alpha}_z (E_x H_y - E_y H_x) ] dx dy \quad (8)$$

We are only concerned with the power out of the chamber so power calculations at a height of 0.075 m, which is at the inlet of the chamber, were accomplished. Once again, since the fields within each designated cell are constant, equation (8) can be modified to

$$\vec{P} = - (E_x H_y - E_y H_x) (0.015)^2 \cdot \hat{\alpha}_z \quad (9)$$

Once the energy and power are calculated, Q is given by

$$Q = \omega \frac{U}{P} \quad (10)$$

where U and P are the total energy stored and power exiting the cavity calculated separately for  $\theta$  and  $\phi$  polarizations.

#### Summary Of Results

Recall that the extent of these calculations is to a high frequency of 1.6 GHz. Calculations at higher frequencies will be conducted at a later time. Figures 2, 3 and 4 are plots of Q, energy, and power versus frequency for both polarizations. At aperture 1 of figure 1a, the  $\theta$  polarized electric field will be more easily maintained because the field lines will terminate on the top and bottom edges of the aperture. However, the  $\phi$  polarized electric fields (in

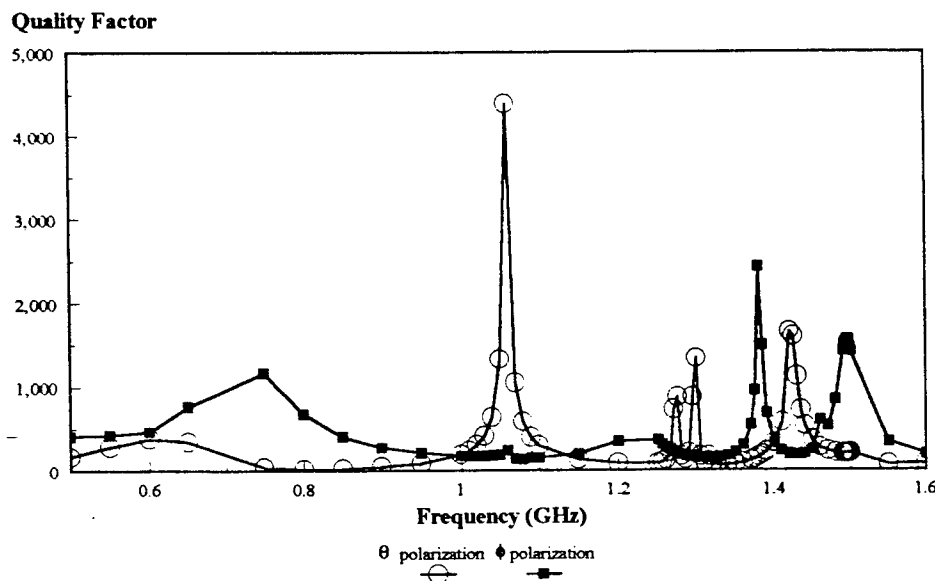


Figure 2. Q of the upper cavity region.

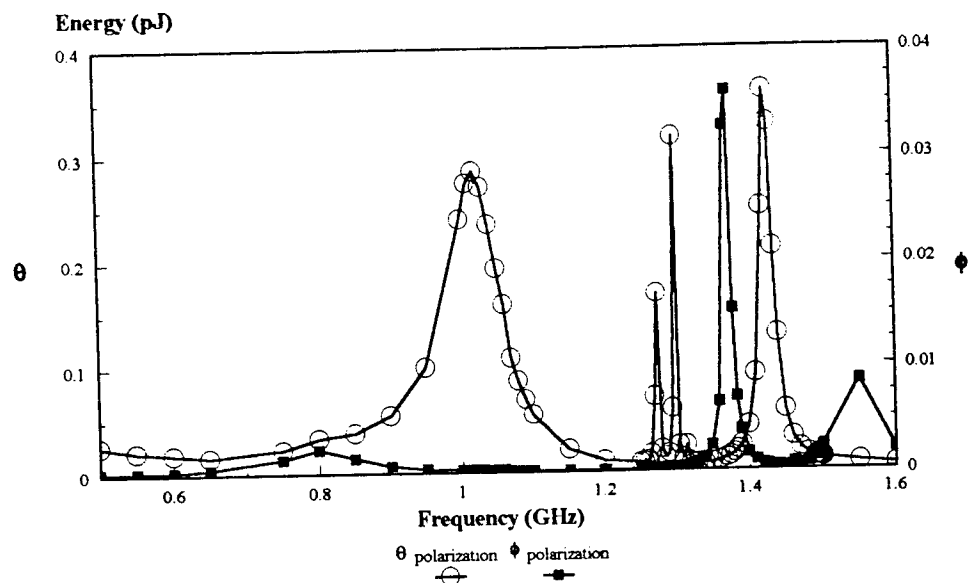


Figure 3. Energy in the upper cavity region.

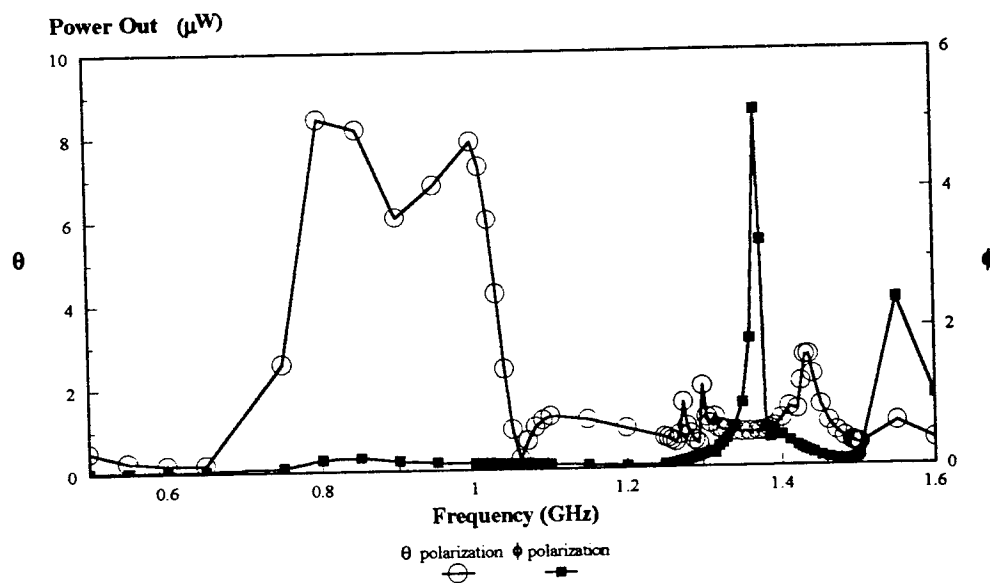


Figure 4. Power leaving the upper cavity region.

the low frequency domain) create  $\phi$  directed currents on the surfaces and hence the aperture fields are not as pronounced. Therefore, as observed in Figure 3, the energy values due to the  $\theta$  polarized fields are much higher than those for the  $\phi$  polarized fields. In Figure 3, one can also observe that at some higher frequencies increases in energy due to the  $\phi$  polarized fields occur. Table II provides resonant frequencies for a frequency sweep over the range of 0.5 GHz - 1.6 GHz. Table II also compares the measured resonant frequencies with those analytical calculations assuming a cylindrical cavity of 8.6 cm supporting TM modes.

The  $TE_{mnp}$  and  $TM_{mnp}$  modes provided in Table II are given respectively by,

$$f_{mnp}^{TE} = \frac{1}{2\pi\sqrt{\mu\epsilon}} \sqrt{\left(\frac{\chi'_{mn}}{a}\right)^2 + \left(p\frac{\pi}{h}\right)^2} \quad \begin{cases} m=0,1,2,3,\dots \\ n=1,2,3,\dots \\ p=1,2,3,\dots \end{cases} \quad (11)$$

$$f_{mnp}^{TM} = \frac{1}{2\pi\sqrt{\mu\epsilon}} \sqrt{\left(\frac{\chi_{mn}}{a}\right)^2 + \left(p\frac{\pi}{h}\right)^2} \quad \begin{cases} m=0,1,2,3,\dots \\ n=1,2,3,\dots \\ p=0,1,2,3,\dots \end{cases} \quad (12)$$

Table II. Resonant frequencies.

Resonant Frequency (GHz)	Quality $\theta$ polarization	Quality $\phi$ polarization	Analytical for the upper Cavity Region
1.06	4392.108		
1.126			TEM( $\lambda$ )
1.275	872.1293		
1.30	1337.026		
1.33			TM <sub>010</sub>
1.38		2433.935	
1.42 -	1659.651		
1.496		1566.211	
2.127			TM <sub>110</sub>
2.639			TE <sub>011</sub>

Where  $x'_{mn}$  represents the nth zero of the derivative of the mth order Bessel function. According to equations (11) and (12), the lowest mode is the  $TM_{010}$  proceeding with  $TM_{110}$  which are well below the first TE mode ( $TE_{011}$ ). The subscript p in equation (12) will remain zero for the lowest TM modes, therefore, guarantee the TM modes to be independent of the height of the cavity. Therefore, the analytical values in Table II are for the  $TM_{mnp}$  modes. Also due to the presence of the coaxial like structure below the chamber, there may exist TEM modes, and hence these are also presented in Table II. The remaining data provided in Table II correspond to CARLOS-3D<sup>TM</sup> calculations. Differences with the numerical results are due to the fact that we have a much more complex cavity.

Radar cross-section (RCS) for the model was also calculated and is shown in figure 5 as a function of frequency. It was hoped that there would be a correlation between resonances and this quantity. Other than a small indication in the region of the 1.3 GHz resonance, there is no correlation. Evidently this is due to the fact that a much greater

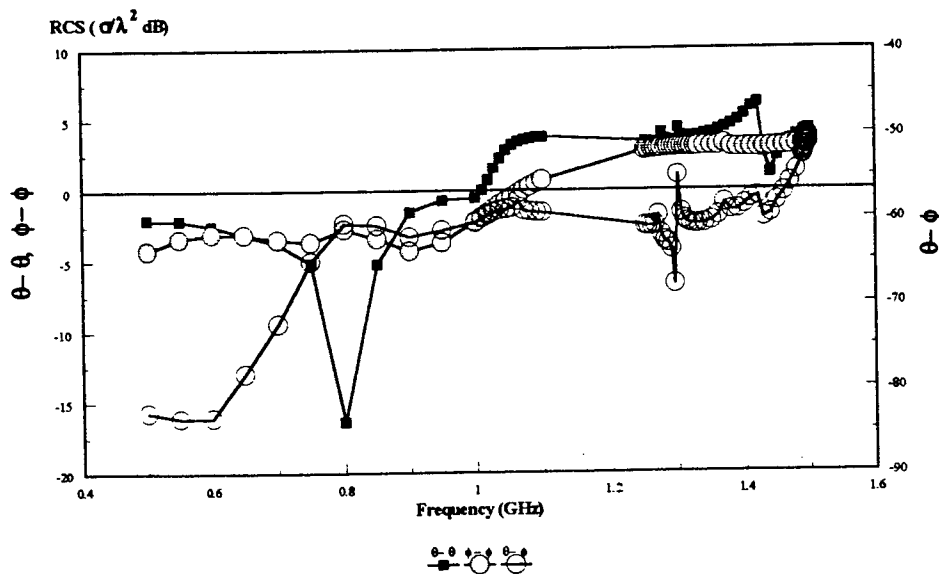


Figure 5. Radar cross-section for the sensor.

amount of energy is scattered than is stored in the cavity. Any dip in the RCS versus frequency graph would have to be due to a much greater amount of energy stored in the cavity relative to that which is scattered.

#### Problems using CARLOS-3D™ and Mathematica

A list of some problems encountered with Mathematica and CARLOS-3D™ follows:

- a) Generating complicated structures using Mathematica, requires many tedious operations which could most likely be avoided with a well designed interface.
- b) As the measurements escalate to higher frequencies, the cell sizes become much smaller. For problems of circular symmetry, the cells near the center of circles become exceedingly small. Mathematica only allows a symmetric gridding like that shown in Figure 6a. Since in this geometry, at a radius of half the outer radius the cells have sides half as large, a simple transition such as that shown in Figure 6b can be used to maintain reasonable cell

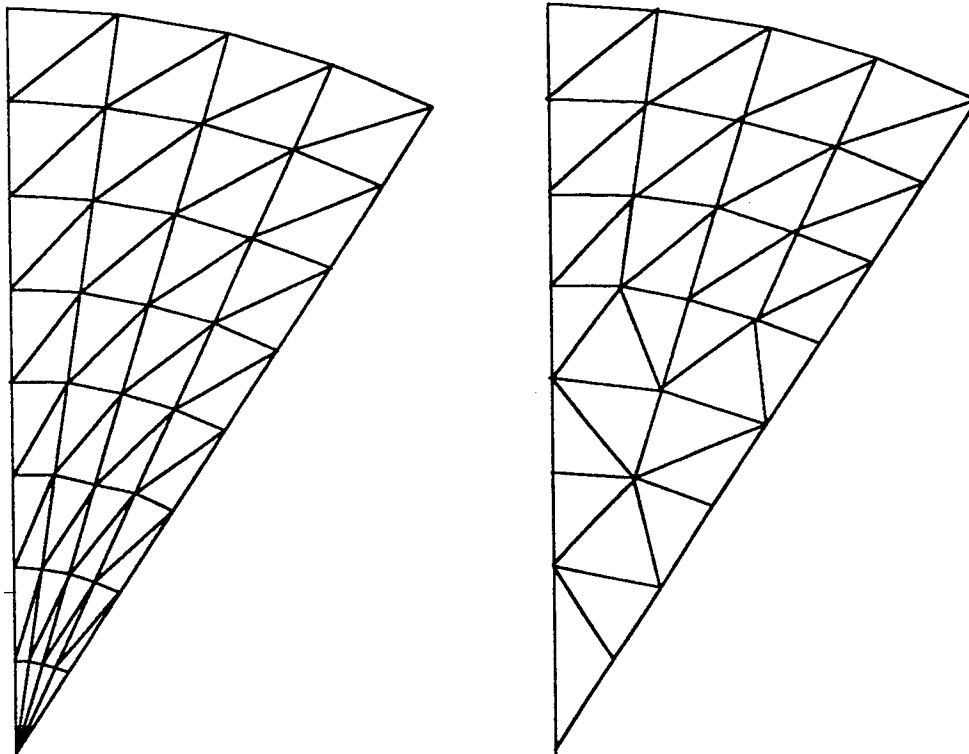


Figure 6. Alternate gridding scheme for circular geometry.

sizes. This is not now possible with the software available at the Phillips SAC.

(c) The largest input files used for calculations were for a frequency of 1.6 GHz. At this frequency, there exists a total of 3990 unknowns. This corresponds to approximately 16 million complex numbers in the impedance matrix. Each complex number requires 8 bytes, which means that at a frequency of 1.6 GHz, the user requires approximately 128 Mbytes of random access memory (RAM). The work station that we were using has this much RAM, but a larger problem will require that the work station do disk swapping. It has been our experience that this slows down the process significantly. Without disk swapping, this large problem has an approximate running time of 1 hour on an IBM RS6000 570 Powerstation. As a test at 3 GHz and approximately 8000 unknowns, CPU time was reduced to 25% of the total process time and it was anticipated that a time of 16 hours to run CARLOS-3D<sup>TM</sup> at one frequency would be necessary.

(d) Calculation of near fields using CARLOS-3D<sup>TM</sup> is possible, even though the user's manual [3] does not state this. However, this option is only available with the bistatic scattering selected. The bistatic scattering option does not allow an incidence angle sweep. This feature (incidence angle sweep with near fields calculations) would allow more efficient generation of data since the excitation vector in the numerical formulation is the only change that needs to be made from one incidence angle to the next. The impedance matrix (which takes most of the cpu time) does not have to be changed. Because of this deficiency in CARLOS-3D<sup>TM</sup> investigation of the effect of varying incidence angle would have been too time consuming for this study and thus was not accomplished.

(e) In an effort to extend our analysis of this model to 3 GHz, we decided to use the plane of symmetry option. This allows input of data for only half of the problem and CARLOS-3D<sup>TM</sup> reduces the matrix size to two matrices of 1/4 the size of the full matrix. These are then solved in sequence. Our model, which was segmented assuming a frequency of 3 GHz, produced matrices of 4982 and 5024 elements and a cpu time of a little more than four hours with no disk swapping. The only problem with using this feature is that the calculated fields at 1.5 GHz in the upper cavity region differed significantly from the same fields calculated with the model used without the plane of symmetry option. This problem needs to be corrected in order to extent this type of analysis to higher frequencies.

(f) New features that should be incorporated into CARLOS-3D<sup>TM</sup> include:

- (1) magnitude and phase of far and near fields,
- (2) dynamic memory allocation to relieve some of the memory problems presented above,
- (3) a figure of merit for the triangulation such as calculations of accumulated charge on patches,
- (4) multi-wire junctions should be handled automatically,
- (5) optional output of the unit vectors in the direction of each current,
- (6) storage and retrieval of filled and/or solved matrices,
- (7) and, capability to read wire geometry from a file.

### GEMACS

The GEMACS program (version 5) supports the solution of electromagnetic radiation and scattering from complex perfectly conducting objects using MoM solution of the EFIE, MFIE, and CFIE formulation. It also uses GTD for large perfectly conducting and impedance surfaces and combines GTD and MoM (called MoM/GTD hybrid) for problems where small radiators near large scatterers are modeled. A FD solution is used for closed cavities which when combined with the MoM, GTD or MoM/GTD hybrid can be used for multiple region problems. This code, because of the efficient use of memory in the FD formulation and the availability of the GTD formulation for the high frequency solution of the exterior problem, is the code of choice for this type of study at frequencies where use of CARLOS-3D™ is prohibitive.

Unfortunately, versions of GEMACS for a workstation or one which could access memory above the DOS limit for the PC were not available at the SAC for this study. However, an ongoing effort to make one of these versions available before the end of this study prompted us to use GAUGE [2] to generate input files for our problem. Hopefully, we will use these input files with GEMACS for the higher frequencies in a follow on study.

The analysis of the simplified model of a sensor using GEMACS begins by dividing the problem into three regions (see Figure 1a): (1) an exterior region that includes the excitation source (a plane wave) and the outer shell of the entire sensor plus aperture 1, (2) an intermediate region containing the lower mirror assembly with apertures 1 and

2, and (3) the interior region of the upper cavity. At the higher frequencies of interest ( $> 3$  GHz) the outer region is a GTD problem where energy is coupled into the intermediate region through aperture 1. The intermediate region is an FD problem with energy coupling into the interior region through aperture 2. Finally, the interior region is an FD problem where we want to calculate the fields. Once the fields are known in the interior region and in aperture 2, we can calculate Q in the same manner as we did using CARLOS-3D™.

### Summary of Work to be Done

The following is a list of work to be done in a follow-on study:

- (1) The use of GEMACS to extend the range of frequencies in this investigation should be the primary focus of a follow-on study.
- (2) Variations in incidence angle and the resulting effect on Q, energy stored in and power exiting the cavity should be studied.
- (3) Even though we think that the grid size inside the cavity to determine the accurate value of Q is adequate, it should be investigated because of the shapes involved. Preliminary study of the variations of the fields indicate fairly smooth changes with the grid used for this study.
- (4) In the transition region of approximately 3 GHz (assuming the problems with the symmetry plane option addressed above are corrected), results from CARLOS-3D™ and GEMACS should be compared.
- (5) Segmentation size for both codes should also be studied. The rule of thumb is to have cell sides smaller than  $0.1 \lambda$ . Since computer memory is at a premium for high frequency excitation, this rule of thumb is well worth investigation.
- (6) Incorporation into CARLOS-3D™ of the new features mentioned above should be accomplished and validated.
- (7) Development or search for a more friendly graphical user interface for CARLOS-3D™ should be accomplished.
- (8) Finally, comparison of numerical results with experimental results is necessary.

References

- [1] Ronald R. DeLyser, "An analysis approach to determine quality factors of large, complex cavities," *Final Report, Summer Faculty Research Program*, Phillips Laboratory, Sponsored by The Air Force Office of Scientific Research Bolling Air Force Base, Washington, D.C., September, 1993.
- [2] *Graphical Aids for the Users of GEMACS (GAUGE)*, Rome Air Development Center, AFSC, Griffiss Air Force Base, NY, February 1989.
- [3] J.M. Putnam, L.N. Madgyesi-Mitschang and M.B Gedera, *CARLOS-3D<sup>TM</sup> Three Dimensional Method Of Moments Code*, McDonnell Douglas Aerospace-East, December 1992.
- [4] *General Electromagnetic Model for the Analysis of Complex Systems (GEMACS) - Version 5*, Rome Air Development Center, AFSC, Griffiss Air Force Base, NY, December 1990.
- [5] Wang, J. J. H. , *Generalized Moment Method In Electromagnetics*, Wiley Interscience, New York, 1991
- [6] Wolfram, S., *Mathematica*, Addison-Wesley, 1991.

INTERIOR SPECTROSCOPIC INVESTIGATION OF  
PLASMA COMPOSITION AND SPECIES PROFILES  
FOR A 26 kW CLASS RADIATIVELY  
COOLED AMMONIA ARCJET NOZZLE

Frank S. Gulczinski III  
Graduate Student  
Department of Aerospace Engineering

University of Michigan  
College of Engineering  
1052 François Xavier-Bagnoud Building  
Ann Arbor, MI 48109

Final Report for:  
Graduate Student Research Program  
Phillips Laboratory

Sponsored by:  
Air Force Office of Scientific Research  
Bolling Air Force Base, DC

and

Phillips Laboratory  
Edwards Air Force Base, CA

September 1994

INTERIOR SPECTROSCOPIC INVESTIGATION OF  
PLASMA COMPOSITION AND SPECIES PROFILES  
FOR A 26 kW CLASS RADIATIVELY  
COOLED AMMONIA ARCJET NOZZLE

Frank S. Gulczinski III  
Graduate Student  
Department of Aerospace Engineering  
University of Michigan  
College of Engineering

Abstract

In order to better understand the operational characteristics of a 26 kW class ammonia arcjet similar to the one which will be used for the United States Air Force's Electric Propulsion Space Experiment, a study of the plasma inside the arcjet's nozzle was performed using emission spectroscopy. Photomultiplier tube scans and charged coupling device readings were taken through optical access ports located axially along the nozzle/anode. Species found in less than trace amounts were: atomic hydrogen ( $H$ ), singly ionized atomic nitrogen ( $NII$ ), molecular nitrogen ( $N_2$ ), and the  $NH$  ion. The Boltzmann plot method was used to determine the excitation temperatures for  $H$  and  $NII$ . As the plasma expanded within the nozzle, both the  $H$  and  $NII$  temperatures decreased. At the exit plane, however, the hydrogen temperature increased; a phenomena that may be due to the presence of a barrel shock. In performing these plots, many of the lower energy states were found to be underpopulated and thus not in local thermodynamic equilibrium. Additionally,  $NII$  was found to be at a much higher temperature than  $H$ , indicating a non-uniform plasma with  $NII$  concentrated at the arcjet core while  $H$  was distributed throughout the nozzle. Electron number density was determined using a method developed by Griem. The results show a decrease in density in the downstream direction resulting from nozzle expansion and electron-ion recombination. These results agree with number density data from earlier studies carried out on low power arcjets, indicating that the increased physical size of a high power arcjet balances with the increased specific power to keep the number density constant for a given area ratio.

INTERIOR SPECTROSCOPIC INVESTIGATION OF  
PLASMA COMPOSITION AND SPECIES PROFILES  
FOR A 26 kW CLASS RADIATIVELY  
COOLED AMMONIA ARCJET NOZZLE

Frank S. Gulczinski III

**Introduction**

With the use of a 1.8 kW hydrazine arcjet on the Telstar IV communications satellite, arcjets have entered operation for satellite stationkeeping. However, even though they are an operational technology, there is still not enough known about the loss mechanisms that occur within the nozzle of the arcjet. These losses result in an electric power-to-useful thrust conversion rate of approximately 30% for the high power 26 kW class radiatively cooled ammonia arcjet that will be flight tested as an orbit transfer device as part of the United States Air Force's Electric Propulsion Space Experiment (ESEX) to be launched in January 1996. It is hoped that by using emission spectroscopy to non-obtrusively investigate the interior of the arcjet nozzle, a better picture of the operating state can be obtained so that loss mechanisms can be quantified and hopefully reduced.

Previously, interior measurements have been performed by Tahara, et al, using quartz optical access ports on water cooled arcjets {1,2}; Storm and Cappelli, using emission spectroscopy for axial measurements {3}; Rutyen, et al, using spectroscopic measurements angled into the arcjet {4}; and Zube and Myers {5} and Zube and Auweter-Kurtz {6} using optical access ports. All of these works, however, have been performed on low and medium power arcjets ( $P_E \geq 10$  kW). A more recent work by Hargus, et al, at the Phillips Electric Propulsion Laboratory examined the interior conditions of a high power arcjet {7}. The work discussed in this report was conducted in conjunction with Mr. Hargus to confirm and refine earlier findings and include photomultiplier tube (PMT) scans of the entire spectrum of interest.

## **Experimental Apparatus and Setup**

### **Experimental Facility:**

These experiments were carried out in Vacuum Chamber #2 of the USAF Electric Propulsion Laboratory located at the Phillips Laboratory, Edwards Air Force Base, California. This cylindrical chamber with an 8 foot diameter and a 12 foot axial test length is connected to a vacuum pump system capable of pumping at 23,400 cubic feet per minute. This permitted experimental operation with a pressure of 80 mTorr for a propellant mass flow rate of 200 mg/sec. The pressure was measured using a MKS Baratron® Type 122B Absolute Pressure Transducer. Mass flow was regulated by a MKS 1542 mass flow controller calibrated for ammonia.

Power was supplied to the arcjet by a Linde L-TEC PHC-601 plasma welding power supply capable of producing 60 kW of power at currents as high as 600 A. In this experiment, the arcjet was operated at 150 V and 120 A (18 kW).

Arcjet positioning was accomplished through the use of a Daedal 12 X 12 inch translation table for horizontal positioning and a 6 inch rail table for vertical positioning. Both of these tables were capable of 0.001 inch repeatability and straight line accuracies of 0.0005 inch/inch. These accuracies were necessary for proper alignment of the optical collection system.

### **Arcjet:**

The arcjet used in this research project was the USAF 26 kW class laboratory thruster {8} shown in Figure 1 (Page 5):

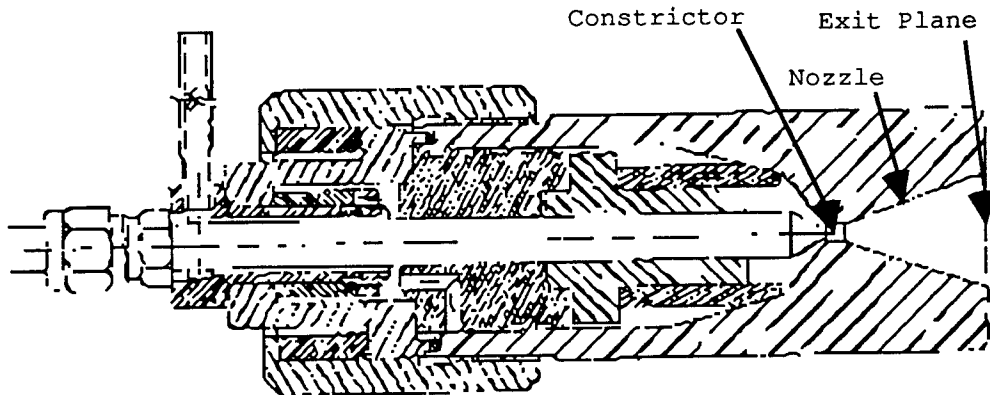


Figure 1: USAF 26 kW Class Laboratory Thruster

The exit plane to constrictor area ratio is 100:1. The constrictor length and diameter are both 0.1 inches. The nozzle length is 1.307 inches with a half angle of  $19^\circ$ .

Optical access to the interior of the nozzle was provided by holes drilled at 3 axial locations, each with a 0.020 inch diameter, created through electron deposition machining. The first is located 0.101 inch downstream of the constrictor. The remaining 2 holes are located equidistant from the first hole and the exit plane (0.402 inch separation). Based on the work of Zube and Myers in reference 5 it is believed that the optical access ports did not affect the performance of the arcjet. Their performance readings showed no measurable deviation with holes both opened and plugged for an arcjet with an access hole area to local nozzle expansion area comparable to that of the arcjet used here.

#### Spectroscopy System:

An optical train is used to focus the emission signal from the arcjet plasma onto the entrance slit of a Czerny-Turner 0.5 meter Acton Research SpectraPro-500 spectrometer. Three gratings were contained on an internal turret: 2400, 1200, and 600 grooves/mm. At 435.8 nm, the 1200 groove/mm grating provides the system with a resolution of 0.05 nm for first order lines. The spectrometer was fitted with both a Princeton Instruments thermo-electrically

cooled CCD detector for fine spectral resolution and an Acton Research Model 438 Photomultiplier Tube (PMT) for wide spectral scans. The entire system was calibrated using a 6.5 Å quartz halogen tungsten lamp with a calibration traceable to the National Institute of Standards and Technology.

Data Acquisition Equipment:

Spectra from the CCD were captured and stored on a Unisys PW<sup>2</sup> Advantage 3256DX personal computer using Princeton Instruments' CCD Spectrometric Multichannel Analysis (CSMA) software. Spectral scans from the PMT were captured and stored on a Tektronix Pep 301 personal computer using Galactic Industries Corporation's Spectra Calc software.

**Theoretical Background and Spectroscopic Techniques**

Emission spectroscopy is a diagnostic technique that uses the radiation emitted when an electron in a plasma falls from a higher quantum energy state to a lower quantum energy state to determine characteristics of the plasma. By making specific assumptions, it is possible to determine the composition of the plasma as well as determining plasma characteristics including: excited state temperatures, electron number density, and vibrational and rotational temperatures. In this report, excited state temperatures for prevalent species and electron number density are presented.

Two of the most important assumptions made are that the plasma is optically thin and that it is in partial local thermodynamic equilibrium. An optically thin plasma is one in which very few of the photons emitted are reabsorbed before they exit the plasma. Partial local thermodynamic equilibrium is a subset of the concept of local thermodynamic equilibrium (LTE). In LTE, it is assumed that when local populations of atomic or molecular energy states are examined they are found to be in thermodynamic equilibrium but that it is not necessary that all parts of the plasma share the same equilibrium state. This is applicable when excitation and de-excitation are primarily the result of collisional as opposed to radiative processes. It is often found, however, that LTE will only hold for energy levels above a cutoff point. Energy levels

that meet this criterion are said to be in partial local thermodynamic equilibrium (PLTE) [9]. States that are not in PLTE tend to appear as underpopulated when compared to those that are.

In order to determine which species are present in a plasma, a PMT scan is made. The observed transitions are then compared with tabulated results to determine which species exist. Most species of interest for arcjet plasma diagnostics have transitions that fall within or near the wavelengths of visible light -- between 300 and 700 nm -- so this is the area scanned in most investigations.

To determine atomic excitation temperatures, a technique known as a Boltzmann plot is used. Quantum theory tells us that for those energy levels which obey LTE, the following equation holds:

$$\ln \left[ \frac{I_{ij} \lambda_{ij}}{c A_{ij} g_i} \right] = - \frac{E_i}{kT} + \ln \left( \frac{hn}{2\pi Z} \right) \quad (1)$$

Where:

- $I_{ij}$ : Intensity of the transition from level i to level j
- $\lambda_{ij}$ : Wavelength of the transition from level i to level j
- c: Speed of light in vacuum
- $A_{ij}$ : Atomic transition probability from level i to level j
- $g_i$ : Degeneracy of the upper level
- $E_i$ : Energy of the upper level
- k: Boltzmann's constant
- T: Temperature
- h: Planck's constant
- n: Species density
- Z: Electron partition function

The intensity of the transition obtained from the spectrographic measurements is used to compute the term on the left hand side of the equation. This is then plotted versus the energy of the transition, which is a known function. For those energy levels in PLTE, the plot will be a straight line from which the temperature (in electron volts) can be determined by taking the negative

inverse of its slope (See Figures 3-6, Pages 10-12 as examples). Additionally, it is important to note that since only the slope of the line is of interest, the absolute intensities of the transitions are not necessary -- only the relative intensities of several transitions.

Electron number density can be determined by using a method developed by Griem {9} for use with hydrogen and hydrogen-like lines. What Griem shows is that for systems in which only the first ionization is important -- which is the case in arcjet plasmas -- the Stark (collisional) broadening of the line is proportional to the two-thirds power of the ion density (which is equal to the electron density). Therefore we can state that:

$$n_e = C(n_e, T_e) \Delta\lambda_s^{2/3} \quad (2)$$

Where:

$n_e$ : Electron number density

$C(n_e, T_e)$ : Function of number density and temperature

$\Delta\lambda_s$ : Full Stark width

Thus, by measuring the full width at half maximum (FWHM) of a well known line -- the hydrogen Balmer beta line in this case -- where  $C(n_e, T_e)$  is known, it is possible to determine the electron number density through an iterative process. Since this method depends on an accurate determination of electron temperature -- which for arcjet plasmas is approximately equal to the hydrogen temperature -- and Debye-shielding effects are not accounted for in the analysis it is believed that there is an experimental uncertainty of approximately 20%.

## Results

Data was taken for the arcjet operating at 18 kW with a mass flow rate of 200 mg/s. These operating conditions were chosen on the low end of the high power regime for two reasons. First, operating at lower power and mass flow rate minimizes erosion of the nozzle and damage to the optical access ports. Second, operating at these conditions offers a better opportunity to compare findings to those of Zube and Myers {5} for low power arcjets. Readings were

taken at the three optical access ports (referred to hereafter, in order downstream from the constrictor, as Hole 1, Hole 2, and Hole 3) as well as at the arcjet's exit plane.

Species composition for the plasma was determined from the PMT scan. Though measurements at the holes varied greatly in line intensity, they did not do so in composition. The following species were identified at all locations: atomic hydrogen ( $H$ ), singly ionized atomic nitrogen ( $NII$ ), molecular nitrogen ( $N_2$ ), and the  $NH$  ion. Given the fact that the propellant is ammonia ( $NH_3$ ) these compounds were expected. However, the lack of non-ionized atomic nitrogen ( $NI$ ) seems to indicate that the  $NH$  found in the plasma results from dissociation of ammonia rather than a combination of hydrogen and nitrogen ( $NI$ ). The most prevalent lines for these compounds are shown in the sample spectra from Hole 1 in Figure 2, below:

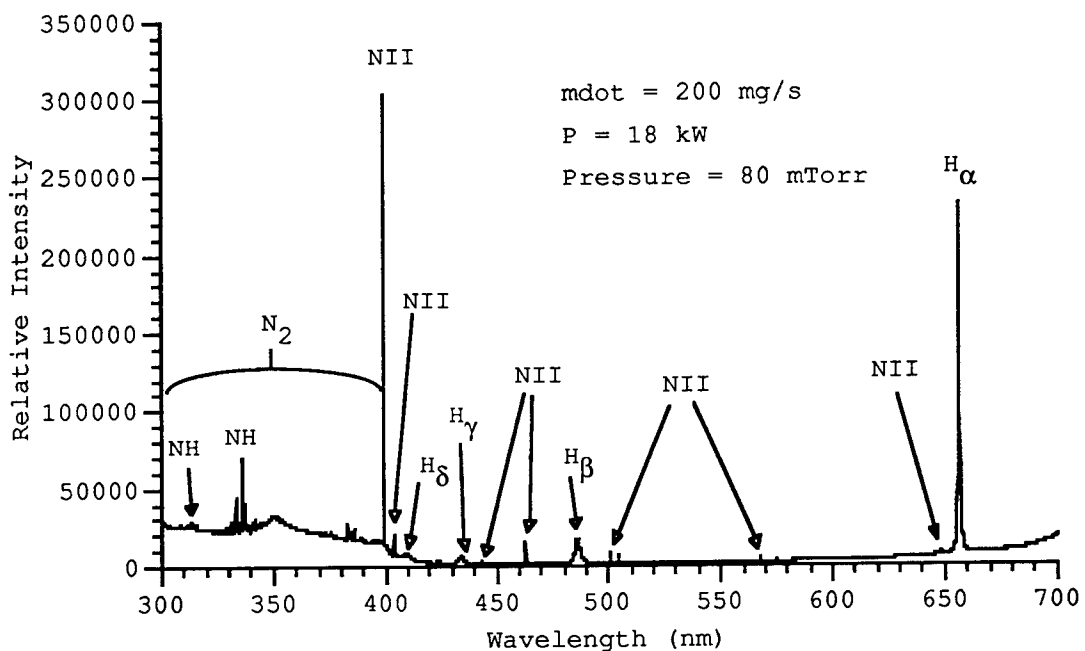


Figure 2: Photomultiplier Tube Scan for Hole 1

We see the presence of  $N_2$  as a wide band below 420 nm, through which other lines protrude. In addition to these compounds derived from ammonia, trace

amounts of CH and CN (cyanide) were detected, indicating that a carbon impurity was being introduced somewhere in the system.

For hydrogen excitation temperatures, the very bright and easily obtained lines of the hydrogen Balmer series were used. In many instances, the lower energy lines were found not to be in equilibrium. The temperatures were determined using the Boltzmann plot method from the plots shown in Figures 3-6 (Pages 10-12):

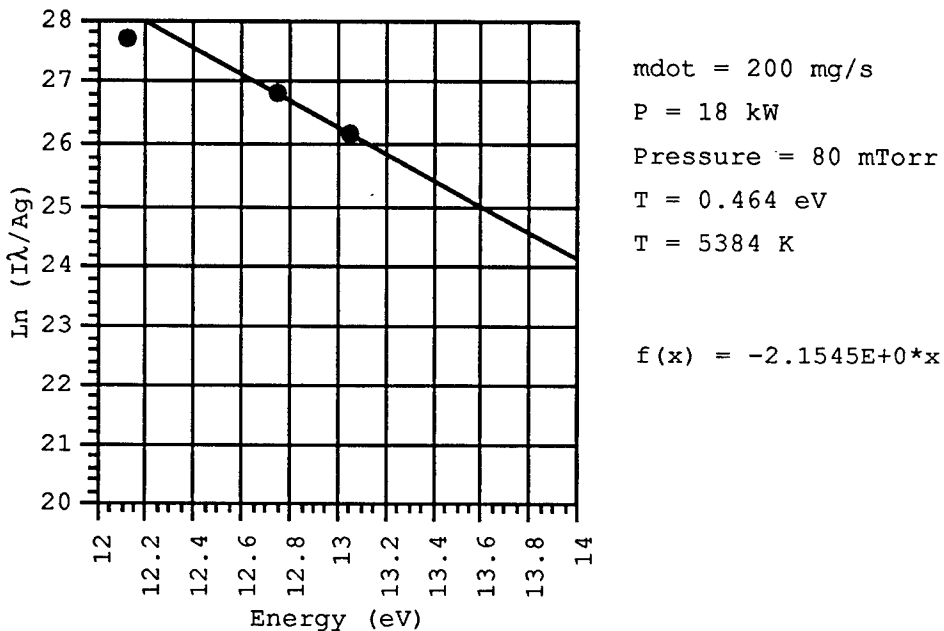
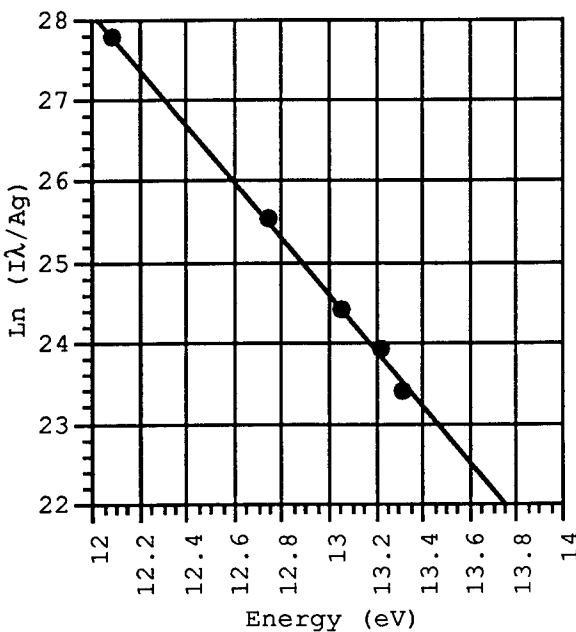
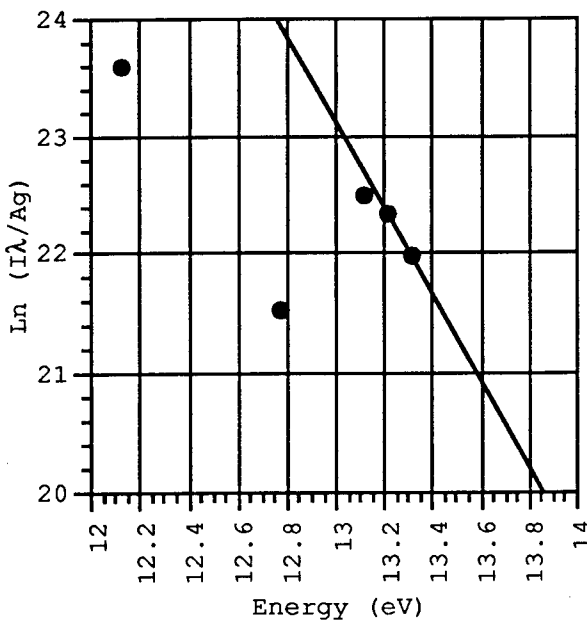


Figure 3: Hydrogen Temperature at Hole 1



$\dot{m} = 200 \text{ mg/s}$   
 $P = 18 \text{ kW}$   
 Pressure = 80 mTorr  
 $T = 0.2875 \text{ eV}$   
 $T = 3335 \text{ K}$   
 $f(x) = -3.4782E+0*x$

Figure 4: Hydrogen Temperature at Hole 2



$\dot{m} = 200 \text{ mg/s}$   
 $P = 18 \text{ kW}$   
 Pressure = 80 mTorr  
 $T = 0.274 \text{ eV}$   
 $T = 3180 \text{ K}$   
 $f(x) = -3.6479E+0*x$

Figure 5: Hydrogen Temperature at Hole 3

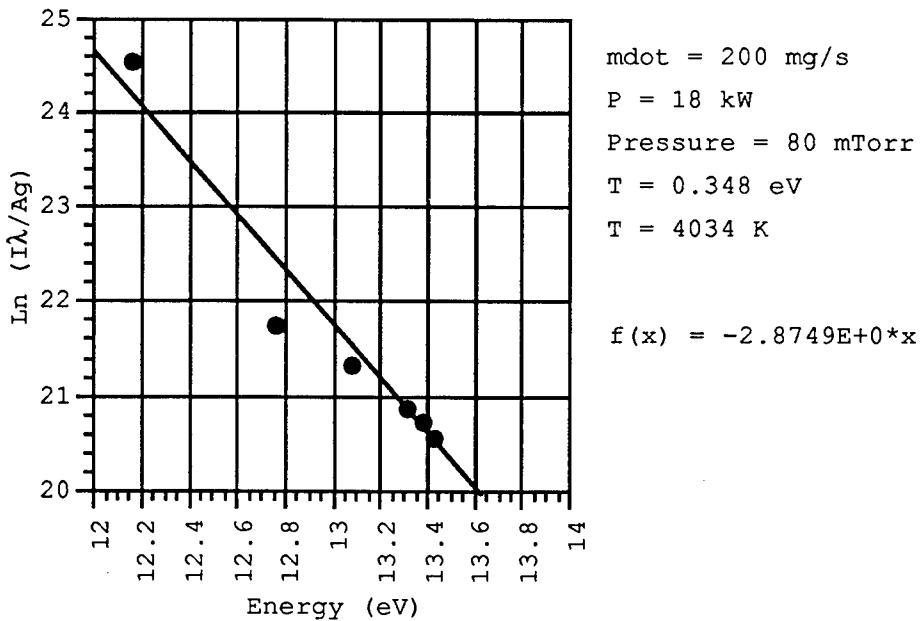


Figure 6: Hydrogen Temperature at Exit Plane

The hydrogen temperatures are calculated by taking the negative inverse of the curve-fit line's slope (the  $f(x)$  quantity shown on the plots). Those points that are significantly below the curve fit line at lower energy levels correspond to underpopulated states that do not meet the criteria for LTE and are therefore not included in the temperature calculations. We note that as we proceed downstream, underpopulated states occur at progressively higher energy levels. We also note that as we proceed downstream from the constrictor, it is possible to resolve higher order (higher energy) transitions due to a lessening of Stark broadening. Both of these facts seem to indicate a decrease in electron density as the plasma flows downstream, since LTE requires a collisionally dominated plasma -- a condition more likely to exist at higher density -- and Stark broadening is proportional to the density raised to the two-thirds power. These suspicions are confirmed by the electron density measurements that follow.

The overall trend in temperature is seen in Figure 7, Page 13 along with previous results obtained by Hargus {7} and Zube and Myers {5} (NOTE: area ratio increases as one proceeds downstream from the constrictor).

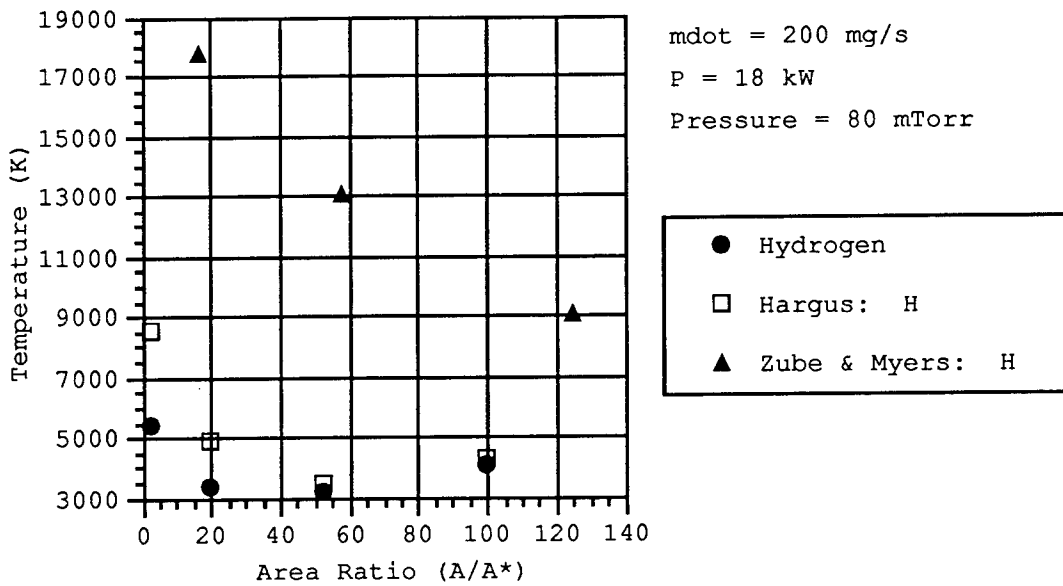


Figure 7: Nozzle Hydrogen Temperature Distribution

So, as we proceed downstream we observe a decrease in hydrogen temperature until the exit plane is reached, at which point there is a jump in temperature. The drop along the nozzle is expected since the atoms will lose the kinetic energy that they gained from the constrictor arc through expansion and collisions. The temperature jump at the exit plane, however, was unexpected and is not fully understood at this time. One hypothesis is that it may be the result of a barrel shock generated when the plasma exits the nozzle. In comparing this data to previous results, we see that it compares well with Hargus' previous results for this arcjet for Hole 3 and for the Exit Plane, but that it is significantly lower for Holes 1 and 2. This is believed to result from a refinement of data gathering techniques and thus reflects a more accurate temperature profile. Comparing this data with that of Zube and Myers, we see temperature differences of approximately 10,000 K. It is believed, however, that this data is more accurate since Zube and Myers used only the hydrogen Balmer alpha and beta transitions which are the lowest energy and thus frequently fail to meet LTE requirements.

NII excitation temperatures were determined using the same method. Based on the work of Tahara, a line at 444.7 nm and two groups of lines -- one near 462

nm the other near 567 nm -- were chosen [2]. However, it was only possible to determine the temperature at Holes 1 and 2 before the intensity diminished to the point where readings were not possible. The plots are shown in Figures 8 and 9:

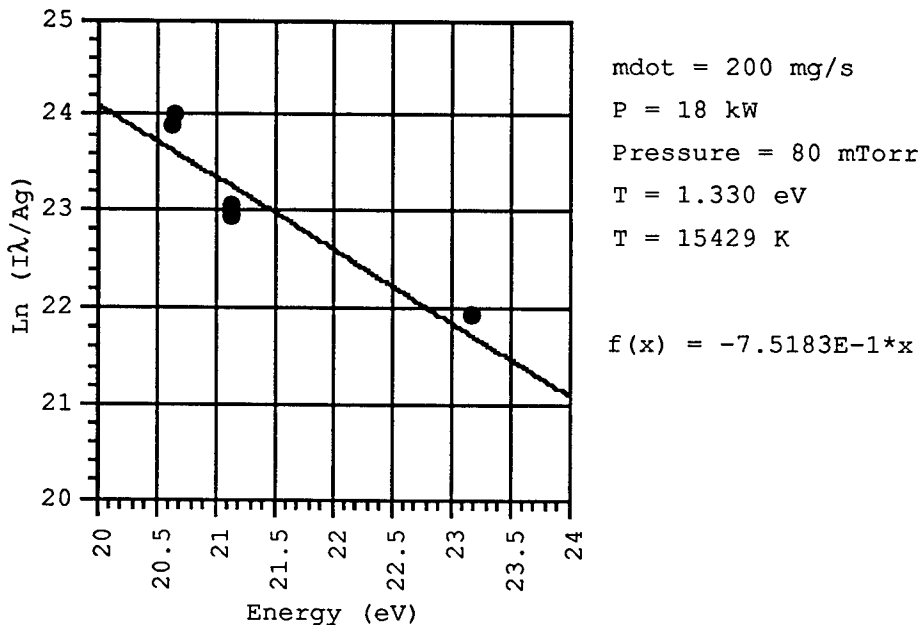


Figure 8: NII Excitation Temperature at Hole 1

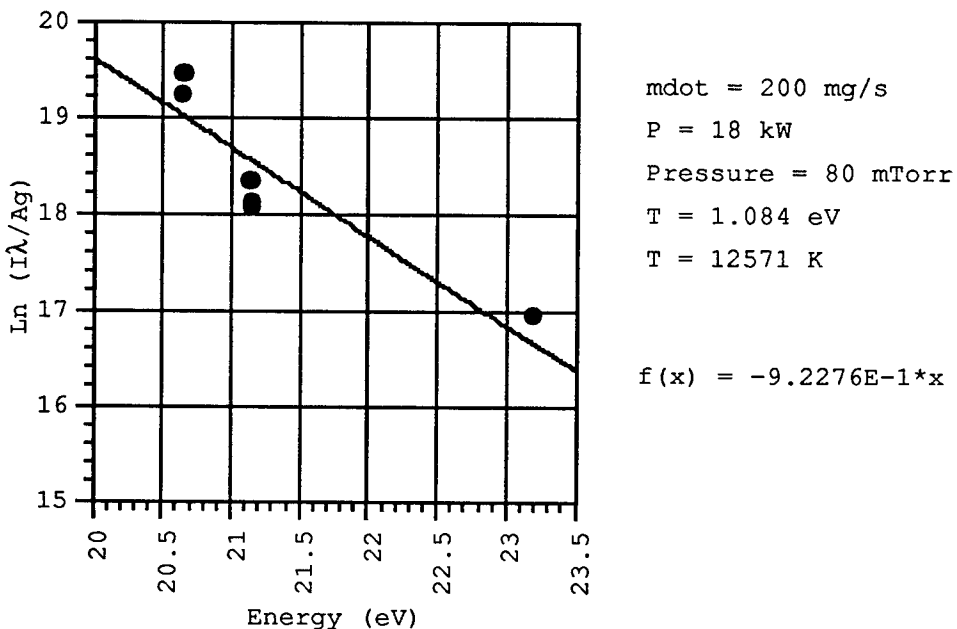


Figure 9: NII Excitation Temperature at Hole 2

The NII temperatures measured are much higher than the hydrogen temperatures at the same location along the nozzle. This is believed to be a result of non-equilibrated non-uniform flow within the arcjet. Whereas the lighter hydrogen atoms tend to expand away from the radial center of the arcjet, the heavier nitrogen ions tend to remain in the core of the arcjet, where they continue to be heated more readily by the electric arc. Thus, the NII represents the center of the arcjet while the hydrogen represents an overall temperature distribution.

The electron number densities were determined using Griem's method. The overall results for the arcjet are shown in Figure 10. As before, they are compared to the results obtained by Hargus {7} and Zube and Myers {5}.

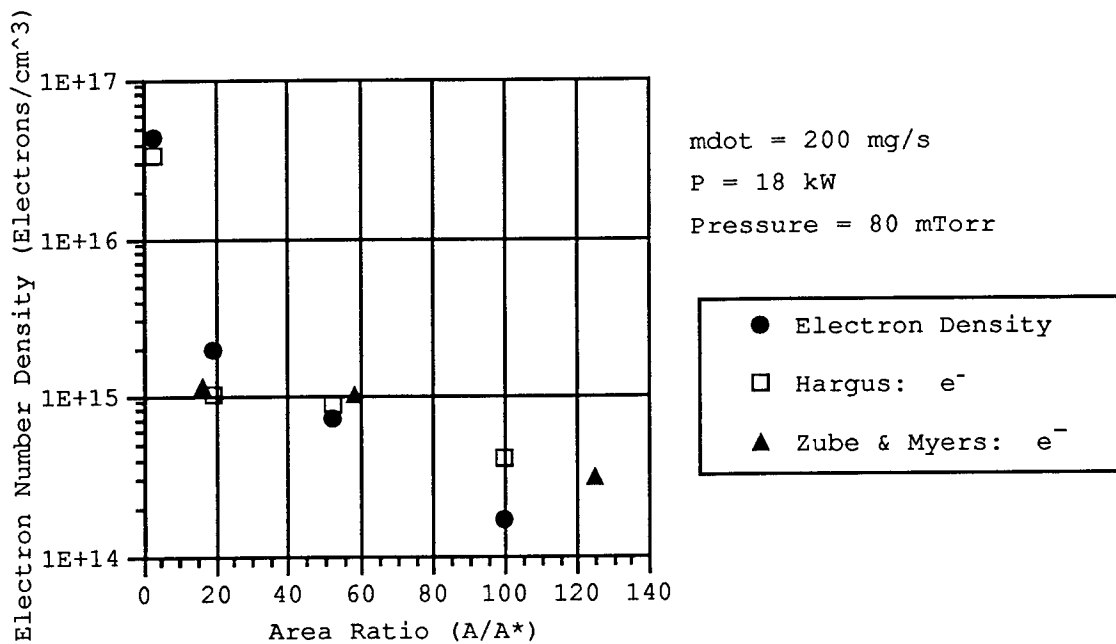


Figure 10: Nozzle Electron Density Distribution

We see that our earlier suspicions of decreasing electron density based on LTE concerns and Stark broadening have been confirmed. The decreasing electron density results from two factors: nozzle expansion and electron-ion recombination. This recombination is made possible by the drop in kinetic energy (which is reflected in a drop of species temperatures) through particle

collisions. We find good agreement when comparing these results and those of Hargus to those found by Zube and Myers for a 1 kW arcjet. This seems to indicate that the increase in specific power between these two arcjets (from 25 MJ/kg for Zube and Myers to 90 MJ/kg here) is balanced by the increased nozzle volume of the high power arcjet such that the electron density becomes a function of area ratio only.

### Conclusions

By studying the spectra of the arcjet plasma, it was determined that the ammonia propellant ( $\text{NH}_3$ ) tends to break down into hydrogen (H), singly ionized atomic nitrogen (NII), molecular Nitrogen ( $\text{N}_2$ ), and NH. The lack of non-ionized nitrogen (NI) shows that NH is not formed by the combination of NI and H.

Studies of hydrogen temperature show a decrease as the plasma expands through the nozzle, with an increase at the exit plane that may be caused by a barrel shock. These measurements also indicate that many of the lower energy states are non-equilibrated so that the assumption of partial local thermodynamic equilibrium must be used.

In examining the NII temperatures, we see a drop in temperature through the first two holes similar qualitatively to that seen for hydrogen, but occurring at much higher temperatures. This indicates that the species within the plasma are not equilibrated with each other and that the plasma itself is spatially non-uniform.

Electron number density decreases in the downstream direction as a result of nozzle expansion and electron-ion recombination. The density measurements agree well with earlier results taken for low power arcjets. This indicates that the mechanisms of increasing specific power and increasing nozzle volume associated with an increase in arcjet power balance to keep electron density constant.

## **Acknowledgments**

This work was sponsored by the Air Force Office of Scientific Research through its Graduate Student Research Program. Thanks to Mr. William Hargus and Dr. Ronald Spores of Phillips Laboratory and Professor Alec Gallimore of the University of Michigan for their theoretical and technical assistance.

## **References**

1. Tahara, H., T. Sakakibara, K. Onoe, and T. Yoshikawa, "Experimental and Numerical Studies of a 10 kW Water-Cooled Arcjet Thruster," Paper IEPC 91-015, 22nd International Electric Propulsion Conference, 14-17 October 1991, Viareggio, Italy.
2. Tahara, H., N. Uda, K. Onoe, and Y. Tsubakishita, "Optical Measurement and Numerical Analysis of Medium Power Arcjet Non-Equilibrium Flowfields," Paper IEPC 93-133, 23rd International Electric Propulsion Conference, 13-16 September 1993, Seattle, Washington.
3. Storm, P.V. and M.A. Cappelli, "Axial Emission Diagnostics of a Low Power Hydrogen Arcjet Thruster," Paper IEPC 93-219, 23rd International Electric Propulsion Conference, 13-16 September 1993, Seattle, Washington.
4. Rutyen, W.M., D. Burtner, and D. Keefer, "Spectroscopic Investigation of a Low-Power Arcjet Plume," Paper AIAA 93-1790, 29th Joint Propulsion Conference, 28-30 June 1993, Monterey, California.
5. Zube, D.M. and R.M. Myers, "Nonequilibrium in a Low Power Arcjet Nozzle," Paper AIAA 93-2113, 27th Joint Propulsion Conference, 24-27 June 1991, Sacramento, California.
6. Zube, D.M. and M. Auweter-Kurtz, "Spectroscopic Arcjet Diagnostic Under Thermal Equilibrium and Non-Equilibrium Conditions," Paper AIAA 93-1792, 29th Joint Propulsion Conference, 28-30 June 1993, Monterey, California.

7. Hargus, W., M. Micci, and R. Spores, "Interior Spectroscopic Investigation of the Propellant Energy Modes in an Arcjet Nozzle," Paper AIAA 94-3302, 30th Joint Propulsion Conference, 27-29 June 1994, Indianapolis, Indiana.
8. Deininger, W.D., A. Chopra, T.J. Pivirotto, K.D. Goodfellow, and J.W. Barnett, "30 kW Ammonia Arcjet Technology: Final Report July 1986-December 1989." JPL Publication 90-4, 15 February 1990.
9. Griem, Hans R., *Plasma Spectroscopy*, McGraw-Hill Book Company, New York, 1964.

**DROP SIZING OF A LIKE-IMPINGING ELEMENT INJECTOR  
IN A HIGH PRESSURE ENVIRONMENT**

**Derik C. Herpfer**  
**Graduate Research Assistant**  
**Department of Aerospace Engineering and Engineering Mechanics**

**University of Cincinnati  
797 Rhodes Hall, ML #70  
Cincinnati, OH 45221**

**Final Report for:  
Graduate Student Research Program  
Phillips Laboratory**

**Sponsored by:  
Air Force Office of Scientific Research  
Bolling Air Force Base, DC  
and  
Phillips Laboratory**

**September 1994**

**DROP SIZING OF A LIKE-IMPINGING ELEMENT INJECTOR  
IN A HIGH PRESSURE ENVIRONMENT**

Derik C. Herpfer

Graduate Research Assistant

Department of Aerospace Engineering and Engineering Mechanics

University of Cincinnati

**Abstract**

The effect of gas density and liquid momentum flux on the average drop size of a like-impinging element injector was studied. These effects were studied over a wide range gas densities and liquid momentum flux. Gas density was varied up to  $159 \text{ kg/m}^3$ , corresponding to a test chamber pressure of 2000 psig. Average drop sizes were measured by a Malvern Instruments Particle Sizer. The Malvern instrument is a laser based optical probe utilizing the Fraunhofer diffraction theory of light to measure particle sizes. Sauter mean diameter, mass median diameter, as well as size distribution are calculated by the Malvern instrument. Correlations for the mean diameters were derived in this study and compared with those available in the open literature. These studies indicate that the average drop size in the spray of a like-impinging element injector decreases with increasing gas density and increasing liquid momentum flux.

DROP SIZING OF A LIKE-IMPINGING ELEMENT INJECTOR  
IN A HIGH PRESSURE ENVIRONMENT

Derik C. Herpfer

Introduction

An injector commonly used in liquid rocket engine combustors is the impinging element injector. In an impinging element injector, two or more liquid jets impact at a single point. Mixing and atomization occur at this point due to the dissipative exchange of momentum between the jets. This injector type can be composed of either unlike or like impinging elements. An unlike element has at least one fuel and one oxidizer jet which may have different flowrates and orifice diameters. A like element injector has two or more jets of the same liquid, orifice diameter, and flowrate. The spray formed by a two element impinging element injector is called a doublet.

Since only atomization occurs at the impingement point of a like-impinging element injector, a rocket motor designed with this type of injector mixes fuel and oxidizer by overlapping individual fuel and oxidizer sprays. Therefore, to analyze the mixing that occurs between the sprays, it is necessary to know the distribution and average size of the droplets within the spray of each individual injector. This paper investigates the drop size characteristics of a like-on-like doublet as a function of the ambient gas density that the doublet is formed in, and the momentum flux of the liquid jets that create the doublet. A comprehensive review of rocket injector elements and their design characteristics is provided in Reference 1.

Experimental Setup

A Malvern Instruments series 2600c Particle Sizer was used to measure the drop size of a like-on-like doublet. The Malvern instrument was fitted with an extended range lens,  $f=600\text{mm}$ , which allowed droplets to be measured within the size range  $11.6\text{-}1128\mu\text{m}$ . The like-on-like doublet was formed by an impinging element injector using demineralized water to simulate liquid fuel. The injector consists of two similar straight edge orifices with an included angle between them of  $60^\circ$ . Each orifice has a  $L/d$  of 27.76 and a diameter of  $0.7925\text{mm}$ . The impingement point of the two jets is  $3.43\text{mm}$  downstream of the plate in which the two orifices are drilled.

The injector was mounted vertically downward in a pressure chamber rated to  $13,790\text{kPa}$ . The chamber is pressurized with nitrogen. Optical access to the chamber is provided by three  $50\text{mm}$  diameter and one  $100\text{mm}$  diameter sapphire windows. A detailed description of this high pressure facility can be found in Reference 2. The Malvern instrument was mounted with the receiving optics on the large diameter window. The laser beam was oriented perpendicular to the centerline of the spray fan of the

doublet 41mm downstream of the impingement point of the injector. A CCD camera and a halogen light were mounted on the other two windows. For an overview of this high pressure chamber, see Figure 1.

Tests were conducted on this injector configuration at various chamber pressures and orifice pressure drops. The chamber pressure was increased in 1,379kPa increments from atmospheric conditions to 13,790kPa. The pressure drop across the orifice was varied between 69-2068kPa at each chamber pressure. Malvern drop size measurements of the doublet were made at the one downstream location at each chamber pressure and orifice pressure drop. The CCD camera was used to record the bulk spray characteristics such as fan angle and as a comparison to the Malvern data.

The chamber was pressurized slowly and allowed to settle before testing in order to eliminate density gradients within the chamber. Variations in gas density within the chamber made it difficult to maintain alignment of the laser and receiving optics.

#### Malvern Background

The Malvern Particle Sizer is based on the principle of laser diffraction. It uses the Fraunhofer diffraction theory to determine a particle size distribution from the light collected by its receiving optics. Light diffracted by droplets in the spray is focused by a Fourier transform lens onto a multi-element photodetector. The incident laser light diffracted by a droplet depends on the diameter of the droplet, a large droplet will diffract light into a small angle, while a small droplet will diffract light into a large angle. An illustration of this can be seen in Figure 2. It should be noted that this instrument measures the drop size along the entire length of the laser beam, it does not discriminate between those droplets within the spray and those outside the flowfield. Also, it does not measure individual droplet sizes, it deduces the volume size distribution that corresponds to the diffraction pattern collected by the receiving optics. Therefore, it can only calculate average drop sizes such as the Sauter mean diameter, and the mass median diameter.

In this study, the volume size distribution calculated by the Malvern instrument was constrained with the additional criteria that it had to fit the Rosin-Rammler size distribution function. The Rosin-Rammler size distribution function relates the fraction of droplets R, whose sizes are less than the a given diameter D, as follows.

$$R = e^{-(D/X)^N}$$

where: X - drop size corresponding to the peak of the volume frequency distribution.  
N - distribution width parameter.

The choice of the Rosin-Rammler function over other distribution models was dictated by the large amount of multiple scattering encountered during the tests. The Malvern instrument assumes that light

diffracted by each droplet is collected independently from other droplets by the receiving optics. In the very dense sprays encountered in this study, some of the light diffracted by each droplet will be scattered by other droplets within the spray. The net result is that the apparent size distribution is broader and smaller in average size than the actual distribution. A significant amount of this secondary scattering occurs at laser obscurations above 50%, where obscuration is the amount of attenuation of the incident laser beam.

The Malvern Particle Sizer compensates for this by applying an empirical correction to the Rosin-Rammler size distribution function. It is of the form.

$$C_x = 1 + [0.036 + 0.49(Ob)^{9.0}]N(1.9 - 3.44Ob)$$

$$C_N = 1 + [0.035 + 0.11N(Ob)^{8.65}](0.35 + 1.45Ob)$$

where: Ob - obscuration  
 $C_x$  - corrected X/X  
 $C_N$  - corrected N/N

The Rosin-Rammler distribution has been extensively used in the past to model liquid droplets in a spray as discussed below. For more information on the theory behind the Malvern Particle Sizer, see Reference 3.

#### Malvern Drop Size Results

Malvern drop size measurements of a like-on-like doublet were made at various gas densities and liquid momentum flux. It was observed that at high gas densities,  $> 48.6 \text{ kg/m}^3$ , the spray became so dense with liquid momentum flux  $> 414,000 \text{ kg/m-s}^2$  that Malvern data could not be collected. From the test conditions where drop size data could be recorded, correlations for Sauter mean diameter and mass median diameter were made by multiple regression of the data using the Marquardt-Levenberg algorithm. The result was the following correlations.

$$SMD = 3.69 \times 10^4 (\rho_l v_i^2)^{-0.44} \rho_g^{-0.15}$$

$$\bar{D} = 1.35 \times 10^4 (\rho_l v_i^2)^{-0.34} \rho_g^{-0.13}$$

where: SMD - Sauter mean diameter,  $\mu\text{m}$ , the diameter of the droplet whose volume to surface area ratio is the average of all droplets in the spray.

$\bar{D}$  - mass median diameter,  $\mu\text{m}$ , the droplet size such that half of the mass of the spray is contained in droplets having a larger diameter.

$\rho_g$  - gas density,  $\text{kg/m}^3$

$\rho_l$  - liquid density,  $\text{kg/m}^3$

$v_l$  - liquid velocity, m/s

Which can be rewritten in the form,

$$SMD = 1.77 \times 10^3 v_l^{-0.88} \rho_g^{-0.15}$$
$$\bar{D} = 1.29 \times 10^3 v_l^{-0.68} \rho_g^{-0.13}$$

Figure 3 plots the measured SMD data in comparison to those calculated by the derived correlation. As can be seen, the correlation produces large errors at the lower SMDs, on the order of 40%. Analysis of the collected data showed that the gas density term did not correlate well at high gas densities, values greater than 127 kg/m<sup>3</sup>. At these high densities, the correlation overpredicted drop size as compared to the experimental values. However, the correlation may still be correct. At the high gas densities, Malvern drop size measurements were made with obscurations > 97%, as compared with an average or 80% for the lower gas densities. At these extreme obscurations, the empirical correction factor used by the Malvern instrument to compensate for the effects of multiple scattering may not have been enough. The drop sizes measured by the Malvern instrument were probably less than the actual sizes in the spray.

The correlations developed by this study are in agreement with those developed for like-on-like doublets by other researchers. Hautman<sup>4</sup> and Lourme<sup>5</sup> both investigated doublets generated by like-impinging element injectors with a Malvern Particle Sizer. Hautman used a Rosin-Rammler size distribution to fit Malvern data over a range of liquid properties, liquid momentum fluxes, gas densities, and injector sizes. He developed the following correlations.

$$SMD = 1.3 \times 10^7 (\rho_l v_l^2)^{-0.7} \sigma_l^{0.6} \rho_g^{-0.09}$$
$$\bar{D} = 5.34 \times 10^6 (\rho_l v_l^2)^{-0.62} \sigma_l^{0.43} \rho_g^{-0.16}$$

where:  $\underline{SMD}$  - Sauter mean diameter,  $\mu\text{m}$

$\bar{D}$  - mass median diameter,  $\mu\text{m}$

$\rho_g$  - gas density, kg/m<sup>3</sup>

$\rho_l$  - liquid density, kg/m<sup>3</sup>

$v_l$  - liquid velocity, m/s

$\sigma_l$  - liquid surface tension, kg/s<sup>2</sup>

Lourme over a smaller range of variation of flow properties developed the correlation.

$$\bar{D} = 240 v_l^{-1} d^{0.3} \sigma_l^{0.5} \rho_l^{-0.2}$$

where:  $\bar{D}$  - mass median diameter,  $\mu\text{m}$   
 $\rho_g$  - gas density,  $\text{kg/m}^3$   
 $v_l$  - liquid velocity,  $\text{m/s}$   
 $\sigma_l$  - liquid surface tension,  $\text{kg/s}^2$   
 $d$  - orifice diameter,  $\text{mm}$

Tests done in the 60's and early 70's on like-on-like doublets, using either photographic techniques or the hot wax technique, also agreed with the results of this study. The hot wax technique consists of injecting hot wax into a test chamber. The hot wax forms droplets which cool and solidify into solid particles which are then collected and sorted into size groups. In this way, a particle size distribution is calculated which corresponds to the liquid drop sizes within the spray. Dickerson et. al.<sup>6</sup> and Zajac<sup>7</sup> used this technique at atmospheric conditions for turbulent jet doublets formed by a like-impinging element injector with an included angle of  $60^\circ$ . Dickerson et. al. developed the correlation.

$$\bar{D} = 4.51 \times 10^3 d^{0.57} v_l^{-0.85}$$

The correlation of Zajac was similar.

$$\bar{D} = 7.67 \times 10^3 d^{0.57} v_l^{-1} (P_c/P_j)^{-0.1}$$

where for both:

$\bar{D}$  - mass median diameter,  $\mu\text{m}$   
 $v_l$  - liquid velocity,  $\text{m/s}$   
 $d$  - orifice diameter,  $\text{mm}$   
 $P_c/P_j$  - centerline to mean dynamic pressure ratio of the liquid jet

Drombowski and Hooper<sup>8</sup> used a photographic technique with water at atmospheric conditions to derive the correlation.

$$SMD = 0.105 v_l^{-0.79} (\sin \alpha / 2)^{-1.16}$$

where: SMD - Sauter mean diameter,  $\mu\text{m}$   
 $v_l$  - liquid velocity,  $\text{m/s}$   
 $\alpha$  - included angle between orifices

A comparison between the mass median diameter correlated in this study and those referenced above can be made in terms of two variables, liquid velocity and gas density. The effect of gas density on drop size is comparable in all three correlations were it is a variable. However, the correlation derived in this study indicates that drop size is not as dependent on gas density as reported previously. This is the result of the larger data base available in this study. In the previous works, gas density was limited to less than 29

$\text{kg/m}^3$ , while for this correlation, it was varied to  $159 \text{ kg/m}^3$ . As noted by others<sup>4</sup>, a change in gas density has a greater effect on drop size at low gas densities than at high gas densities.

The comparison of the effect of liquid velocity on the correlations shows a greater difference. The correlation derived in this study was far less dependent on liquid velocity than the others, even though the velocity range sampled was comparable. The only difference in test conditions between the correlations that could affect this term is that the correlation developed in this paper is for one orifice diameter, while the others are based on a wide range of orifice diameters.

### Video Results

The like-on-like doublets were videotaped at all flow conditions where Malvern data was recorded. The trends observed with both instruments were similar. For a given gas density, drop size decreased with increasing liquid momentum flux. For a fixed liquid momentum flux, drop size decreased with increasing gas density. The video data was also analyzed to correlate spray fan angle to liquid momentum flux and gas density. After multiple regression of the video data, the fan angle, the angle measured from the centerline to one edge of the spray, was reduced to the following relationship.

$$\theta = 88.95 (\rho_g v_l^2)^{-0.048} \rho_g^{-0.044}$$

where:  $\theta$  - fan angle, degrees

$\rho_g$  - gas density,  $\text{kg/m}^3$

$\rho_l$  - liquid density,  $\text{kg/m}^3$

$v_l$  - liquid velocity, m/s

As can be seen, the fan angle has only a weak dependence on these properties. That is, high gas density does not significantly change the shape of the doublet. Although droplets generated by an injector operating at a given pressure drop will be smaller at a high gas density than a low one, they will form a spray of approximately the same dimensions.

### Conclusion

The correlations developed in this study will prove useful for the design and integration of impinging element injectors in liquid rocket engine combustors. They also provide a useful insight on the effect of high gas density on liquid atomization. However, the correlations are limited. They do not take into account variations in orifice diameter, liquid properties, and impingement angle, which are of great importance in a rocket injector design. They also are not based on realistic rocket injector pressure drops. Although the gas densities used in this paper were high enough to simulate a rocket combustor, the Malvern instrument could not measure drop size in the sprays produced by large injector pressure drops at high gas density. The rule of thumb for a like-impinging element injector to suppress chug instability in the combustion chamber is that the pressure drop across the injector be approximately 15 to 25 percent of

the chamber pressure. The correlations in this paper are based on a pressure drop of less than 2 percent at the highest gas densities.

#### Acknowledgments

This work was sponsored by the Air Force Office of Scientific Research, Bolling AFB, DC. Experiments were conducted at the facilities of the USAF Phillips Laboratory OL-AC PL/RKCC, 1-14 Satellite Propulsion Complex, Edwards AFB, CA.

#### References

- 1)NASA, *Liquid Rocket Engine Injectors*, National Aeronautics and Space Administration SP-8089, March 1976
- 2)K.O. Farner, W.M. Grissom, and G. Miller, "High Pressure Flow Facility for the Study of Injector Design Impacts on Spray Characteristics," Extended abstracts of the Sixth Annual Conference on Liquid Atomization and Spray Systems, Worcester, MA, May 17-19, 1993
- 3)J. Swithenbank, J.M. Beer, D.S. Taylor, D. Abbot, and G.C. McCreath, "A Laser Diagnostic Technique for the Measurement of Droplet and Particle Size Distribution," AIAA Paper 76-79, 1976
- 4)D.J. Hautman, "Spray Characterization of Liquid/Liquid Like-on-Like Doublet and Pentad Impinging Injectors," United Technologies Research Center Report R89-252389-1, East Hartford, CN, March 1990
- 5)D. Lourme, "Like-on-Like Injector Spray Characterization for the Ariane Viking Engine," AIAA/SAE/ASME 22nd Joint Propulsion Conference, Huntsville, AL, June 16-18, 1986
- 6)R. Dickerson, K. Tate, and N. Barsic, "Correlation of spray Injector Parameters with Rocket Engine Performance," Rocketdyne Report R-7499, AFRPL-TR-68-147, June, 1968
- 7)L. Zajac, "Correlation of Spray Dropsize Distribution and Injector Variables," Rocketdyne Report R-8455, Contract NAS7-726, February, 1971
- 8)A. Ferrenberg and V. Jaqua, "Atomization and Mixing Study Interim Report," Rockwell International Rocketdyne Division Report RI/RD83-170, Canoga Park, CA, July, 1983

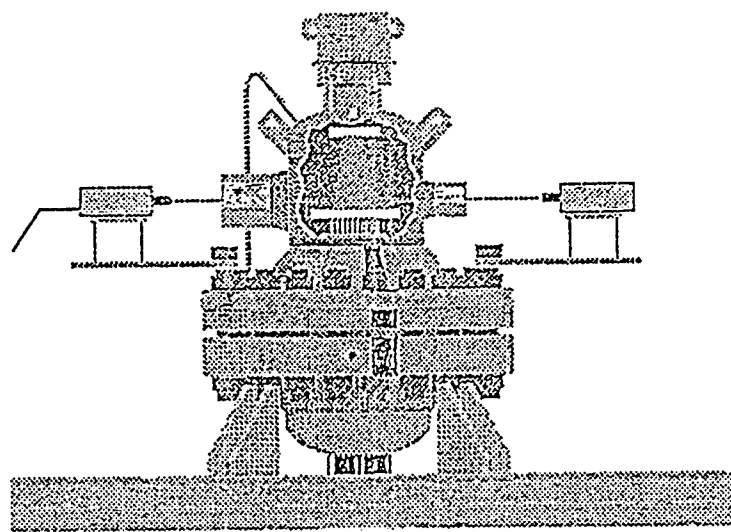


**Figure 1. Experimental Facilities**

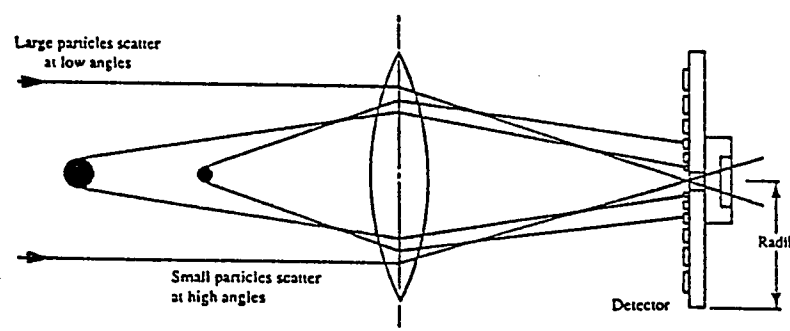


**Figure 2. Malvern Theory**

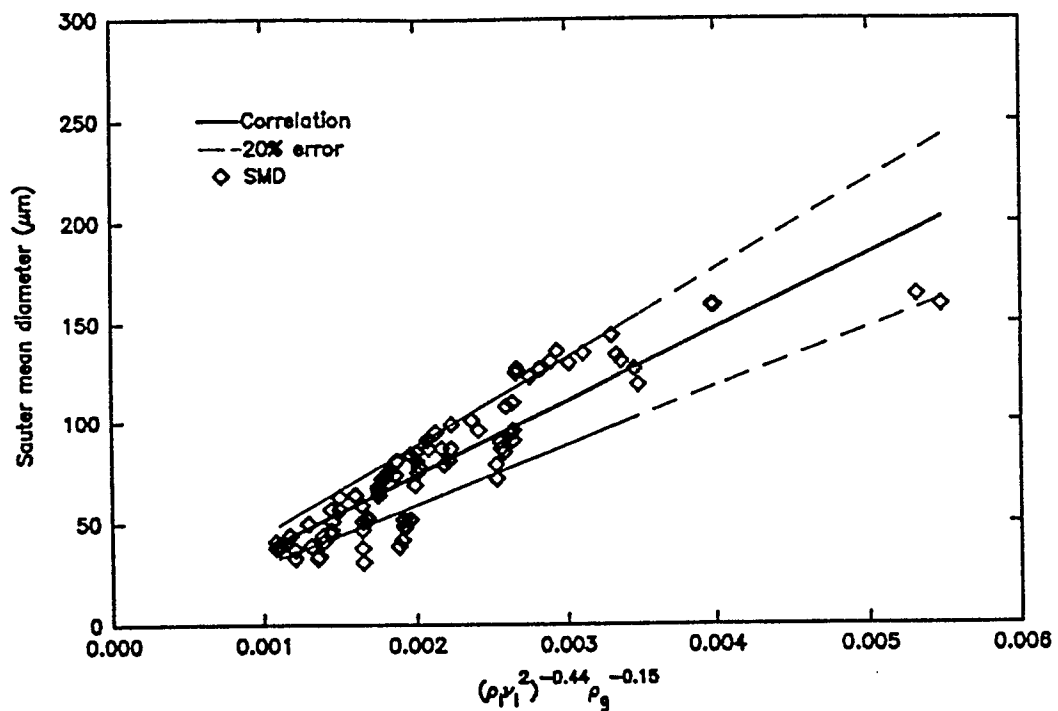


**Figure 3. Comparison of correlation and measured SMD's**

## EFFECTIVENESS OF THERMIONIC HEAT PIPE MODULE

Phillip N. Hutton  
Department of Physics

Old Dominion University  
Norfolk, VA 23529

Final Report for:  
Graduate Student Research Program  
Phillips Laboratory

Sponsored by:  
Air Force Office of Scientific Research  
Bolling Air Force Base  
Washington DC

and

Phillips Laboratory  
Kirkland Air Force Base  
Albuquerque, NM

September 1994

## EFFECTIVENESS OF THERMIONIC HEAT PIPE MODULE

Phillip N. Hutton  
Department of Physics  
Old Dominion University

Timothy Way  
Senior Airman, USAF  
Kirkland AFB, NM

### **Abstract**

The Thermionic Heat Pipe Module (THPM) is a thermionic converter. The design of the THPM utilizes a lithium filled annular heat pipe whose interior annular ring serves as the emitter surface. The annular emitter heat pipe surrounds a lithium filled cylindrical heat pipe whose outer surface is the collector. The emitter heat pipe is radiatively coupled to an exterior heat source. This configuration allows for efficient heat transport from the heat source to the heat rejection system.

This paper characterizes the performance of the emitter heat pipe when a non-uniform heat source is applied. A temperature profile of the emitter surface was recorded through a temperature range of 300K to 2100K. This profile can be used as a baseline for future THPM tests and can be used to verify the accuracy of various models of the emitter heat pipe.

## EFFECTIVENESS OF THERMIONIC HEAT PIPE MODULE

Phillip N. Hutton

### Introduction

The purpose of this experiment is to characterize the steady state thermal profile of the emitter surface as a function of input temperature, and determine whether the annular heat pipe can effectively isothermalize the emitter surface under non-circumferential heating. The Thermionic Heat Pipe Module is a high efficiency, high temperature converter. These characteristics make it suitable for use in space nuclear power systems. The original design of the THPM required the emitter heat pipe to be surrounded by a uniform heat source. This would ensure an isothermal emitter surface which would maximize the efficiency of the THPM. Subsequent design options are investigating the possibility of surrounding the heat source with a series of THPM's. This configuration would allow for a greatly reduced size in the heat source and its accompanying control components. The disadvantage to this type of configuration is that the emitter heat pipe is only partially exposed to the heat source. The thermal profile of the emitter surface must be investigated under these conditions to determine if the emitter heat pipe can effectively stabilize the temperature along the emitter surface so that the efficiency of the THPM is not adversely affected.

### Experimental Setup

This experiment is designed to characterize the temperature profile of the emitter surface when the emitter heat pipe is subjected to partial circumferential heating. For the test the collector heat pipe is removed and replaced by a water calorimeter. K type thermocouples are run down along the side of the calorimeter and bent out to make contact with the emitter surface. The water calorimeter serves the dual purpose of heat removal and keeping the thermocouples relatively cool. The emitter heat pipe is then placed inside an evacuated chamber next to a ten inch long, one inch wide tungsten filament. This whole apparatus is surrounded by six layers of heat shields and a water cooled copper jacket to protect the surrounding environment and equipment. A pyrometer is used to measure the temperature of the filament, and a blackbody probe is used to measure the exterior surface temperature of the emitter heat pipe. All temperature readings are fed into a computerized data acquisition system and recorded at one second intervals.

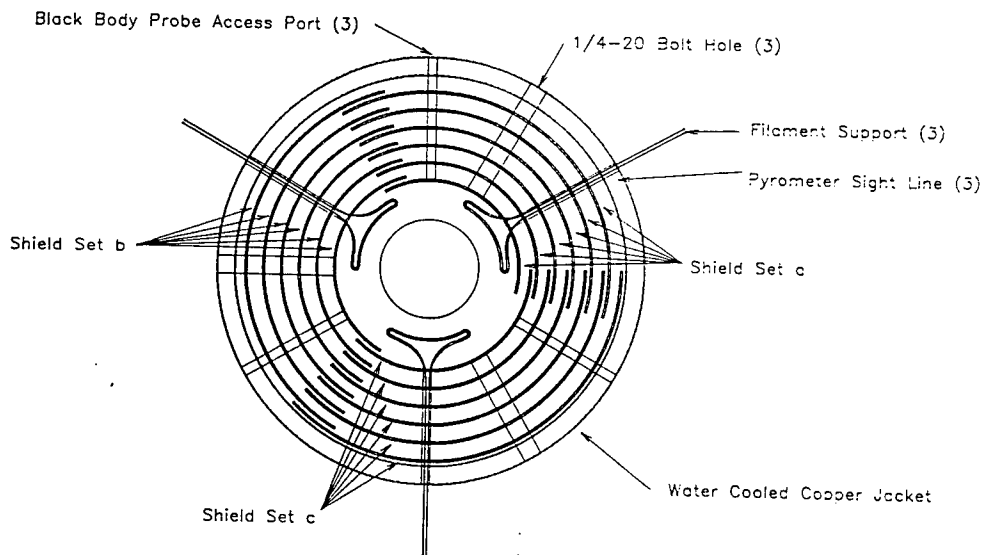
### Vacuum System

The vacuum chamber is a 16 X 30 inch bell jar resting on a standard 8 port feedthrough. This feedthrough is supported by a modified MDC BP-18 baseplate. The BP-18 has 12 feedthrough ports to allow the introduction of electrical power and cooling water. This system is serviced by a 6 inch diffusion pump which allows vacuums into the micro-torr region.

### Heater construction

The heating apparatus is designed to provide either a relatively uniform heat source or a non-uniform heat source to the emitter heat pipe, depending on the number of tungsten filaments used. Figure 1-a and 1-b provide a detailed top and side view of the heating apparatus. In this experiment only one tungsten filament was used to provide non-uniform circumferential heating around the emitter heat pipe. The emitter heat pipe was placed next to the tungsten filament. Six layers of heat shields completely enclose the filament and heat pipe. These, in turn, are surrounded by a hollow copper jacket. Water is circulated through the copper jacket to a heat removal system. This setup thermally isolates the interior of the furnace from the surrounding environment. The copper jacket and heat shields have small instrument ports positioned every 60 degrees to allow passage of temperature sensors to the heat pipe and filament.

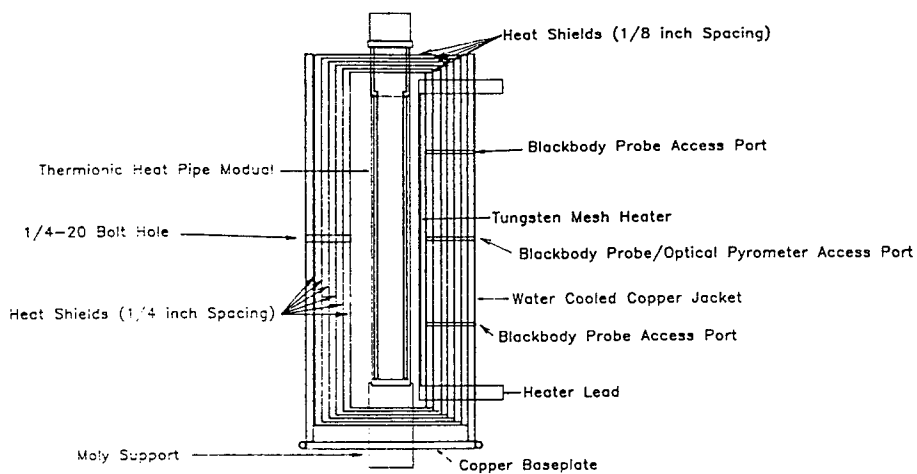
### HEATER CONSTRUCTION



TOP VIEW

FIGURE 1-a

## HEATER CONSTRUCTION



SIDE VIEW

FIGURE 1-b

### Instrumentation

Ten K-type thermocouples were run down along the calorimeter and bent out to make contact with the interior of the annular heat pipe. The thermocouples were arranged to provide axial and circumferential temperature profiles along the interior of the annular heat pipe (emitter surface). Figures 2-a and 2-b depict the arrangement of the temperature sensors. The redundancy of these sets of data points was used to provide the maximum number of data points possible in case some of the thermocouples should fail during the test. Physical space limitations between the emitter heat pipe and the calorimeter (approximately 0.05 inches) prohibited any more data points.

## THERMOCOUPLE GEOMETRY

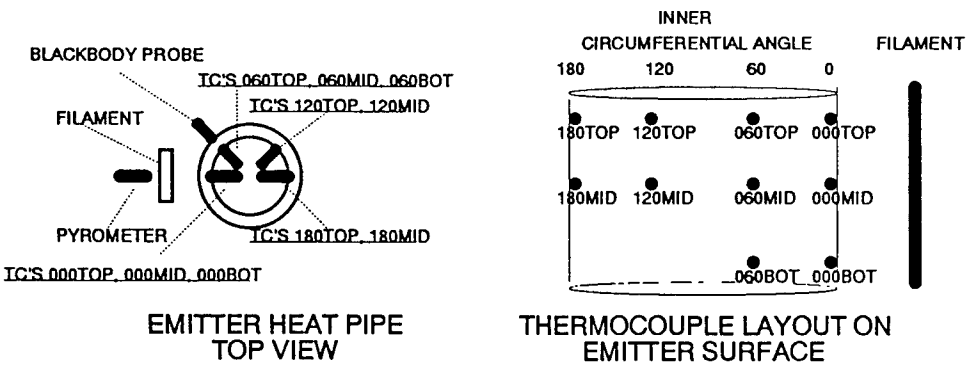


FIGURE 2-a AND 2-b

The thermocouples were given titles denoting their axial and circumferential positions. As an example, the thermocouple labeled 000TOP denotes the thermocouple located directly in front of the heat, near the top of the emitter heat pipe. The thermocouple labeled 060MID is the thermocouple located 60 degrees circumferentially away from the heater and near the middle of the emitter heat pipe.

A blackbody probe was positioned along the exterior of the emitter heat pipe opposite the 060TOP thermocouple (see figure 2-a). This position was chosen because it could be correlated with data from previous tests performed on the emitter heat pipe. A pyrometer was used to measure the temperature of the tungsten filament (see figure 2-b).

### **ANALYSIS**

The temperature of the filament was taken through the operating range of the emitter heat pipe in a series of runs to spot inconsistencies in individual thermocouple readings that may have been due to problems such as bad contact points or partially open ends. The data on two runs is shown on figures 3-a through 5. Thermocouple 060MID is not included in these graphs because it gave erratic readings throughout the test. Thermocouple 060TOP is not included on figure 3-b, 3-d, and 3-f because the connector visibly burned out after the first run.

## EMITTER SURFACE TEMPERATURE

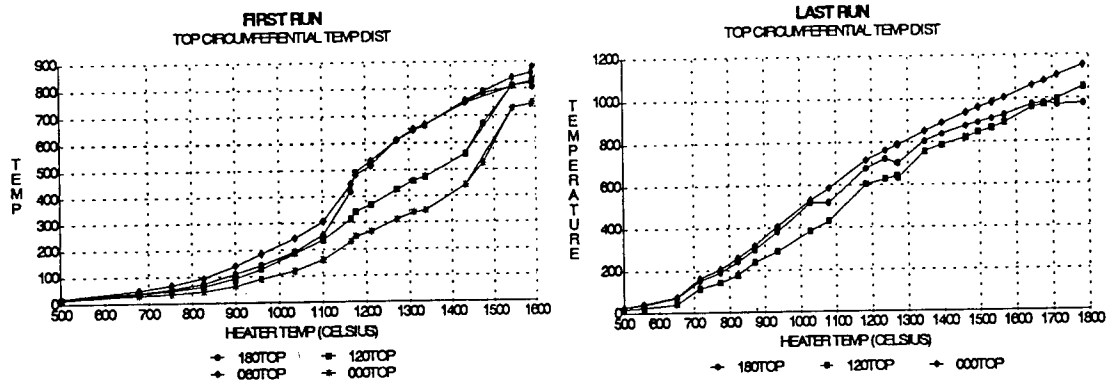


FIGURE 3-a and 3-b

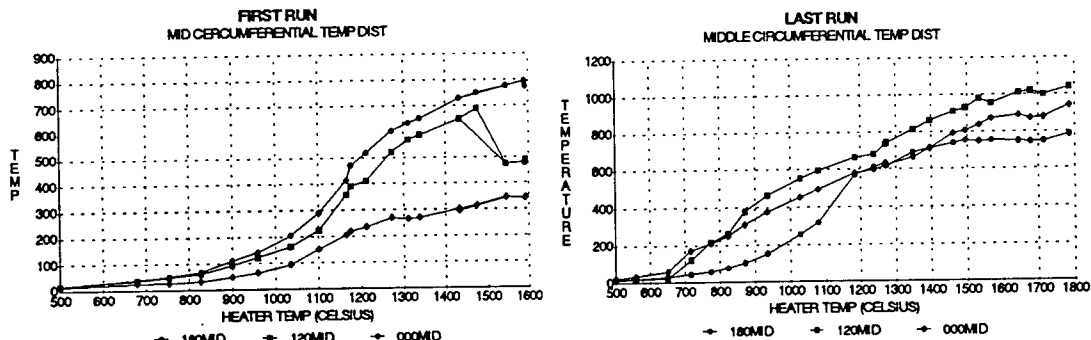


FIGURE 3-c and 3-d

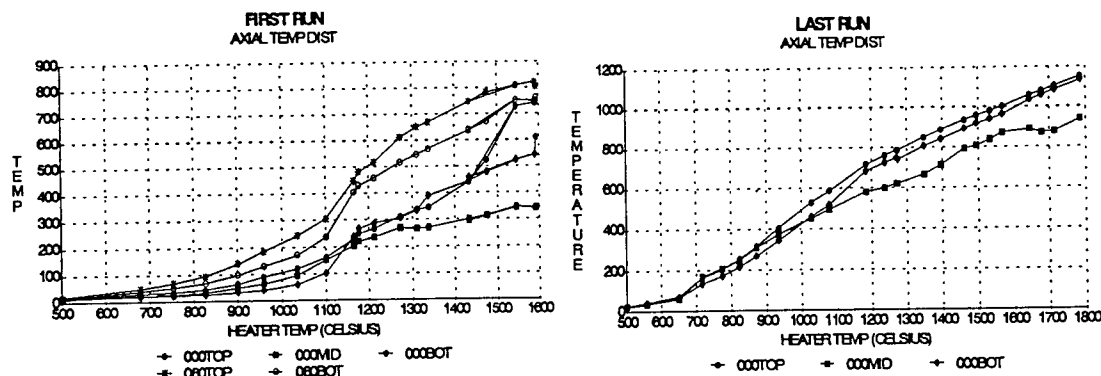


FIGURE 3-e and 3-f

Figures 3-a through 3-f separates the data into the circumferential and axial sets of readings. Figures 4-a and 4-b have been included to give a compact graphical view of the range, mean, standard deviation, and percent difference in error of the thermocouple readings in each test run. Figure 5 depicts the difference in temperature between the outer surface of the annular heat pipe and the inner surface.

## RELEVANT STATISTICS

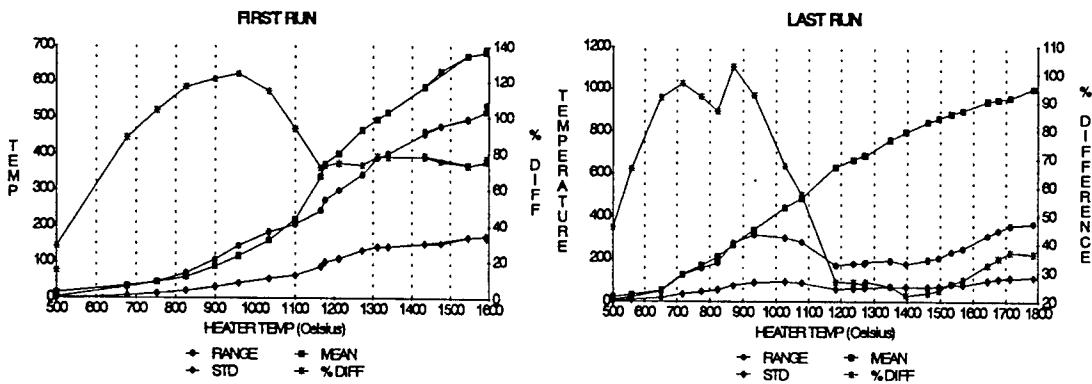


FIGURE 4-a and 4-b

In both runs, heat pipe action became apparent between 1100 and 1200 degrees celsius. Within this region figures 3,4 and 5 show the temperature difference between the inner and outer surface of the heat pipe decrease dramatically as the mean temperature of the emitter surface takes a disproportional jump with an increase in filament temperature. After heat pipe action occurred, it was expected that the range in temperature measurements would decrease. A small decrease in the range of temperature readings was observed in the last run, but the overall range never decreased below 150 degrees Celsius. The plot of the standard deviation of the data points follows the general pattern of the range, while the percent difference between the maximum and the minimum data points illustrate a marked decrease and levelling off after heat pipe action occurred.

## INNER/OUTER SURFACE TEMPERATURES

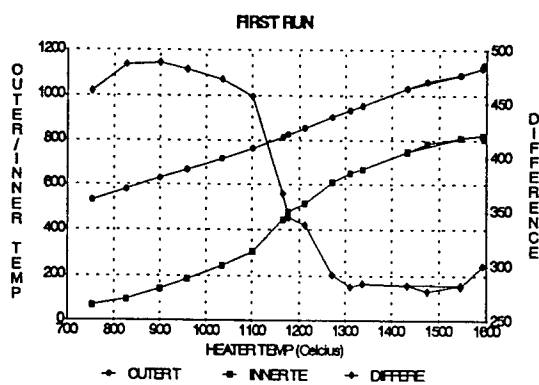


FIGURE 5

### CONCLUSION

Under partial circumferential heating the annular heat pipe was only partially effective in equalizing the temperature along the emitter surface. Temperature differences between maximum and minimum thermocouple readings varied between 150 and 350 degrees celsius, well above that required for efficient operation of a THPM.

### ACKNOWLEDGMENTS

Appreciation is extended to ORION International Laboratory for their engineering and technical support. Special thanks is extended to Captain David Hidinger, Mr. Matt Clark, and Mr. John Merrill for their technical support in this experiment.

**A SINGLE TEMPERATURE/MATERIAL ABLATION ALGORITHM  
FOR THE NON-IDEAL MHD CODE, MACH2**

**Robert John Leiweke**

**Graduate Research Associate**

**Department of Aeronautical & Astronautical Engineering**

**The Ohio State University**

**2036 Neil Avenue Mall, Room 326**

**Columbus, Ohio 43210**

**Final Report for:**

**AFOSR Summer Research Program**

**Phillips Laboratory**

**Sponsored by:**

**Air Force Office of Scientific Research**

**Kirtland Air Force Base, Albuquerque, NM**

**September, 1994**

**A SINGLE TEMPERATURE/MATERIAL ABLATION ALGORITHM  
FOR THE NON-IDEAL MHD CODE, MACH2**

Robert John Leiweke

Graduate Research Associate

Department of Aeronautical and Astronautical Engineering

The Ohio State University

**Abstract**

Ablation is an important physical mechanism in re-entry vehicle engineering, material processing, and the operation of pulsed (or steady state) plasma devices. The non-ideal MHD code MACH2 has the capability to model ablation of materials, but has areas on which improvements may be made. The three most critical areas are the inclusion of condensation physics leading to zero net mass flux at equilibrium, localized heat fluxes into the wall based upon Fourier's Law, and tracking of the interface between the ablated vapor and the surrounding gas so that the work done by the vapor on the gas can be accounted for. The new ablation algorithm is based upon an equilibrium vapor state. A simple bench-test of the new model was performed for a single material at a single temperature. A one-dimensional, ideal gas, singly ionized copper plasma at 0.50 eV,  $1.0 \times 10^{-2}$  kg/m<sup>3</sup> was pre-filled in a 0.20m x 0.10m x 1.00m closed box free of fields and currents. All walls except one (0.10m) was defined as thermally insulative. The solid copper (thermally conductive) wall, initially at 0.026 eV (300K), served as an ablation surface. Qualitative preliminary results indicate that heat flows into the wall with the proper magnitude and direction. Also, condensation of the warm copper plasma was observed during early times. Interface tracking was not used due to time constraints.

**A SINGLE TEMPERATURE/MATERIAL ABLATION ALGORITHM  
FOR USE WITH THE NON-IDEAL MHD CODE, MACH2**

Robert John Leiweke

**INTRODUCTION**

Re-entry vehicles, electrodes of pulsed and steady state plasma devices, high energy density gas stagnation at walls (including large radiation flux impingements), and many material processing environments are examples where ablation may require consideration for an engineering design. In general, magnetohydrodynamics (MHD) problems with complex geometries and chemical processes do not lend exact (or even approximate) analytic solutions. Ablation physics for two-dimensional, non-ideal MHD problems can be simulated using MACH2 v.9402, a code developed by the USAF Phillips Laboratory, Kirtland AFB, New Mexico. The existing MACH2 ablation model may be improved in several ways.

**DESCRIPTION OF MACH2**

MACH2 is a 2½-dimensional arbitrary geometry, Lagrangian-Eulerian (ALE) code for use on Cray™ supercomputers (XMP, YMP, C90, and Cray2), Sun™ SparcStations™ (2, 10, and 20), and IBM™ RISC workstations.<sup>1</sup> It is written in FORTRAN 77, and uses the Cray™-type pointer and namelist extensions.<sup>2</sup> The code runs under the Unix and Unicos operating systems.<sup>2</sup>

In either rectilinear or cylindrical coordinates, MACH2 allows a user specified computational domain built out of "blocks". Cells within the computational domain are labeled as "real". Each block contains "icells" mesh increments in the x (or r) direction and "jcells" mesh increments in the y (or z) direction.<sup>1</sup> Physical quantities such as mass, momentum, forces, and thermal flux are defined at a cell vertices, whereas pressure, temperature, density, magnetic field, specific internal energy, diffusivities,

and thermal conductivities are located at cell centers.<sup>1</sup> Boundary conditions are implemented upon a single layer of "ghost" cells surrounding each block. A "zero-volume" ghost cell is one that has a very small volume,  $\epsilon$ , and the cell center falls exactly upon the locus of two "real" cell vertices at a block boundary.<sup>1,3</sup> The code allows multi-materials and three temperatures. The version used for this study is v.9402 (no manual exists for this version, yet). A new feature called "interface tracking" makes possible the definition of a sub-grid material interface for two or more materials with a minimal amount of numerical diffusion. Physics for mass diffusion is not included in MACH2.

### PROBLEM DISCUSSION

The MACH2 wall ablation algorithm is based upon constant heat flux across the surface boundary of a semi-infinite solid.<sup>4</sup> Heat flux from the plasma is assumed to be that of a blackbody at an adjacent real cell electron temperature. At time  $t$ , this heat soaks into the (virtual) wall a characteristic distance<sup>5</sup>

$$\delta(t) = \sqrt{\frac{\kappa_w t}{\rho_w c_{p,w}}} \quad (1)$$

where  $\rho_w$ ,  $\kappa_w$ ,  $c_p$ , and  $t$  represent the solid wall material density (kg), thermal conductivity (W/m-K), specific heat (J/kg), and time (s). The exact solution for the temperature distribution within a semi-infinite solid goes like a Gaussian Error Function. This depth is proportional to a volume,  $\delta V$ , of wall material. The amount of energy per unit area required to vaporize the mass contained within this  $\delta V$  is<sup>4</sup>

$$q''_{vap} = \delta H_{vap} \quad (2)$$

where  $H_{vap}$  is the heat of vaporization of the wall material. Using the problem timestep,  $\Delta t$ , an approximate expression for the heat flux required to ablate the mass within this volume<sup>2,4</sup>

$$q''_{vap} = \frac{B \sqrt{t}}{\Delta t} \quad (3)$$

where  $B$  is the "ablation threshold".<sup>2,4</sup>

The algorithm itself is rather simple; at each timestep, we compare the heat storage ability of the mass within  $\delta V$  to the heat (flux) of the incoming blackbody radiation. Specifically, the comparison

$$\dot{q}''_{vap} - \dot{q}''_{store} > ? \dot{q}''_{BB} \quad (4)$$

is made.<sup>2,4</sup> If the blackbody flux is less than the left side of equation (4), then ablation does not occur, and the "bit" of blackbody energy is accumulated within a scalar variable, *absenrg*, representing the heat stored within  $\delta V$ . If the blackbody flux is greater than the left side of (4), then ablation occurs, and the heat liberated by the evaporation process is

$$\dot{q}''_{ab} = \dot{q}''_{BB} - (\dot{q}''_{vap} - \dot{q}''_{store}) \quad , \quad (5)$$

the mass flux ablated is

$$\dot{m}''_{ab} \equiv \frac{\dot{q}''_{ab}}{H_{vap}} \quad , \quad (6)$$

with a characteristic speed<sup>2,4</sup>

$$v_{ab} = \frac{\dot{m}''_{ab}}{\rho_{vap}} \quad . \quad (7)$$

Here,  $\rho_{vap}$  is the equilibrium vapor density of the ablated wall material. This inflow mass velocity is set along the *entire* block boundary. The ghost cells along this boundary are set to the equilibrium vapor pressure and density for the wall material at its melting point.

The accuracy of the ablation model is restricted in seven ways.

1) condensation physics at the boundary is non-existent.<sup>6</sup>

2) the existing model cannot capture the physics of high frequency energy bursts on short characteristic timescales commonly associated with pulsed power applications because the "ablation threshold" criteria creates non-physical delays in phase transition.<sup>6</sup>

3) low density "slip" flows for which the fluid continuum assumption does not hold. Velocity

and temperature gradients at a solid boundary cannot be accurately accounted for, leading to improper computation of heat fluxes and ultimately, ablated mass (which in turn gives the wrong heat fluxes).<sup>6</sup>

4) heat flux into an ablation wall was not based upon Fourier's Law, but rather as the electron blackbody radiation flux at an adjacent real cell.<sup>1,4,6</sup>

5) the ablation model was based solely upon a single temperature plasma.

6) the interface position between newly ablated mass and that of the previous time step is not tracked.<sup>6</sup>

7) ablation state variables and mass properties are specified for an *entire* boundary so that local heat fluxes into a wall cannot lead to local ablation of wall material. In fact, the wall temperature must be held at a user specified, fixed value for all time.<sup>1,2,4</sup>

Improvements of the utmost concern are to first allow for the possibility of net mass flux at the surface goes to vanish as the system approaches equilibrium. Second, use a local temperature gradient and plasma thermal conductivity at the surface to compute the proper *local* heat flux. Third, to keep track of the interface between newly ablated material vapor and "mixed" gas. This last requirement is important because the ablated mass, acting as a piston, does work on the surrounding gas as it expands outward. The pistons' ability to do work is related to enthalpy, and so one must have a means of accurately estimating the volume swept out each timestep.<sup>6</sup>

### THE NEW MODEL

If a liquid is placed into a closed container, the amount at first decreases but eventually becomes constant because the rate of condensation equals the rate of evaporation.<sup>7</sup> The net mass transfer between states vanishes, and the system is in equilibrium.<sup>8</sup> However, at the phase transition region on a molecular level, the system is highly dynamic, with molecules constantly escaping from and entering the liquid at a high rate.<sup>8</sup> In reality, the escaping molecules do not have a Maxwellian velocity distribution, so a surface temperature cannot be defined. However, the molecules must

eventually reach an equilibrium state at a new temperature. Then, heat transfer back to the wall must raise or lower its specific internal energy to that associated with the equilibrium state. This model will assume that a surface temperature,  $T_s$ , may be defined based upon the solid wall's specific internal energy.

Let each variable be a *locally* defined quantity applied to each real vertex or ghost cell along the wall boundary. During the transition to equilibrium, the fluxes of vapor molecules moving away from the wall and that of the incoming gas are<sup>6,7</sup>

$$\mathcal{F}_{off} = \frac{n_{vap} \bar{C}_{vap}}{4}, \quad \mathcal{F}_{gas} = \frac{n_{gas} \bar{C}_{gas}}{4} \quad (8)$$

where  $k$  is the Boltzmann constant (J/K),  $n$  is the number density (1/m<sup>3</sup>) and

$$\bar{C}_{vap} = \sqrt{\frac{8kT_s}{m_s\pi}}, \quad \bar{C}_{gas} = \sqrt{\frac{8kT_{gas}}{m_{gas}\pi}} \quad (9)$$

are the mean molecular speeds for the vapor and incoming gas molecules.<sup>6,7</sup> For simplicity, this model assumes a single material (plasma and wall), so that  $m_s \equiv m_{gas} \equiv m$ . The net mass flux is

$$\dot{m}''_{net} \equiv m(\mathcal{F}_{off} - \mathcal{F}_{gas}) \quad . \quad (10)$$

The net mass ablated becomes

$$m(t) = \int_0^t \dot{m}''_{net} d\tau \quad . \quad (11)$$

But,  $T_s$  and  $n_{vap}$  are unknowns at  $t + \Delta t$ , so we require more information about how heat is distributed within the wall and how its specific energy changes with time.

Observe that the average specific kinetic energy of particles coming off the wall is (found by integrating the Maxwellian distribution function over  $2\pi$  steradians, ignoring work done by the vapor on the surrounding gas):<sup>6</sup>

$$\dot{E}''_{off} = 2kT_s \mathcal{F}_{off} = \left( \frac{2kT_s}{m} \right) \dot{m}''_{off} . \quad (12)$$

If one considers the work done by this vapor, then the factor of "2" must be replaced with "5/2", in equation (12).<sup>6</sup> The total heat carried away from the surface is

$$\dot{Q}''_{off} = \dot{m}''_{off} (H_{vap} + \frac{2kT_s}{m}) . \quad (13)$$

In (13), the expression in parenthesis represents both kinetic and potential energies. Heat flux into the wall is described by Fourier's Law, but with a modified thermal conductivity to account for radiation transport:<sup>1</sup>

$$\dot{q}''_{in} = -\nabla \cdot (\kappa' T) , \quad (14)$$

where

$$\kappa' = \kappa + \frac{4\sigma c T_e^3}{3\rho\chi} . \quad (15)$$

and  $\sigma$  is the Stephan-Boltzmann constant,  $c$ , the speed of light in vacuum,  $T_e$ , the plasma electron temperature,  $\rho$ , the total plasma density, and  $\chi$ , the opacity.<sup>1</sup> The net heat flux (or power density) at the wall is

$$\dot{q}''_{net} \equiv \dot{q}''_{in} - \dot{q}''_{off} . \quad (16)$$

Now, the condition of constant heat flux across the wall requires that the net heat flux balance the time rate-of-change of energy within the solid material. Mathematically,

$$\dot{q}''_{net} \equiv \frac{dH}{dt} , \quad (17)$$

where  $H$  ( $J/m^2$ ) is the heat fluence into the wall.<sup>6</sup> Recall that the spacial temperature profile for a semi-infinite wall with constant heat flux has the form of a Gaussian Error Function. As a simplification, use of equation (1) treats the profile as a constant value up to the depth  $\delta(t)$ . So, the specific energy stored within this diffusion volume  $\delta V(t) = \text{Area} \cdot \delta(t)$ , is

$$e(t) = \frac{H(t)}{\rho_w \delta(t)} + e(0) . \quad (18)$$

where  $e(0)$  is the initial specific internal energy. Using a solid density, the average specific energy (18), and an appropriate equation-of-state, one may obtain a characteristic.<sup>6</sup> Figure 1 shows an equation-of-state for copper.<sup>9</sup> At solid density ( $8933 \text{ kg/m}^3$ ), notice that the temperature is almost a linear function of the base-10 log of specific internal energy.<sup>9</sup> So in this particular case, an approximation of the temperature (K) is

$$T_s(e(t)) \approx 300 + 5.5 \times 10^4 \left( \log_{10} \left[ \frac{e(t)}{10^6} \right] + 0.93742 \right) . \quad (19)$$

MACH2 moves mass within the computational domain based upon pressure gradients within the plasma.<sup>1,3</sup> So, at the ablation boundary, all ghost cells must have updated information about the local equilibrium vapor pressure,  $p_{eq}$ . For non-alkaline metals which adhering to a hard-sphere collision model (such as copper), the equilibrium vapor pressure in atmospheres is

$$p_{eq}(T_s) \approx e^{\frac{-H_{vap}}{N_A k T_s} + C} , \quad (20)$$

where  $N_A$  is Avogadro's number, and  $C$  is related to the entropy of vaporization (for copper,  $C=12.9$ ).<sup>10,11</sup> To determine the equilibrium vapor density,  $n_{vap}$ , we may again use a tabular data or, for the case of most vaporized metals, the perfect gas law<sup>11</sup>

$$n_{vap} = \frac{P_{vap}}{k T_s} . \quad (21)$$

Solid material properties such as thermal conductivity, specific heat, and density are generally a function of temperature, however here they are set equal to their respective values at 300K (0.026 eV).

### MODELING PARAMETERS

A one-dimensional "bench test" of the new ablation algorithm was chosen as a rectilinear "box" with wall boundaries, 0.20 m wide and 0.10 m long (for rectilinear geometries, MACH2 defines the

transverse depth to be unity). The box is initially pre-filled with a uniform 0.50 eV copper plasma with a density of  $1.0 \times 10^{-2}$  kg/m<sup>3</sup>. The equation-of-state is ideal gas,  $\gamma = 5/3$ . Both ionization state and thermal conductivity were chosen to be spatially uniform, time-independant quantities; singly ionized and  $\kappa = 1.0 \times 10^{-8}$  W/m-eV, respectively. A Spitzer resistivity model was selected, and radiation diffusion was turned "off". There were no externally applied circuits or initial magnetic fields. Both 0.20 m walls and one of the 0.10 m walls were defined as perfect thermal insulators. The other 0.10 m wall allowed thermal conduction according to the new ablation algorithm. The wall has material properties of solid copper at 300 K (0.026 eV). Figure 4 displays the single block mesh. This mesh has a quadratic spacing of 32 icells in the "x" direction, with the fine increments near the ablation wall where large thermal gradients are anticipated. The finest x-increment was adjusted to be  $8.0 \times 10^{-4}$  m based upon a characteristic thermal diffusion length scale at 1  $\mu$ s. The initial conditions and geometry suggest that the flow will have no physical variations in the y-direction, so only four jcells were defined. Initially, the heat flux at the wall computed by MACH2 was  $2.375 \times 10^{11}$  W/m<sup>2</sup>, which correlated well with the expected value of  $2.370 \times 10^{11}$  W/m<sup>2</sup> (0.2%).

## RESULTS

Using a Sun™ SparcStation™ 2, this case ran to normal termination at 30  $\mu$ s with a total of 30,007 cycles. Figure 3 shows a typical plot of the heat flux vectors. Note that the direction of the vectors is towards the ablation wall as expected. A plot of this heat flux vs. time is shown in Figure 4. With increasing time, the heat flux decreases in an exponential-like manner (the trend is not quite  $Ae^{-\alpha t}$ ). As the wall temperature increases and the plasma temperature decreases, the difference  $\Delta T$ , will decrease in smaller increments as the two temperatures approach each other. Figures 5, 6, 7, 8, and 9 show slice plots of plasma temperature (eV), density (kg/m<sup>3</sup>), pressure (J/m<sup>3</sup>), and x-component of velocity (m/s) at 0.2  $\mu$ s, 3  $\mu$ s, 10  $\mu$ s, 20  $\mu$ s, and 30  $\mu$ s, respectively. At 0.2  $\mu$ s (Figure 5), a nice thermal diffusion profile has developed. Some wall material appears to have ablated, since the density there has increased slightly to 1.0012 kg/m<sup>3</sup>. The pressure profile follows the temperature profile

because the density is still constant throughout most of the domain. At  $3\mu\text{s}$  (Figure 6), the temperature profile has become less full. Notice that the temperature at the left insulative wall has dropped to about 0.47 eV, some more copper has ablated, and the x-velocity is zero at the left and right walls. The x-component of velocity is still only about 4% of the local sound speed,  $a \sim 850 \text{ m/s}$ . At  $20\mu\text{s}$  (Figure 7), the left wall temperature has decreased to 0.27 eV and the pressure within the ablated material has increased due to the density increase. Notice that the x-component of velocity increases linearly from zero at the left wall to 80 m/s, then drops suddenly within the region occupied by the cold ablated copper. Also, notice that the density within the domain unoccupied by the cold ablated material is lower than its initial value of  $1.0 \times 10^{-2} \text{ kg/m}^3$ . This is consistent with the observation that the temperature has decreased uniformly in time due to the heat loss. Because ablated material is acting as a piston, one might expect a more well defined shock front. However, in this case, each successive compression wavelet in front of the piston moves into a region of higher temperature gas, with a higher sound speed. Because wavelets do not bunch up as quickly, the x-component of velocity shows a more diffuse shock front. At  $30\mu\text{s}$  (Figure 8), the results are not surprising. Time restrictions did not allow the recording of total ablated mass as a function of time. A futile attempt was made to graphically integrate under the density curves and subtract off the initial plasma mass.

## CONCLUSIONS

The rather simple one-dimensional ablation bench test of a copper plasma pre-fill and a copper wall shows that the new MACH2 algorithm conducts thermal energy into a wall and vaporizes wall material in a qualitatively correct manner. State variables and velocities behave as expected. The model simulates the evaporation and condensation of plasma at an external boundary. The implementation of the "zero-volume" ghost cell was successful for this simple problem. Modification of the thermal flux at the ablation boundary to account for "slip flow" conditions is now "easy"; one only needs change the temperature gradients at the wall by a multiplicative factor. Due to time

restrictions, we were unable to test the model's ability to ablate mass due to *local* heat concentrations such as an arc discharge at an electrode surface. Future studies will incorporate multiple temperatures and materials, set up MACH2 to call vapor-state tables, include solid-liquid phase transition physics, and incorporate the "interface tracking" capability.

#### ACKNOWLEDGMENTS

A very big thank you is in order here to Dr. Robert E. Peterkin for making special arrangements for my visit to Phillips Laboratory this summer. I also wish to thank him for many hours of insightful philosophical discussion, tough criticism, helpful advice, and his valuable time. His impact on the way I view the universe is immeasurable. Also, people to note who graciously donated time and patience are Dr. Norm Roderick, Dr. Peter Turchi, Dr. Uri Shumlak, Mr. Jim Havranek, and Mr. Chris Lamb. A big thanks goes to my friend Ms. Amy Jann for helping me remain sane after my apartment was burglarized.

#### REFERENCES

- [1] Peterkin, R.E. Jr., Giancola, A.J., Sturtevant, J.E., *MACH2: A Reference Manual-Fifth Edition*, MRC/ABQ-R-1490, July, 1992.
- [2] USAF Kirtland AFB, Phillips Laboratory, WSP, *MACH2 v.9402*, Code Listing, 1994.
- [3] Peterkin, R.E. Jr., private communications, USAF Kirtland AFB, Phillips Laboratory, WSP, 1994.
- [4] Roderick, N., private communications, Professor, Univ. New Mexico, Albuquerque, New Mexico, Chemical and Nuclear Engineering Dept., 1994.
- [5] Kreith, F. and Bohn, M.S., *Principals of Heat Transfer, Fourth Edition*, Harper & Row Publisher, New York, 1986.
- [6] Turchi, P.J., private communications, Professor, The Ohio State University, Columbus, Ohio, Aeronautical & Astronautical Engineering Dept., 1994.
- [7] Kruger, C.H. and Vincinti, W.G., *Introduction to Physical Gas Dynamics*, Robert E. Krieger

Publishing Co., Malabar, Florida, Reprinted and Revised, 1986.

- [8] Zumdahl, S.S., *Chemistry*, D.C. Heath and Co., Lexington, Mass., 1986.
- [9] Holian, K.S., Editor, *T-4 Handbook of Material Properties Data Bases, Vol. Ic: Equations Of State (SESAME)*, LA-10160-MS, UC-34, Los Alamos National Lab, New Mexico, 1984.
- [10] March, N.H., *Liquid Metals, Concepts and Theories*, Cambridge University Press, Cambridge, 1990.
- [11] Anderson, P.D., Hultgren, R., Kelley, K.K., and Orr, R.L., *Selected Values of Thermodynamic Properties of Metals and Alloys*, John Wiley & Sons, Inc., New York, 1965.

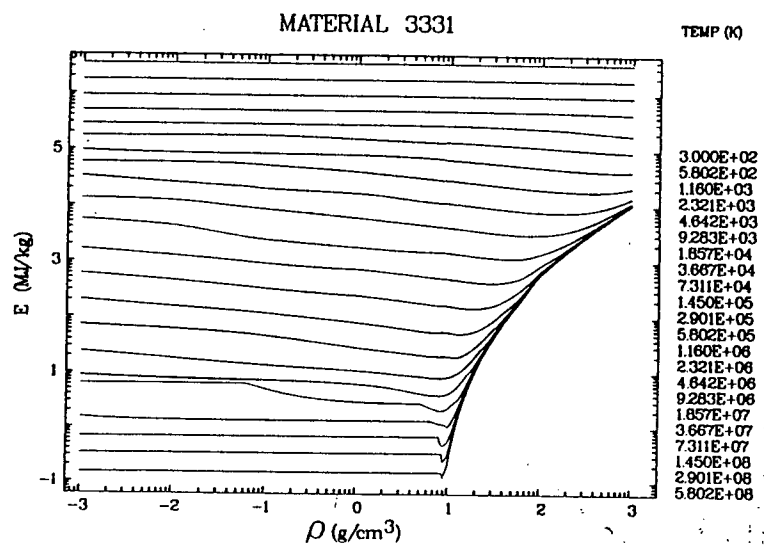


FIGURE 1 Copper EOS

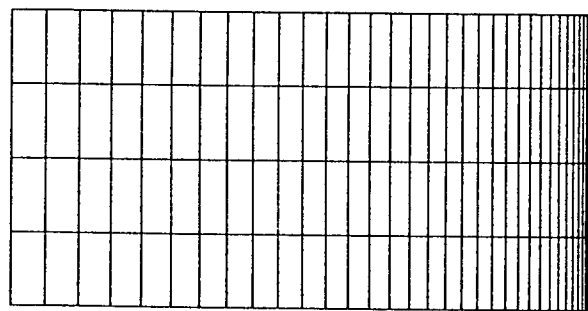


FIGURE 2 Computational Mesh

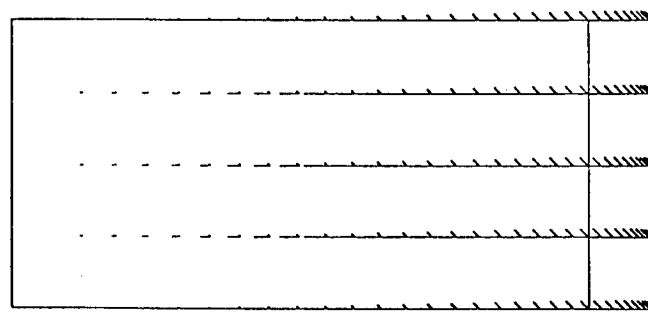


FIGURE 3 Typical Heat Flux Vectors

WALL HEAT FLUX vs. TIME  
New MACH2 Ablation Algorithm

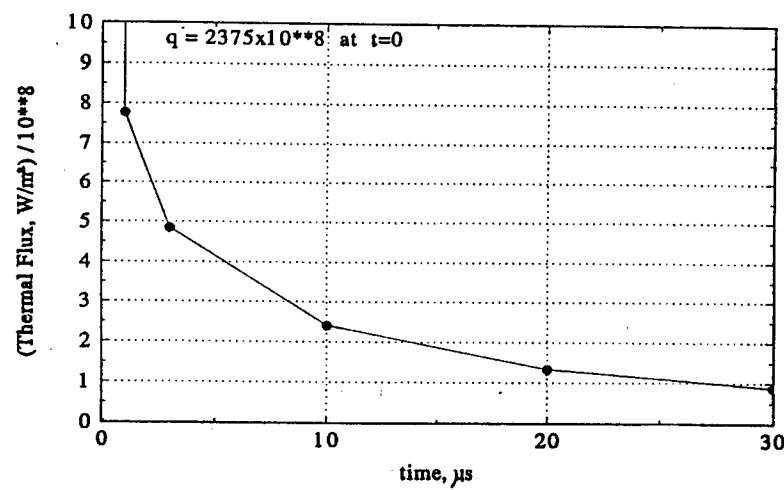
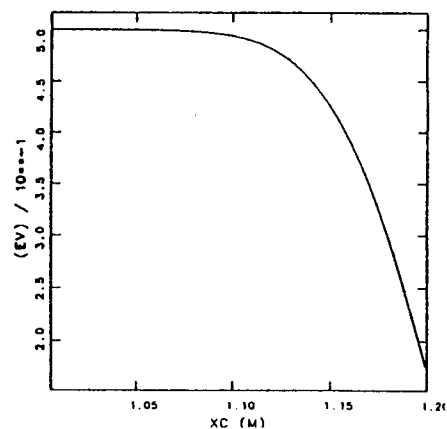
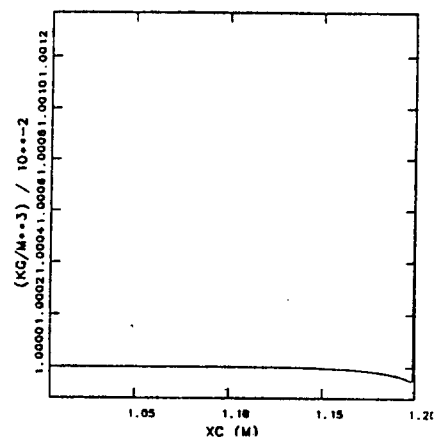


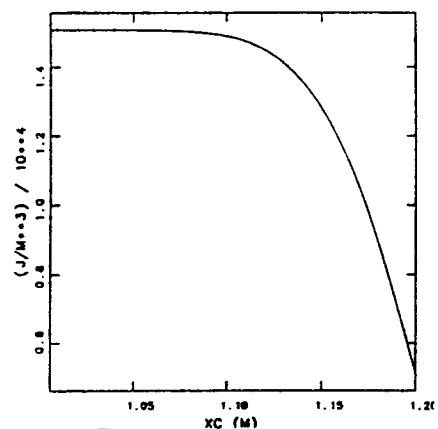
FIGURE 4 Heat Flux At Wall



Temperature



Density



Pressure

**FIGURE 5 Time = 0.20 us**

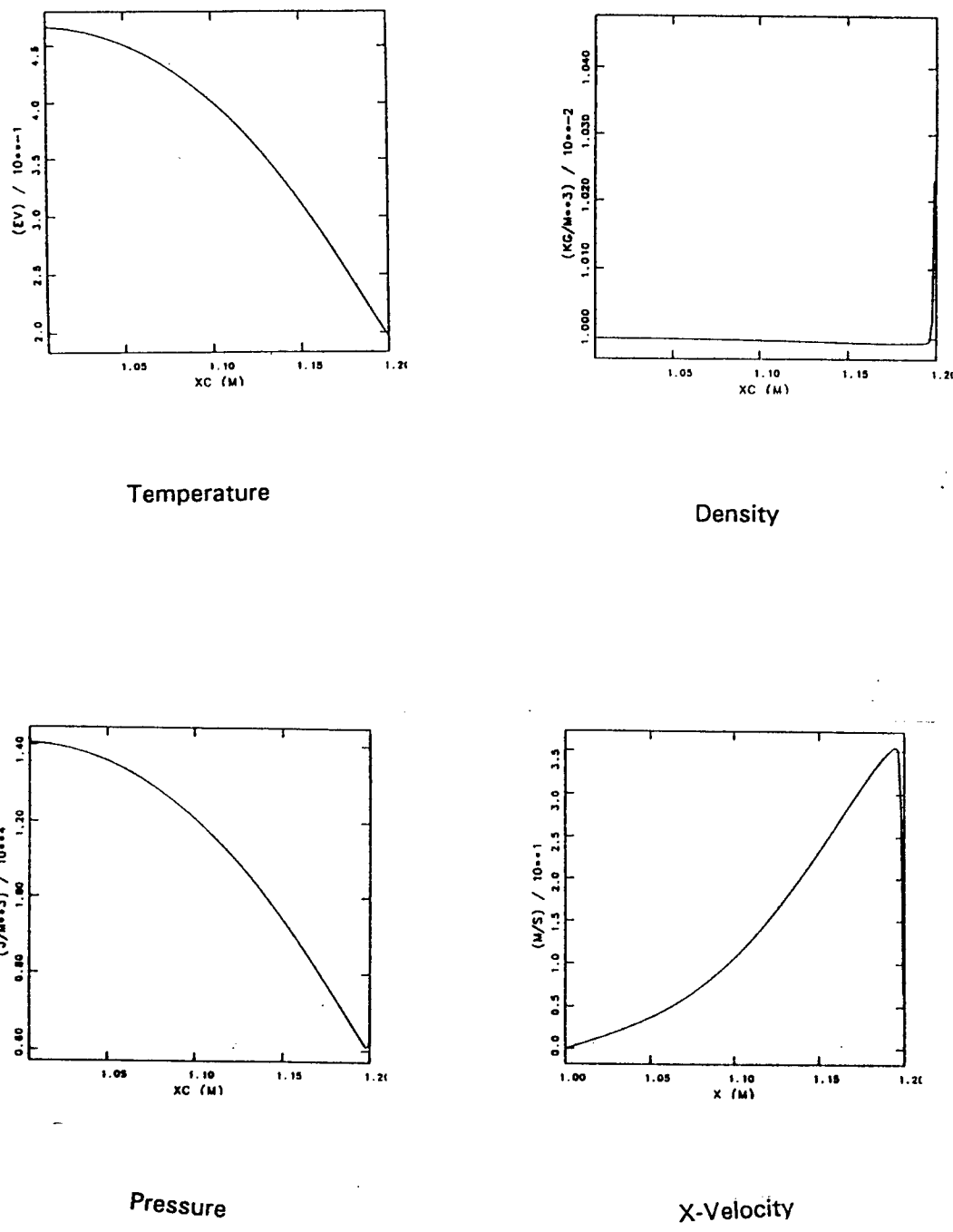
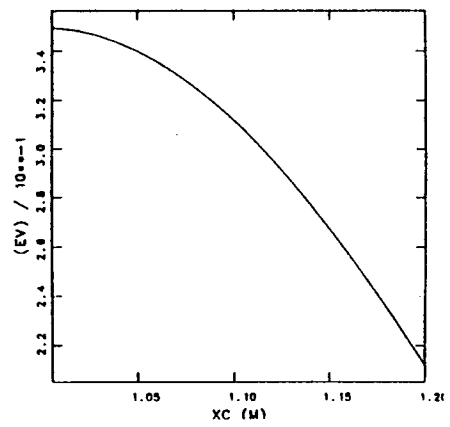
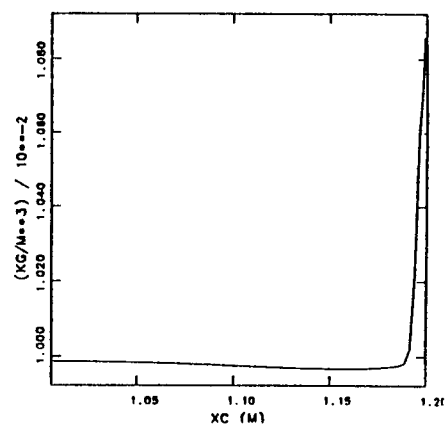


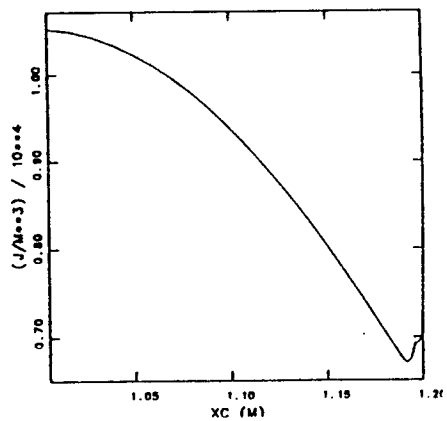
**FIGURE 6 Time = 3  $\mu\text{s}$**



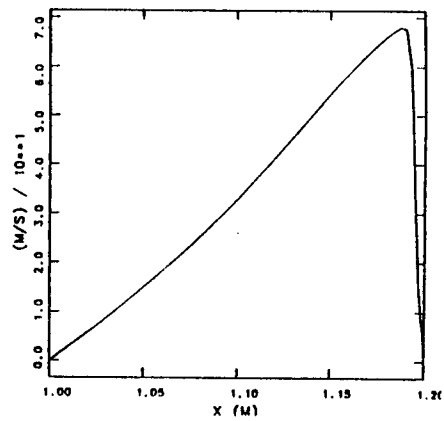
Temperature



Density

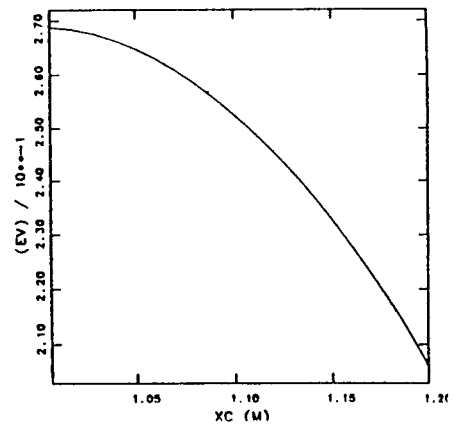


Pressure

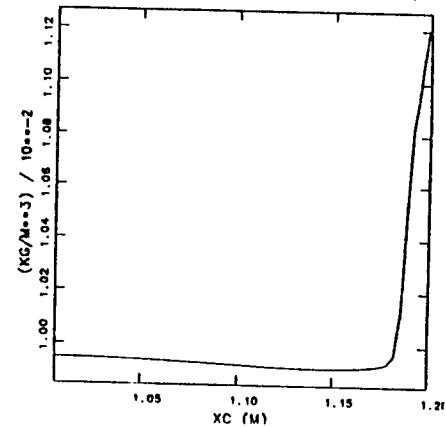


X-Velocity

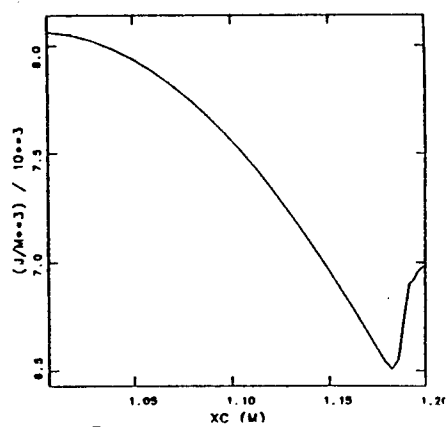
FIGURE 7 Time = 10 us



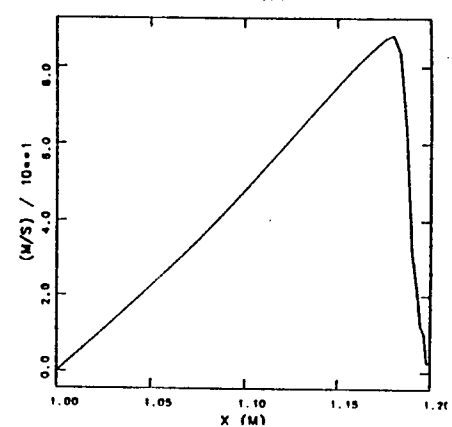
Temperature



Density

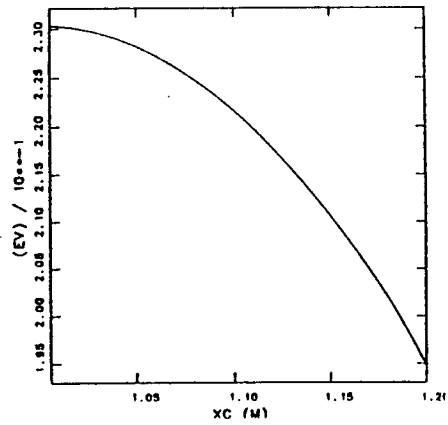


Pressure

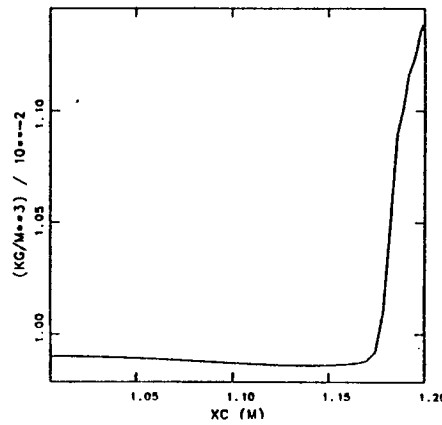


X-Velocity

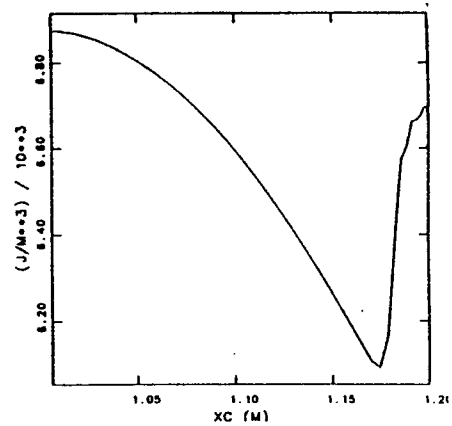
FIGURE 8 Time = 20  $\mu\text{s}$



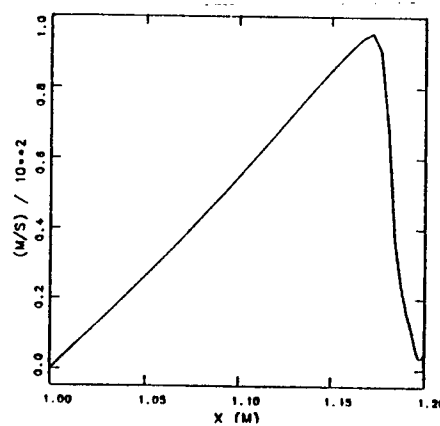
Temperature



Density



Pressure



X-Velocity

FIGURE 9 Time = 30  $\mu\text{s}$

ESTIMATION OF TILTS OF EXTENDED IMAGES IN THE PRESENCE OF ATMOSPHERIC  
DISTURBANCES USING OPTICAL FLOW ALGORITHMS

John I. Lipp  
Doctoral Candidate  
Department of Electrical Engineering

Michigan Technological University  
Houghton, MI 49931

Final Report for:  
Summer Graduate Student Research Program  
Phillips Laboratory  
Laser Imaging Airborne Experiments (PL/LIAE)

Sponsored by:  
Air Force Office of Scientific Research  
Bolling Air Force Base, DC  
and  
Phillips Laboratory

August 1994

ESTIMATION OF TILTS OF EXTENDED IMAGES IN THE PRESENCE OF ATMOSPHERIC  
DISTURBANCES USING OPTICAL FLOW ALGORITHMS

John I. Lipp

Doctoral Candidate

Department of Electrical Engineering  
Michigan Technological University

Abstract

One of the components of the Air Borne Laser (ABL) system is an optical, infra-red wavelength Acquisition, Tracking and Pointing (ATP) system. This system is to acquire a missile target at ranges of 200–300 km, track this missile target, and then point a High Energy Laser (HEL) at a critical target fiduciary for the purpose of destroying the missile in its boost phase.

To date, the only tracking algorithm examined in the ATP system is a biased centroid algorithm [1]. This report details research into other algorithms useful for tracking which are broadly classed in the literature as *optical flow* (OF) algorithms. The algorithms newly examined for this application were the Transformed Domain Maximum Likelihood (TDML) algorithm [4] [5], Generalized Maximum Likelihood algorithm (GML) [3], Horn and Schunk's optical flow (HS-OF) algorithm [6], and Fitts' Correlation Tracker (FITTS) [8]. This work presents simulation results from a simulated target image. Comparisons of these algorithms are made to the centroid algorithm. Moreover, the experiments uncovered an interesting and challenging problem with the atmospheric effects on the missile imaging scenario.

-

ESTIMATION OF TILTS OF EXTENDED IMAGES IN THE PRESENCE OF ATMOSPHERIC  
DISTURBANCES USING OPTICAL FLOW ALGORITHMS

John I. Lipp

## 1 Introduction

U. S. theater missile defense is exploring the use of an air-borne laser (ABL) system capable of destroying theater missiles in their boost phase. This requires a high energy laser (HEL) to be directed at critical missile aim points over ranges of 200–300 km. Three stages of processing are necessary for this objective: missile acquisition, missile tracking, and precise pointing of the HEL. The work here is concerned with the second stage of this process, high bandwidth tracking of the missile aim point.

The tracking system is designed to keep the missile in the camera's field of view (FOV). This in turn stabilizes the line-of-sight (LOS) to the missile. An important step in this process is measuring the LOS *tilts*<sup>1</sup> of the missile images. These measurements are fed into a control system to adjust the camera position to maintain the missile in the FOV. In addition, the HEL beam is aligned to the tracker LOS. This ensures that stabilizing the target LOS keeps the HEL on target.

This report explores algorithms which process camera images and estimate tilt information. Computer simulations of synthesized missile data are used to evaluate the performance of the

1. The Transformed-Domain Maximum Likelihood algorithm (TDML) [4][5],
2. The Generalized Maximum Likelihood algorithm (GML) [3],
3. Horn and Schunk's Optical Flow algorithm (HS-OF) [6], and
4. Fitt's correlation tracking algorithm (FITTS [8]).

Note that there are many other algorithms suitable to tracking. The algorithm selection was based on the focal point's familiarity with the problem and his anticipation that optical flow measurements would prove appropriate. Future work may involve extensions and/or refinements of these algorithms.

## 2 Image Sequences

Three sequences of images were used in the simulations performed in this paper:

---

<sup>1</sup>By tilts, it is meant the spatial shifts of an object within an image necessary to "center" it in the field of view. The term tilts has its origins in optics where tilting a mirror has the effect of causing the observed field of view to shift in proportion to the angle of mirror tilt and lens focal length.

1. A missile traveling 900 km/sec imaged at a range of 200 km. The missile is illuminated by a laser. The laser illumination is assumed to be uniform at the missile body, i.e. no degradation of the laser occurs as it propagates to the missile. Also, no speckle effects are present (the coherent nature of the laser is ignored). The return passes through the atmosphere and is collected through a 2 meter aperture onto a  $64 \times 64$  focal plane detector array with a  $32 \times 32$  micro-radian<sup>2</sup> FOV. The detector is assumed noise-free.
2. A point source imaged at a range of 200 km. The point source shines with the same wavelength as the illumination laser used for the missile sequence. The light from the point source propagates along the same path as the missile and is seen by a detector identical to that used to image the missile. The point source is used to compare single, isoplanatic patch responses with the multiple-patch missile image.
3. High Energy Laser (HEL) propagating to a distance of 200 km. The direction of light propagation is opposite that of the missile and point source. The HEL passes through the 2 meter tracking system aperture. Its wavelength is different from the target illumination (this means its propagation path is different than the missile and point source). Also note that the propagation time to the missile is long enough that the HEL arrival point is affected by the missile's velocity.

The propagation of the light for all three sequences was performed simultaneously to simulate the actual conditions that would be present during operation of the system. It is worth noting that by storing the individual light propagations in separate sequences, the atmosphere is assumed to be linear so that the principle of superposition applies. The atmosphere through which the light is propagating is moderately turbulent which causes a characteristic blurring and shifting of each image sequence. The simultaneous propagation of all three beams allows a comparison of the atmospheric distortions on each beam to be made on a frame-to-frame basis.

Processing the missile data was the priority since it is the tracking processor input. The point source data set is for reference; one of the tracker options is not to track the missile, but to track a scoring beam (approximately a point source) that is pointed at the missile aim point. The HEL is a different wavelength than the missile and therefore suffers slightly different distortions in passing through the atmosphere. This issue is further discussed in section 7.

### 3 Problem Nature

The tilt of the missile image in the FOV is from two sources:

1. "Apparent" movement of the missile caused by the atmospheric imaging distortions.

2. “Real” missile movement caused by its velocity. (In the simulated data, the missile, point source, and HEL beam are not moving. This implies the simulated missile data is for a missile being perfectly tracked.)

It is not necessary for the tracker to distinguish between these two sources of image tilt. This is because the HEL beam passes through the same atmosphere as the missile illumination return, and therefore suffers similar atmospheric distortions. That is, to hit the missile, the HEL must be pointed at the imaging system’s missile location, not the true missile location; discrimination between the tilt from the atmosphere and the missile velocity is unnecessary *and* undesirable.

Ordinarily, computing this tilt with a centroid or optical flow algorithm is a straight-forward problem. The situation here, tracking through the atmosphere, presents a unique problem to tracking that has not been seen before. The fundamental problem observed is the combining of the atmospheric distortions with the missile’s velocity. The distortion of the missile, as a phenomenon, appears to move along the body of the missile opposite in direction of the missile’s velocity. All of the optical flow algorithms used in the simulations identified the movement of the distortion phenomenon in preference to the movement of the missile unless an average of past images was used as a reference image for the algorithm.

An explanation for the distortion movement phenomenon is as follows. The desired frame rate for the FTM is 10,000 frames per second, or  $0.1 \mu\text{sec}$  between image frames. In that short period of time, the atmospheric turbulence changes are small, so that if a non-moving target is viewed through the atmosphere, several consecutive frames would appear similarly blurred (by the atmosphere). The missile, however, is a moving target. The distortions of the atmosphere remain spatially fixed while the missile moves “through” them. The visual effect this generates is for the distortions to appear to move along the missile body opposite the direction of missile movement. The distortions evolve slowly compared to the frame rate so that after about 10 pixels of movement the distortions have changed significantly in fine structure. Overall the missile images look like the smoky trail from a rocket engine just as much as they do a missile.

## 4 Simulation Details

The missile images are numbered 0–100 as  $I(n_1, n_2; 0)$  through  $I(n_1, n_2; 100)$ . The co-ordinate direction  $n_1$  is the vertical direction (“y-axis”) with positive values being downward and the co-ordinate direction  $n_2$  (“x-axis”) is the horizontal direction with positive values being right. (This corresponds with the co-ordinate system used by MATLAB<sup>TM</sup> to display image data.) Direction  $n_1$  extends for  $n_1 = 1, \dots, N$  and direction  $n_2$  for  $n_2 = 1, \dots, M$ . The 31st and 46th image of the missile sequence are shown in Figure 1 to illustrate the types of effects the atmosphere has on the received missile images. In particular, note the bending of the nose and mid-missile body which is distinctly different in each frame.

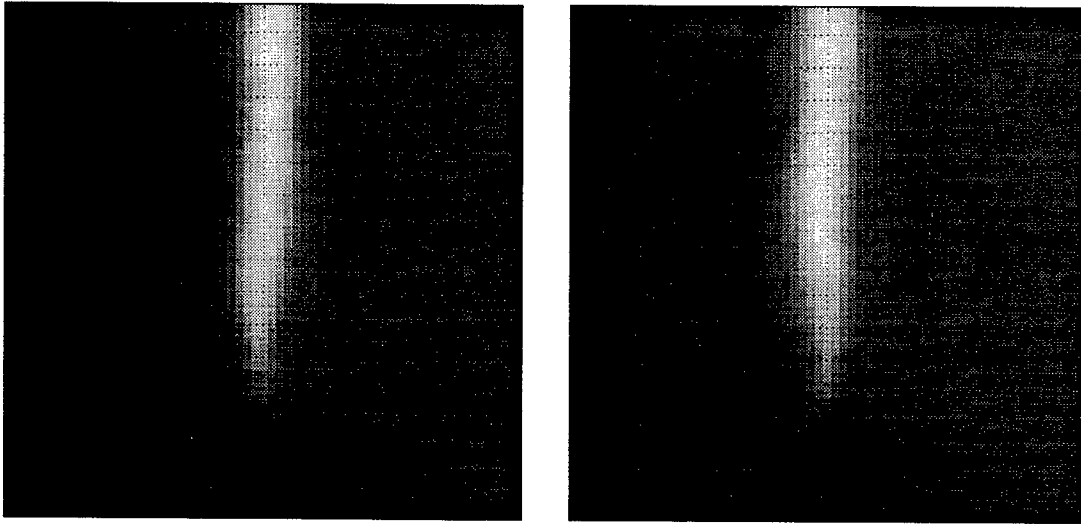


Figure 1: Sample distorted missile images.

#### 4.1 Image Size

Three different regions of the missile image sequence where used in the simulations:

FULL        The full  $64 \times 64$  base image

RECT        A  $64 \times 32$  rectangular region with the upper left corner at pixel location (1, 17)

SQUARE      A  $32 \times 32$  region with upper left-hand corner at (25, 17).

The rectangular image was chosen to eliminate as much background as possible without loosing any missile data. The GML algorithm is very computationally expensive; to minimize its running time the SQUARE image region was chosen which contains just the missile tip.

### 5 Centroid Algorithm

As mentioned earlier, a biased centroid algorithm is a proven algorithm for providing tilt measurements. A biased centroid is generated from a “normal” centroid

$$\text{cen}_1(i) = \frac{\sum_{n_1=1}^N \sum_{n_2=1}^M n_1 I(n_1, n_2; i)}{\sum_{n_1=1}^N \sum_{n_2=1}^M I(n_1, n_2; i)} \quad (1)$$

by adding a DC shift

$$\text{cen}_1^b(i) = \text{cen}_1(i) + c_1 \quad (2)$$

where  $c_1$  is the DC shift. For these experiments, the centroid calculation (1) was used because the DC shifts of a biased centroid algorithm do not effect the correlation analysis.

## 6 Optical Flow Algorithms

The centroid algorithm output consists of a coordinate pair. The difference between the coordinate pairs of two image frames is closely related to the tilt between those image frames. Compare this with optical flow algorithms. Optical flow algorithms produce displacement vectors (also interpreted as velocity vectors) which indicate the movement of pixel intensities between two images. Here, the first<sup>2</sup> of these images will be called the *reference image* since OF vectors indicate movement with respect to the first image. When integrated, OF vectors result in coordinate vectors. Note that the integration of the displacement vectors requires an additive constant, representing the initial coordinate position, *which cannot be recovered from the image data alone*. That is, OF algorithms have an *arbitrary* reference. For this reason, OF algorithms are referenceless, shift-invariant, or “AC” type algorithms. I prefer the first terminology because it emphasizes an important issue when using OF algorithms to measure tilt.

The displacement vectors can be functions of pixel position, e.g.  $d_1(n_1, n_2; i)$  and  $d_2(n_1, n_2; i)$ . Extracting a tilt measurement from spatially non-uniform displacements is an important issue. The most obvious method is to average  $d_1(n_1, n_2; i)$  and  $d_2(n_1, n_2; i)$  over the region of the image containing the missile. The procedural details for this averaging are described in subsection 6.1.

The remainder of this section briefly describes the OF algorithms and some important implementation details. All of the algorithms in this section are presented so that the units of the answers are pixels (or pixels/frame, if you like to think of optical flow as velocities). This avoids unnecessary equation clutter from including sampling units. Also, to avoid clutter, whenever an algorithm has separate equations for the  $n_1$ - and  $n_2$ -directions which differ only in appropriate subscripts, only the equation in the  $n_1$ -direction is shown.

### 6.1 Exceedence Map

An *exceedence map* is a tool utilized to determine the region within an image where the missile resides. The exceedence map is formed by first computing a threshold. The *ad hoc* threshold used here is the average of all the image pixel values

$$Thresh = \frac{1}{100NM} \sum_{i=0}^{100} \sum_{n_1=1}^N \sum_{n_2=1}^M I(n_1, n_2; i) \quad (3)$$

The exceedence map is then formed by testing each pixel in each image against the threshold. Pixels exceeding the threshold are assigned to be part of the missile, and those that do not are assumed to be background.<sup>2</sup> Mathematically, the exceedence map  $M(n_1, n_2; i)$  for image frame  $i$  is

$$M(n_1, n_2; i) = \{I(n_1, n_2; i) > Thresh\} \quad (4)$$

where the boolean expression evaluates to 1 (true) or 0 (false).

---

<sup>2</sup>First with respect to the temporal ordering of the images.

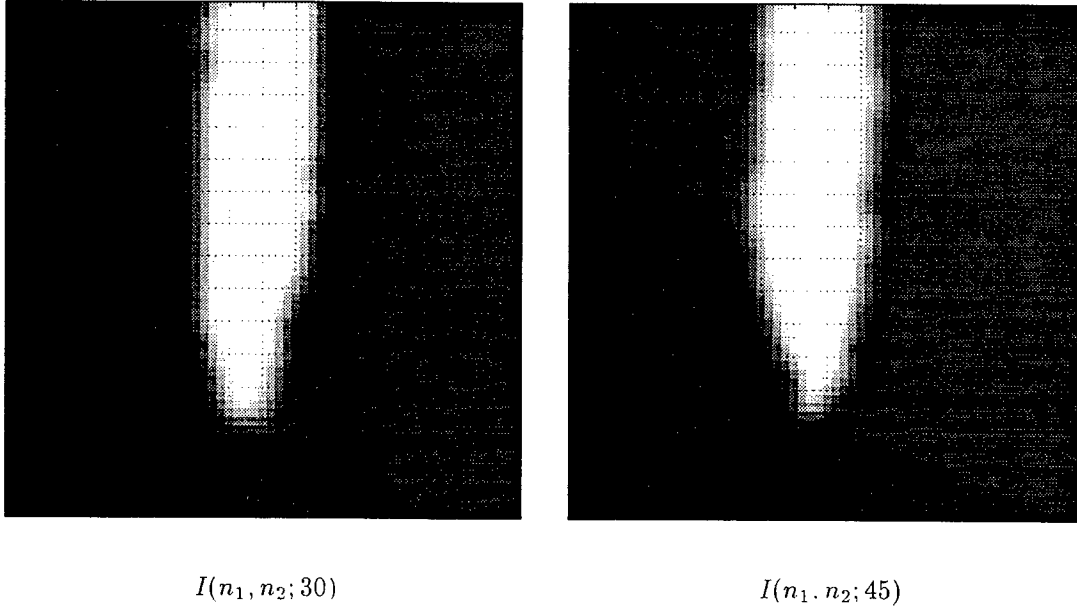


Figure 2: Missile images  $I(n_1, n_2; 30)$  and  $I(n_1, n_2; 45)$  thresholded & smoothed.

The exceedence map can be used to average the motion vectors over the missile while excluding the background pixel motions. For the  $n_1$ -direction the calculation for this average motion is

$$\overline{d_1(i)} = \sum_{n_1=1}^N \sum_{n_2=1}^M d_1(n_1, n_2; i) M(n_1, n_2; i) / \sum_{n_1=1}^N \sum_{n_2=1}^M M(n_1, n_2; i) \quad (5)$$

## 6.2 Eliminating Missile Blur

In some simulations, an attempt to eliminate the effects of the atmospheric turbulence on the OF calculations was made. The technique employed was to use the images' exceedence maps  $M(n_1, n_2; i)$  in place of the image data  $I(n_1, n_2; i)$ . In this application of the exceedence maps, the maps were smoothed. Smoothing was accomplished by filtering the  $n_1$ - and  $n_2$ -directions separately with the FIR filter [1 6 15 20 15 6 1] and then scaling to take advantage of the dynamic range of the video display format (256 maximum colors/grey scales). Image smoothing was used to smooth the edges and thereby improve the quality of the OF estimates. Figure 2 shows the 31st and 46th images after the threshold/smoothing process.

## 6.3 Gradients and Interpolation

All of the OF algorithms use image gradients (derivatives) in their computations. Since the continuous image fields are not available, numerical estimates of the image gradients must be used. Except where noted, the

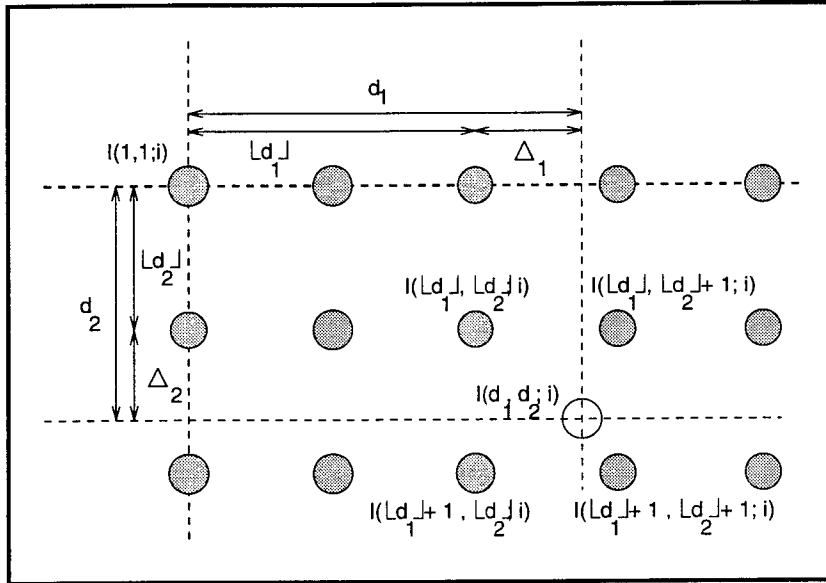


Figure 3: Illustration of bilinear interpolation procedure.

spatial gradients for all simulations were determined using the two point difference function of the form

$$\frac{\partial I(n_1, n_2; i)}{\partial n_1} \approx \frac{I(n_1 + 1, n_2; i) - I(n_1 - 1, n_2; i)}{2} \quad (6)$$

At the edges of images, where just one of the data points in (6) is unavailable, the other is assumed to be zero. This is even though it is known (roughly) which points near the image border contain missile data.

The TDML and GML algorithms also require the estimation of image pixels at non-integer sampling grid locations. Again, the continuous image frame is not available and a numerical technique is needed. To evaluate these points, *bilinear interpolation* was used [9]

$$I(n_1, n_2; i) = I(\lfloor n_1 \rfloor, \lfloor n_2 \rfloor; i)(1 - \Delta_1)(1 - \Delta_2) + I(\lfloor n_1 \rfloor + 1, \lfloor n_2 \rfloor; i)\Delta_1(1 - \Delta_2) + \\ I(\lfloor n_1 \rfloor, \lfloor n_2 \rfloor + 1; i)(1 - \Delta_1)\Delta_2 + I(\lfloor n_1 \rfloor + 1, \lfloor n_2 \rfloor + 1; i)\Delta_1\Delta_2 \quad (7)$$

where  $\Delta_1 = n_1 - \lfloor n_1 \rfloor$  and  $\Delta_2 = n_2 - \lfloor n_2 \rfloor$ . The operator  $\lfloor \cdot \rfloor$  represents the floor operator. If pixels outside the image frame boundaries were needed, their values were interpolated to be the value of the nearest boundary pixel.

Figure 3 illustrates (7).

## 6.4 Reference Image

The OF algorithms used here utilize 2 images. Two scenarios for tilt measurement with them are:

1. The two required images can be a temporal consecutive pair, i.e.  $I(n_1, n_2; r)$  and  $I(n_1, n_2; r + 1)$ . Then the image  $I(n_1, n_2; r)$  is the *reference image* for the computation. In this form, the algorithm

is computing the movement of pixels in the first frame necessary to match the second. These pixel displacements (also referred to as velocities) are differential quantities (distance traveled over time differential). The integration of them results in pixel location sans an offset equal to the initial object location (equal to  $\sum_{-\infty}^{-1} d_1(i)$ ).

2. Form the *reference image* by using some combination of past image frames. The OF field represents the relative motion of an image with respect to the reference image. No integration is necessary to get the tilts, nor is it necessary to add in an initial reference location. This is taken care of by using the same image as a reference for each calculation. In essence, using an OF algorithm in this manner is using it as a fast correlation-peak search algorithm.

Both uses of OF algorithms were investigated in the simulations. For the simulations, four types of reference images were used:

- The first image of the sequence,  $I(n_1, n_2; 0)$ .
- The exceedence map of the first image,  $M(n_1, n_2; 0)$ .
- The average of all the images,

$$\overline{I(n_1, n_2)} = \frac{1}{101} \sum_{i=0}^{100} I(n_1, n_2; i) \quad (8)$$

- A *Map* built up by low-pass filtering the past images after correcting them for past movement. This is described in detail in [7] and was used only in the FITTS simulations for which it was designed.

The average reference image for the missile sequence,  $\overline{I(n_1, n_2)}$ , is illustrated in Figure 4.

## 6.5 Transform-Domain Maximum Likelihood algorithm

The Transformed-Domain Maximum Likelihood (TDML) algorithm is given in [4] and [5]. It is an iterative update equation

$$d_{1jk}^+(i) = d_{1jk}^-(i) - \alpha_1(i) \sum_{n_1=1}^N \sum_{n_2=1}^M \frac{\partial Map(n_1 - d_1^-(n_1, n_2; i), n_2 - d_2^-(n_1, n_2; i); i)}{\partial n_1} \times \\ [I(n_1, n_2; i) - Map(n_1 - d_1^-(n_1, n_2), n_2 - d_2^-(n_1, n_2); i)] \phi_{jk}(n_1, n_2) \quad (9)$$

where  $j = 1, \dots, N'$ ,  $k = 1, \dots, M'$ ,  $1 \leq N' \leq N$ ,  $1 \leq M' \leq M$ ,  $\alpha_1(i)$  is a *convergence parameter*,  $\{\phi_{jk}(n_1, n_2)\}$  are the transform basis vectors, and  $d_{1jk}(i)$  are the OF transform coefficients for the  $i$ th image in the  $n_1$ -direction. The “+” and “-” superscripts on the coefficient estimates denote the new and old estimates, respectively. The convergence parameter  $\alpha_1(i)$  controls both the stability and speed of convergence. For  $(N', M')$  near  $(N, M)$ , a suitable value for  $\alpha_1(i)$  is [5]

$$\alpha_1(i) = 2 \sqrt{\max_{n_1=1 \text{ to } N} \max_{n_2=1 \text{ to } M} \left[ \frac{\partial Map(n_1, n_2; i)}{\partial n_1} \right]^2} \quad (10)$$

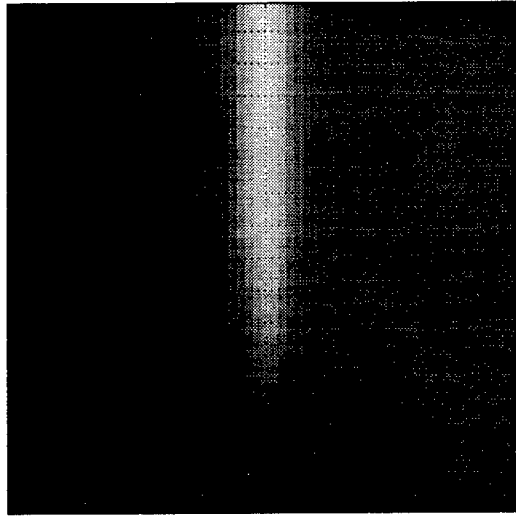


Figure 4: Reference image frame formed by averaging all missile image frames.

When  $N' = M' = 1$ , a better choice is

$$\alpha_1(i) = 2\sqrt{NM} \left/ \sum_{n_1=1}^N \sum_{n_2=1}^M \left[ \frac{\partial Map(n_1, n_2; i)}{\partial n_1} \right]^2 \right. \quad (11)$$

For the simulations, (10) and (11) were used for the convergence parameter (as appropriate) and the algorithm was allowed to iterate for 50 iterations (enough for convergence with a  $64 \times 64$  image).

The values of  $N'$  and  $M'$  are nominally equal to  $N$  and  $M$ , respectively. By selecting  $N' < N$  and  $M' < M$ , TDML finds OF estimates with varying degrees of smoothness. Using techniques similar to a Fourier transform, the algorithm solves for the OF field in a transform domain and low-pass filters the result before returning to the spatial domain. Smoothness is controlled by the values of  $N'$  and  $M'$  [5]. For  $N' = M' = 1$ , the OF field is uniform<sup>3</sup>, i.e.  $d_1(n_1, n_2; i) = d_1(i)$  and  $d_2(n_1, n_2; i) = d_2(i)$ . In this case a 1-iteration TDML algorithm is identical to the FITTS algorithm. As  $N'$  and  $M'$  get larger, the OF field is less and less smooth. The maximum values of  $N'$  and  $M'$  are the size of the image,  $N \times M$ , as previously mentioned. When  $N'$  and  $M'$  are this large, no smoothing of the OF field takes place and the motion vectors follow the image's gradients significantly more than they follow object OF [5].

In the situation where  $N' = M' = 1$ , a reference-less centroid is easily formed from the OF data with

$$cen_1(i) = \sum_{k=0}^i d_1(k) \quad (12)$$

As discussed in subsection 6.1, for non-uniform OF fields ( $N' > 1$  and  $M' > 1$ ), an average over the missile may be taken to arrive at the desired tilt differentials, that is, (5) may be substituted into (12) for  $d_1(k)$ .

---

<sup>3</sup>This is true for most CON transform basis sets  $\{\phi_{jk}(n_1, n_2)\}$  [5]. An example where it is not true is for the discrete sine transform.

## 6.6 The Generalized Maximum Likelihood algorithm

The Generalized Maximum Likelihood (GML) algorithm is derived as a special case of the TDML algorithm where the transform CON set  $\{\phi_{jk}(n_1, n_2)\}$  is a Karhunen-Loeve transform basis for the motion vectors. The GML algorithm is [3]

$$\begin{aligned} d_1^+(n_1, n_2; i) = & d_1^-(n_1, n_2; i) - \alpha_1(i) \sum_{m_1=1}^N \sum_{m_2=1}^M K_{d_1}(n_1 - m_1, n_2 - m_2) \times \\ & [I(n_1, n_2; i) - Map(n_1 - d_1(n_1, n_2; i), n_2 - d_2(n_1, n_2; i))] \times \\ & \frac{\partial Map(n_1 - d_1(n_1, n_2; i), n_2 - d_2(n_1, n_2; i))}{\partial n_1} \end{aligned} \quad (13)$$

The indexes  $n_1$  and  $n_2$  range over  $1, \dots, N$  and  $1, \dots, M$ , respectively, and  $\alpha_1(i)$  is a convergence parameter. The function matrix  $K_{d_1}$  is the covariance matrix for the motion in the  $n_1$ -direction

$$K_{d_1}(n_1 - m_1, n_1 - m_2) = E\{d_1(n_1, n_2)d_1(m_1, m_2)\} \quad (14)$$

where the operator  $E\{ \}$  is the expected value (ensemble average) operator. For the simulations the model

$$K_{d_1}(n_1 - m_1, n_1 - m_2) = \sigma_{d_1}^2 \rho_1^{|n_1 - m_1|} \rho_2^{|n_2 - m_2|} \quad (15)$$

was used which is a 2-dimensional, separable, Markov-1 model. The parameters  $\rho_1$  and  $\rho_2$  are correlation coefficients in the range  $[-1, 1]$ . High absolute values represent spatially smooth motion, and low values represent spatially uncorrelated motion.

For GML simulations the  $32 \times 32$  RECT image data with a motion correlation coefficients  $\rho_1 = \rho_2 = 0.8, 0.9$  and  $0.95$ . 50 iterations were run each time with the convergence parameter value

$$\alpha_1(i) = 2 \left/ \sigma_{d_1}^2 \sum_{n_1=1}^N \sum_{n_2=1}^M \left[ \frac{\partial Map(n_1, n_2; i)}{\partial n_1} \right]^2 \right. \quad (16)$$

## 6.7 Horn and Schunk's Optical Flow algorithm

Horn and Schunk's optical flow algorithm attempts to minimize

$$\epsilon(n_1, n_2; i) = \int \int_{\Gamma} [\alpha(i)^2 \epsilon_b^2(n_1, n_2; i) + \epsilon_c^2(n_1, n_2; i)] dn_1 dn_2 \quad (17)$$

where

$$\epsilon_b(n_1, n_2; i) = \frac{dI(n_1, n_2; i)}{di} = \frac{\partial I(n_1, n_2; i)}{\partial n_1} d_1(n_1, n_2; i) + \frac{\partial I(n_1, n_2; i)}{\partial n_2} d_2(n_1, n_2; i) + \frac{\partial I(n_1, n_2; i)}{\partial i} \quad (18)$$

is the change in brightness error, and

$$\epsilon_c(n_1, n_2; i) = \nabla^2 d_1(n_1, n_2; i) + \nabla^2 d_2(n_1, n_2; i) \quad (19)$$

is the velocity smoothness error. The rational behind minimizing (17) to estimate  $d_1$  and  $d_2$  is

- For small motion,  $\epsilon_b \approx 0$ .
- The motion vectors  $d_1(n_1, n_2)$  and  $d_2(n_1, n_2)$  should be smooth, i.e. their Laplacians should be zero. This implies  $\epsilon_c \approx 0$ .

Thus, a solution for  $d_1$  and  $d_2$  can be found by using Lagrange multipliers on (17). Applying numerical approximations for the temporal gradients, spatial gradients, and Laplacian operator results in an iterative algorithm for finding nonuniform estimates of  $d_1$  and  $d_2$  [6]. Note that  $\alpha(i)$  in (17) is a relative weighting factor of the two errors. In Horn's and Schunk's simulations, this parameter was tuned for optimum performance—a method for calculating  $\alpha(i)$  was not presented. The parameters used for HS-OF simulations were 50 iterations, and  $\alpha(i) = 70$ .

## 6.8 Fitts' Algorithms

Fitts has two algorithms, both similar, which he describes as “correlation trackers” [7] [8]. Both algorithms result in a uniform optical flow field estimate  $\{d_1(i), d_2(i)\}$  and have provisions for generating a reference image. The second algorithm, FITTS, is [8]

$$d_{1corr}(i) = -\frac{\sum_{n_1=1}^N \sum_{n_2=1}^M \frac{\partial Map(n_1, n_2; k)}{\partial n_1} [I(n_1, n_2; i) - Map(n_1, n_2; i)]}{\sum_{n_1=1}^N \sum_{n_2=1}^M \left[ \frac{\partial Map(n_1, n_2; i)}{\partial n_1} \right]^2} \quad (20)$$

where  $Map(n_1, n_2; i)$  is the reference image (nominally equal to the noise-free, centered object of interest). The partial derivatives in (20) are to be computed numerically. In (20), Fitts uses the computation

$$\frac{\partial Map(n_1, n_2; i)}{\partial n_1} = \frac{Map(n_1 + 1, n_2; i) - Map(n_1 - 1, n_2; i)}{2} \quad (21)$$

The reference image  $Map(n_1, n_2; i)$  is generated by the iterative procedure

$$Map(n_1, n_2; i) = (1 - w_1)Map(n_1, n_2; i - 1) + w_1 I(n_1, n_2; i - 1) \quad (22)$$

which is simply a low-pass filter operation on previous images. Fitts found that using this method of creating and updating the reference image required corrections to the tilt calculations of the forms

$$d_{1map}(i) = d_{1map}(i - 1) + w_1 d_{1corr}(i - 1) \quad (23)$$

$$d_1(i) = d_{1corr}(i) + d_{1map}(i) \quad (24)$$

where  $d_{1map}(i)$  is memory used to compensate the calculated tilts,  $d_{1corr}(i)$ , and arrive at a final estimate of the OF,  $d_1(i)$ . In the FITTS algorithm simulations (22) - (24) were used.

## 7 Simulation Results

This section details the results of all simulations. Two measures are used to express the quantities of interest: correlations (objective) and graphs (subjective). The following subsections give more details and relevant discussion.

### 7.1 Performance Evaluation

The overall goal of the tracker is to provide tilt information which will allow the HEL to be pointed accurately at the missile aim point. To quantify the accuracy of using tilts from a calculation to estimate an unknown tilt, the correlation of the tilts was used. This calculation is

$$\rho(c, d) = \sum_{i=0}^{100} [c(i) - \bar{c}][d(i) - \bar{d}] / \sqrt{\sum_{i=0}^{100} [c(i) - \bar{c}]^2 \sum_{i=0}^{100} [d(i) - \bar{d}]^2} \quad (25)$$

where  $c(i), d(i)$  are any two tilts (measured or actual) and  $\bar{c}, \bar{d}$  are the average values of these tilts, respectively. As previously noted, OF algorithms do not produce tilt outputs directly, so (12) was used to “integrate” their outputs into tilts. Note that the lack of a reference does not matter for calculating the normalized correlations in (25).

### 7.2 Data Correlations

Using the FULL image sequences, the correlation between point source and HEL centroids were found to be -0.90 in the  $n_1$ - and  $n_2$ -directions. The correlation between HEL and missile centroids was found to be -0.69 in the  $n_1$ -direction and -0.81 in the  $n_2$ -direction. (The negative sign on the correlations reflects a co-ordinate swap which is an artifact of way in which the simulation data was generated.) The correlations between the missile and point source were found to be 0.71 in the  $n_1$ -direction and 0.67 in the  $n_2$ -direction. The low correlation of the missile sequence with the HEL and point source is due to the fact that the missile is an extended object which is much larger than an isoplanatic region. The point source and HEL are similar in size and propagate through the same region of atmosphere. This explains the high correlations between their centroids. If the point source and HEL propagated through very different regions of the atmosphere, the centroid correlations would be expected to be much smaller.

### 7.3 Interpretation of correlation

This section will try to provide some intuitive insight into the meaning of the correlation parameters in the previous and next sections. The correlation parameter indicates how much (random) error is introduced by using one of the correlated signals in place of the other. Specifically,

$$\text{Var} \left\{ c(i) - \frac{\sigma_c}{\sigma_d} d(i) \right\} = [1 - \rho(c, d)^2] \sigma_c^2 \quad (26)$$

where  $\text{Var}\{ \}$  is the statistical variance. A correlation of 0.5 means 25% of the (normalized) power is similar between the two processes. A correlation of 0.7 brings this up to 49%, and a correlation of 0.9 represents only 81% similarity. This square law behavior demonstrates that very high correlations are desirable.

Consider the specific example of using the centroid of the point source as a predictor of the location of the HEL centroid for the image sequences used in this work. This specific example is being considered because it represents a nearly ideal tilt estimate situation for the HEL: both beams are of comparable size and propagate through the same region of the atmosphere. So it is expected they should undergo very similar tilt perturbations. The correlation parameter for the  $n_1$ -centroids is  $-0.9$ , the point source centroid RMS value is  $\sigma_{\text{point}} = 0.83$ , and the HEL centroid RMS is  $\sigma_{\text{HEL}} = 1.89$ . Thus, using the point source centroid as the negative centroid of the HEL propagation would result in an error of 0.81 pixels RMS between the predicted and actual locations in the  $n_1$ -direction. That is, 0.81 pixels RMS is the expected limit of HEL pointing accuracy under the proposed scenario. There is still an issue of the accuracy of the simulation data (which is worthy of further investigation) as well as the possibility of superior HEL pointing techniques which exploit information not contained in the point source centroid.

## 7.4 Experiment Correlations

As measures of algorithm performance, the correlation of the centroids for the missile, point source, and HEL were computed using (25). Higher correlation absolute values are desirable (taking as a given that the centroids are tilt truth).

Table 1 summarizes the correlation parameters in the  $n_1$ - and  $n_2$ -directions calculated with respect to the point source, missile, and HEL centroids in those directions. In the table,

- “F” refers to the FULL ( $64 \times 64$ ) image,
- “R” refers to the RECT ( $64 \times 32$ ) image,
- “S” refers to the SQUARE ( $32 \times 32$ ) image,
- “T” denotes the image was thresholded with the exceedence map and then smoothed,
- “0” denotes that image  $I(n_1, n_2; 0)$  was used as the reference image (after threshold/smoothing, if applicable), and
- “A” denotes the average of all images,  $\overline{I(n_1, n_2)}$ , was used as a reference image.

The correlations with centroids reveal interesting results. First, The calculated tilts correlate better with the missile centroids than with the HEL and point source centroids. This is not a surprising result since the algorithms are using missile data for their input and the centroids of the missile data do not correlate well with the HEL and point source centroids.

Test Condition(s)		Correlation with centroid of					
		Point Source		Missile		HEL	
Algorithm	Image	$\rho_1$	$\rho_2$	$\rho_1$	$\rho_2$	$\rho_1$	$\rho_2$
TDML ( $N' = M' = 1$ )	F	0.34	0.66	0.64	1.00	-0.34	-0.82
TDML ( $N' = M' = 2$ )	F	0.33	0.68	0.65	1.00	-0.34	-0.83
TDML ( $N' = M' = 4$ )	F	0.34	0.71	0.64	1.00	-0.35	-0.85
TDML ( $N' = M' = 1$ )	FT	0.40	0.77	0.71	0.97	-0.37	-0.89
TDML ( $N' = M' = 1$ )	R	0.34	0.66	0.64	1.00	-0.29	-0.77
TDML ( $N' = M' = 2$ )	R	0.33	0.68	0.64	1.00	-0.30	-0.79
TDML ( $N' = M' = 4$ )	R	0.33	0.68	0.64	1.00	-0.30	-0.79
TDML ( $N' = M' = 1$ )	R0	0.34	0.70	0.45	1.00	-0.37	-0.78
TDML ( $N' = M' = 1$ )	RT0	0.38	0.75	0.34	0.99	-0.27	-0.83
TDML ( $N' = M' = 1$ )	RA	0.51	0.66	0.80	0.98	-0.46	-0.77
GML ( $\rho = 0.80$ )	S	0.57	0.90	0.59	0.99	-0.57	-0.90
GML ( $\rho = 0.90$ )	S	0.47	0.88	0.64	0.98	-0.53	-0.91
GML ( $\rho = 0.95$ )	S	0.45	0.87	0.68	0.98	-0.51	-0.91
HS-OF	R	0.37	0.70	0.58	1.00	-0.34	-0.81
HS-OF	RT	0.44	0.77	0.69	0.98	-0.40	-0.85
HS-OF	RT0	-0.22	0.79	-0.10	0.97	0.38	-0.86
FITTS ( $w_1 = 0.10$ )	F	0.65	0.67	0.86	1.00	-0.64	-0.82
FITTS ( $w_1 = 0.03$ )	F	0.83	0.71	0.83	1.00	-0.82	-0.84
FITTS ( $w_1 = 0.01$ )	F	0.70	0.72	0.56	1.00	-0.72	-0.84

Table 1: Centroid Correlations

Second, the ability of all algorithms under all conditions to estimate the centroid/tilt in the  $n_2$ -direction is rather insensitive to simulation conditions. In the case of the missile centroid, the correlations are high in the  $n_2$ -direction. The  $n_1$ -direction shows considerably greater variability in the correlation results and the simulation conditions. Most important is that the TDML algorithm with the average reference image and all of the FITTS simulations (which dynamically build an average image) did considerably better than any other scenario. Since the FITTS algorithm is a special case of the TDML algorithm<sup>4</sup>, an important conclusion to be drawn is the use of an average image for the reference image appears to be the best strategy.

Increasing the dimensions of the TDML transform domain did not dramatically improve the correlations. Using threshold/smoothed images did not improve the results as much as expected. The reason for this is that the edge contour of the thresholded/smoothed images moves upwards due to the atmospheric distortions.

<sup>4</sup>Even though FITTS is a sub-case of TDML, the results of using each algorithm differ. This is primarily due to the use of very different reference images in the simulations

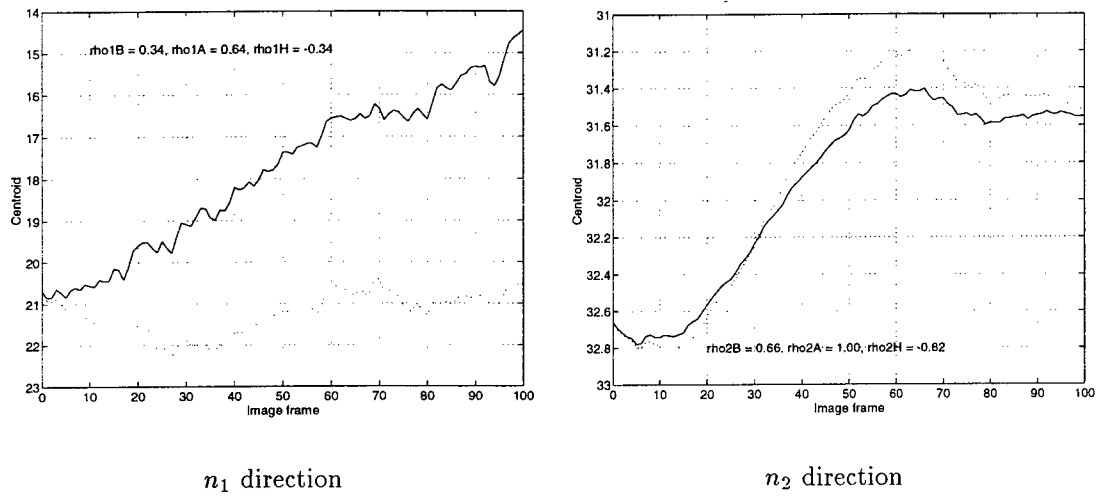


Figure 5: TDML algorithm,  $N' = M' = 1$ .

Since the edges contain most of the useful tracking information [7], the algorithms still get confused by the blur motion. For the GML simulations with the SQUARE data the correlations with the HEL and point source were higher in the  $n_2$ -direction and lower in the  $n_1$ -direction due to the smaller region of the image used.

## 7.5 Centroid Graphs

In this section some of the more interesting tilt results will be examined graphically. All of the graphs discussed in this section show the results of an algorithms tilt calculations (solid line) displayed with the missile centroid (dotted line). To make the graphs compact, these referenceless centroids were given a reference tilt equal to the centroid of the first image used in the simulation.

It was claimed in the introduction that the movement of the missile blur effect along the body was detected by the algorithms. Figure 7.5 shows the results for one of the TDML experiments. Notice that the  $n_1$ -direction tilt calculation general trend is an upward ramp caused by the blur movement while the local trends follow the centroid calculation. This was observed in the GML and HS-OF simulations as well. By using an average image for the reference image, this ramp trend is eliminated as shown in Figure 7.5. (The initial jump in the  $n_2$ -direction shown in Figure 7.5 is from the offset of the average image tilt to all the images.) It was also found that increasing the  $N'$  and  $M'$  for the TDML algorithm significantly reduced the slope of the ramp even though the correlations were only marginally improved.

Figure 7.5 shows the results from the best FITTS simulation for comparison to Figure 7.5. Note that even though the correlation is better with FITTS than this TDML case, the graphic results are comparable.

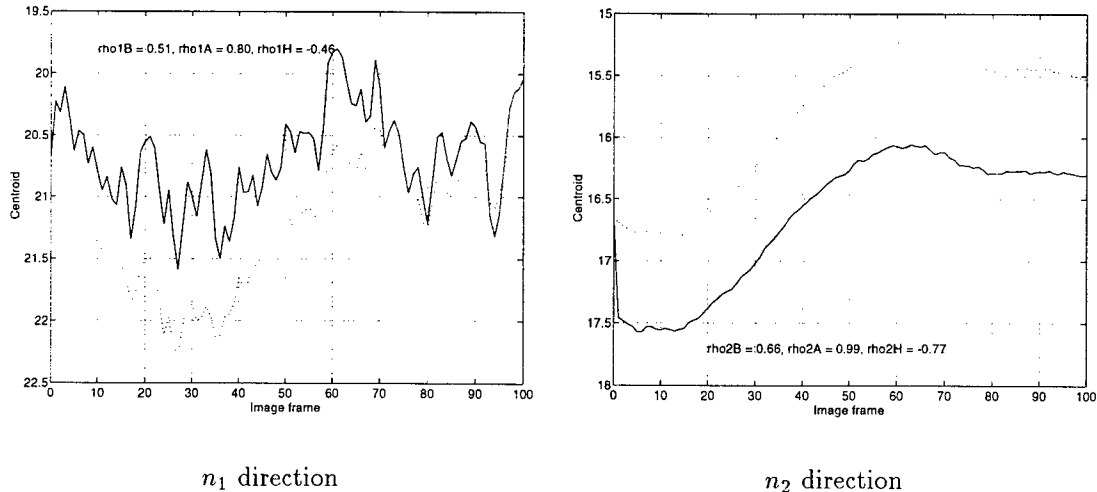


Figure 6: TDML algorithm, RECT,  $N' = M' = 1$ ,  $\overline{I(n_1, n_2)}$  reference image.

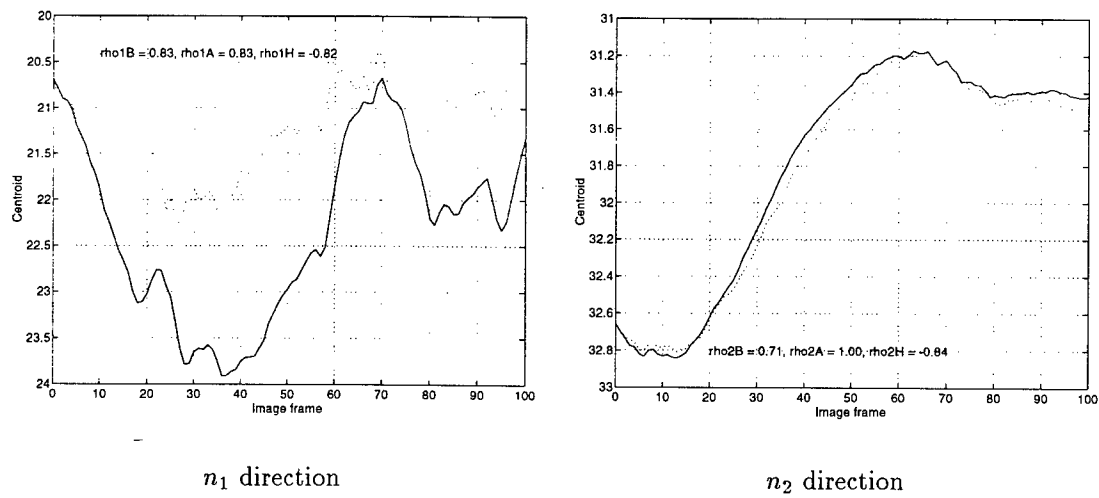


Figure 7: FITTS,  $w_1 = 0.03$

## **8 Conclusions**

The effects of the atmosphere on the motion estimation techniques used thus far are significant. The TDML, GML, and Horn & Schunk's OF algorithms all see the atmosphere caused blur movement. They attempt to combine the motion of the blur with the motion of the missile; this is in their nature of operation. Threshold filtering of the image to eliminate the effects of the blur is not enough—the edges of the filtered missile still have significant upward-moving artifacts. The only effective technique found in the simulations for solving this problem was using the average of all images  $\overline{I(n_1, n_2)}$ . This makes the OF algorithms essentially fast correlation-peak search algorithms. Using the averaged image in a dynamic form in the FITTS algorithm also was very viable.

The formation of a reference image is not well investigated in the literature on optical flow. Most authors (including this one) have assumed in their works a reference image is easily available. From these experiments, I have rethought my position on this and now believe calculating optical flow is easy compared to generating a good reference image.

### **8.1 Future Work**

Suggestions for future work include:

- Try other OF algorithms. The brevity of this tour prevented a widespread literature search for algorithms suitable for this application. Examples include fast correlation peak search algorithms, and Fourier techniques.
- Develop a (new) algorithm which takes into account the specific nature of the observed motion from the atmospheric turbulence.
- Investigate the behavior (from a control stand-point) of Fitts' technique for accumulating a reference image. Examine extensions or generalizations of it as a Kalman filter and apply this to other algorithms as well as FITTS.
- Investigate the temporal correlation of the atmospheric distortions as additional, useful information for computing OF.

### **8.2 Acknowledgments**

The author is greatly indebted to Dr. Sal Cusumano, the Air Force Office of Summer Research, and Philips Laboratory. The experience gained during my summer tour has heightened my interest in the fields of image processing and its upcoming applications. I would also like to thank Dr. Schulz for telling me of this opportunity, my advisor Dr. Burl for letting me go for the summer, and RDL for accepting my application by FAX on the day it was due.

## References

- [1] R. Vernon, D. Link, F. Gebhardt, D. Lyman. Presentation for *Science Applications International Corporation* at Kirtland AFB, August 24, 1993.
- [2] S.J. Cusumano, D. Jordan, D.J. Link, and R. Vernon. "An Overview of the Acquisition, Tracking, and Pointing System (ATP) for the Airborne Atmospheric Compensation and Tracking Aircraft", Internal report Phillips Laboratory LIAE, Kirtland AFB.
- [3] N.M. Namazi and D.W. Foxall, "Use of the Generalized Maximum Likelihood Algorithm to Estimation of Markovian Modeled Image Motion," *Journal of Optical Engineering*, Oct. 1991.
- [4] N.M. Namazi and J.I. Lipp, "Nonuniform Image Motion Estimation in Reduced Coefficient Transformed Domains," *IEEE Transactions on image Processing*, Vol. 2, No. 4, April 1993, pp. 236-246.
- [5] J.I. Lipp, "Implementation and Convergence Criterion of a New Iterative Algorithm for Nonuniform Image Motion Estimation in the Presence of Noise." Masters Thesis, Michigan Technological University, 1994.
- [6] B.K. Horn and B.G. Schunk, "Determining Optical Flow," *Artificial Intelligence*, Vol. 17, 1981, pp. 185-203.
- [7] J.M. Fitts, "Correlation Tracking Via Optimum Weighting Functions," Report No. P73-240 from Hughes, Culver City, CA, 1973.
- [8] J.M. Fitts, "Optimal Weighting Function Correlation Tracker", Hughes Aircraft Co. Internal Report.
- [9] W.K. Pratt, *Digital Image Processing*. New York: Wiley, 1978.

DETERMINING CLOUD COVERAGES FOR  
INPUT TO THERMAL CONTRAST MODELING

Stephen A. Luker  
Research Assistant  
Department of Biological Sciences

The University of Alabama  
Box 870344  
Tuscaloosa, AL 35487-0244

Final Report for:  
Summer Graduate Research Program  
Phillips Laboratory

Sponsored by:  
Air Force Office of Scientific Research  
Bolling Air Force Base, DC

and

Phillips Laboratory  
Hanscom AFB, MA

August 1994

DETERMINING CLOUD COVERAGES FOR  
INPUT TO THERMAL CONTRAST MODELING

Stephen A. Luker  
Research Assistant  
Department of Biological Sciences  
The University of Alabama

Abstract

The percent cloud cover greatly affects the amount of transmitted solar radiation as well as its rate of attenuation through the atmosphere. A whole sky imaging unit was used to capture one and ten minute resolution data for analysis through various image processing techniques. These processed images were then used to provide input to a thermal contrast model for predicting thermal crossovers (in the 8-12 micron range) between targets and their background environments.

## DETERMINING CLOUD COVERAGES FOR INPUT TO THERMAL CONTRAST MODELING

Stephen A. Luker

### Introduction

It is clear that in spite of substantial and well documented study of the earth's atmosphere by a myriad of able and willing investigators, the ability to portray concisely the optical state of the local atmosphere in a manner suitable for many specific and intermediate needs is severely limited. It is equally clear that a major and pervasive contaminant, from an image transmissions scenario point of view, is the ubiquitous and ever changing cloud cover in any one of its infinite variations. Thus in an effort to provide an experimental approach that would enable automatic assessment of local cloud cover and statistics, a whole sky imager (wsi) was used and several image processing procedures were developed. The wsi (developed by Marine Physical Laboratory of Scripps Institute of Oceanography) is designed to acquire whole sky visible spectrum at a 175 degree field of view in pre-selected wavelengths that can be recorded in a digital format suitable for subsequent automated cloud analysis (Johnson et. al., 1989).

The wsi is a ground-based electronic imaging system which monitors the upper hemisphere. It is a passive, i.e. non-emissive system, which acquires calibrated multi-spectral images of the sky dome. The system, shown in Figure 1, views the sky through a series of spectral and neutral density filters, using a fisheye lens to attain most of the sky dome. A fixed gain CID (charge injection device) solid state camera is utilized, and a full set of radiometric and geometric calibrations are acquired prior to fielding the system. Data are acquired in 512 column X 480 row format, which yields 1/3 degree spatial resolution. This corresponds to a 17 meter footprint, for a cloud layer at 3 km height.

In the field, cloud images are acquired under the control of a microcomputer. This is a stand-alone unit, requiring essentially no user intervention; control of all peripheral functions if fully automatic. Four digital images are acquired either every minute or every ten minutes and archived on 8 mm tape for post-processing. During a single three day experimental run, approximately 750 megabytes of data are archived for post-processing.

**IMAGE & ANALYSIS SYSTEM  
HARDWARE BLOCK DIAGRAM E/O SYSTEM 5**

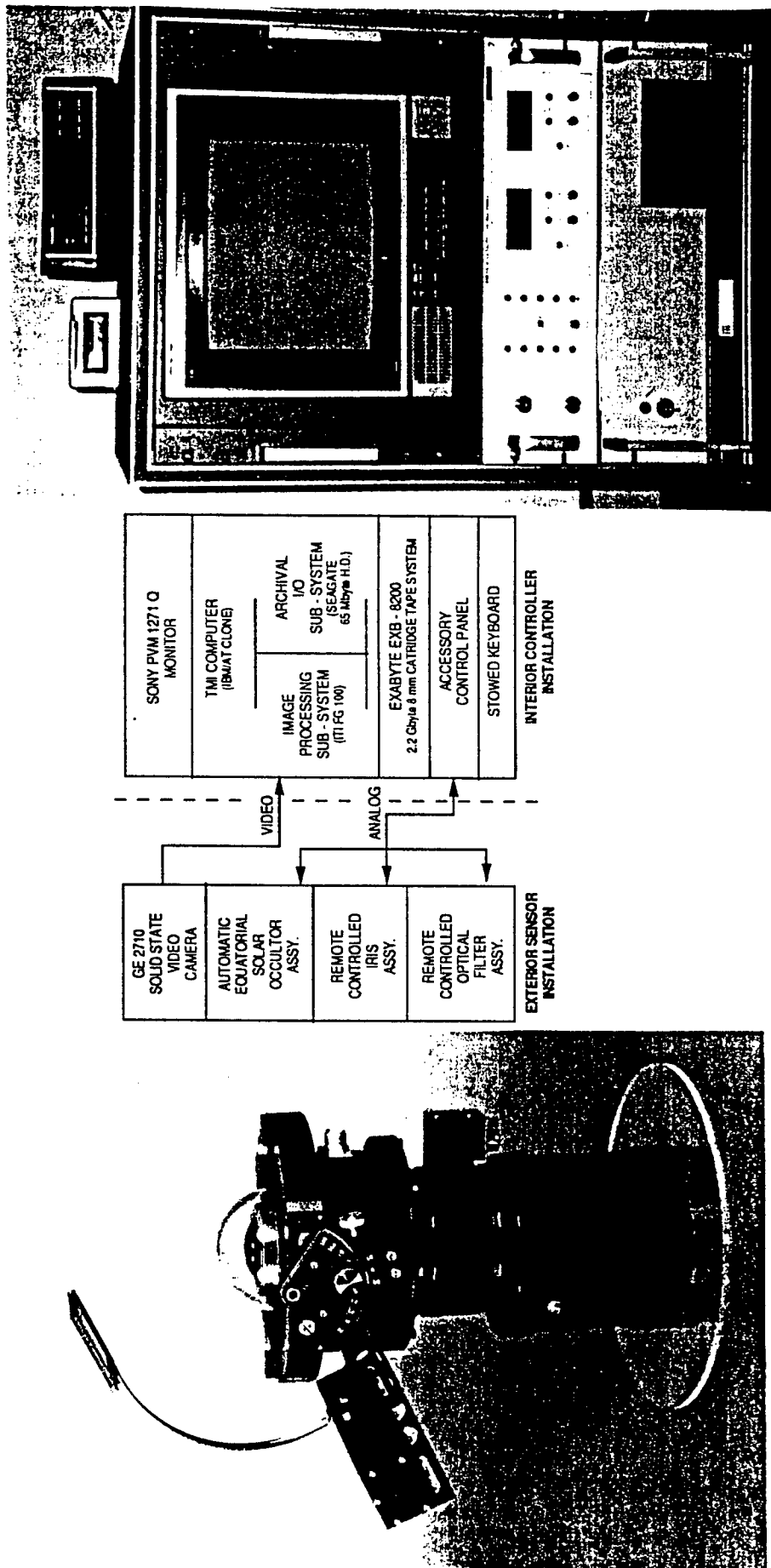


Figure 1. Whole sky imager (wsi) camera and analysis system.

Imaging IR sensors actually respond to the difference in radiance between a wavelength band that is approximately 8-12 microns. The thermal contrast model used to compute target background and target temperatures (calculated from radiances), TCM2 (Thermal Contrast Model #2), treats the target as a distinctive three-dimensional network of nodes that exchange heat with one another and with their environment-- both exterior and interior (Touart et. al., 1993). Many phenomena interact to produce the thermal scene containing the target and its background. Solar load is distributed by its components: direct, diffuse, and reflected. This allows the proper directionality, shadowing, and optical properties to be considered. Percent cloud cover and density greatly influence these properties and require accurate estimations from an analyst or an automated process.

The Simlab at Phillips Lab has been involved in the evaluation of the TCM2. Using a full meteorological instrument suite to gather atmospheric and environmental data, the Simlab is designing and implementing a series of experiments to test the physics of the models within the TCM2 for varying weather conditions. The objective of the TCM2 is to be able to simulate target and background temperatures for a given set of atmospheric and environmental conditions enabling pilots to use IR guided "smart" weapons not only in optimal weather conditions but also in adverse conditions as well. This information would then be used to provide tactical decision aid to mission planning or mission training operations.

#### Methodology

Experiments for evaluating the TCM2 are conducted over a three day period. A full compliment of meteorological and environmental instruments begin gathering data two days prior to the experiment. These initial startup data are required by the TCM2 to establish an atmospheric baseline. The instrument suite includes two anemometers, recording rain gauges, barometers, thermistors, soil moisture probes, pyrometers (including both direct and diffuse, downwelling, and upwelling), ground-based 35 gigahertz radar, a whole sky imaging system, and a FLIR (forward looking infrared sensor). The FLIR records IR wavelengths in the 8-12 micron range and gathers data on both a target (flat green metal plates) and a background (short grass). The FLIR is also calibrated with two black body sources.

Two days prior to, and during, the experiment the wsi records data for a 10 to 12 hour period corresponding to the available daylight hours. Unfortunately this particular wsi does not record images at night due to the lack of light amplification devices in the camera. Consequently, the camera can not "see" at night. Every ten minutes the wsi downloads an image to 8 mm tape. C code (Appendix A) was then written to extract the raw 16-bit (8-bit for each red and blue band) data from the tape and convert it to 8-bit ascii format. The images were then read into the commercial image processing software package, Khoros (Khoros, 1991), and converted to a viff file format for processesing and analysis and then to tiff file format for storage and hardcopy output. Various methods for determining cloud coverages were used including edge detection, cluster analysis, principle components analysis, and threshholding. Samples from the ten minute wsi image archive were subjected to these analyses and individual pixels were assigned a binary value of either 1 (cloud) or 0 (no cloud). Percent cloud cover was then determined for the image.

For this experiment, threshholding was determined to be the most beneficial. Histograms were generated for each image and visual perception was used as the discriminating factor to set the lower limits of the threshhold. The contributing pixel values associated with text were removed by establishing a baseline for the number of pixels with a brightness value of 255 (white) directly corresponding to the text. Cloud data (usually grey to white in brightness) were clipped to a value of 255 while all other values were set to 0 for calculating percent cloud cover.

### Results

Figure 2 depicts an unprocessed wsi 10 minute cloud image. Due to limitations of computer hardware, the processed images appear striped and were not included in a figure. However, threshholding digital brightness values for the wsi image did produce favorable results. The resulting elliptical shape of the image is an artifact of the wsi itself. In addition, geometric relationships exist between the position of a pixel in the imagery and a particular point in the sky. Table 1 illustrates the linear and parabolic relationships between the position of the pixel in the image and the position of that pixel in the sky along with their associated areal representations.

HAN OD #2

LONG 71 DEG 17 MIN 0

LAT 42 DEG 28 MIN N

DATE=10/JUL/10

TIME=20:10:02 B

IRIS=000

OCCL=140

ND=2

SP=1

TEMP=+17

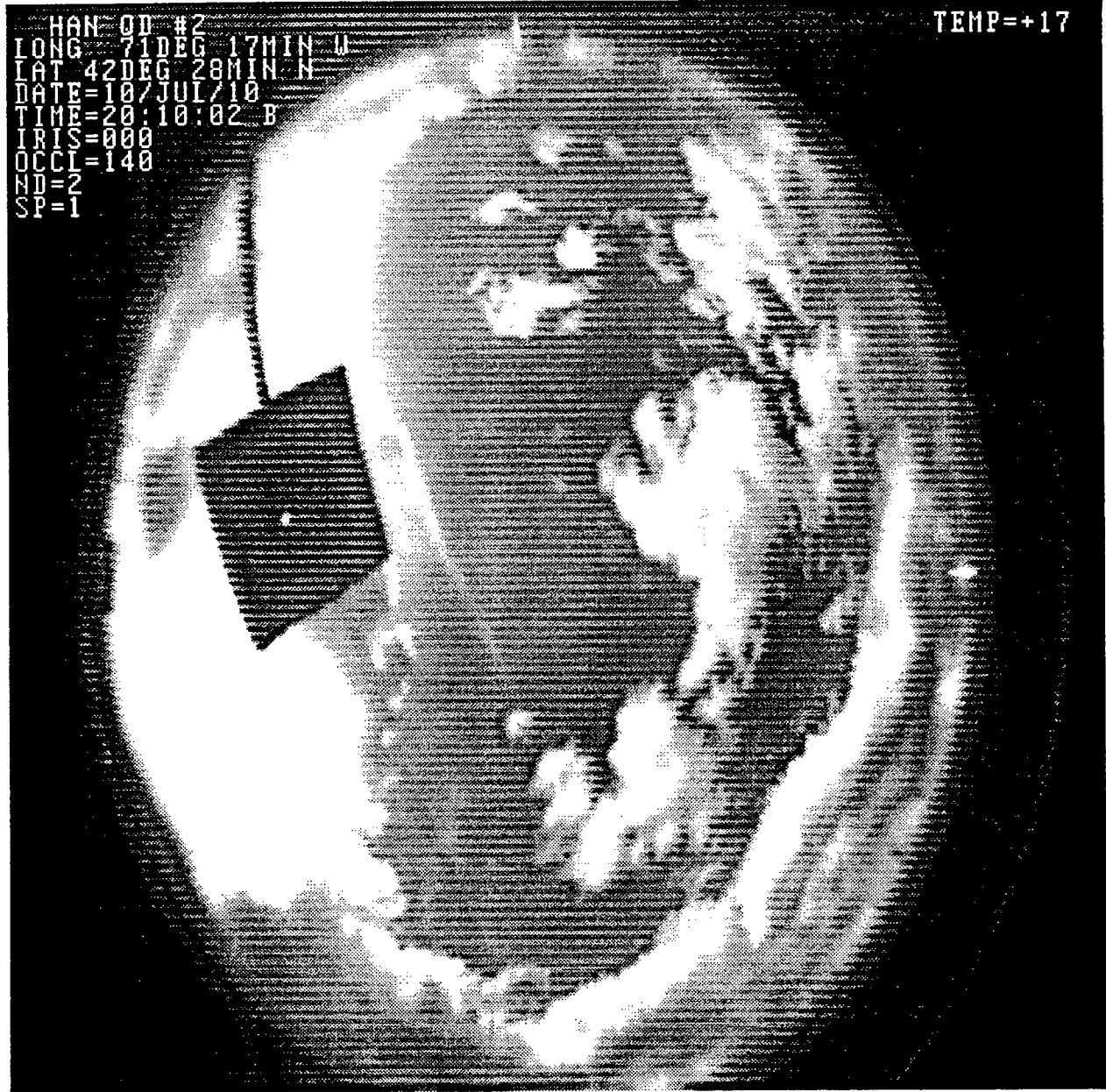


Figure 2. Visible cloud image from the whole sky imaging system.

Table 1. Geometric relationships between the position of a pixel on the image and its position in the sky.  
The angle represents the peripheral viewing angle in one direction.

	0°	10°	20°	30°	40°	50°	60°	70°	80°
Linear	1.000	0.995	0.980	0.955	0.921	0.878	0.827	0.769	0.705
Parabolic	1.000	1.021	1.032	1.033	1.023	1.003	0.971	0.929	0.877

### Discussion

Of the four techniques used for determining cloud cover (edge detection, cluster analysis, principle components analysis, and threshholding), threshholding provided the most favorable results. Although the processed images were not subjected to statistical analyses, visual inspection provided strong evidence that the threshholding technique produced accurate results. Although there are limitations to threshholding (e.g. not fully automated, problems with misidentifying dark clouds), the other image processing techniques were found to have even more drawbacks. For example, edge detection produced an excessive amount of edges corresponding to not only cloud-sky boundaries, but also within cloud boundaries. The resulting image greatly overestimated the amount of cloud cover. Cluster analysis (statistical clustering of the brightness values) often underestimated the amount of cloud cover and is highly dependent upon the minimum distances used for separating clusters.

Weighting factors to relate the position of a pixel on the image to its position in the sky were considered and determined unnecessary because the parabolic relationship (Table 1) only loses at most 12.3% at a peripheral view of 80 degrees per direction and 7.1 % at a 70 degree peripheral. This would only result in an overestimation of cloud cover by 2.1% for the 60-80 degree peripheral angle.

Threshholding does offer disadvantages. First, the process is not fully automated and requires the presence of an analyst. This is a serious limitation due to the amount of images needing to be processed. During a single experimental run the wsi produces 6 images per hour over 4 different filters (total 24) for 10-12 hours of run time during daylight over a 5 day period. This adds to be 1200 to 1400 images per experiment. Most of the discrimination required by an analyst involves selecting the filter with the most contrast and determining the threshhold value. Secondly, clouds represented by higher brightness values often include regions that are dark as those associated with a cumulous cloud. These regions may fall below the determined threshhold value and not be considered as cloud cover, although in reality they are. Finally, with threshholding determining the threshhold value is highly subjective. The analyst must visibly or statistically (with the use of histograms) estimate the areas considered sky or cloud. This is often difficult as the sun tends to illuminate the image with glare.

### Conclusions

Currently, the TCM2 requires a percent cloud cover input to aid in the calculation of incident radiation reaching a target and its background. A fully automated methodology has been developed for downloading the wsi data from 8 mm tape and converting those images to a compressed tiff file format thus reducing the amount of storage space required while maintaining the quality of the data. In addition, a semi-automated methodology exists for post-processing the wsi data and determining the percent cloud cover via thresholding non-cloud regions within the image. Although user interaction is minimal, a user independent system would allow for much faster processing while freeing the analyst for other tasks. Unfortunately, sensitivity analysis on the TCM2 may show that the percent cloud cover is not always effective in determining the portion of solar radiation that reaches the target and background. In the near future it may be determined that another approach needs to be addressed for estimating the incident solar radiation, however, the current methodology does provide reasonable estimations of percent cloud cover.

### Literature Cited

- Johnson, R.W., Hering, W.S., and J.E. Shields. 1989. Automated Visibility & Cloud Cover Measurements with a Solid-State Imaging System. Marine Physical Laboratory, Scripps Institute of Oceanography, San Diego, CA, Final Report GL-TR-89-0061.
- Khoros, 1991. Khoros Programmer's Manual. The University of New Mexico.
- Touart, C.N., Gouveia, M.J., DeBenedictis, D.A., Freni, M.L., Halberstam, I.M., Hilton, P.F., Hodges, D.B., and D.M. Hoppes. 1993. Electro-Optical tactical Decision Aid (EOTDA) User's Manual, Version 3, Technical Description, Appendix A. Hughes STX Corporation, Lexington, MA, Scientific Report No. 48, Volume II.

## Appendix A

```
#import <stdio.h>
#import <fcntl.h>
#import <libc.h>

int readexa(int efd, unsigned char *buf, unsigned int nbytes );
#define BLOCKSIZE 1024

main (int argc,char *argv[])
{
    int a = 0;
    int i = 0;
    int k = 1;
    int j = 0;
    int frxt;
    int total_read;
    char test[4];
    char hold[4];
    unsigned char buf1[1024];
    FILE *fp, *fpa;

    char file[10];
    char filea[10];

    if ( (frxt = open ( "/dev/nrxt0", O_RDONLY ) ) == -1 )
    {
        fprintf( stderr,"ERROR: Open failed on exabyte device /dev/nrxt0\n" );
        return ;
    }
    else
    {
        sprintf(stderr,"exabyte device /dev/nrxt0 is open\n");
    }

    sprintf (test, "%s",argv[1]);
    printf("this is test %s \n", test);
    readexa(frxt,buf1,BLOCKSIZE);
    strncpy(hold, buf1,3);
    printf("\nthis is hold %s \n", hold);

    a=1;
    for (i=0; i <= 1 ; i++)
    {
        sprintf(file,"ten.%d",a);
        sprintf(filea,"ten.%d",a+1);
        a+= a+2;
        if( ( fp = fopen(file,"w") ) == NULL)
        printf("error opening file");

        if( ( fpa = fopen(filea,"w") ) == NULL)
        printf("error opening file");

        readexa(frxt,buf1,BLOCKSIZE);

        bzero(hold, sizeof(hold));
        strncpy(hold, buf1,3);

        while(strcmp( hold, test, 3 ) != 0 )
```

```

{
    for(j=0;j<=511;j++)
        fprintf(fp,"%d ",buf1[j]);
    fprintf(fp,"\\n");
    for(j=512;j<=1023;j++)
        fprintf(fpa,"%d ",buf1[j]);
    fprintf(fpa,"\\n");
    readexa(frxt,buf1,BLOCKSIZE);
    strncpy(hold, buf1,3);
}
fclose(fp);
fclose(fpa);
printf("close file %d \\n",i);
fflush(stdout);
}

}

int readexa(int efd, unsigned char *buf, unsigned int nbytes )
{
#define MAXTRIALS 100
int ntrials = 0;
int rbytes, sbytes;

while (ntrials < MAXTRIALS)
{
    rbytes = 0;
    rbytes = read ( efd, buf, nbytes);

    if (rbytes == nbytes)
    {
        return(nbytes);
    }
    else
    {
        ++ntrials;
    }
}
return(-1);
}

```

LABORATORY EXPERIMENTS WITH THE VERSATILE TOROIDAL FACILITY(VTF)

Daniel T. Moriarty  
Graduate Student  
Nuclear Engineering Department

Massachusetts Institute of Technology  
167 Albany St.  
Cambridge, MA 02139

Final Report for:  
Graduate Student Research Program  
Philips Laboratory, Hanscom AFB, MA

Sponsored by:  
Air Force Office of Scientific Research  
Bolling Air Force Base, Washington, D.C.

August 1994

LABORATORY EXPERIMENTS WITH THE VERSATILE TOROIDAL FACILITY(VTF)  
TO INVESTIGATE IONOSPHERIC PLASMA TURBULENCE

Daniel T. Moriarty  
Graduate Student  
Nuclear Engineering Department  
Massachusetts Institute of Technology  
Cambridge, Massachusetts 02139

Abstract

Laboratory experiments with the Versatile Toroidal Facility (VTF) have been conducted to investigate plasma turbulence and effects on electromagnetic waves. These experiments are aimed at simulating the ionospheric plasma environment and cross-checking our ionospheric heating experiments at Arecibo, Puerto Rico. Reported here is some of the research Daniel T. Moriarty has conducted over the past five and half years under the supervision of Prof. Min-Chang Lee since his junior year at M.I.T. Dan Moriarty participated in the construction of VTF, which can generate magnetized plasmas with sharp density gradients and intense magnetic field-aligned currents. The VTF Plasmas thus have the key characteristics of the ionospheric plasmas, especially in the auroral region. The VTF plasma turbulence is structured with low-frequency wave modes which can be similarly produced by the sharp plasma density gradients and/or field-aligned currents in the ionospheric F region and in the topside ionosphere. The results of the VTF laboratory experiments are compared with those of the rocket experiments in space. We show that VTF can adequately simulate the naturally occurring plasma turbulence in the auroral ionosphere and complement the active plasma experiments in space.

---

**LABORATORY EXPERIMENTS WITH THE VERSATILE TOROIDAL FACILITY(VTF)**  
**TO INVESTIGATE IONOSPHERIC PLASMA TURBULENCE**

**Daniel T. Moriarty**

**1. Introduction**

In early 1989, Professors Min-Chang Lee and Ronald R. Parker proposed that a large plasma chamber be constructed at the Plasma Fusion Center, aimed at simulating the ionospheric plasma environment and cross-checking results of ionospheric plasma heating experiments at Arecibo, Puerto Rico. The construction of a toroidal plasma device, known as the Versatile Toroidal Facility (VTF) began in the summer of 1989 with a moderate budget.

Under the sponsorship of the Air Force Office of Scientific Research and the MIT Undergraduate Research Opportunities Program (UROP) office, the construction of VTF was made possible via two main sources. A majority of the construction materials - the main toroidal field magnets, the poloidal field support structures, and the multi-megawatt power supplies - were made available from discontinued fusion programs at the Oak Ridge National Laboratory (ISX-B machine) and the MIT Plasma Fusion Center (Tara Tandem Mirror machine). The second main resource was over 25 undergraduate and graduate students from various disciplines including electrical, mechanical, chemical, and nuclear engineering. Beginning as an undergraduate thesis student of Professor Min-Chang Lee, I installed the ohmic transformer or inner "torque cylinder".

One and half years later, the construction of VTF ended with VTF's first plasma, generated on New Year's Eve, 1990! Preliminary experiments began after the installation of diagnostics and an upgraded magnetron for Electron Cyclotron Resonance Heating (ECRH). Since 1991, I have designed several diagnostics including a computer controlled Langmuir probe and antenna array that provides plasma density and fluctuation spectra across the radius of the toroidal chamber. After completing a Master's Degree in Nuclear Engineering in 1992, I have continued ionospheric plasma chamber experiments on VTF to be included in my Ph.D. dissertation. The characteristics of VTF are illustrated in Section 2, showing how VTF can appropriately simulate ionospheric plasma environments, especially those of the auroral region. Described in Section 3 are our laboratory experiments conducted to investigate ionospheric plasma turbulence and its effects on radio wave propagation. The VTF experimental results are discussed and

compared with those of rocket experiments in Section 4. Finally, presented in Section 5 are discussions and conclusions.

## 2. Characteristics of VTF

The Versatile Toroidal Facility (VTF) has a large toroidal vacuum chamber with a major radius, minor radius, and height of 0.9 meters, 0.35 meters, and 1.1 meters, respectively. It has 18 electromagnets mounted around the chamber generating toroidal fields up to 0.5 Tesla. There are 48 access ports - 16 each on the side, top and bottom of the chamber - for plasma diagnostics. Vertical magnetic fields up to 40 Gauss can be superimposed on the intense toroidal fields to form a helical magnetic field in the chamber [C. Yoo, M.S.Thesis, M.I.T., 1989]. The generation of helical magnetic fields serves two purposes: (1) to increase the plasma confinement time up to a millisecond, and (2) to guide electric currents flowing throughout the plasma chamber.

VTF can produce plasmas by either injected microwaves or electron beams. Microwaves at a frequency of 2.45 GHz are injected from a 3 kW CW magnetron. Hydrogen, the typical fill gas, is leaked into VTF to a working pressure around  $7 \times 10^{-5}$  Torr. Steady state plasmas produced by the microwaves via ECRH can have a peak density on the order of  $10^{17} m^{-3}$ .

The VTF electron beam system may provide seconds-long plasmas with densities as high as ten times that of ECRH plasmas. The principal elements of the electron beam system are two  $LaB_6$  filaments installed at the bottom of the vacuum chamber. Each filament is heated to emit electrons that are subsequently accelerated by a 300 Volt potential applied between the filament and the vacuum chamber. Electrons flow upwards along the helical magnetic field producing field-aligned electric currents whose intensities can exceed 200 Amperes.

The geometry and characteristics of the VTF plasmas are delineated in Figures 1(a) and 1(b). Schematically shown in Figure 1(a) is the injection of microwaves and electron beams into the VTF plasma chamber. The density profile of the VTF plasmas produced by microwaves is illustrated in Figure 1(b). The peak density occurs at the location where the frequency of the incident microwave approximately matches the upper hybrid resonance frequency. Also illustrated in Figure 1(b) are magnetic field intensity and fractional density fluctuations versus the major radius of VTF. The helical magnetic field whose intensity is approximately equal to the toroidal field varies inversely with the major radius. Large fractional density fluctuations ( $> 10\%$ ) appear at the edges of the plasma density profile resulting from various plasma

instabilities driven by field-aligned electric currents and sharp density gradients, as discussed in Section 4.

Several features of the VTF plasmas can reasonably simulate the ionospheric plasma environment. For instance, the turbulent auroral ionosphere is characterized by a sharp density gradient in the north-south direction and intense field-aligned electric currents. This auroral plasma condition can be simulated well by the VTF plasmas which have sharp density gradients in the radial direction and field-aligned electric currents in the azimuthal direction. The helical magnetic field of VTF is ideal for the studies of whistler waves that can interact with not only magnetospheric plasmas but also prominently with ionospheric plasmas [Lee and Kuo, 1984 (a) & (b); Groves et al., 1988; Liao et al., 1989; Dalkir et al., 1992].

### 3. VTF Experiments

Early experiments were aimed at characterizing the VTF plasmas. In one instance plasma density profiles were determined via two separate diagnostic instruments: a Langmuir probe and an interferometer. However, considerable discrepancy was found between the locations of the upper hybrid resonance layer as determined by each probe separately [D.T. Moriarty, M.S. Thesis, M.I.T., 1992]. The primary experimental difficulty came from the presence of substantial interferometer signal fluctuations - noise. Compounding the problem was the reduced signal level along the test wave propagation path.

The decrease in signal to noise level may be due to several effects including antenna gain pattern, refraction, and turbulent scattering. The first two effects may be reduced by an antenna array for launching test waves as directed plane waves. However the effect of turbulent scattering in VTF is significant due to the presence of substantial density fluctuations. The incident diagnostic waves can be significantly scattered when  $\frac{\delta n}{n} \gg \frac{\rho_i}{L_n}$  where  $\frac{\delta n}{n}$  is the fractional density fluctuation,  $\rho_i$  is the ion Larmour radius, and  $L_n$  is the scale length of the plasma density gradients [Ott et al., 1980; Hui et al., 1981]. Using the following VTF parameters:  $L_n \sim 0.15m$  and  $\rho_i < 0.1mm$ , we find that turbulent scattering can be an important effect for wave propagation in the VTF plasmas if  $\frac{\delta n}{n} \gg 0.2\%$ . As mentioned before, the VTF plasmas possess large fractional density fluctuations that are estimated to exceed 10%.

Our subsequent experiments on plasma turbulence in VTF are aimed at investigating source mechanisms that cause the large fractional density fluctuations. The sharp density gradients and field-aligned electric currents are the potential sources of free energy generating plasma modes via instabilities. The excited plasma waves can be associated with intense density fluctuations. Because the VTF plasmas can simulate various ionospheric plasma environments, our investigation of VTF plasma turbulence is

conducive to the understanding of ionospheric plasma turbulence.

The scenario of our experiments is as follows. With a hydrogen gas fill pressure of  $7 \times 10^{-5}$  Torr, a toroidal magnetic field of 876 Gauss, 3 kW of microwaves at 2.45 GHz injected in the O-mode create a plasma with a peak density near  $7 \times 10^{16} m^{-3}$  at the location where the upper hybrid resonance frequency matches the microwave frequency. A typical microwave (RF) produced plasma density profile is shown in Figure 2(a). An electron beam generated by the heated  $LaB_6$  filament at the bottom of the chamber was accelerated by a potential of -300 V and guided by the helical magnetic field to form field-aligned currents flowing throughout the chamber. The electron beam can cause additional ionization, enhancing the plasma density by nearly a factor of ten. Figures 2(b) and 2(c) show beam plasma densities for low and high currents, respectively.

Langmuir probes together with a spectrum analyzer were used to measure the excited plasma modes. Figure 3 provides a wideband view of all measurable modes in VTF with both the electron beam and microwaves as the plasma sources. We should point out that the excited modes have a broad range of frequencies up to about half of the electron gyrofrequency. Displayed in Figure 4 are the low frequency spectra of plasma modes corresponding to 3 cases wherein different electric currents ( $I=0, 10, 100$  Amperes) were carried by the electron beam in addition to the injected microwaves. The ion plasma frequency ( $f_{pi}$ ), the lower-hybrid resonance frequency ( $f_{lh}$ ) and the ion gyrofrequency ( $f_{ci}$ ) are marked in the figure, typically having values of 57 MHz, 40 MHz and 1.3 MHz respectively. It is clear that low-frequency modes are favorably produced by intense field-aligned currents.

There are good reasons for us to speculate that several mechanisms play dominant roles in generating the spectra of the plasma modes in different frequency regimes. These mechanisms may be driven by field-aligned currents and/or sharp density gradients. For convenience, we divide the frequency spectra shown in Figure 3 into three regions labelled as (I), (II), and (III). Our spectral measurements indicate that “low-frequency” modes in region (I) can be preferentially excited at locations where sharp density gradients exist. By contrast, the excitation of the “medium-frequency” modes in region (II) and the “high-frequency” modes in region (III) is not sensitive to the density gradients. Spectral measurements of excited modes at different locations across the plasma were made with a radially scanning electrostatic probe. The spectra of excited modes as a function of major radius is displayed in Figure 5. These results corroborate our speculation that different mechanisms contribute additively to the excitation of plasma modes in different frequency regimes.

In order to determine the dimensions of the field-aligned currents, measurements of plasma density profile across the magnetic field were made in both the radial and vertical directions. Plasma density along the magnetic field is uniform. The dimensions of the currents were estimated to be 0.25 meters (radial direction) by 0.05 meters (vertical direction) at the location of a Langmuir probe. This information will be used in the next section to examine source mechanisms that generate the turbulent VTF plasmas.

#### 4. Comparison with Space Experiments

Experiments on the injection of electron beams into the ionosphere from sounding rockets or space shuttles have been conducted by several groups to investigate beam-plasma interactions and wave-particle interactions in the auroral region [e.g., Winckler et. al., 1984; Kellogg et al., 1986; Gurnett et al., 1986; Reeves et al., 1988; Winckler et al., 1989; Winglee and Kellogg, 1990; Ginet and Ernstmeyer, 1991]. These experiments have shed light on the production of ionospheric plasma turbulencd by auroral electron beams. The geometry of the rocket experiments we will discuss here [Winckler et al., 1984; Winckler et al. 1989; Ginet and Ernstmeyer, 1991] is shown in Figure 6.

A plasma diagnostics package abbreviated PDP for short in the figure has two orthogonal sets of electric probes in the spin plane of the payload. A fifth probe projects upward along the PDP spin axis. These probes consist of insulated rods terminating in spherical sensors coated with graphite. The main payload (denoted by MAIN) injected two independent electron beams: one (gun 2) at a constant pitch angle of  $100^\circ$  or  $110^\circ$  and the other (gun 1) with a pitch angle nearly parallel to the magnetic field. Gun 1 operated at 36 kV and 250 mA, and gun2 was swept from 40 kV to 8 kV with a corresponding current in each 1 ms interval.

Presented in Figures 7(a) and 7(b) are typical electric field power spectra measured on the PDP during beam injection at a pitch angle of  $110^\circ$  [Winckler et al., 1989; Ginet and Ernstmeyer, 1991]. The plotted spectra include four different measurements of  $E_x$  and  $E_y$  denoted by a dashed line, solid line, dot-dashed line, and dotted line. Here,  $E_x$  and  $E_y$  refer to the electric field components measured by the two orthogonal sets of electric dipole antennas (see Figure 6). The dashed line represents the Fourier transform of the DC  $E_y$  component measured over a 200 ms interval every 0.4 ms. The solid line is the Fourier transform of the VLF broadband receiver measurement of  $E_y$  sampled every 0.05 ms over 100 ms. The dot-dashed line is the  $E_x$  component measured by the high swept frequency analyzer (HSFA) with a frequency resolution of 30 kHz and a sweep time of 102 ms between 60 kHz and 5.5 MHz. A composite background spectrum constructed in the same manner from data taken when there was no beam injection is shown by a dotted

line.

Marked in Figure 7(b) on the top of the frame are the ion gyrofrequency ( $f_{ci}$ ), the lower hybrid resonance frequency ( $f_{lh}$ ), the ion plasma frequency ( $f_{pi}$ ), the electron gyrofrequency ( $f_{ce}$ ), the electron plasma frequency ( $f_{pe}$ ), and the upper hybrid frequency ( $f_{uh}$ ). Compare the date from space experiments with those recorded in our laboratory experiments as displayed in Figure 3 or Figure 5. It appears that they are quite similar. But careful examination of them as elucidated below indicates that different mechanisms operate in the space experiments and in the laboratory experiments.

First, high-frequency modes with frequencies exceeding the electron gyrofrequency ( $f_{ce}$ ) were not excited in our VTF plasmas, while they were present in the beam injection experiments in space. This difference arises from the fact that 36 keV electron beams were injected in space experiments, whereas 300 eV electron beams were produced in the VTF plasmas. Note that the thermal electron energy in the ionosphere and in the VTF are 0.1 eV and 5-8 eV, respectively. In fact, the 300 eV electron beams reduced their speeds to nearly the electron thermal speed at the location of the probe via the ionization of neutrals along the beam path to the top of the chamber. Thus, the low-energy electron beams are unable to excite Langmuir waves and upper hybrid waves in VTF. By contrast, whistler waves (viz. modes in the frequency range:  $f_{lh} < f < f_{ce}$ ) were produced in both space experiments and laboratory experiments possibly by the convective beam amplification of incoherent Cerenkov noise [Maggs, 1976].

One distinctive difference between the two experimental results is noted regarding the modes with frequencies near the lower hybrid resonance frequency ( $f_{lh}$ ). These modes were favorably excited in the ionospheric plasmas by energetic electron beams, presumably by the modified two stream instability [Ginst and Ernstmeyer, 1991]. But the electron beams injected into VTF were not intense enough, as explained before, to cause the modified two stream instability. Although the modes at  $f_{lh}$  were not so highly peaked in the VTF plasmas, excited modes with frequencies adjacent to  $f_{lh}$  are clearly seen in Figure 4.

The other distinctive difference is noted regarding the low-frequency modes whose frequencies are less than the ion gyrofrequency ( $f_{ci}$ ). One can see from Figures 7(a) and 7(b) that the ionospheric plasmas had large thermal noises in the low-frequency band (region I) and the medium-frequency band (region II). The energetic electron beams injected into the ionosphere cannot excite the low-frequency modes significantly, whereas prominent excitation of these modes occurs in the VTF plasmas.

The characteristics of the excited waves by injected electron beams in the ionosphere and in VTF can

be summarized as follows. Langmuir waves, upper hybrid waves, whistlers, and lower hybrid waves can be excited by energetic electron beams in the ionospheric plasmas. In the VTF plasmas, the injected electron beams produce whistler waves and especially low-frequency modes with frequencies less than the lower hybrid resonance frequency ( $f_{lh}$ ) and even the ion gyrofrequency ( $f_{ci}$ ).

## 5. Discussions and Conclusions

We pointed out earlier that the VTF was constructed to simulate the ionospheric plasma environment. Then how can we explain the discrepancies between the results of space experiments and those of VTF laboratory experiments? The excitation of high-frequency modes (i.e. Langmuir waves and upper hybrid waves) depends on the energy of the electron beams, as discussed before. This offers a reasonable explanation for the discrepancy only in the high-frequency regime of the wave spectra.

We believe that the discrepancy in the low-frequency regime of the spectra stems from the different background plasma environments. This fact can be understood from Figure 6. In the space experiments, the sounding rocket carried the electron guns as its main payload and the electric field probes on a plasma diagnostic package (PDP). During the experiments, the PDP separated at 1.5 m/s relative to the main payload. Thus the electron beam-plasma interactions and their subsequent diagnoses were carried out in a rather small ionospheric region which can be reasonably considered to be a uniform plasma. Furthermore, the electron temperature and ion temperature are approximately equal in the ionospheric region where the rocket experiments were conducted.

By contrast, the VTF plasmas created by microwaves and/or electron beams have sharp density gradients across the magnetic field. They also have hot electrons but relatively cold ions. Hence, the VTF plasmas are inhomogeneous and have a large ratio of electron temperature ( $T_e$ ) to ion temperature ( $T_i$ ). Sharp density gradients and large  $T_e/T_i$  together with field-aligned electric currents are the important sources of free energy to excite ion acoustic waves and very low-frequency modes as explained below.

Kindel and Kennel (1971) suggest that field-aligned currents in the topside ionosphere can excite plasma turbulence that may have the structure of electrostatic ion cyclotron waves (i.e., obliquely propagating ion Bernstein waves) and ion acoustic waves. Both kinds of waves can be favorably excited by electric currents with drift velocities smaller than the electron thermal velocity in plasmas with  $T_e/T_i \geq 1$ . The damping increment of the ion cyclotron waves is quite small even if the ion temperature is comparable to the electron temperature. This contrasts the ion acoustic waves which are highly damped when  $T_i \approx T_e$ .

Kindel and Kennel [1971] showed that when  $T_e/T_i \gg 1$ , say, 10, the threshold drift speed of the ion acoustic instability would be much less than that of the ion cyclotron instability. In the VTF plasmas, the electron drift velocity ( $\sim 5 \times 10^4$  m/s) is less than the electron thermal velocity ( $\sim 4 \times 10^6$  m/s) and the ion acoustic velocity ( $\sim 4 \times 10^5$  m/s). However, the  $(T_e/T_i)$  of the VTF plasmas is estimated to be greater than 20. Therefore, the ion acoustic waves can be favorably excited in the VTF plasmas. It is probably difficult to excite ion acoustic waves in the ionosphere where  $T_e \simeq T_i$ , as seen in Figures 7(a) and 7(b).

The current convective instability was proposed by Ossakow and Chaturvedi [1979] as a potential mechanism to produce plasma turbulence with low-frequency modes in the auroral ionosphere. The auroral ionospheric plasma has a large density gradient in the horizontal plane (i.e., the North-South direction) and field-aligned currents flowing in the vertical direction. This plasma environment can be reasonably approximated by the VTF plasmas which have sharp density gradients in the radial direction and field-aligned currents in the azimuthal direction. Using the following VTF parameters:  $T_e = 8$  eV,  $T_i = 0.1$  eV,  $f_{ce} = 2.45$  GHz,  $f_{ci} = 1.3$  MHz,  $I = 10$  Amperes,  $L = n(\delta n)^{-1} = 0.1$  m,  $A$  (beam c/s) =  $0.25$  m  $\times$   $0.05$  m, and  $k_{parallel}/k_{perpendicular} = 10^{-3}$ , we find from Ossakow and Chaturvedi [1979] that the growth time of the convective instability in VTF is 0.1 msec. It indicates fast excitation of the current convective instability in the VTF plasmas in comparison with the 1 ms confinement time. The frequencies of the excited modes are  $kV_d$ , where the electron drift velocity ( $V_d$ ) is  $5 \times 10^4$  m/s, which is less than the ion acoustic wave velocity,  $V_s \sim 4 \times 10^5$  m/s. We expect that the frequencies ( $kV_s$ ) of the excited ion acoustic waves are greater than those ( $kV_d$ ) of the low-frequency modes excited by the current convective instability for two reasons. One is that  $V_d < V_s$ . The other is that the current convective instability [Ossakow and Chaturvedi, 1979] and the ion acoustic instability [Kindel and Kennel, 1971] excite preferentially large-scale (i.e., small  $k$ ) modes and short-scale (i.e., large  $k$ ) modes, respectively. Thus, modes with frequencies less than the ion gyrofrequency ( $f_{ci}$ ) were basically excited by the current convective instability in the VTF. As mentioned before, in the space experiments, the beam-plasma interactions occurred in a rather small region of the ionosphere. Hence, the beam-plasma interaction region in space experiments can be modelled as a uniform background plasma and, consequently, the current convective instability does not occur.

Comparison of our VTF experiments with space experiments have shown that we can simulate several features of the electron beam injection experiments in space plasmas. However, we can more closely simulate the naturally occurring plasma turbulence in the auroral ionosphere. The latter was one of our original goals in constructing VTF. Our other goal is to cross-check our ionospheric (EM wave) plasma

heating experiments at Arecibo, Puerto Rico with VTF. This work, not mentioned here, will be reported in the future.

In conclusion, I have discussed some of our laboratory experiments with the Versatile Toroidal Facility (VTF) aimed at investigating ionospheric plasma turbulence. I participated in the construction of the VTF beginning my junior year and later completed my Bachelor's thesis. The subsequent design of plasma diagnostic instruments and experiments on wave propagation in the turbulent VTF plasmas constituted my Master's thesis research. The current work on the laboratory studies of plasma turbulence is part of my Ph.D. research effort. The accumulated research results reported here have demonstrated that the VTF plasma device is capable of simulating some characteristic features of ionospheric plasma turbulence. Although the parameters of the VTF plasmas are quite different from those of ionospheric plasmas, our work has shown that laboratory experiments can adequately study some processes responsible for space plasma phenomena and thus complement the active experiments in space.

## References

- Dalkir, Y.R., M.C. Lee, and K.M. Groves, A mechanism responsible for the observation of symmetric lower hybrid sidebands and a low frequency mode in the upper ionosphere, *J. Geophys. Res.*, 97, 17195, 1992.
- Ginet, G.P., and J. Ernstmeyer, VLF plasma waves generated by an electron beam in space, *Physics of Space Plasmas*, SPI Conference Proceedings and Reprint Series, Cambridge, Massachusetts, Number 11, 209, 1991.
- Groves, K.M., M.C. Lee, and S.P. Kuo, Spectral broadening of VLF signals traversing the ionosphere, *J. Geophys. Res.*, 93, 14683, 1988.
- Gurnett, D.A., et. al., Whistler mode radiation from the Spacelab 2 electron beam, *Geophys. Res. Lett.*, 13, 225, 1986.
- Hui, B., et. al., Scattering of electron cyclotron resonance heating waves by density fluctuations in tokamak plasmas, *Nucl. Fusion*, 21, 339, 1981.
- Inan, U.S., et. al., Modulated beam injection from the space shuttle during magnetic conjunctions of STS 3 with the DE 1 satellite, *Radio Sci.*, 19, 487, 1984.
- Kellogg, P.J., S.J. Monson, W. Bernstein, and B.A. Whalen, Observations of waves generated by electron beams in the ionosphere, *J. Geophys. Res.*, 91, 12065, 1986.
- Lee, M.C., and S.P. Kuo, Production of lower hybrid waves and field-aligned plasma density striations by whistlers, *J. Geophys. Res.*, 89, 10873, 1984.
- Liao, C.P., J.P. Freidberg, and M.C. Lee, Explosive spread F caused by Lightning-induced electromagnetic effects, *J. Atmos. Terr. Phys.*, 51, 751, 1989.

Maggs, J.E., Coherent Generation of VLF Hiss, *J. Geophys. Res.*, 81, 1707, 1976.

Moriarty, D.T., *Electron cyclotron range of frequencies propagation in critically dense cold magnetoplasmas*, M.S. Thesis, M.I.T. Nuclear Engineering Department, 1992.

Ossakow, S.L., and P.K. Chaturvedi, Current convective instability in the diffuse aurora, *Geophys. Res. Lett.*, 6, 332, 1979.

Ott, E., Hui, B., and Chu, K.R., Theory of electron cyclotron resonance heating of tokamak plasmas, *Phys. Fluids*, 23, 1031, 1980.

Kindel, J.M., and C.F. Kennel, Topside current instabilities, *J. Geophys. Res.*, 76, 3055, 1971.

Reeves, G.D. et al., VLF wave emissions by pulsed and DC electron beams in space: 1. Spacelab 2 observations, *J. Geophys. Res.*, 93, 14699, 1988.

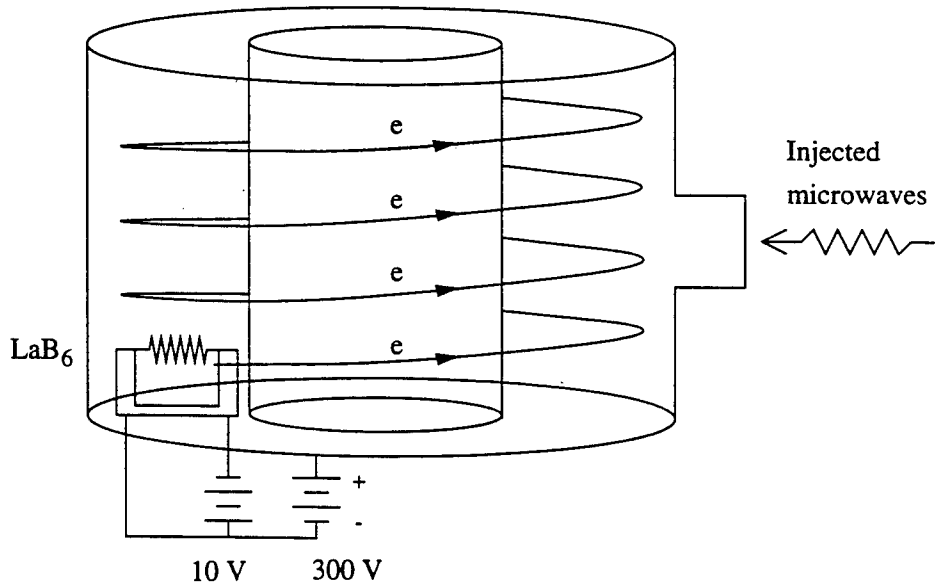
Winckler, J.R. et. al., Ion resonances and ELF wave production by an electron beam injected into the ionosphere: ECHO 6, *J. Geophys. Res.*, 89, 7565, 1984.

Winckler, J.R. et al., ECHO 7: An electron beam experiment in the magnetosphere, *EOS Trans. AGU*, 70, 657, 1989.

Winglee, R.M., and P.J. Kellogg, Electron beam injection during active experiments: 1. Electromagnetic wave emissions, *J. Geophys. Res.*, 95, 6167, 1990.

Yoo, C., *Plasma confinement optimization of the Versatile Toroidal Facility for ionospheric plasma simulation experiments*, M.S. Thesis, M.I.T. Nuclear Engineering Department, 1989.

(a)



(b)

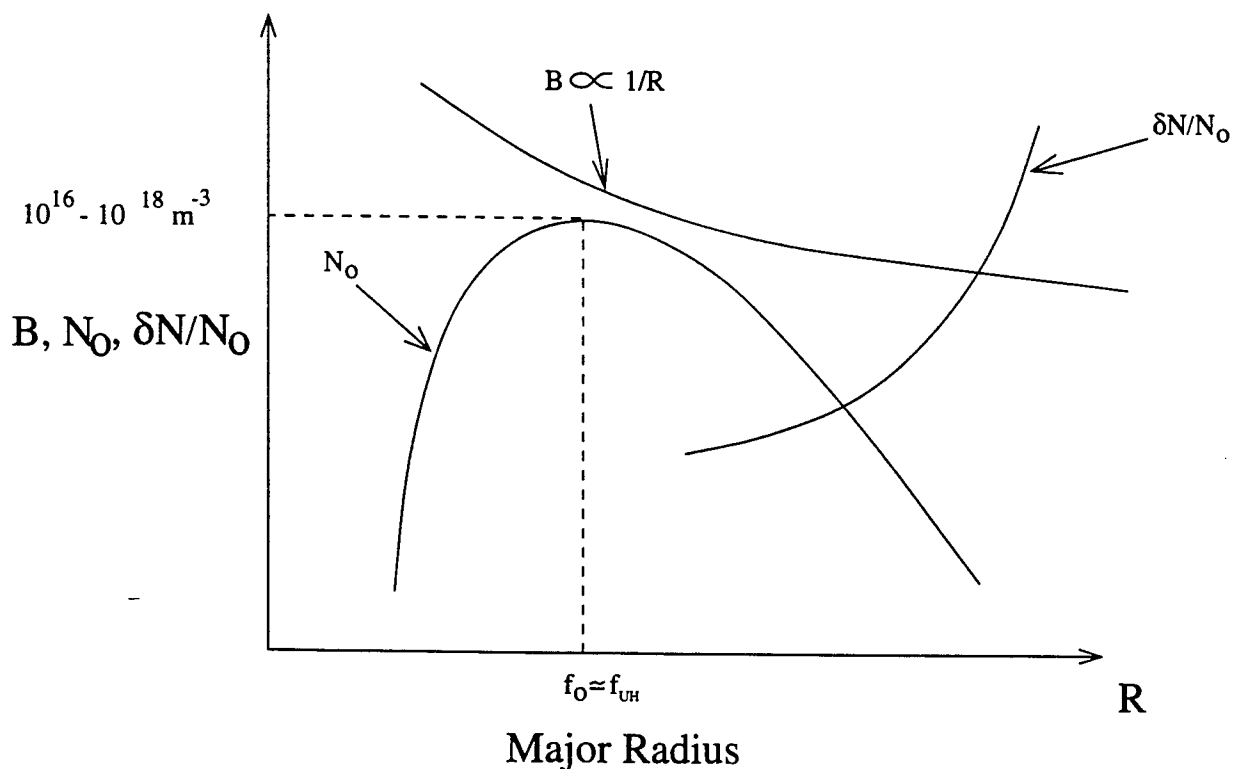
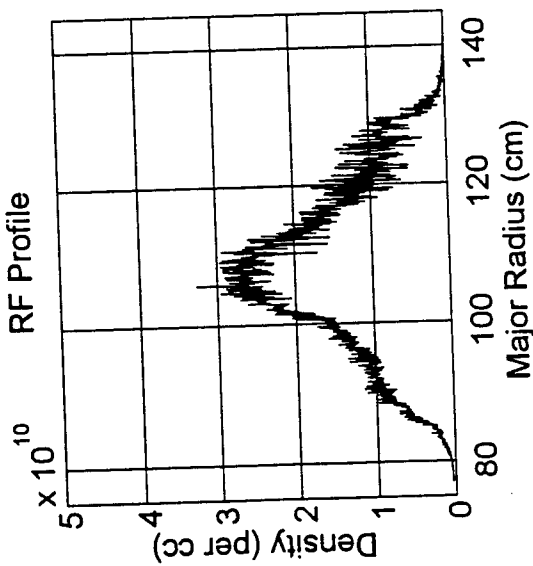
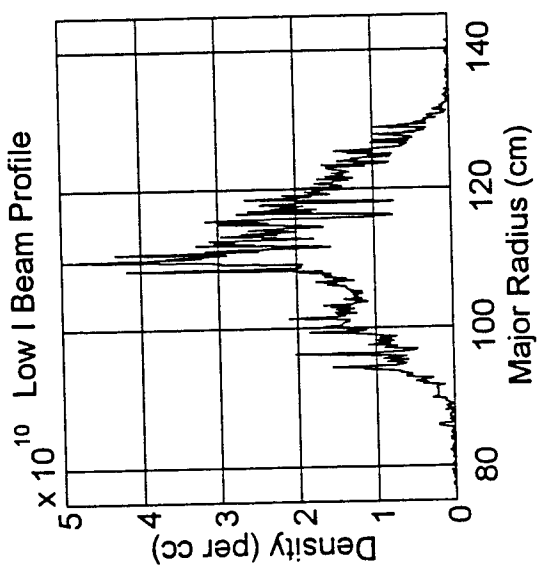


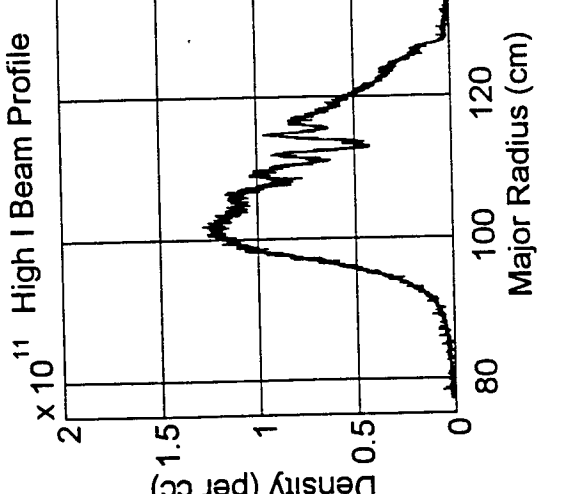
Figure 1 (a) Injection of microwaves and electron beams into VTF;  
1 (b) Density profile, magnetic field, and fractional density fluctuations in VTF.



(a)



(b)



(c)

Figure 2(a) Microwave-produced plasma density profile in VTF;  
 2(b) Electron beam produced plasma density profile with lowe electric current;  
 2(c) Electron beam produced plasma density profile with high electric current.

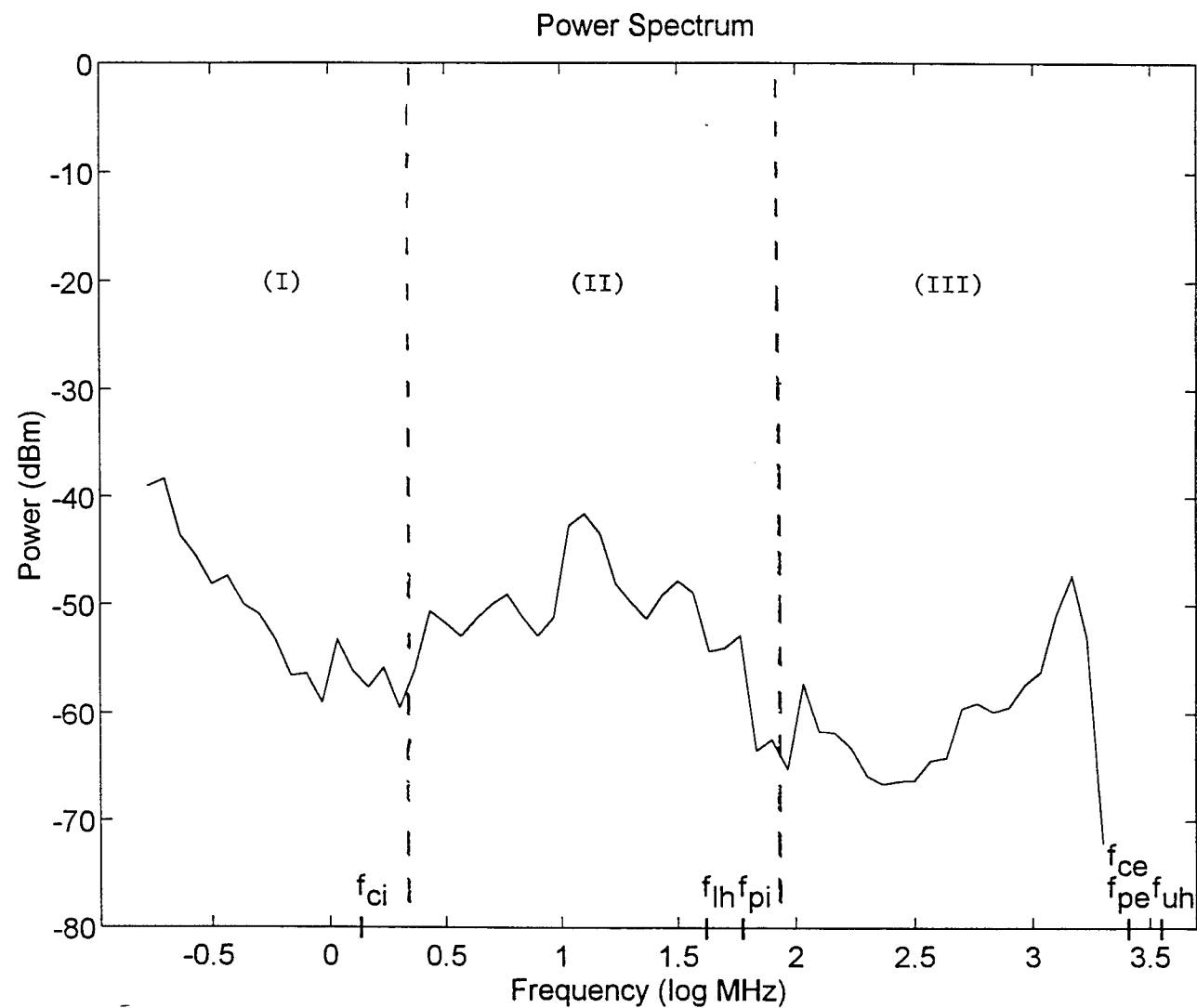


Figure 3. Spectra of plasma modes measured in the turbulent VTF plasmas produced by both the injected microwaves and electron beams. Marked with (I), (II), and (III) are regions representing low-frequency, medium-frequency, and high-frequency regimes.

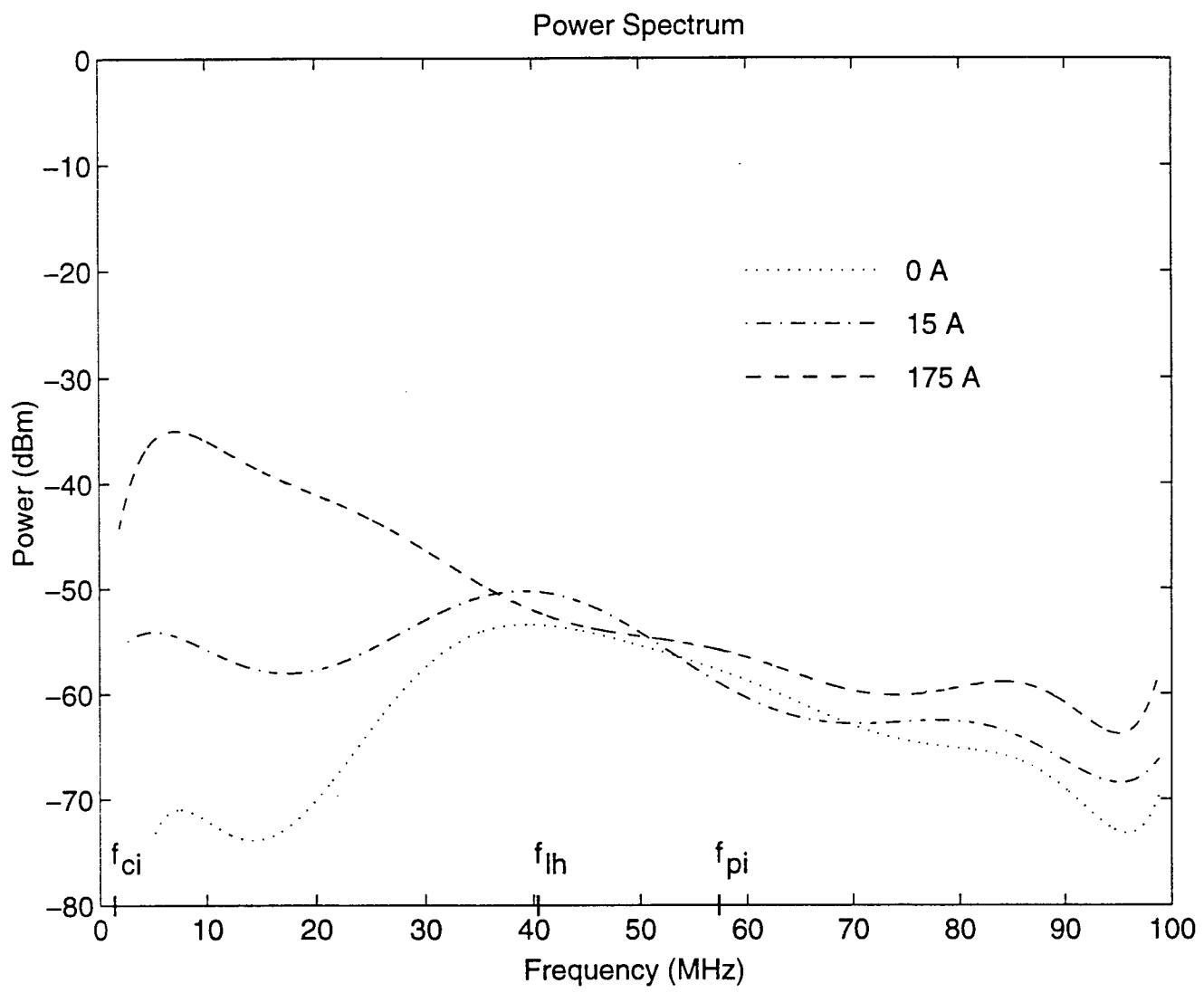


Figure 4. Illustration of excitation of lower frequency modes (primarily region (II), see Figure ) by electric currents with different intensities.

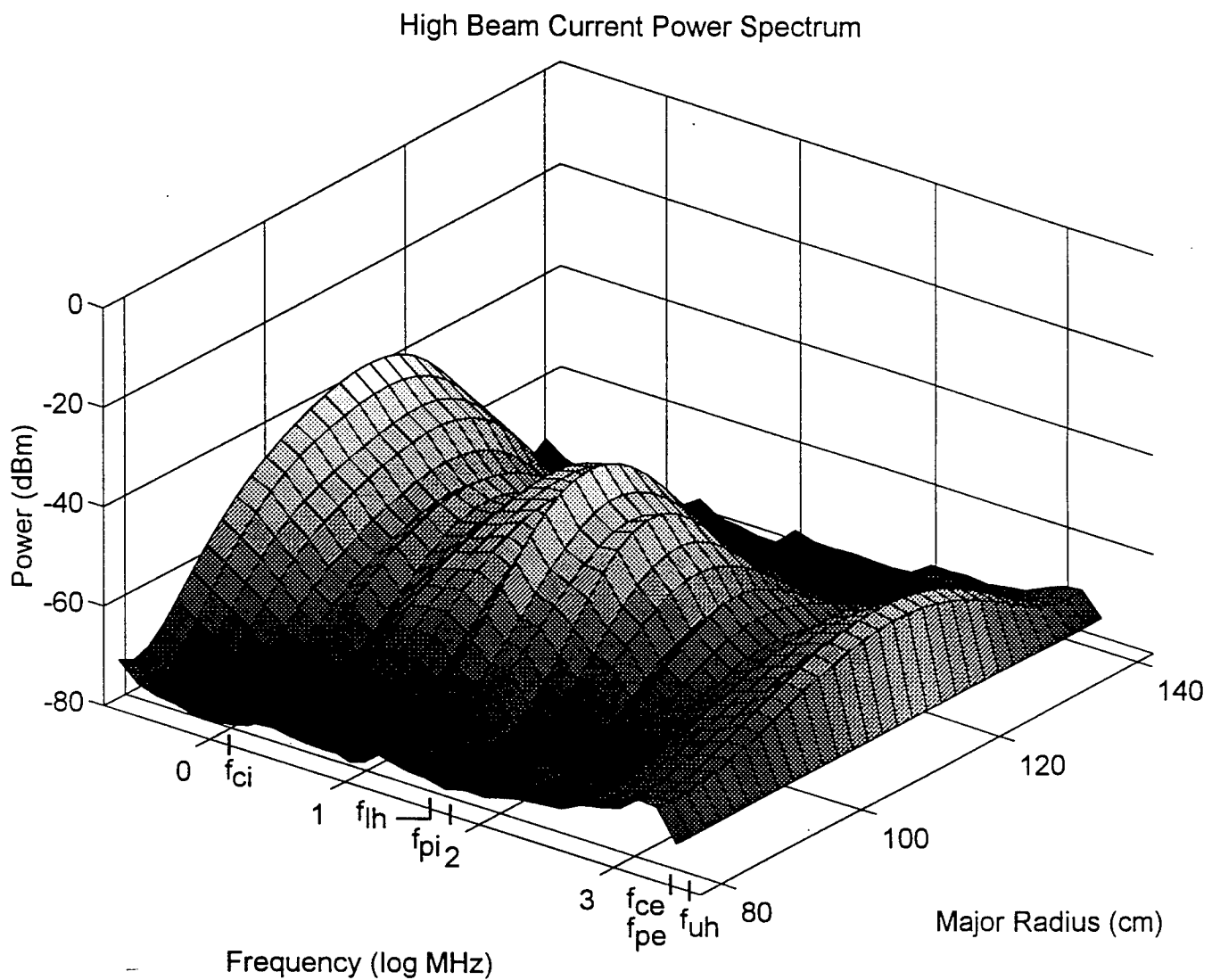


Figure 5. Spectra of excited modes in VTF as a function of major radius of the toroidal plasma chamber.

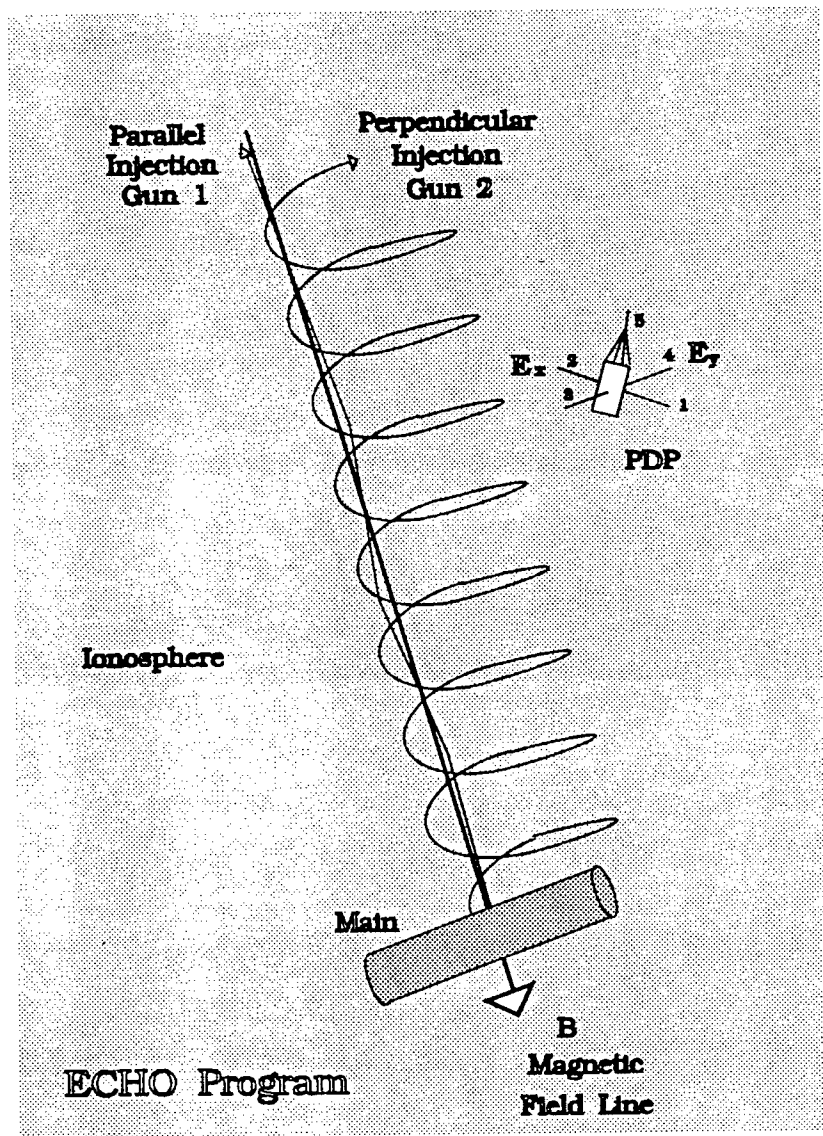


Figure 6 Geometry of electron beam injection experiments in space with a rocket which has five electric probes on a plasma diagnostics package (PDP) and two electron guns on the main payload (MAIN) (Winckler et al., 1984).

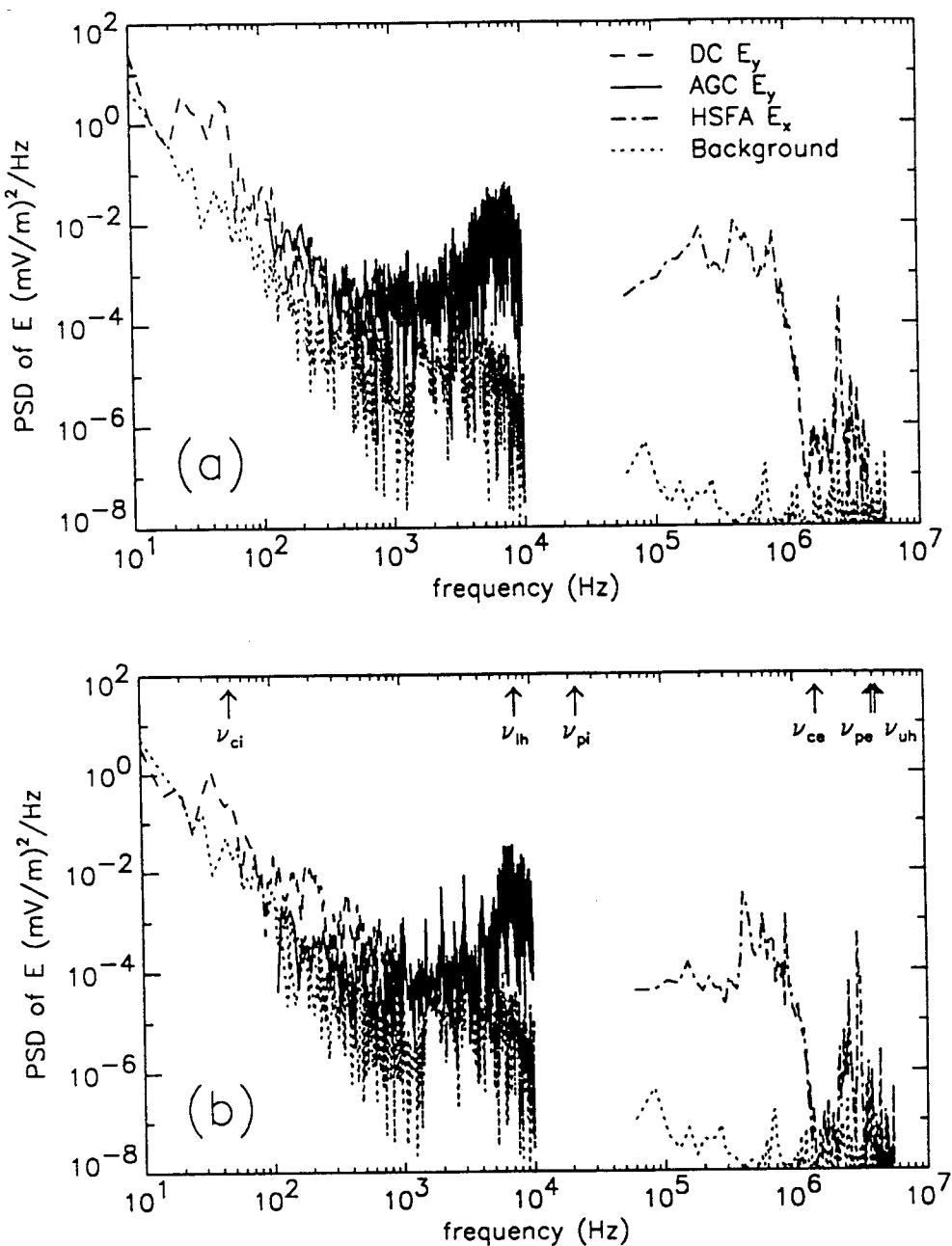


Figure 7 . Typical electric field power spectra measured on the PDP associated with a 250 mA beam pulse injected at a pitch angle of  $110^\circ$  where (a) the beam energy is constant at 36 keV, and (b) the beam energy is swept through the range 40-8 keV every 1 ms (Ginet and Ernstmeier, 1991).

# **SYNCHRONIZATION USING CONTROL:**

## **CHAOTIC DIODE RESONATORS**

Timothy C. Newell

Department of Physics  
University of North Texas  
North Texas Station, Denton, TX 76203-5368

Final Report for:  
Graduate Student Research Program  
Nonlinear Optics Center  
Phillips Laboratory

Sponsored by:  
Air Force Office of Scientific Research  
Bolling Air Force Base, Washington DC

August 1994

---

## SYNCHRONIZATION USING CONTROL: CHAOTIC DIODE RESONATORS

Timothy C. Newell

Department of Physics

University of North Texas

North Texas Station, Denton, TX 76203-5368

### Abstract

Investigations of the synchronization of chaos by control process [Y.C. Lai and C. Grebogi Phys. Rev. E **47** 2357 (1993).] as applied to diode resonators are presented. It is shown that required synchronizing factors may be obtained from a time series of the resonator. Calculations made of the global and local Lyapunov multipliers of the dynamical system show that synchronizing perturbations force these multipliers to be less than one. When the global Lyapunov multiplier is forced less than one, synchronization of chaos will occur.

# SYNCHRONIZATION USING CONTROL: CHAOTIC DIODE RESONATORS

Timothy C. Newell

## I. INTRODUCTION

The Ott, Grebogi, and Yorke (OGY) [1] proposition to control the unstable periodic orbits has been successfully tested in mechanical [2], electric [3], laser [4,5], and chemical [6] dynamical systems. A natural extension of OGY is to implement the theme of *control* to stabilize one chaotic orbit about another. This synchronization technique was proposed by Lai and Grebogi [7]. The goal of synchronization using control is to make a minute perturbation to an existing dynamical parameter of a slave system in order to stabilize its orbit about a free operating chaotic master system. To generate the stabilizing feedback, we first identify the stable and unstable manifolds of the chaotic dynamical system ( $f_s$  and  $f_u$ ) which, in general, will rotate in some manner governed by the underlying dynamics of the system as the orbit wanders along the attractor. This requires some knowledge of the mapping so that a small circle of points can be propagated forward in time in order to estimate this unstable direction [7,8]. Next, we need an estimation of the Jacobian matrix of the map ( $D\mathbf{F}$ ) and the derivative of the map with respect to the parameter to be modulated ( $D_p\mathbf{F}$ ). These latter two terms are iterate dependent since they depend on the current value,  $\mathbf{x}_n$ , of the master orbit. The perturbation necessary to synchronize a slave signal  $\mathbf{y}_n$  to a master signal  $\mathbf{x}_n$  is given by

$$\delta p_n = \frac{[D_y\mathbf{F}(\mathbf{y}, p) \cdot \{\mathbf{y}_n - \mathbf{x}_n(p_0)\} \cdot f_{u(n+1)}]}{-D_p\mathbf{F}(\mathbf{y}, p) \cdot f_{u(n+1)}} \Big|_{\mathbf{y}=\mathbf{x}, p=p_0}, \quad (1.1)$$

where in the above, only the derivative terms are evaluated at  $\mathbf{y} = \mathbf{x}, p = p_0$ . This formula is derived by expanding the chaotic slave orbit  $\mathbf{y}_n$  locally about the master orbit  $\mathbf{x}_n$  and

requiring that the next iteration of  $\mathbf{y}_n$ , after falling into a small neighborhood around  $\mathbf{x}_n$ , lie on the stable direction of  $\mathbf{x}_{n+1}(p_0)$ , i.e.  $[\mathbf{y}_{n+1} - \mathbf{x}_{n+1}(p_0)] \cdot \mathbf{f}_{u(n+1)} = 0$ . In principle the perturbation is to be applied whenever it is a small fraction of the unperturbed parameter. Hence, one should not apply the feedback if the separation between the two orbits is large or the denominator of Eq. 1.1 is small.

The physical interpretation of this formula is straightforward. The proximity of the slave orbit to the master is amplified by a factor which is directly dependent on the magnitude of the instability in the unstable direction and inversely dependent to the sensitivity of the map to a variation in the dynamical parameter. Naturally, the greater the instability the larger the perturbation factor must be. Also, a map with a sensitive dependence to the dynamical parameter requires a relatively small perturbation.

In section II we describe the dynamics of the nearly 1-dimensional diode resonator. In section III we show so that in the 1-dimensional case, the iterate dependent feedback factor can be obtained from a scalar time series of the resonator. In section IV the ability of the resonator to synchronize using the prescribed iterate dependent term is analyzed by means of Lyapunov multipliers. The main points are summarized and a conclusion is drawn in section V.

## II. THE DIODE RESONATOR

Our system of interest is the diode resonator composed of a 1N4004 silicon rectifier diode, a  $33mH$  inductor (DC resistance  $243\Omega$ ), and a  $90.5\Omega$  resistor in series. The circuit is sine wave driven at a frequency of  $70kHz$ . The diode and inductor give rise to the nonlinear resonator while the resistor influences the quality factor,  $Q$ , of the resonator and provides a convenient method of measuring the chaotic current.

The dynamical system can be numerically modeled by an application of Kirchoff's laws.

The inductor and resistor combination is straightforward while the rectifier diode can be represented as an ohmic resistance in series with a parallel nonlinear resistor and nonlinear capacitors [9,10]. The voltage drop of the model circuit is given by:

$$V_o \sin \omega t = V + L \frac{dI}{dt} + I(R + R_s) \quad (2.1)$$

where  $V_o$  is the amplitude of the drive wave,  $V$  is the voltage drop across the resistor,  $L$  is the inductance,  $I$  is the total current through the circuit,  $R$  is the inline resistance, and  $R_s$  a small added resistance to take into account an ohmic element to the diode. From the conservation of current,

$$I = I_d + I_{c_d} + I_{c_t} \quad (2.2)$$

where  $I_d$  is the current through the nonlinear resistor branch,  $I_{c_d}$  and  $I_{c_t}$  are currents in nonlinear capacitances described below. The capacitor currents can be expressed in terms of a differential equation for the voltage by:

$$(C_d + C_t) \frac{dV}{dt} = I_{c_d} + I_{c_t}. \quad (2.3)$$

Here  $C_d$  and  $C_t$  are nonlinear capacitances.

The nonlinear resistance describes the well known current-voltage characteristics of the diode and is given by the Shockley equation

$$I_d = I_s [\exp(eV/nkT) - 1] \quad (2.4)$$

where  $I_s$  is the reverse bias saturation current,  $e/kT$  is the thermal voltage, and  $n$  is an emission coefficient implemented to take into account carrier recombination in the depletion zone.

The capacitance terms are modeled from a consideration of the applied AC signal. Charge carrier recombination near the  $p-n$  junction creates a depletion region populated primarily

by immobile charges. The fixed charges create a junction potential which, under no applied signal, induces a carrier drift that exactly balances their thermal diffusion. When a forward voltage is applied, charge is injected into the diode, builds up nearby the depletion region, and is moved into the depletion region thus shrinking its width. This variance of the depletion region due to the applied voltage causes a depletion (or space-charge) capacitance which can be thought of as a parallel plate capacitance with a voltage dependent width. While the diode is reversed biased, this term is given by:

$$C_t = C_b \left(1 - \frac{V}{V_J}\right)^{-m}, \quad (2.5)$$

where  $V_J$  is the junction potential,  $C_b$  is the zero voltage bias capacitance and  $m$ , a grading coefficient, refers to the variation of the doping concentration across the  $pn$  junction. Since this term would become infinite when  $V = V_J$ , it is used whenever  $V < \frac{V_J}{2}$ . A forward bias modification of the capacitance applied whenever  $V \geq \frac{V_J}{2}$  is

$$C_t = C_b \left( \frac{b_1 + \frac{mV}{V_J}}{b_2} \right) \quad (2.6)$$

where  $b_1$  and  $b_2$  are parameters to ensure continuity of the capacitance,  $b_1 = 0.5^{(1+m)}$  and  $b_2 = 1 - \frac{1}{2}(1+m)$ . The latter formula is derived from a curve fit to experimental data and is valid as long as the forward applied voltage is not excessively high.

In addition to the space-charge capacitance, a second capacitive effect arises when the finite response time of the mobile charge to the changing field is considered. Since the diode cannot respond immediately to injected charge, a charge build up occurs in the vicinity of the depletion region. The charge build up,  $Q$ , is proportional to the injected current,  $I$

$$Q = \tau I \quad (2.7)$$

where the proportionality factor,  $\tau$ , describes the amount of time it takes the majority carriers to cross the  $p$ -type or  $n$ -type material. The variance of this charge with respect to the voltage defines this capacitance, viz.

$$C_d = C_o e^{\frac{eV}{nkT}} \quad (2.8)$$

When the nonlinear terms are inserted into the equations of Kirchoff's laws, the resulting dynamical equations can be integrated in time to produce an accurate model of the physical resonator. The modelled results are in good agreement with that observed experimentally.

### III. SYNCHRONIZING THE DIODE RESONATOR

The goal is to apply the synchronization algorithm to the case of two diode resonators which are operating chaotically. From the two chaotic dynamical variables, current ( $I$ ) and voltage drop across the diode ( $V_d$ ), we select the current through the resonator as the observable signal. This is measured as the voltage drop across the resistor element,  $V^M(t)$ , of the resonator. (Note that the superscript  $M$  refers to the master resonator and  $S$  to the slave.) Since the amplitude chaotic resonator is driven with a defined frequency, it is logical to evaluate the feedback at the peaks of the current and modulate the amplitude of the drive wave for some fraction of the known period. Thus we rename the iterative dependent factor as a peak dependent factor so that  $\Delta p_n \rightarrow \Delta p[t_p(n)]$  where  $t_p(n)$  refers to the time of occurrence of the  $n$ th peak.

The next step is to determine the desired feedback  $\Delta p[t_p(n)]$ . Because the diode resonator can be shown to have a one dimensional attractor, the peak dependent formula reduces to a 1 dimensional calculation. Next the voltage drop across the diode,  $V_d$ , for both master and slave resonator is virtually identical at 0.7V on the current peaks since the diodes are forward biased. Hence  $V_d^S - V_d^M$  is considered negligible with respect to the current. We therefore need only the difference in the voltage drops across the resistors,  $V^S(t) - V^M(t)$  to calculate the perturbation. Applying these conclusions to the feedback formula yields a much simpler factor to calculate. The unstable eigenvector,  $f_u$ , cancels in the numerator and denominator. The Jacobian matrix becomes scalar. The shift of the map with respect

to a variation in the drive amplitude is also one dimensional. By combining the above, the feedback factor becomes

$$\Delta p = -\frac{\partial F_1}{\partial V^M} \frac{\partial F_1^{-1}}{\partial p} [V^S(t_p) - V^M(t_p)]. \quad (3.1)$$

In the above,  $F_1$  refers to the 1 dimensional Jacobian term. Thus we need to calculate and apply in real time the ratio of the Jacobian matrix to the shift. This can be accomplished using the first return maps. Fig. 1 displays two return maps taken at a drive amplitude of  $4.6V$  and  $5.1V$  respectively. Since each return map is composed of approximately 300 points and are contaminated by noise a curve fit is interpolated so as to average the fluctuations in nearby points. Both return maps are divided into four sections so as to create a piecewise continuous curve and a low order polynomial curve fit is determined for each section.

For the 1-dimensional consideration of this system, the slope of the return map at each point is the Jacobian evaluated at that point. This can be shown by differentiation of the map

$$v_{n+1} = F(v_n) \quad (3.2)$$

with respect to  $v_n$  which leads to the 1-dimensional Jacobian

$$\frac{\delta v_{n+1}}{\delta v_n} = \frac{\delta F(v_n)}{\delta v_n} \equiv DF. \quad (3.3)$$

The shift of the map,  $D_p F$ , is obtained from the first return map of the resonator by considering how the return map reacts to a perturbation applied to the amplitude of the drive voltage. For a driving voltage  $V_0$ , we look at how the point  $x_n(V_0)$  is mapped into  $x_{n+1}$ . Then at a slightly higher voltage,  $V_0 + \delta$ , we look at how the same point,  $x_n(V_0)$  is mapped into the new point  $x_{n+1}(V_0 + \delta)$ . The shifting is seen in Fig. 1; the  $5.1V$  return map has slid along the upper branch of the  $4.6V$  map. The experimental approximation for the shift is then

$$D_p F \approx \frac{[x_{n+1}(V_0 + \delta) - x_{n+1}(V_0)]}{\delta}. \quad (3.4)$$

Since we are using a shift large enough to prevent the return maps from overlapping, we see that the highest points along the abscissa of the  $5.1V$  map have no correspondence on the  $4.6V$  map, and the lowest abscissa points of the  $4.6V$  map have no corresponding points on  $5.1V$  map. A meaningful approximation for  $D_p F$  is made only for points which occur on both maps. For the periphery points, we extrapolate  $D_p F$ .

The 1-dimensional iterate dependent amplification factor is the negative of the quotient of the two above terms. Fig. 2(a) plots the result of the calculation versus the peaks of  $V^M(t)$ . While both branches of the lower folded region produce a relatively constant factor, in the upper region the factor drops off rapidly. The diode resonator shifts along an axis almost parallel to the upper branch and the shift,  $D_p F$ , approaches zero. Hence the feedback factor becomes quite large. It is not possible to apply the exact feedback perturbation since the large amplification of the unavoidable noise along with any differences in  $V^S(t)$  and  $V^M(t)$  would unacceptably over modulate the drive wave. A numerical calculation of the feedback factor, shown in Fig. 2(b), displays a similar shape, but does not drop off as drastically. When the infinities occur, one either chooses to not apply feedback or approximate the feedback from the nearby regions. Finally it must be pointed out that this type of analysis is applicable because of the simple shape of the return map for the diode resonator.

On inspection of the return maps, one remarks that the slope of the lower branches is greater than unity while the slope of the upper section is less than one. It follows from the linearized dynamics of the one dimensional system that the lower section is unstable; nearby orbits in this region are divergent. On the other hand, the upper branch is stable and adjacent orbits here should remain temporarily adjacent until the phase space trajectory wanders into the unstable regime. The salient feature to capitalize is that a feedback perturbation need only be applied when the system is in an unstable region of the attractor.

In the stable regions, the magnitude of the Jacobian is less than one and the feedback factor should become unnecessary. Therefore, synchronization should be possible if feedback is only applied when the Jacobian is greater than one. For the diode resonator, this means that if feedback is applied only when the voltage peaks are less than 48mV synchronization can occur. In the critical regions of the attractor below 48mV, this factor is constant (see Fig. 2(a)).

#### IV. EFFECT OF THE FEEDBACK PERTURBATION ON THE LYAPUNOV MULTIPLIERS

An understanding of the ability for systems to synchronize can be gained by computing the Lyapunov multipliers (or exponents) *locally* as well as *globally*. The often used global Lyapunov multipliers quantify the average instability of the entire phase space to small perturbations. Local Lyapunov multipliers, on the other hand, characterize instabilities of the attractor along small sections of the orbit. They are dependent on the location of the evaluated point and provide detailed information about the regional stability of the attractor. [11]

Lyapunov exponents are determined by considering the evolution of an infinitesimal displacement,  $\vec{y}_n$ , from some initial point,  $\vec{x}_n$ . A linearization of the mapping yields the resulting displacement,  $\vec{y}_{n+1}$

$$\vec{y}_{n+1} = DF(\vec{x}_n) \cdot \vec{y}_n \quad (4.1)$$

where DF is the Jacobian matrix of the mapping function. The direction of the displacement is given by  $\vec{y}_n/|\vec{y}_n|$  while the magnitude is given by

$$m_n = \frac{|\vec{y}_{n+1}|}{|\vec{y}_n|}. \quad (4.2)$$

The value  $m_n$  is referred to as the local Lyapunov multiplier (LLM). It expresses the amount of growth ( $m_n > 1$ ) or contraction ( $m_n < 1$ ) of the deviation in a localized region of the attractor surrounding  $x_n$ . Note that in general, the value obtained for  $m_n$  is dependent on the direction chosen for the displacement and that for each dimension of the dynamical system there will be a corresponding Lyapunov exponent.

For the diode resonator, we start  $y_n$  as a displacement of the current at a current peak  $n$ . The differing trajectory is propagated to the  $n+1$ th peak where it is compared to the trajectory which would have occurred had no initial displacement occurred. The ratio of the final difference,  $\vec{y}_{n+1}$ , to the initial displacement,  $\vec{y}_n$ , is taken to be the local Lyapunov multiplier for the peak  $n$ . At the  $n+1$ th peak the process is repeated with a new infinitesimal displacement in order to determine  $m_{n+1}$ . Global Lyapunov multipliers are then defined by stepping the deviation through the linearized mapping indefinitely and calculating the geometrical mean of the local multipliers. In time the initial perturbation will have grown enough so that the linear approximation is rendered invalid. At these points, the perturbation is renormalized. The global Lyapunov multiplier is then

$$m_g = \prod_{n=0}^{\infty} \left( \frac{|\vec{y}_{n+1}|}{|\vec{y}_n|} \right)^{\frac{1}{n+1}}. \quad (4.3)$$

The global Lyapunov exponent is defined as  $\lambda = \ln(m_g)$ .

Lyapunov multipliers can be used to predict the occurrence of synchronization. Consider the above mentioned infinitesimal displacement,  $\vec{y}_n$ , as a vector pointing from one orbit to a second orbit. However, instead of the linearizing the mapping of the single orbit, one observes the linearized relationship between the difference of the master and slave orbits. Explicitly, the evolution of the displacement is measured by evaluating the propagation of a point along the primary trajectory and an equivalent point along the secondary orbit. The secondary orbit is perturbed by the effect of some feedback; otherwise, this calculation would simply duplicate the above estimate of the Lyapunov exponent. The evolution of

the displacement defines whether synchronization of the second orbit to the first is to be achieved or not. For synchronization to occur, the corresponding global Lyapunov multiplier must be less than one.

The significance of the algorithm proposed by Lai and Grebogi for maps is that it provides a technique to calculate and apply perturbations so as to set the local Lyapunov multipliers along the unstable directions to zero at every iteration. Since the global Lyapunov multiplier will be minimized as well, this technique represents the ideal situation and presents the most rapid scheme possible for synchronization. However, the requirement for convergence is only that the global Lyapunov multipliers have a magnitude less than unity. Since this is less stringent than the demand of the original theory, it is possible to adapt the Lai and Grebogi perturbation formula to the experimentally feasible calculation of simply using a constant amplification factor. The implementation of the constant factor can be successful if it satisfies the criteria of the global Lyapunov multipliers being less than unity.

A numerical calculation of the LLM's versus the voltage peaks of the resistor component of the resonator (designated as  $V^M(t)$ ) are obtained by first synchronizing a slave system to the master and then applying a small randomly generated kick to the slave system at each peak. Both systems are propagated forward in time until the next peak at which point the resulting difference between the two systems is evaluated. The ratio between the final trajectory difference and the initial kick was considered to be the LLM for the initial peak. Global Lyapunov multipliers are then obtained by the geometrical averaging method described above. In the event of no applied feedback to the second orbit, Fig. 3(a) the LLM's are predominantly greater than one and no synchronization is achieved. Note that even with no feedback, the LLMs along the upper branch are less than one. Though globally unstable, the attractor has regions of stability.

We next look at amplitude modulating the drive wave of the second system by the term  $\alpha(V^S(t) - V^M(t))$  where  $\alpha$  is simply a constant amplification factor. The dimensionless

factor, ( $\alpha = 0.3$ ), applied in Fig. 3(b) is just sufficient to shift enough of the LLMs downward so that synchronization is realized. Even though some of the LLMs are greater than one, the global product remains below unity. Fig. 3(c) shows the optimum constant value ( $\alpha = 0.5$ ) for synchronization. The iterative dependent term prescribed by the Lai and Grebogi algorithm, Fig. 3(d), presents the optimum case. However, since the algorithm was obtained for maps, the LLM will not necessarily be zero. Synchronization can be achieved for the range of constant amplification values which produce a negative global Lyapunov exponent. Fig. 4(a) is a graph of the largest and least global Lyapunov exponents versus constant amplification factors. Fig. 4(b) is plot of the standard deviation of the difference between peaks of the voltage drops across the master and slave resistor. The graph shows the range of constants for which synchronization can be achieved. Only for a band of values is the global Lyapunov exponent negative. The corresponding synchronization of the master and slave is striking as the standard deviation drops to zero for the band.

## V. CONCLUSIONS

The goal was to demonstrate that an experimental implementation of synchronization using control as proposed numerically by Lai and Grebogi [7] is feasible and to show how synchronization can occur through the effect on the Lyapunov multipliers.

For our system of interest, the diode resonator, the attractor is approximately 1-dimensional. In such cases the synchronizing peak dependent feedback simplifies considerably. It is composed of the difference between the voltage drop across the slave and master resonator resistors multiplied by a factor which is a function of the peaks of the voltage drop across the master resistor. The peak dependent factor is the negative of the ratio of the Jacobian to the shift of the map. These latter two terms can be computed by observing first return maps of the resonator. The resulting perturbation modulates the

amplitude of the drive wave for a large fraction of the period. The technique is tolerant to variations in the components of each system, to the drive signal to each resonator, and to the feedback perturbation.

A quantitative understanding of the ability of systems to synchronize can be understood by observing the local and global Lyapunov multipliers derived from linking the two chaotic systems. By calculating the Lyapunov multipliers, we find that the algorithm proposed by Lai and Grebogi presents the optimum method of calculating a stabilizing feedback. While this represents the most effective scheme of synchronization, the necessary criteria is to merely force the global Lyapunov exponent to be less than one. In the case of the diode resonator, this relaxed condition allows the implementation of a constant amplification factor to be incorporated instead of a term which must be calculated on each peak of the drive wave.

From observing the local Lyapunov multipliers and, equivalently for the 1-dimensional case, the slope of the first return map, regions of stability and instability can be ascertained. In order to synchronize two chaotic systems, stabilizing perturbations need be made only when the systems are operating in the unstable region of the attractor.

## VI. ACKNOWLEDGEMENTS

T.C.N. wishes to thank the Air Force Office of Scientific Research for a summer fellowship.

## REFERENCES

- [1] E. Ott, C. Grebogi, and J. A. Yorke, Phys. Rev. Lett. **64**, 1196 (1990).
- [2] W.L. Ditto, S.N. Rauseo, and M.L. Spano, Phys. Rev. Lett. **65**, 3211 (1990).
- [3] E. R. Hunt, Phys. Rev. Lett. **67**, 1953 (1991).
- [4] C. Reyl, L.Flepp, R.Baddi, and E. Brun, Phys. Rev. A **47**, 267 (1992).
- [5] R. Roy, T.W. Murphy, T.D. Maier, Z. Gills and E.R. Hunt, Phys. Rev. Lett. **68**, 1259 (1992).
- [6] B. Peng, V. Petrov, and K. Showalter, J. Phys. Chem., 4957 (1991).
- [7] Y.C. Lai and C. Grebogi, Phys. Rev. E **47**, 2357 (1993).
- [8] Y.C. Lai, M. Ding and C. Grebogi, Phys. Rev. E **47**, 86 (1993).
- [9] See, e.g. *SPICE*, ed. P. Antognetti and G. Massobrio, McGraw-Hill (1988).
- [10] Z. Yu, J. Steinshnider, C.L. Littler, J.M. Perez, and J.M. Kowalski, Phys. Rev. E **49** 220 (1994).
- [11] H.D.I. Abarbanel, R. Brown, and M.B. Kennel, Jnl. of Nonlinear Sci. **2**, 343 (1992).

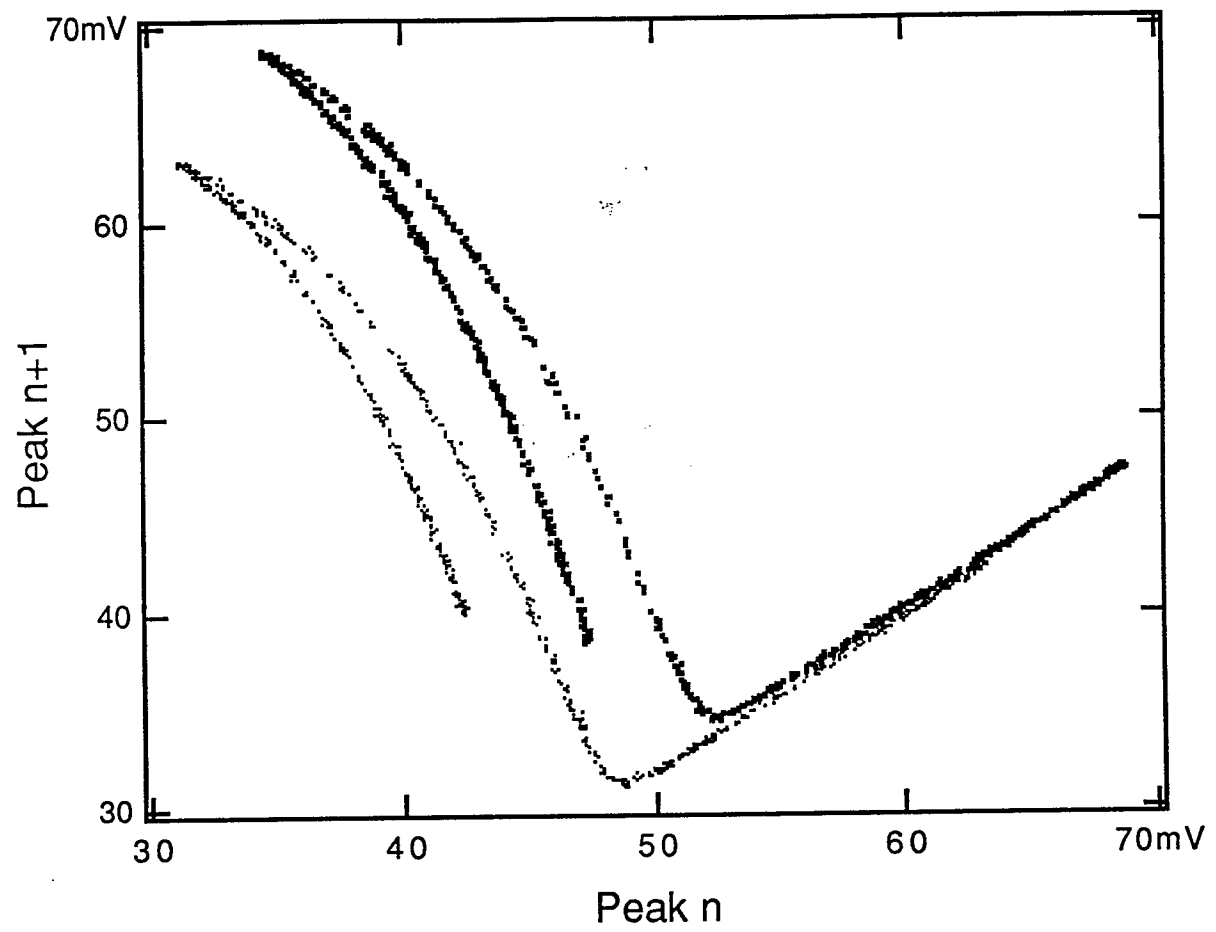
## FIGURES

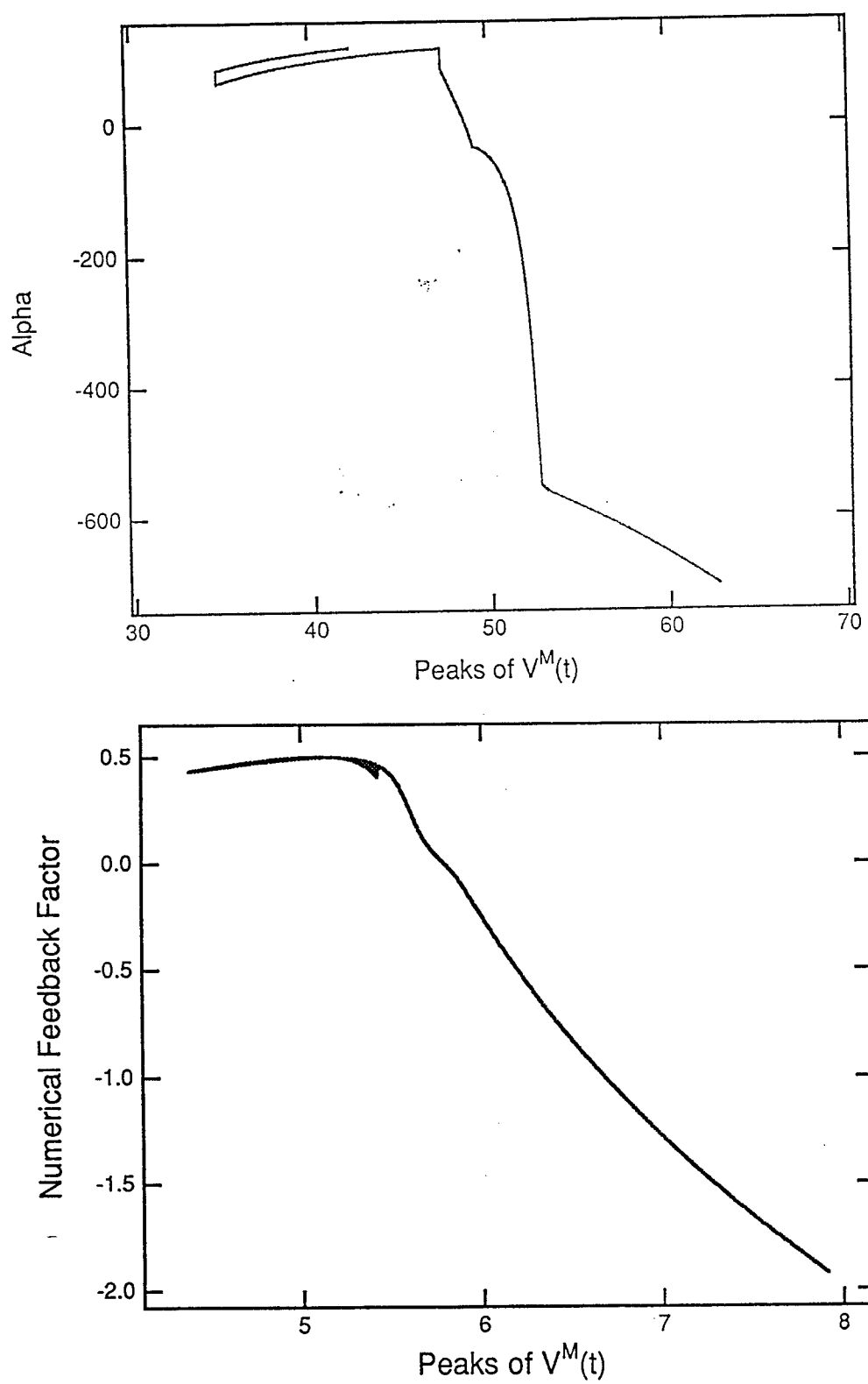
FIG. 1. Two return maps recorded at  $4.6V$  and  $5.1V$  (upper) show the effect of a perturbation to the drive wave amplitude. The shift of the map is obtained by measuring:  $(x_n(5.1V) - x_n(4.6V))/0.5V$ . The 1-dimensional Jacobian matrix is the slope of the  $4.6V$  map. Above 48mV the slope is less than one. The attractor is locally stable in this region.

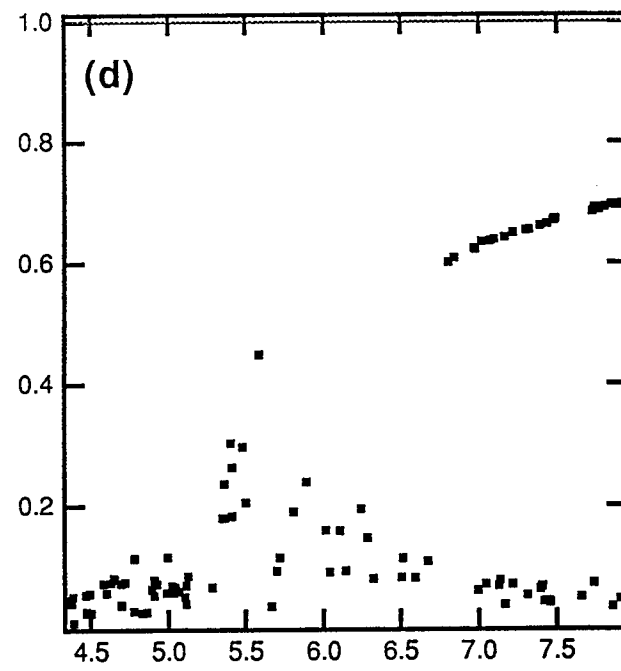
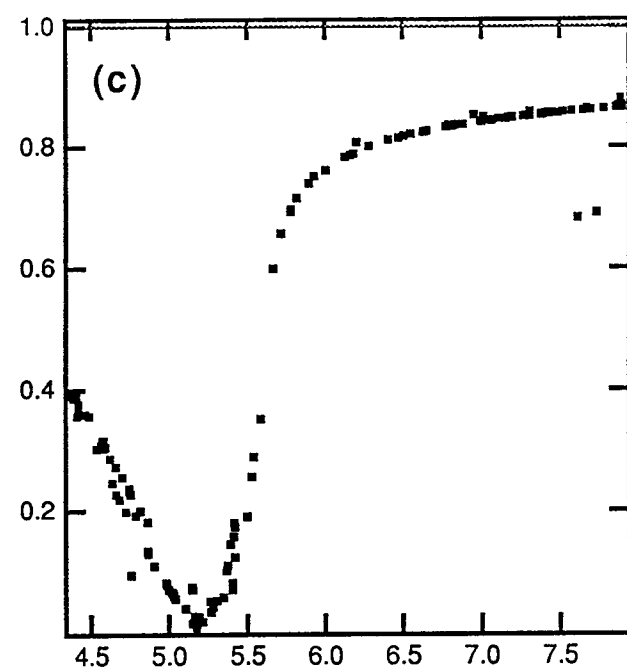
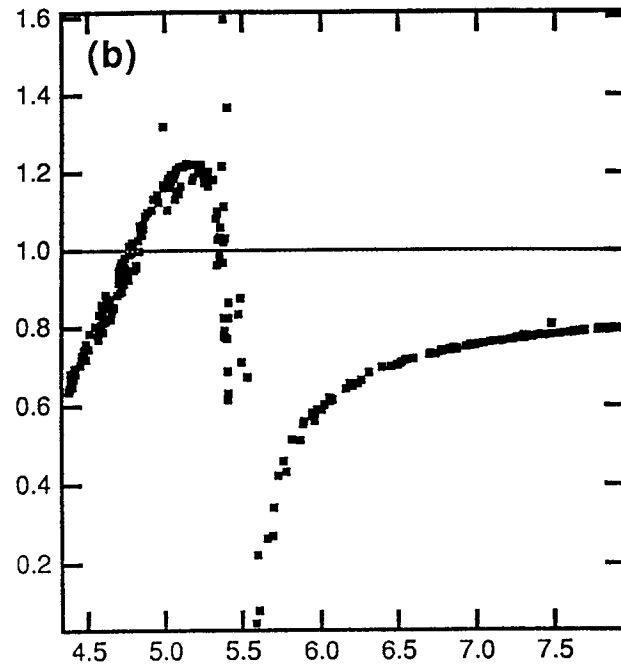
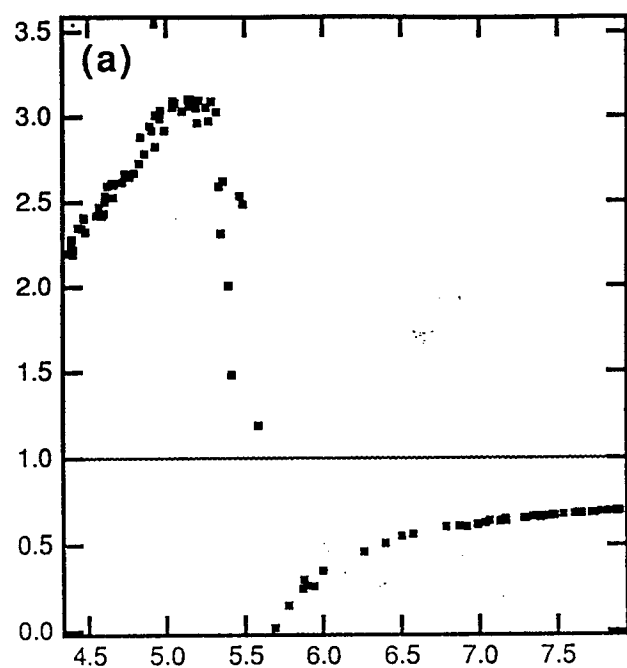
FIG. 2. The peak dependent feedback amplification factor as a function of the resistor peaks. This is obtained using experimental data. Since the return map shifts along the upper branch, the denominator is quite small and the factor drops off rapidly. Below 48mV the factor is approximately constant regardless of the two lower branches of the return map. (b) A numerical calculation of the peak dependent feedback amplification factor is similar to (a). Numerically the return map shifts upwards more than experimentally observed and the drop off of the upper section is not as severe.

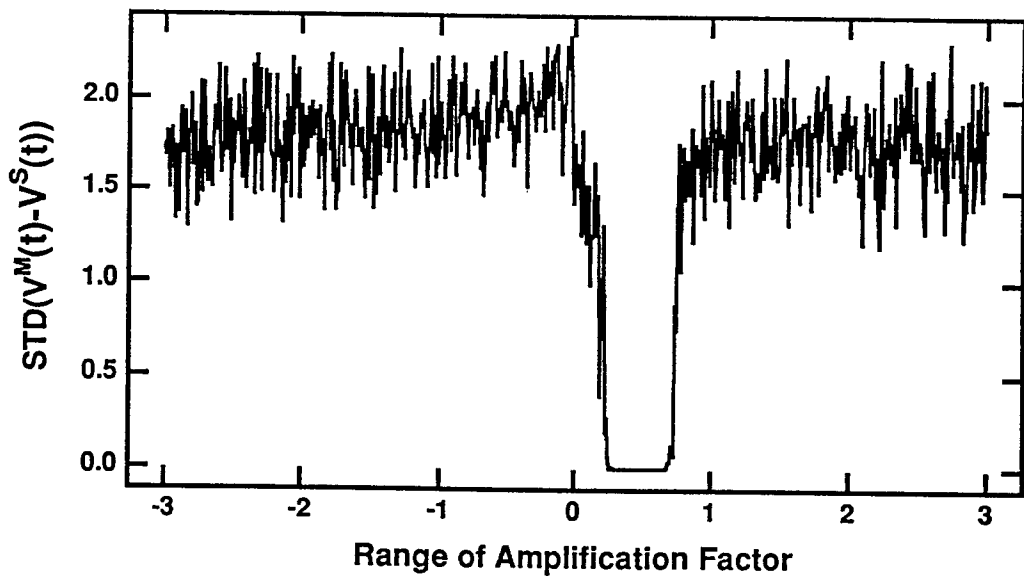
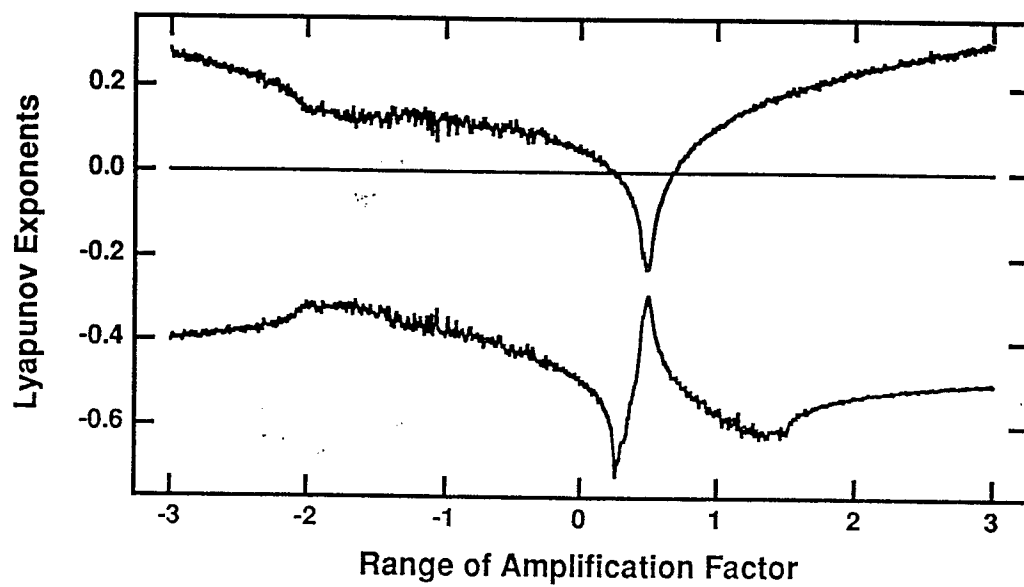
FIG. 3. A calculation of the local Lyapunov multipliers which describe the expansion or contraction of the master and slave orbits as they are propagated from one peak to the next. (a) The master and slave resonator are operating independently. (b) The feedback amplification factor is taken to be a constant of 0.3. Though some local multipliers remain greater than unity, the global Lyapunov multiplier is less than unity and synchronization occurs. (c) An optimum constant feedback factor of 0.5. The perturbation reduces substantially the multipliers in the unstable region of the attractor but does little to influence those in the stable regions. (d) The peak dependent feedback factor according to the Lai and Grebogi algorithm influences the local Lyapunov multipliers strongly. This represents the optimum feedback factor possible to obtain synchronization using the control technique.

FIG. 4. (a) The Lyapunov exponents  $\lambda_1$  and  $\lambda_3$  of the linked master slave system versus the applied constant feedback factor. (b) The standard deviation of the difference between the master and slave orbits. Synchronization is achieved for a band of values.









## **RELAXATION PROCESSES IN GAIN SWITCHED IODINE LASERS**

**Jeff Nicholson**  
Graduate Student  
**Wolfgang Rudolph**  
Associate Professor  
Department of Physics and Astronomy  
The University of New Mexico  
Albuquerque, NM 87131

Report for:  
Graduate Summer Research Program  
Phillips Laboratory

Sponsored by:  
Air Force Office of Scientific Research  
Phillips Laboratory, Albuquerque

September 1994

## RELAXATION PROCESSES IN GAIN SWITCHED IODINE LASERS

Jeff Nicholson  
Graduate Student  
**Wolfgang Rudolph**  
Associate Professor  
Department of Physics and Astronomy  
The University of New Mexico  
Albuquerque, NM 87131

### Abstract

The dynamics of a gain switched, low pressure photolytic iodine laser were investigated experimentally and theoretically. The pulse shape, build-up and decay time were measured as function of the pressure of the active medium ( $\text{CF}_3\text{I}$ ) and of the pressure of the buffer gas. At low pressure, the pulse develops a second peak, and the build-up and decay times become longer. The distinct features of the iodine pulse could be explained in terms of two relaxation processes involving collisions that change the direction and magnitude of the velocity vector. A computer model based on the rate equations which includes collisional relaxations allowed us to derive quantitative estimates for the corresponding relaxation times as a function of pressure and buffer gas.

## **RELAXATION PROCESSES IN GAIN SWITCHED IODINE LASERS**

Jeff Nicholson and Wolfgang Rudolph

### **1 Introduction**

A great deal of interest has been devoted to the development of iodine lasers for different types of applications, see e.g., [1],[2],[3]. The potentials of chemical pumping are particularly attractive for applications requiring high-power. Normally, lasing is achieved between the hyperfine levels 4 and 3 of excited atomic iodine,  $I^*$ , which exhibits a total of six hyperfine transitions. The wavelength of this transition is  $1.315 \mu\text{m}$ . The dominance of the 3-4 transition is because its magnetic dipole moment is about two times greater than that of the next largest transition (2-2). For the past twenty years a number of fundamental studies of iodine lasers have been undertaken involving longitudinal mode-beating and mode-locking [4],[5],[6]. Photolytic pumping employing an excimer laser is a convenient technique for laboratory operation of iodine lasers. However little effort has been devoted to the primary processes in photodissociation lasers working at low pressure. From Doppler spectroscopy experiments [7] and the theory of collisional relaxation [8] it is known that a short dissociation pulse creates a nonthermal velocity distribution of excited iodine. Depending on the parent molecule and buffer gas (if any) two different relaxation types with different time constants can be distinguished - collisions that change only the direction of the velocity vector but not its magnitude with a time constant  $T_b$  and those determining the rate by which the velocity relaxes towards its equilibrium value (time constant  $T_v$ ). A photolytic, single mode iodine laser is thus expected to experience a dramatic change in gain during the evolution of the gain switched pulse. Since in a single mode laser, saturation of the gain is associated with hole burning, collisional cross relaxation will effect the shape and duration of the laser pulse.

The aim of this project was to study the evolution of gain switched pulses in low - pressure photolytic iodine lasers with and without buffer gas. From a comparison of theory and experiment the possibility of determining relaxation constants was explored.

### **2 Experimental results**

#### **2.1 Experimental setup**

The experimental setup is shown in Fig. 1. The active medium used in this experiment was  $\text{CF}_3\text{I}$ . The length of the gain cell was 85 cm. The cavity consisted of a mirror with a 5 m focal length and a mirror with a 25 m focal length, both with 100% reflectivity. With a cavity length of 1.1 m, this gave a radius for the beam waist of 1.1 mm and a confocal parameter of 2.9 m.

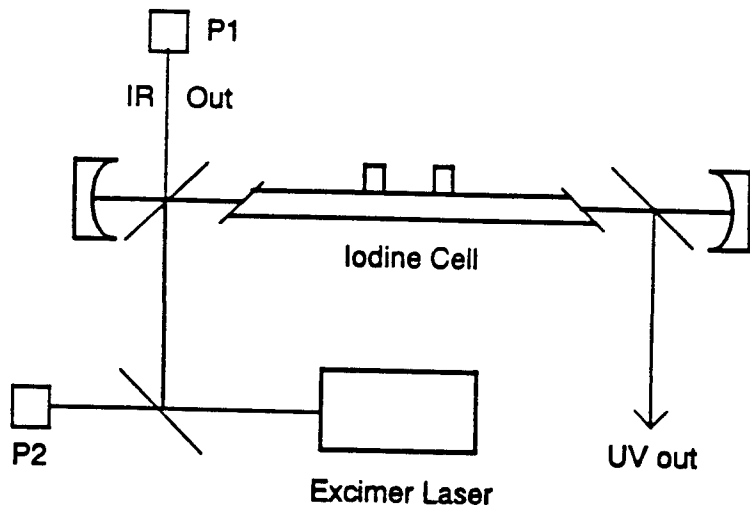


**Figure 1:** Experimental setup of a photolytic iodine laser pumped by an excimer laser. P1 was a fast photodiode used to measure the iodine pulse profile. P2 was a photodiode used to trigger the oscilloscope.

The pump was a KrF excimer laser operating at 248 nm, with pulse widths of about 20 ns and maximum pulse energies of approximately 200 mJ. The pump was focused with a 2 m fused silica lens, and coupled into the cavity with a dichroic beam splitter. The excimer pulse was coupled out of the cavity with a second dichroic mirror, in order to avoid damaging the end mirror of the iodine cell when working in the low absorption regime (low CF<sub>3</sub>I pressure). The second dichroic mirror was placed at Brewster's angle for 1.3 μm in order to reduce the cavity losses.

The iodine laser output was taken from the dichroic beam splitter that coupled the excimer pump laser into the iodine cavity. With the cavity arranged as outlined above, the cavity losses per round trip were approximately 6%, and the cavity lifetime was about 60 ns. The iodine laser, under these conditions, lased at pressures as low as 0.2 Torr.

Longitudinal mode beating is an inherent property of gain switched and Q switched iodine lasers operating at low pressures [5]; therefore, an aperture was used in the iodine cavity to control the number of longitudinal modes in the cavity. When the aperture was sufficiently small, (~1.5mm in diameter) not only was the iodine laser forced to run in TEM<sub>00</sub> mode, but strong longitudinal mode beating was eliminated in approximately 50% of the shots.

After laser action, only about 90% of the molecular fragments recombine to form CF<sub>3</sub>I, the rest of the fragments going into processes such as dimerization [2]. I<sub>2</sub> is a strong quencher of the <sup>2</sup>P<sub>1/2</sub> state, leading to a degradation of the iodine laser output after multiple shots of the excimer laser. Therefore, the iodine cell was refilled after every fourth or fifth excimer pulse. Note, that while these processes proved to be important for multiple shot experiments, they do not play a significant role in single shot pulse dynamics because of their slow (e. g.  $\sim 4 * 10^{-31} \text{cm}^6 \text{mol}^{-2} \text{s}^{-1}$  for dimerization) rate.

The iodine pulse was detected with a fast (rise time < 500 ps) photodiode and viewed on a digital oscilloscope with a 200 MHz analog bandwidth and a 1 Gs sampling rate. The oscilloscope was triggered with a signal from a second photodiode that was sensitive to the UV excimer pulse. The delay was then set digitally with the oscilloscope itself.

The pulse dynamics were measured as a function of pressure of  $\text{CF}_3\text{I}$  plus buffer gas (if any). The quantities of interest were:

- $\tau_1$  The build up time of the iodine pulse. This was defined as the time between the excimer pulse peak and the time when the iodine pulse builds to 10% of its peak intensity.
- $\tau_2$  The exponential rise time of the iodine pulse.
- $\tau_3$  The duration of the iodine pulse. This was defined as the time from  $\tau_1$  to the point when the iodine pulse fell to 10% of its peak value. The iodine pulse did not decay in an exponential fashion at low pressures, making an exponential fit impossible.

## 2.2 Results without buffer gas

Initially, the iodine pulse dynamics were measured as a function of the pressure of  $\text{CF}_3\text{I}$ , without the use of any buffer gas. Although the iodine laser would lase at pressures as low as 0.2 Torr, under these conditions the laser was near threshold, and consequently, the pulse characteristics varied greatly from shot to shot. Therefore, measurements were generally made for pressures of 0.4 Torr and greater.

Typical pulse shapes are shown in Fig. 2 for pressures of 0.6, 2, and 6 Torr of  $\text{CF}_3\text{I}$ . At low pressures, the iodine pulse shows a distinct second peak, caused by repumping due to the velocity relaxation. As the pressure increases, the peak becomes less distinct, becoming a shoulder, and finally disappears altogether at pressures above 3 Torr.

The buildup and decay time of the iodine pulse as a function of  $\text{CF}_3\text{I}$  pressure are shown in Fig. 3(a). Fig. 3(b). shows the exponential rise time of the iodine pulse as a function of pressure. The characteristic shape of these plots can be explained by the increased relaxation rate as the pressure increases as will be detailed in Section 3.3. Note, that by changing the  $\text{CF}_3\text{I}$  pressure, we also change the amount of absorbed pump pulse energy and thus, the overall gain.

## 2.3 Results with buffer gas

The same measurements outlined in the previous section were made using a buffer gas. The cell was filled with 0.6 Torr of  $\text{CF}_3\text{I}$ , and Xenon was added on top of this. Typical pulse profiles are shown in Fig. 4. Pulse buildup time and duration as a function of buffer gas pressure are shown in Fig. 5. The behavior of the build up time and pulse duration – and even the overall pulse

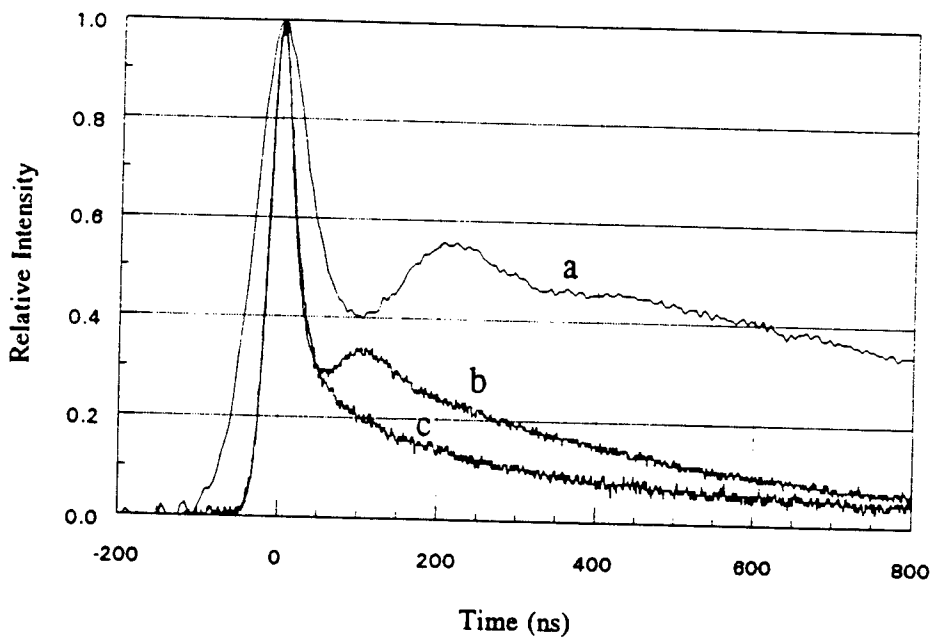


**Figure 2:** Pulse profiles for (a) 0.6 Torr, (b) 2 Torr, and (c) 6 Torr of  $\text{CF}_3\text{I}$ . The pulse peaks have been normalized to one and moved to the origin of the time axis for comparison purposes.

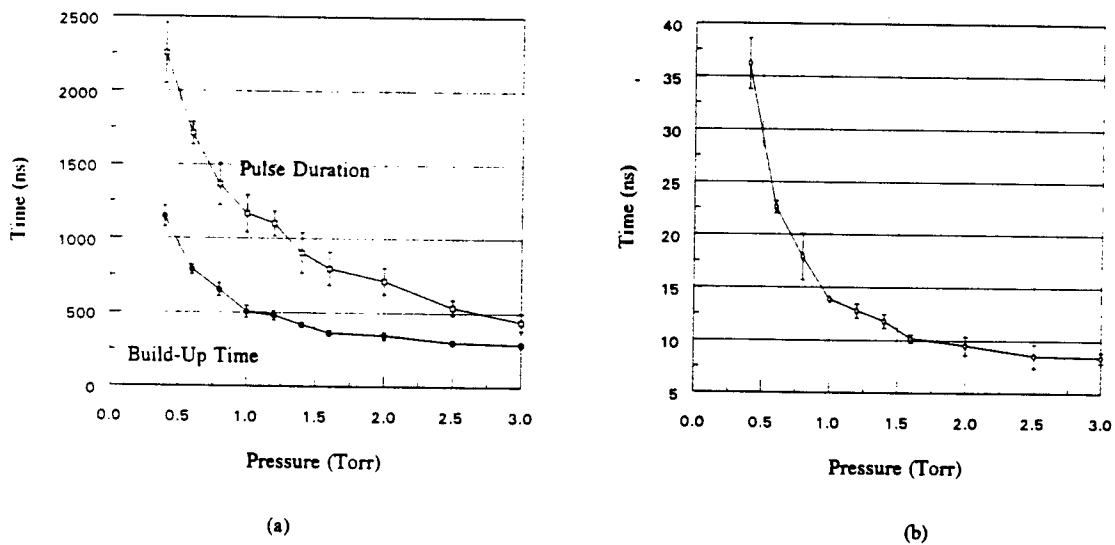


**Figure 3:** (a) Build up time and duration and (b) Rise time of the iodine pulse as a function of  $\text{CF}_3\text{I}$  pressure. No buffer gas was used.

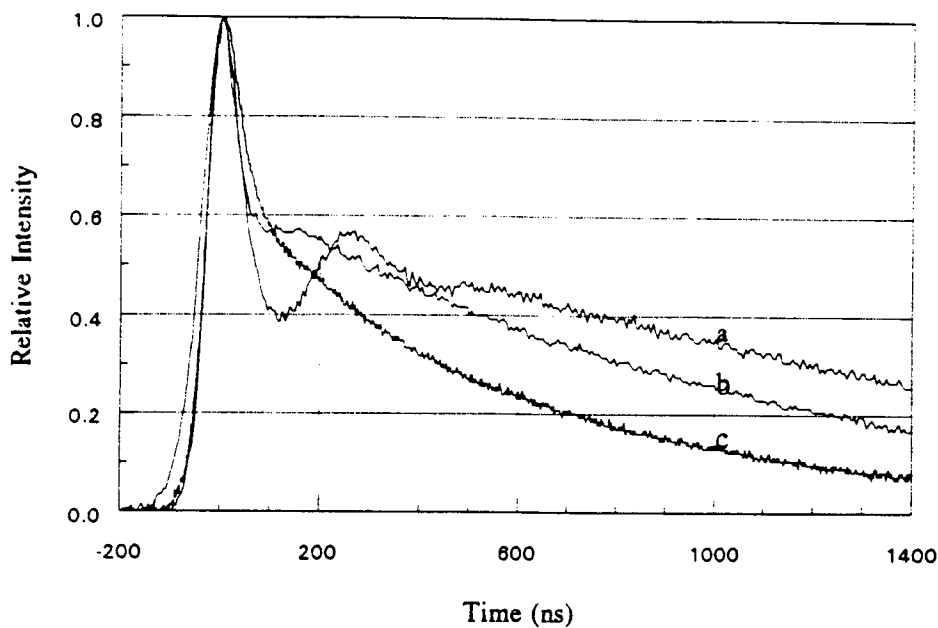


**Figure 4:** Pulse profiles for (a) 0.0 Torr, (b) 0.6 Torr, and (c) 1.2 Torr of Xenon added to 0.6 Torr of  $\text{CF}_3\text{I}$ . The pulse peaks have been normalized to one and moved to the origin of the time axis for comparison purposes.

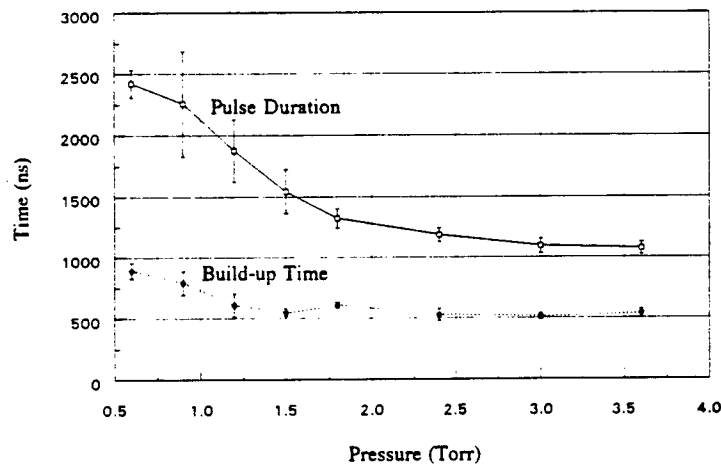


**Figure 5:** Build up time and duration of the iodine pulse as a function of buffer gas (Xe) pressure.  $\text{CF}_3\text{I}$  pressure was 0.6 Torr

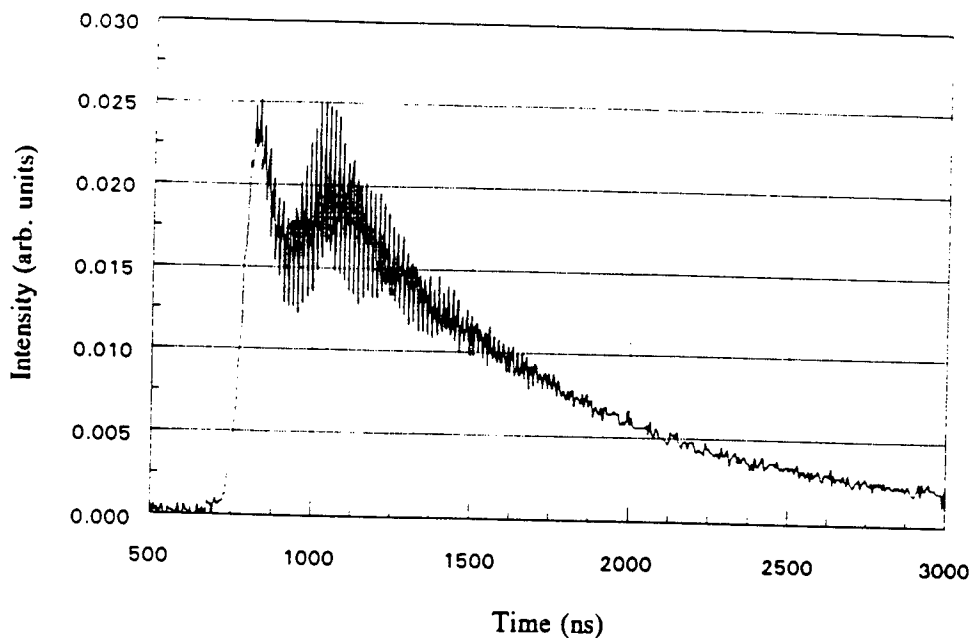


**Figure 6:** Typical iodine laser pulse showing two longitudinal mode exceeding threshold.  $\text{CF}_3\text{I}$  pressure was 0.6 Torr.

profiles – as a function of pressure is similar for pulses with and without buffer gas. However, the exponential rise time of the iodine pulse is essentially unaffected by the addition of Xenon. A discussion of these features and a comparison with the computer model are given in Section 3.3.

The effects of mode beating could never be fully eliminated in 100% of the shots. However, as mentioned above, the probability of mode beating could be decreased by reducing the aperture in the iodine cavity significantly, thus preventing all but one mode from exceeding threshold. A typical laser output in the regime where two modes can exist is shown in Fig. 6. The mode beating can clearly be observed, as can the fact that the second mode starts oscillating at a later time than the first. This is consistent with the higher losses this mode experiences. A complex beating of both longitudinal and transverse modes was observed when the iodine aperture was fully open.

### 3 Theoretical description of low pressure photolytic iodine lasers

#### 3.1 Relaxation processes

A rate equation approach was chosen for the simulation of the gain switched pulse. Since the pump pulse (duration 20 ns) is much shorter than all time constants of the processes of interest the initial conditions simply represent a distribution of excited atomic iodine. This distribution, however, differs from a thermalized Doppler profile. It exhibits a larger mean velocity and a

velocity anisotropy. In [7] it was shown that to a good approximation the velocity distribution can be written as a product of a  $|v|$  and a  $\theta$  dependent term

$$F(\vec{v}, t) = f(|v|, t)\beta(\theta, t) \quad (1)$$

where  $v = \sqrt{|\vec{v}|^2}$  is the mean velocity of the gas and  $\theta$  is the angle between the exciting electric field vector and the propagation direction of the probe laser. The latter in our case is the resonator axis (z-axis) of the iodine laser, i.e.,  $\theta = 90^\circ$ . Two different relaxation processes can be distinguished, both being collisional. Collisions which change the direction of the velocity vector are responsible for the relaxation of the anisotropy with a characteristic time constant  $T_b$ . Collisions changing the magnitude of the velocity (time constant  $T_v$ ) cause the relaxation to a thermalized Doppler profile with a mean velocity determined by the room temperature. For heavy collision partners it was found that  $T_b < (<)T_v$ . An exact modeling of the thermalization would require an extensive analysis of the collision processes including the particular properties of the participating particles. As done successfully for the interpretation of the pump-probe experiments in [7] we shall instead describe the thermalization in terms of the two time constants  $T_v$  and  $T_b$ . To model the evolution of the laser pulse we need to include the interaction with the laser field and its effect on the relaxation.

Let us assume that we must consider  $2N+1$  groups of excited iodine of number density  $N_n$  ( $n = 0, 1, \dots, N$ ) with velocity components along the z-axis such that the separation of their transition frequencies is  $\Delta\omega_h$ . A Doppler velocity profile is characterized by the following distribution of excited iodine with transition frequency  $\omega_n = \omega_0 \pm n\Delta\omega_h$

$$N_n^e = N_0 \exp \left[ -4 \ln 2 \left( \frac{\omega_n - \omega_0}{\Delta\omega_D(t)} \right)^2 n^2 \right] \quad (2)$$

where  $\Delta\omega_D \sim \frac{v}{c}\omega_0$ . Since the velocity profile is always symmetric,  $n = -N, (-N+1), \dots, N$ . For the time dependence of the Doppler width we can thus use the known time dependence of the mean velocity and have

$$\Delta\omega_D(t) = \Delta\omega_{Df} + (\Delta\omega_{in} - \Delta\omega_D) e^{-t/T_v} \quad (3)$$

where  $\Delta\omega_{in}$ ,  $\Delta\omega_{Df}$  are the Doppler width of the profile of the "hot" gas immediately after excitation and after complete thermalization with the surrounding, respectively.

At any given instant the number densities obey the following set of differential equations describing the relaxation towards a Doppler profile

$$\frac{dN_n}{dt} = \frac{N_n^e - N_n}{T_b} \quad (4)$$

where  $N_n^e$  is given by Eq. (2). Under laser action we need to distinguish between excited and ground state iodine, each group undergoing similar relaxation processes. While excited iodine is generated

at many different transition frequencies ground state iodine is only produced by stimulated emission at the transition frequency  $\omega_0$ . Collisional relaxation processes then cause a redistribution towards a thermalized Doppler profile.

### 3.2 Laser model

To model the operation of a photolytic iodine laser the typical rate approximation approach was chosen. In accordance with the experiments we assume single longitudinal mode operation. Therefore at a certain time  $t$  only atoms with resonance frequency  $\omega_0$  interact directly with the laser field (photon flux  $F$ ). The set of rate equations can then be written as

$$\frac{d}{dt}N_0 = \sigma_{0\ell}F(N_{0\ell} - N_0) + \frac{1}{T_b}(N_0^e - N_0) \quad (5)$$

$$\frac{d}{dt}N_{0\ell} = \sigma_{0\ell}F(N_0 - N_{0\ell}) + \frac{1}{T_b}(N_{0\ell}^e - N_{0\ell}) \quad (6)$$

$$\frac{d}{dt}F = \sigma_{0\ell}cF(N_0 - N_{0\ell}) - \frac{F}{T_R} \quad (7)$$

$$\frac{d}{dt}N_n = \frac{1}{T_b}(N_n^e - N_n) \quad n = 1, 2, \dots, N \quad (8)$$

$$\frac{d}{dt}N_\ell = \sigma_{0\ell}(N_0 - N_{0\ell}) \quad (9)$$

where  $\sigma_{0\ell}$  is the amplification cross section,  $N_{0\ell}$  is the number density of de-excited atoms of transition frequency  $\omega_0$ ,  $T_R$  is the resonator decay time,  $N_n^e$  is the number density of atoms if distributed according to a Gaussian profile of width  $\Delta\omega_D$ , and  $c$  is the velocity of light. The quantity  $N_\ell$  describes the total number of iodine atoms in the ground state. The total number of excited iodine atoms is

$$N_{total}(t) = N_0(t) + 2 \sum_{n=1}^N N_n(t) \quad (10)$$

and the equilibrium numbers can be calculated from

$$N_0 = N_{total} \left[ 1 + 2 \sum_{n=1}^N e^{-n^2(\Delta\omega_h/\Delta\omega_D)^2} \right]^{-1} \quad (11)$$

and

$$N_n = N_0 \exp \left[ - \left( \frac{\Delta\omega_h}{\Delta\omega_D} \right)^2 \right] \quad (12)$$

for  $n = 1, 2, \dots, N$ . After each integration step these equilibrium numbers have to be determined with the modified  $N_{total}$  and  $\Delta\omega_D$  according to Eqs. (10) and (3), respectively. The same procedure must be applied for the atoms in the ground state. Their total number is given by the total number

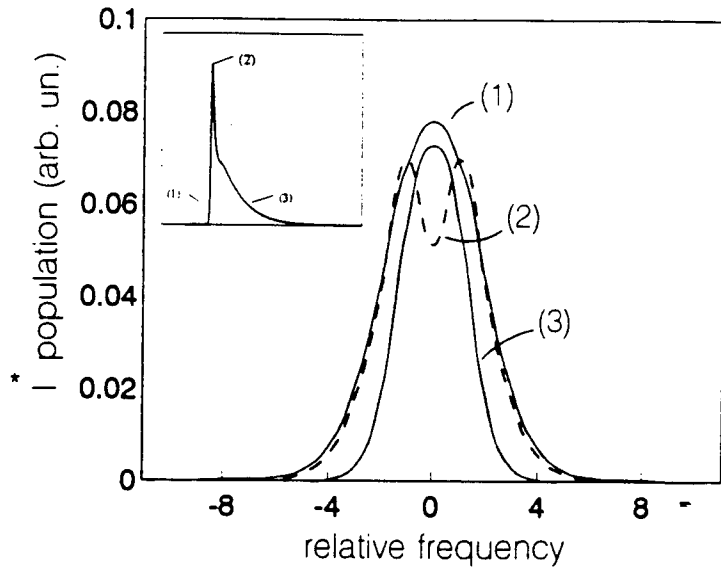


**Figure 7:** Calculated gain profile vs frequency as seen by different parts of the iodine laser pulse. The inset shows a typical iodine pulse and the corresponding times.

of de-excitation events, where each event results in the occupation of  $N_{0\ell}$  only. Note that we can neglect spontaneous emission for this process because of the smallness of the  $A$  coefficient ( $\approx 10 s^{-1}$ ) of the magnetic dipole transition of iodine. A small number of (spontaneously emitted) photons are injected at  $t = 0$ , though, to induce the build up of the laser pulse. The integration of the preceding system of differential equations (5)-(9) was performed using a Runge-Kutta routine.

### 3.3 Results of the computer simulation and comparison with the experiment

Figure 7 shows the occupation numbers in the excited state as a function of the transition frequency for different times after excitation. The inset shows the corresponding iodine laser pulse. Curve (1) describes the distribution at the pulse leading edge (at 10% of the peak value). The non Gaussian distribution here has already relaxed into a Gaussian (relaxation time  $T_b$ ) which still corresponds to a velocity much larger than the equilibrium value. At the pulse peak (curve (2)) spectral hole burning is clearly visible which causes a relaxation from excited groups of atoms into those in resonance with the laser field. This means a repumping of the laser transition. The relaxation of the magnitude of the velocity (relaxation time  $T_v$ ) is another process which results in an effective repumping. As the Doppler profile narrows the number of excited atoms with transition frequency  $\omega_0$  increases to a constant that depends on the total number of excited iodine atoms and room temperature as described by Eqs. (2) and (3). (if we neglect de-population by the laser

pulse). Curve (3) shows the gain profile seen by the trailing edge of the pulse (at 10% of the peak value). A comparison of curves (1) and (2) illustrates our discussion. Due to the laser action the area under curve (3) is smaller. Of course, for the actual laser action, the difference ( $N_0 - N_{0t}$ ) is of importance. Due to the combined action of stimulated emission and the thermalization of ground state iodine,  $N_{nt}$  is constantly increasing with time; therefore, the qualitative features of the gain can be explained in terms  $N_n$ .

As seen in the experimental section, at low  $\text{CF}_3\text{I}$  pressure the laser pulse exhibits a characteristic shape-a sharp rise time and a distinct shoulder. The pulse duration and decay time are significantly longer than the resonator life time. Figure 8 compares preliminary results of measured and calculated pulse profiles. From the experiment the resonator life time and the number density of excited iodine can be estimated. For the homogeneous line width we assumed  $\Delta\omega_D = 60 \text{ MHz}$ . The only remaining input parameter for the simulation are the two relaxation times  $T_b$  and  $T_v$ . For  $\text{C}_3\text{F}_7\text{I}$  and a gas pressure of 0.2 Torr values of  $1 \mu\text{s}$  and  $2.5 \mu\text{s}$  have been measured [7]. For the simulation we assumed that both relaxation constants are inversely proportional to the pressure and that their ratio is constant. all other input parameters were not changed. From the simulation it becomes obvious that the measured features are a consequence of the collisional relaxations. The shoulder at low pressure is a result of the hole burning and a fast refill of excited iodine at the laser frequency owing to the short relaxation involving  $T_b$ . With increasing pressure and thus shorter  $T_b$  the second maximum vanishes and the main peak simply broadens. The decay of the iodine pulse is essentially controlled by the  $|v|$  relaxation proceeding more slowly.

Another important feature is the delay between excimer pump pulse and the occurrence of the iodine pulse. The decrease of the delay with increasing buffer gas pressure is also a result of the faster relaxation. Figures 9 (a) and (b) show the delay and the decay time as function of the pressure (here as function of  $T_b$  while keeping  $T_b/T_v$  constant). The behavior of the curves describes the experimental findings qualitatively.

For a more complex (future) quantitative comparison of simulation data and experiments we plan to implement the following in the discussion: The addition of a buffer gas (BF) requires the introduction of two different relaxation rates. If the buffer gas pressure is changed their value will change accordingly while their ratio remains. In the simulation we then need to use

$$\frac{1}{T_{b,v}} = \frac{1}{T_{b,v}(\text{CF}_3\text{I})} + \frac{1}{T_{b,v}(\text{BF})} \quad (13)$$

where only the second summand changes with a change in buffer gas pressure. The different effect of adding  $\text{CF}_3\text{I}$  or buffer gas on the measured pulse characteristics suggests the necessity of this approach.

Since the photolytic iodine laser is a relatively simple system with most parameters well documented we believe that the performed experiments can be used to determine relaxation constants

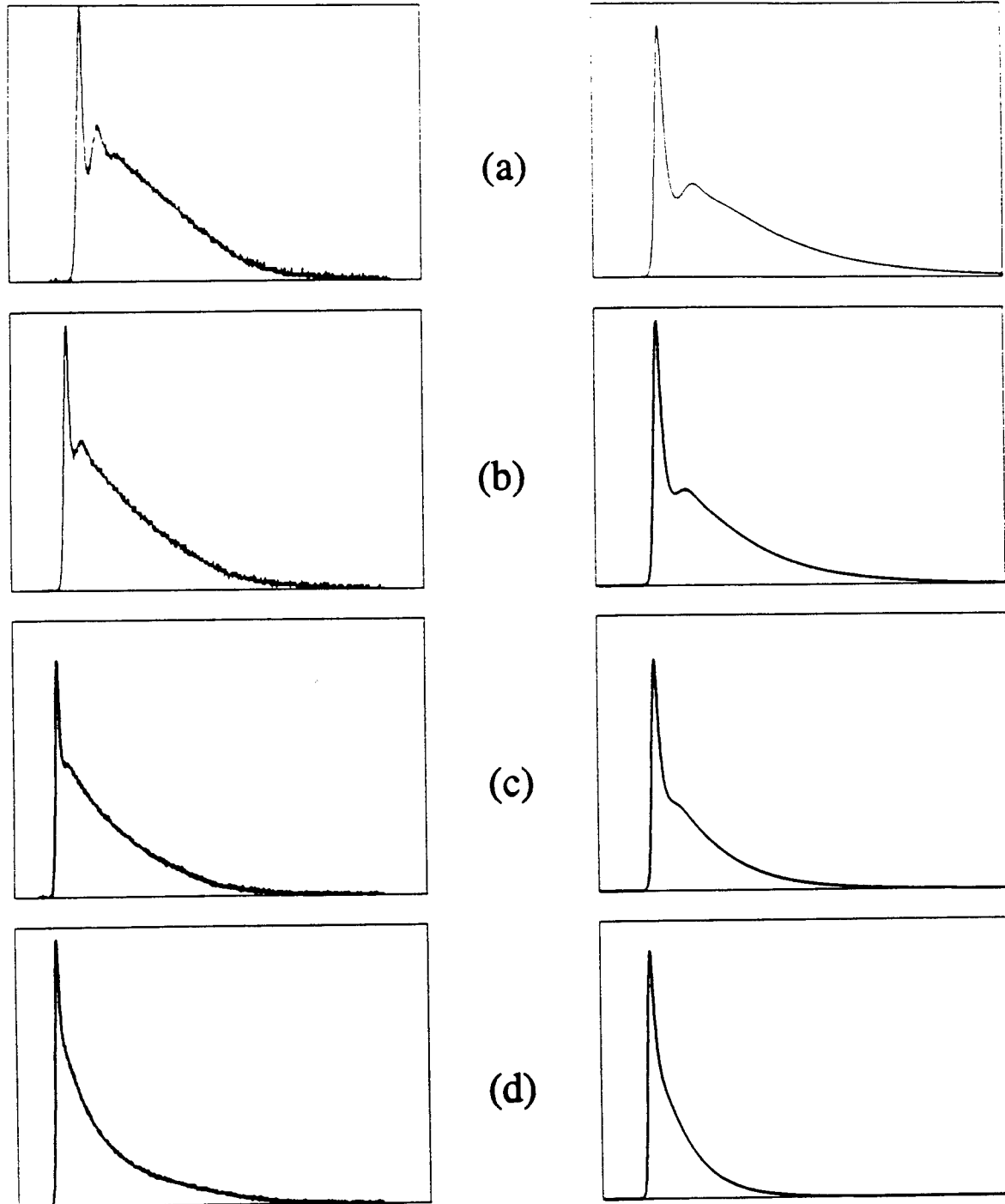


**Figure 8:** Measured (left) and calculated (right) pulse profiles. The experimental data corresponded to 0.6 Torr CF<sub>3</sub>I plus (a) 0 Torr, (b) 0.3 Torr, (c) 0.6 Torr, and (d) 0.9 Torr Xenon buffer gas. For the numerical simulation we assumed  $T_b/T_v = 0.38$  and changed  $T_b$  from 650 ns to 260 ns from top to bottom in increments equal to the total gas pressure change. The length of the time axis is 6  $\mu$ s for all the profiles.

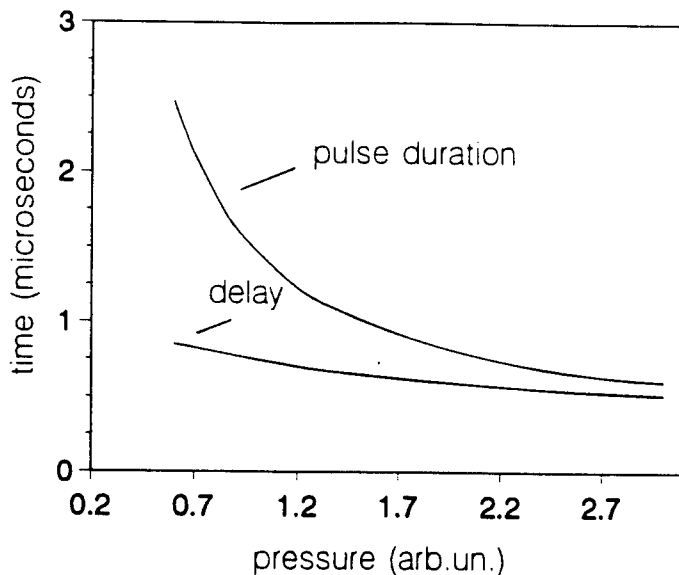


**Figure 9:** Delay between pump pulse and the ten percent of peak value of the iodine pulse and decay time of the iodine pulse as a function of the buffer gas pressure. In the simulation we actually changed the values of  $T_v$ ,  $T_b$  as described in the text.

as function of buffer gas composition and pressure. This new type of "spectroscopy" would not require an additional probe laser.

## 4 Summary

The dynamics of gain switched iodine lasers at low pressure is determined by collisional relaxation processes involving a change in the direction of the velocity vector and a change of its magnitude. Both relaxation constants depend on the gas pressure and the type of buffer gas (if any). A comparison of experimental data with a computer simulation allows one to determine these relaxation rates. Important pulse features that need to be analyzed and modeled are the pulse build-up time, the pulse shape and its decay time. The two relaxation mechanisms provide a repumping mechanism of a single mode iodine laser which manifests itself in the occurrence of a distinct shoulder and a second pulse peak at low gas pressure.

## References

- [1] M.A.Kelly, J.K.McIver, R.F.Shea, and G.D.Hager. *IEEE J. Quantum Electron.*, QE-27:263, 1991.
- [2] G.Brederlow, E.Fill, and K.J.Witte. *The high-power iodine laser*. Springer, 1983.
- [3] L.A.Schlie and R.D.Rathge. *Opt.Commun.*, 66:289, 1988.

- [4] C. M. Ferrar. *Appl. Phys. Lett.*, 12:381, 1968.
- [5] H.J.Baker and T.A.King. *J.Phys.D:Appl.Phys.*, 8:L31, 1975.
- [6] A.S.Grenishin, V.M.Kiselev, and T.N.Koltlikova. *Opt.Spectrosc. (USSR)*, 52:212, 1982.
- [7] J. I. Cline, C. A. Taatjes, and S. R. Leone. *J. Chem. Phys.*, 93:6543, 1990.
- [8] R. Schmiedl, H. Dugon, W. Meier, and K. H. Welge. *Z. Phys. A*, 304:137, 1982.

AN INVESTIGATION OF FLIGHT CHARACTERISTICS  
OF THE ROCKET ELECTRIC FIELD SOUNDING VEHICLE

Sean R. Olin  
Graduate Student  
Department of Aerospace and Mechanical Engineering

Boston University  
110 Cummington St.  
Boston, MA 02215

Final Report for:  
Graduate Student Research Program  
Phillips Laboratory

Sponsored by:  
Air Force Office of Scientific Research  
Bolling Air Force Base, DC

and

Phillips Laboratory

September 1994

AN INVESTIGATION OF FLIGHT CHARACTERISTICS  
OF THE ROCKET ELECTRIC FIELD SOUNDING VEHICLE

Sean R. Olin  
Graduate Student  
Department of Aerospace and Mechanical Engineering  
Boston University

Abstract

The Rocket Electric Field Sounding (REFS) rocket is part of a program at Phillips Laboratory which examines electric fields present in thunderstorms. Numerous flights of this rocket have occurred, and some peculiarities have arisen. The rockets did not achieve the predicted apogee values, and the roll characteristics of the rocket show a region where the spinup is either stopped or significantly impeded. The work carried out this summer focused on the potential for higher drag occurring during flight to account for the lower altitudes as well as an investigation of the fin aerodynamics with respect to the rolling motion of the rocket. The preliminary results of the research show that the roll plateaus can be explained due to high induced fin angles of attack in the thrusting phase, and that a combination of higher than expected drag and lower than expected thrust probably caused the lower apogee of the rocket.

AN INVESTIGATION OF FLIGHT CHARACTERISTICS  
OF THE ROCKET ELECTRIC FIELD SOUNDING VEHICLE

Sean R. Olin

I. Introduction

The program for the Rocket Electric Field Sounding (REFS) payload and rocket arose from a need to determine the conditions in thunderstorms. Lightning activity can be particularly dangerous when a rocket launch is involved. A rocket, since it maintains the electric potential of the ground from whence it was launched, can be vulnerable to a lightning strike. As can be shown from several of these occurrences in the past, a lightning strike has the potential for causing damage to equipment and can jeopardize a mission. The REFS program is aimed at measuring the electric field in a thunderstorm. This information is used to derive a vertical picture of the conditions related to lightning activity. A rocket is superior to a balloon or an aircraft in this instance due to the nearly instantaneous nature of the data which can be collected.

The REFS rocket consists of a motor and a payload, shown in Figure 1. The motor is a surplus Folding Fin Aircraft Rocket (FFAR), and the experimental payload is housed in a design which incorporates a rotating outer shell. The rotation of this shell allows electrodes to be periodically exposed to the electric field through which the rocket passes. The entire rocket is imparted with a spin as well, as the rocket motor nozzles are scarfed. The fins of the FFAR are folded back to be in line with the axis of the rocket at launch. Upon leaving the launch tube, the fins rotate about their pinned axes to assume a near 45 degree sweep angle. The burn time of the rocket motor is approximately

1.6 seconds, after which the REFS coasts for up to a minute. Data for the electric field as well as accelerometer and roll rate information is collected for as much of the flight as is possible.

Initial flights were made from the NASA Wallops Flight Facility in 1990, using 40 FFAR motors with mass models of the payload attached. The motors had scarfed nozzles but no fin cant. REFS flights into thunderstorms were launched at Langmuir Laboratory in New Mexico in 1992. The flights made in 1992 are the basis for the research performed this summer. One problem was the overprediction of flight apogee. Figure 2 shows altitude versus range data for the 1992 flights. The nominal prediction for the trajectory is compared to the trajectories for the flights. In all cases, the apogee was the flight characteristic deemed most important to match. Previous work done on this problem involved manipulating the drag coefficients of the rocket in a trajectory simulation program until the altitudes predicted by the program closely followed the flight data. The drag coefficient manipulation involved drag multiplication factors of 1.65 and 2.25 for the 0.87 degree and 1.68 degree fin cant flights, respectively {1}. The need for such large drag multipliers which increased as a function of fin cant pointed to an additional problem to be addressed. Specifically, some mechanism must have caused the flights to achieve lower than expected altitudes, and the apogee values decreased as more fin cant was present.

The REFS flights in 1992 used rocket motors whose fins had varying degrees of cant angle, which is akin to an inherent angle of attack for the fin. The fins for a particular motor would all have the same cant, but these cants were measured to be 0 degrees (no fin cant), 0.87 degrees, and 1.68 degrees. It is reasonable to infer that a fin cant would impart a spin to a

rocket in addition to that induced by the scarfed nozzles. This is borne out in Figure 3, which shows the rotation rates of the rocket during the first ten seconds of the flight. Note that flight data for an earlier flight with no fin cant has been included. Careful examination of the graph shows one of the problems to be investigated. There is a region in each of the flights which begins at approximately  $T +0.4$  seconds and ends at approximately  $T +1.0$  seconds during which the roll rate (spin) of the rocket is held constant or increases at a rate which is lower than either before or after the time period noted. The phenomenon would also be looked at as a thrust of the summer research.

## II. Methodology

### A. Familiarization with the Project

The first phase of the research involved learning about the REFS project and previous work involved with the problems seen. Some potential causes for higher than expected drag were found in this phase. The flights in 1990 did not involve fins that were canted. Cant angle could provide an additional surface for pressure drag, and the higher roll rates induced could induce the effective drag divergence of the fins earlier in the flight, i.e. at a lower Mach number. In addition to the fin cant, there are two bumps, or protuberances, present on the body of the rocket that were not extant for the 1990 flights [1]. Rocket geometry alteration was the first issue to be addressed when seeking to alter the rocket drag coefficients.

### B. Use of Missile Datcom

An aerodynamic coefficient predictor program was an integral part of the research. Missile Datcom, developed in conjunction with the U. S. Air Force, is just such a program [2]. It allows for the input of desired flight conditions for a vehicle, the geometry of the vehicle, and an indication of desired

output. The program then uses various potential flow and Newtonian flow methods to determine coefficients for the input vehicle over a range of Mach numbers and angles of attack. These coefficients, such as those for drag, lift, moment, rolling, pitching, and yawing, as well as the changes of these with angle of attack, can then be used in a trajectory prediction program to ascertain flight characteristics of a rocket.

Since drag prediction was the most erroneous to date, the drag coefficients of the REFS rocket were altered through the addition of the latest bump geometries and most recent rocket lengths. The results showed a slight increase in drag coefficient, especially in the transonic regime (Mach 0.7 to Mach 1.3). It was hoped that this drag increase could account for the lower apogees, but it was immediately seen that the order of magnitude of the drag coefficient increase from geometry alone was not sufficient. In addition to the geometry alteration in Missile Datcom, a potential for the addition of fin cant angle was incorporated. However, the program showed the increase in drag coefficient due to fin cant to be so slight as to be negligible. At this point, the latest aerodynamic coefficients were taken to be incorporated into a trajectory program.

#### C. Usage of Trajectory Program

One of the trajectory programs used by the researchers at Phillips Laboratory is known as GEM, which is another name for the program LRC-MASS {4}. It is a code maintained by the NASA Wallops Flight Facility, and it provides trajectory estimates in three and six degree of freedom situations. There is an extensive input deck which must be built up for the program. Dr. George Jumper {3} has written a code for an input deck generator known as GIP. It was used to build up the input deck for the REFS research. The three degree of freedom

solution was sought and achieved first, and it showed an apogee for the zero fin cant angle case which was significantly higher than that achieved by the 1992 flights. Since the rocket spins throughout its flight, the six degree of freedom (6DOF) solution was generated next.

The input deck for the 6DOF solution involves the listing of launch conditions, rocket motor information, burn time, rocket aerodynamic conditions, choice of flight phases, and selection of desired output. What results is a coherent input deck that is easily altered as updated rocket information becomes available. The ease of input deck alteration proved to be a bonus during the summer, as numerous GEM runs could be made with a minimum of lead time once the initial input deck had been constructed.

The first 6DOF runs using GEM involved the new aerodynamic coefficients determined through Missile Datcom. The flight prediction was set to emulate the 1992 Langmuir flights, which were at an altitude of 10400 feet. The earlier work had predicted a baseline apogee of 30213 feet above sea level (ASL), which corresponds to 19813 feet above ground level (AGL). The first successful GEM run showed a new prediction of 29011 ft. ASL (18611 ft. AGL). Although this was deemed a better prediction of the zero fin cant flight apogee, it was clear that geometry alteration alone could not account for the lower apogee.

Another facet of the flights investigated using GEM was the spinup of the rocket during thrusting flight, and the subsequent coasting roll rates. Since no fin cant was incorporated into the input deck, the corresponding roll inducement coefficient ( $C_{l\delta}$ ) was set to zero. Roll inducement for this baseline case was solely due to the scarfed nozzles. This was reflected during the input of the rocket motor characteristics. Previous work assumed that 1.468 lb thrust would be directed normal to each of the four nozzles to impart a spin

{5}. The initial rocket angular acceleration (rate of spinup) can be seen to be nearly constant before the roll plateau (Figure 3), so the rocket torque was inferred for this period of the flight by the following relation:

$$(I_{xx} \times \alpha) = RT$$

where  $I_{xx}$  is the second moment of inertia about the x (longitudinal) axis,  $\alpha$  is the angular acceleration of the rocket, and  $RT$  is the rocket torque induced by the scarfed nozzles. Using known values for  $I_{xx}$  at launch and the angular acceleration during the first 0.33 seconds of flight from flight data, a rocket torque of 1.076 ft-lb was calculated. The position of the nozzles on the rocket was known, so the actual thrust from each nozzle could be determined. The thrust from each nozzle turned out to be 4.56 lb, much greater than the previously assumed 1.468 lb value.

The two mechanisms for spinup, namely roll inducement from the fins (using  $C_{l\delta}$ ) and the rocket torque, are opposed during the flight by roll damping. Roll damping is defined by the relation

$$Cl_p \times \left( p \frac{b}{2v} \right) \times qSb = RD$$

where  $Cl_p$  is the roll damping coefficient,  $p$  is the roll rate,  $b$  and  $S$  are reference length and area, respectively,  $q$  is the dynamic pressure, and  $v$  is the rocket velocity. For a roll damping (RD) which opposes the roll inducing torques,  $Cl_p$  will be negative. The roll damping coefficient had previously been set at -0.667. The combination of  $Cl_p$  with the previously mentioned

rocket torque estimation yielded a roll damping after burnout which was a fair match to previous data from FFAR flights {5}. Some time was devoted to determination of a reliable estimate for roll damping based on missile geometry. J. L. Nielsen {6} provides an initial estimation for defining  $C_{l_p}$  based on the rocket fin to body diameter ratio. For the REFS rocket, the ratio is 4.158, which results in a  $C_{l_p}$  of -1.01. This is higher than the previous prediction.

The new values for roll damping and rocket spin were incorporated into a GEM input deck. The resulting spinup prediction can be seen in Figure 4. It is clear that the initial spinup is well accounted for, but there is no indication that GEM predicts a roll plateau. Further investigation was needed.

#### D. Roll Rate Plateau

Since the major contributor to roll damping is the fin set of a rocket, fin aerodynamics were looked at to determine the cause of the unexpected reduction in spinup rates. As a rocket spins, its fins 'see' an angle of attack based on the roll rate of the rocket and the rocket velocity according to the relation

$$\alpha(y) = (p \times r(y)) / V$$

where this 'induced' angle of attack at any lateral location along the fins ( $\alpha(y)$ ) is based on roll rate  $p$ , lateral location  $r(y)$ , and free stream velocity  $V$ . The small angle assumption is used, allowing for disregard of a tangent term. This rolling angle of attack clearly varies along the fin, with the highest value being at the tip and the lowest being at the root of the fin. If there is an existing fin cant ( $\delta$ ), the local angle of attack can be found by the subsequent formula:

$$\beta(y) = (\delta - \alpha(y))$$

A local angle of attack is equivalent to the angle of attack which the fin 'sees' for the incoming flow. Figures 5 is set up to show the relationship between induced angle of attack and the roll rate to free stream velocity ratio ( $p/V$ ) for one of the flights of REFS. The angle  $\alpha$  varies linearly with  $P/V$  and lateral distance along the fin. The graph shows that the entire fin is in the 'overspeed' condition for the majority of thrusting flight. Overspeed occurs on a fin when the induced angle of attack is greater than the fin cant angle, thus causing the local angle of attack for the entire fin to be negative.

An opposing aerodynamic torque is then set up whereby there is a normal force on each section of the fin acting opposite to the direction of rotation. A sectional method was applied using the Missile Datcom normal force coefficients at Mach number and angle of attack to find a torque. Each discrete lateral location on the fin has a local angle of attack, normal force, and torque contribution at any time in the flight. The normal force coefficients, normalized by the fin length (tip - root) were integrated over the fin length from root lateral distance ( $rr$ ) to tip lateral distance ( $rt$ ) to calculate a torque coefficient for the fin.

$$Ct = \int_{rr}^{rt} ((Cn)/L) r dr$$

The aerodynamic torque opposing the rocket rotation could then be determined by the following formula:

$$AT = 4 \times C_d \times q \times S$$

For the case of the 0.87 degree fin cant flight where the time was chosen to be the onset of the roll plateau, this opposing torque was calculated to be -0.9294 ft-lb, which is nearly equal to the rocket torque (1.076 ft-lb). This result, along with similar indications at other times in the roll plateau, leads to the conclusion that a slowdown or halt to the spinup will occur in the flight of the rocket whenever the induced angles of attack over the whole fin are sufficiently high enough to create relatively high negative total angles of attack and significant impeding aerodynamic torques.

The roll plateau begins when the roll rate is high enough to cause high  $\alpha$  values, and it ends when the free stream velocity is high enough to reduce the induced angle of attack. The plateau is only seen in thrusting flight, where the high overspeeding is in effect. Well behaved spin-down behavior is predicted and seen after burnout, as the roll rates are near equilibrium.

#### E. Examination of Accelerometer Data

With the roll plateau explanation worked out, a solution for the lower apogees was again actively sought. The new baseline drag profile set up and used in the flight predictions did not adequately explain the lower burnout velocities and altitudes, so an intense survey of flight data was begun.

Accelerometer data exists for three of the 1992 Langmuir flights. This data was manipulated to set up a profile of each flight which listed flight time, acceleration, velocity, altitude, flight path angle, and downrange distance. Based on this information, the drag that the rocket experienced during its flight was calculated. The rocket drag was found from the relation:

$$Drag = (T - m \times (a + g \sin \gamma))$$

where T is the rocket thrust, m is rocket mass, a is rocket acceleration, g is gravitational acceleration, and  $\gamma$  is flight path angle.

To be able to determine drag, the thrust profile needed to be known. The rocket motor used has documentation which includes the measured thrust profile and average thrust. Since the motors are quite old, a lower value of average thrust was used [3]. This is the thrust that had previously been incorporated into the GEM input decks for flight predictions. Since the total thrust profile by no means showed a constant thrust during the burn (Figure 6), the varying thrust was used in the accelerometer data analysis. It was scaled to meet the total impulse that would result from an average thrust value over the burn time. Total impulse is defined as the integral of thrust over the burn time. For the REFS rocket, total impulse was calculated to be 1106 lb-sec. Rocket weight was also needed, and it was determined according to the relations:

$$Weight(t) = (Weight(t - \Delta t) - Impulse(t) \times (W_p) / (I))$$

$$I = \int_0^{bo} Thrust(t) dt$$

where  $Impulse(t)$  is the total impulse up to the time in question,  $W_p$  is the propellant weight (6.4 lb), and I is the total impulse as defined.

By synchronizing the start of the burn phase to coincide with the start of nonzero accelerometer data, a drag profile for the flight was generated. It

became apparent that very high drag values were being calculated. The drag, when divided by reference area ( $S$ ) and dynamic pressure ( $q$ ), can be expressed as a drag coefficient  $C_d$ . Figure 7 shows  $C_d$  vs. Mach number for the best estimate of thrust and start time to date. After burnout, a picture of coasting drag conditions was generated, and coasting  $C_d$  vs. Mach number is shown in Figure 8.

What results is apparently a much greater amount of drag during the flights than has been previously estimated. However, the magnitude of the increase is too great to be accounted for by the transonic drag rise due to roll alone. One of the first indications that this is so is the fact that the flight data drag and  $C_d$  values are much higher than the Missile Datcom predictions throughout the entire thrusting phase; yet the actual drag coefficients bracket the Datcom predictions during coasting flight. It is also interesting to note that coasting drag coefficients are generally predicted to be higher than thrusting drag coefficients, yet this is not borne out in the flight data.

The thrust values used are a likely source of the anomaly in the accelerometer data. Due to the nature of the drag determination, an erroneous thrust profile will cause an erroneous drag result. Another set of accelerometer data was manipulated to set up the flight characteristics given from accelerometer data and thrust and weight equations. This set of flight data is from a flight which used fins with 1.68 degrees of cant. The hypothesis was that the effects of increased drag due to the fins and rocket rotation, which were present with 0.87 degrees cant, would be even more pronounced for 1.68 degrees cant. Any discrepancies in thrust from predicted to actual values were assumed to be the same for both flights. Figures 7 and 8, which also compare the  $C_d$  values (thrusting and coasting, respectively) given for the two flights

examined as well as the Missile Datcom predicted Cd values, show that the Cd values are higher in the transonic range, as expected, for the 1.68 degree fin cant flight. Erroneous thrust data would be present in both cases, and any Cd increase between the two cases could therefore not be due to thrust variation. What is interesting is that the effect of increased drag for increased fin cant shows up in thrusting as well as coasting flight. Sudden discontinuities at start and burnout result in the lack of knowledge as to exact times for those occurrences.

After the increased drag had been shown to be present, the flight data drag coefficient values were incorporated into a GEM input deck, and a prediction was run. If the apogee predicted was sufficiently close to the actual flight in question, the results of the previous analysis could be trusted. The GEM run to predict the apogee of a 0.87 degree fin cant flight showed a value of 26757 ft. ASL (16357 ft. AGL), which is comparable to the previous work which predicted an apogee of 26080 ft. ASL (15680 ft. AGL) using drag multipliers.

### III. Results

The summer research focus was on the problems of the roll rate plateaus and the lower than expected apogees seen during the rocket flights. Use of Missile Datcom allowed aerodynamic coefficients to be found, which, combined with rocket dynamic theory, give a suitable explanation for the roll plateau.

The drag problem is more difficult to solve. The flight data was analyzed, and the analysis was constantly checked using trajectory predictions. What results is a clearer picture of what happens to the rocket during its flight, especially with respect to thrust and drag. It has been shown that a definite effect of fin cant on drag exists.

Another result of the work is that the assumed thrust values used in previous analyses are too high. The best estimate for flight apogees were found with a thrust profile which was 20% lower than previously assumed. This allowed for a drag multiplier to be necessary only during coasting flight, and it was set to a much more reasonable value.

#### IV. Conclusions and Recommendations

The project is by no means complete, although the summer term has reached an end. The success of the aerodynamic analysis with respect to rolling flight leads to the conclusion that a thoroughly worked out solution can be achieved. More work in this area will include checking and publishing the results of the roll rate plateau investigation.

In addition to the roll plateau, the entire roll profile from flight data should be developed and continued. A cogent prediction for torques acting on the rocket has been described, and this can be incorporated into a means of predicting roll more accurately.

The problem of added drag from bumps on the body of REFS was addressed through the use of Missile Datcom, but it is to be noted that the program does not deal well with jump discontinuities in body geometry. The resulting geometry is smoother than the actual bumps, but the flow profile over these bumps most likely follows a smooth path as well. Research should be devoted to determining whether this is indeed the case.

An analysis of drag due to rolling was performed in a manner similar to that which solved the roll plateau problem. However, it did not predict a greater drag on the fins due to induced angles of attack. An application of the sectional method to drag in fact induced a thrust due to the overspeed condition. There must be a means of quantifying the drag rise, if any, on rocket

fins due to rolling. There persists an effect seen in the flight data in both thrusting and coasting flight. Coasting flight remains of interest due to the fact that it accounts for the vast majority of the flight time.

The summer research provided an excellent means of applying previous and new knowledge to an interesting flight mechanics study. Portions of the problem were solved, while valuable insight was gained on other aspects which will prove useful to future research.

#### V. Figures

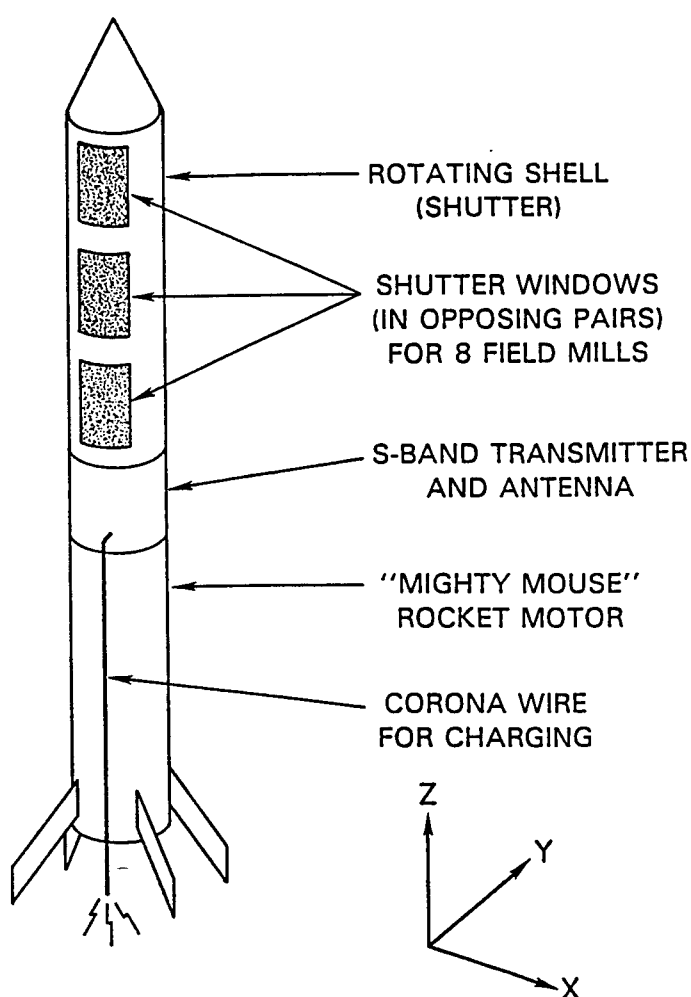


Figure 1

REFS Vehicle Diagram {1}

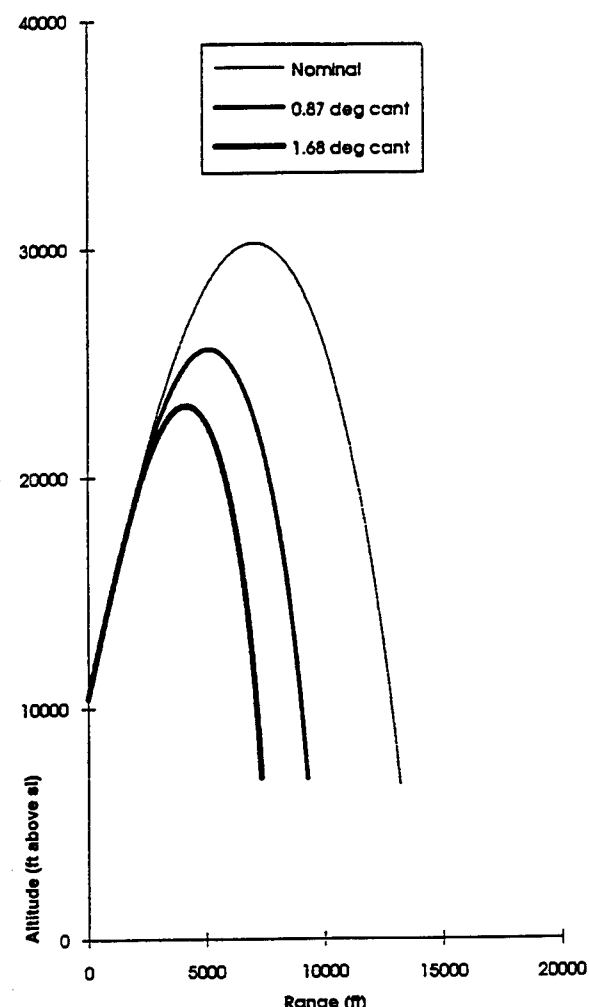


Figure 2

Altitude vs. Range for 1992 Flights {1}

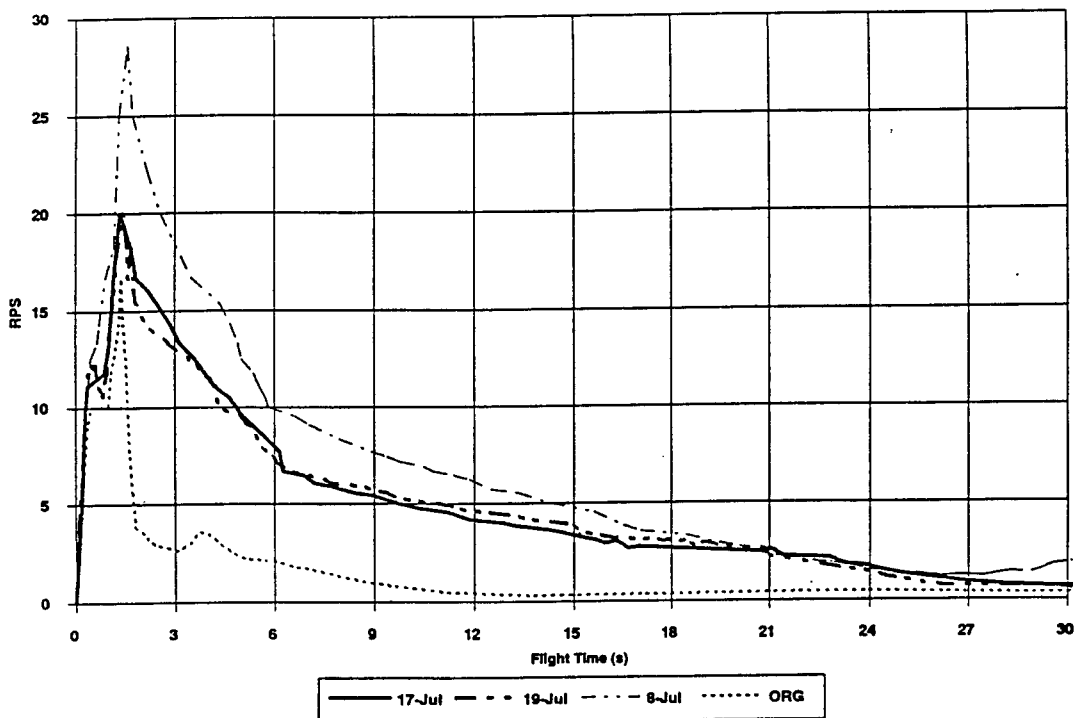


Figure 3  
Rocket Rotation Profile (1)

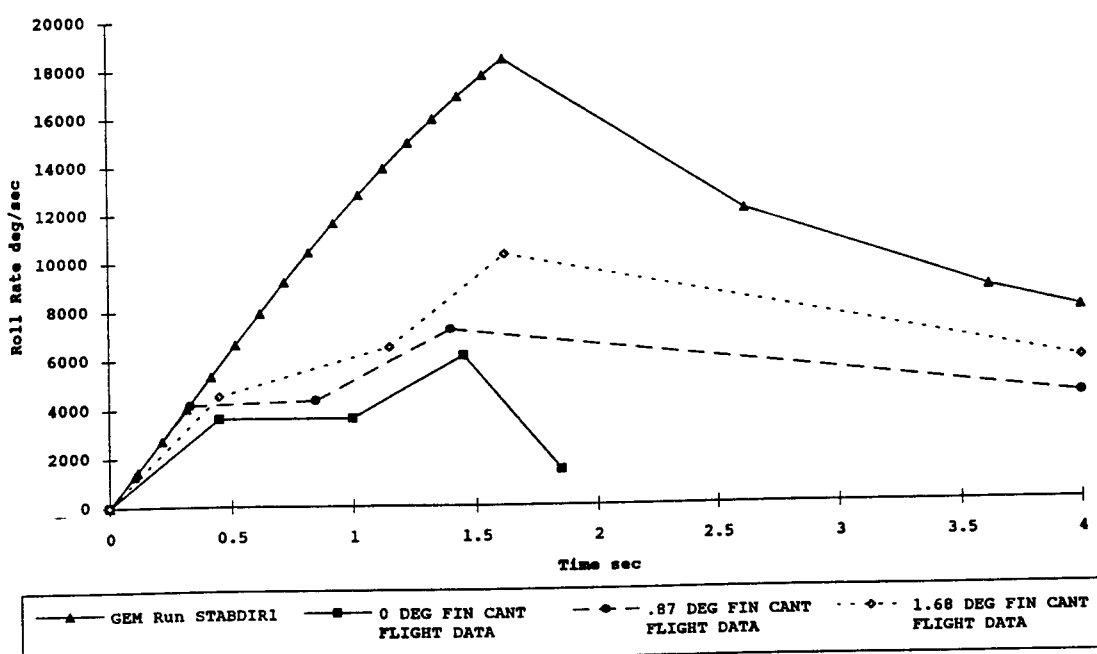


Figure 4  
Roll Rate vs. Time for Predictions and Flight Data

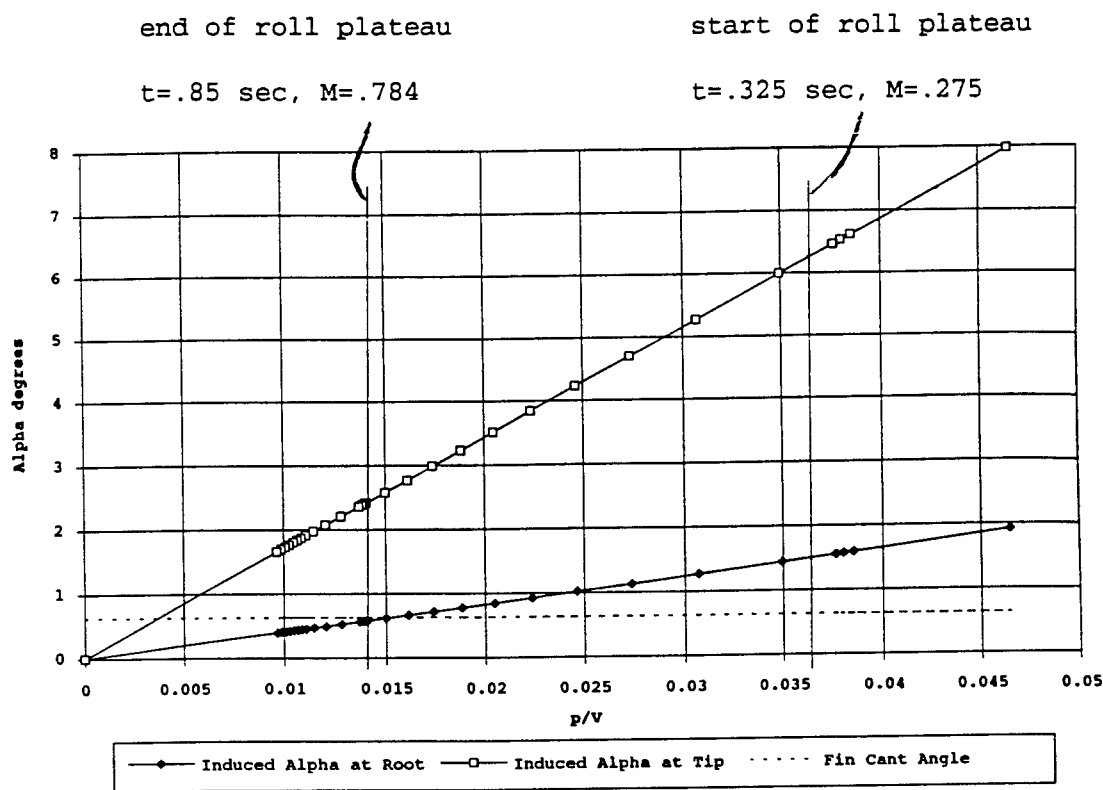


Figure 5  
Induced Angle of Attack Variation

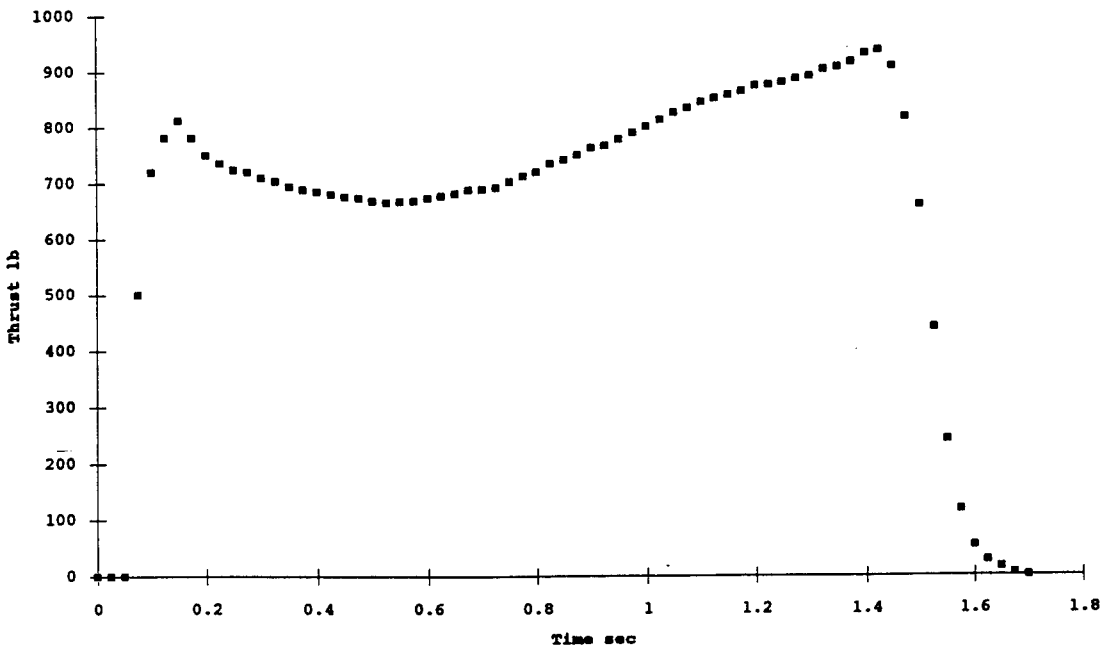


Figure 6

Thrust Profile for REFS

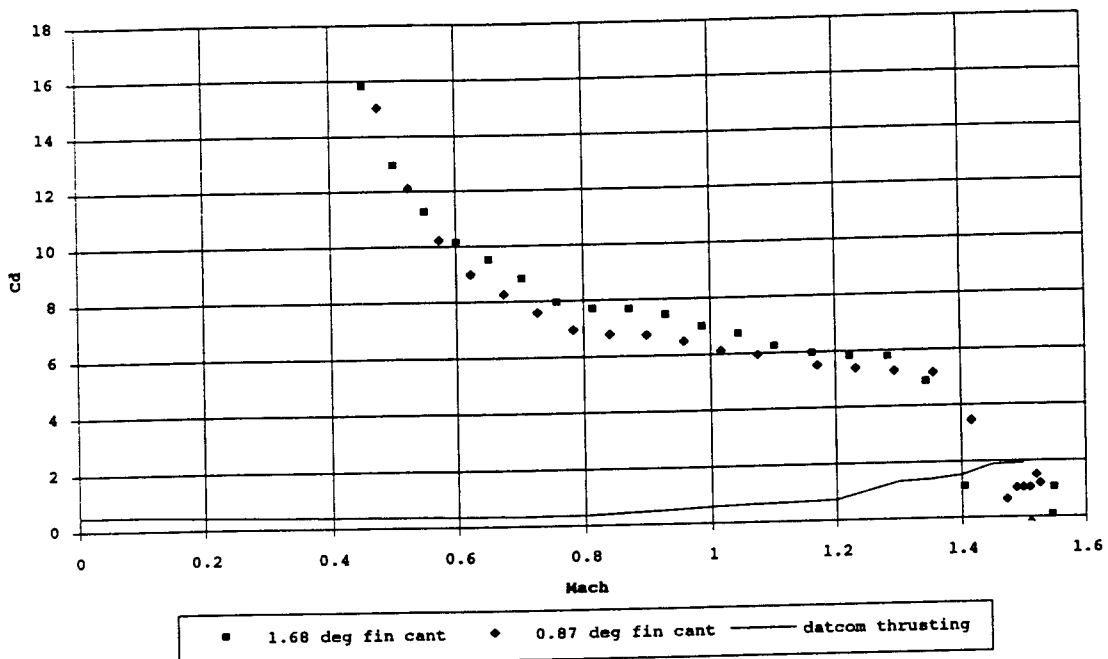


Figure 7

Drag Coeff. Comparisons (Flight Data and Datcom) for Thrusting Flight

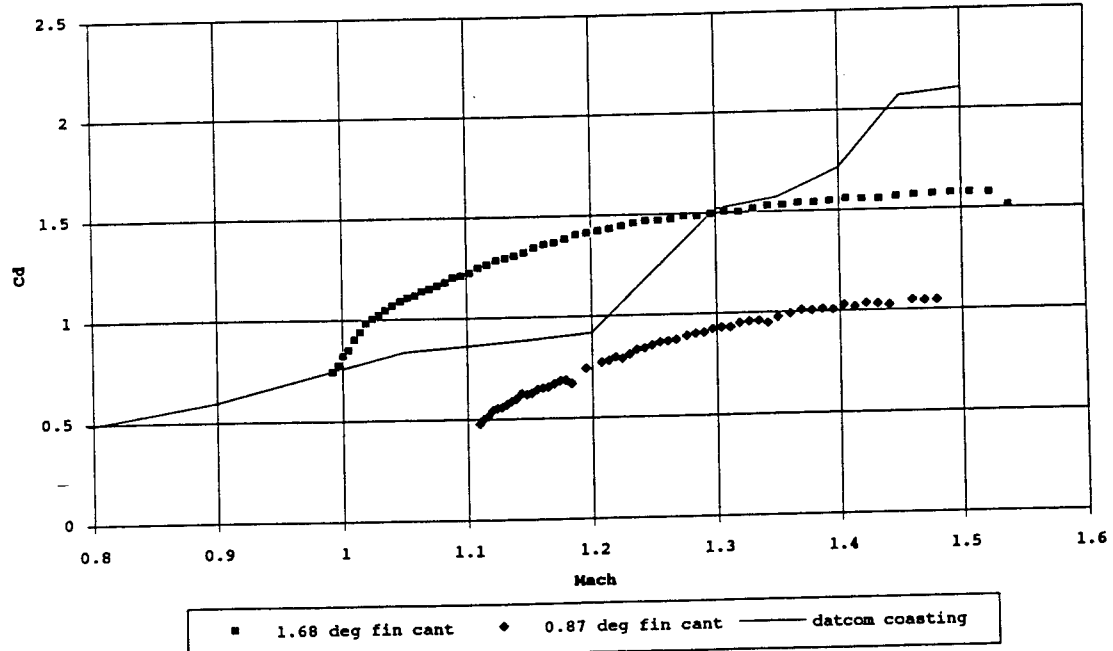


Figure 8

Drag Coeff. Comparisons (Flight Data and Datcom) for Coasting Flight

## VI. References

1. Willett, J. C., Curtis, D. C., Jumper, G. Y., and Thorn, W. F., (1993) *Three Flights Into Thunderstorms with the Revised Rocket Electric Field Sounding (REFS) Payload*, PL-TR-93-2182, Phillips Laboratory, Directorate of Geophysics, Hanscom AFB, MA.
2. Vukelich, S. R., Stoy, S. L., and Moore, M. E., (1988) *Missile Datcom User's Manual*, AFWAL-TR-86-3091, Flight Dynamics Laboratories, Wright Patterson AFB, OH.
3. Jumper, G. Y., Phillips Laboratory, Directorate of Geophysics, Hanscom AFB, MA, (9/21/94) Teleconference with Walter O'Keefe, ARDEC, SMCAR-AET-A, Picatinny Arsenal, NJ.
4. Smith, K. A., and Lewis, J. L., editors, (1970) *LRC-MASS Program User's Manual*, Langley Research Center, Langley, VA.
5. Jumper, G. Y., Frushon, C. J., Longstreth, R. K., Smith, J., Willett, J., and Curtis, D., (1991) *Effects of Magnus Moments on Missile Aerodynamic Performance*, PL-TR-92-2168, Phillips Laboratory, Directorate of Geophysics, Hanscom AFB, MA.
6. Nielsen, J. N., (1960) Missile Aerodynamics, McGraw-Hill Book Company, New York, NY.

THERMOLUMINESCENCE OF SIMPLE SPECIES  
IN MOLECULAR HYDROGEN MATRICES

Janet Petroski  
Graduate Research Associate  
Department of Chemistry

California State University, Northridge  
18111 Nordhoff Avenue, CHEM  
Northridge, CA 91330-8262

Final Report for:  
Graduate Student Research Program  
Phillips Laboratory

Sponsored by:  
Air Force Office of Scientific Research  
Bolling Air Force Base  
Washington, DC

and

Phillips Laboratory  
Edwards Air Force Base, CA

September, 1994

THERMOLUMINESCENCE OF SIMPLE SPECIES IN SOLID MOLECULAR HYDROGEN MATRICES

Janet Petroski  
Graduate Research Associate  
Department of Chemistry  
California State University, Northridge

Abstract

In an attempt to develop chemical propellants which would exceed the performance of the current state of the art liquid oxygen/liquid hydrogen system, we are revisiting the concept of using atomic and molecular radicals as high energy additives to cryogenic solid molecular hydrogen (SMH) fuels. This report details our efforts to produce and characterize samples of prototypical SMH fuels which will yield visible thermoluminescence (TL) from radical recombination upon warm up. This TL property will be used as a diagnostic of fuel stability in subsequent storage and handling experiments. The simple gases: N<sub>2</sub>, O<sub>2</sub>, CO, CO<sub>2</sub>, and CH<sub>4</sub>, as well as various mixtures of N<sub>2</sub> with the others, passed through a microwave discharge and were co-deposited with gaseous D<sub>2</sub> at 3 K. The TL emission spectra, and total TL intensity were recorded during warm up of these samples. Most TL emission from the D<sub>2</sub> matrices occurred between 4 and 8 K. N<sub>2</sub> was the only gas which yielded TL by itself, while O<sub>2</sub> and CO were the only gases to yield new TL emissions in N<sub>2</sub> mixtures. N<sub>2</sub> was also discharged and deposited without D<sub>2</sub> gas, and TL was observed from these samples. The transitions evident in the TL emission spectra have been assigned and a kinetic scheme has been proposed for nitrogen TL due to recombining N atoms. The strongest feature in these spectra was assigned to the Vegard-Kaplan bands A<sup>3Σ<sub>u</sub>+</sup> → X<sup>1Σ<sub>g</sub>+</sup> of molecular nitrogen. Along with an N atom emission due to the 2p<sup>3</sup> (<sup>2</sup>D) → 2p<sup>3</sup> (<sup>4</sup>S) transition, a peak assigned to the 2p<sup>4</sup> (<sup>1</sup>S) → 2p<sup>4</sup> (<sup>1</sup>D) transition of the O atom was also observed (due to an air impurity). The analysis of the total TL intensity data includes a first attempt at fitting to a first-order kinetic model, which unfortunately yielded unphysical values for the N atom detrapping frequency factors and activation energies.

# THERMOLUMINESCENCE OF SIMPLE GASES IN MOLECULAR HYDROGEN MATRICES

Janet Petroski

## Introduction

This study was done to determine which simple gases can be discharged and co-deposited with D<sub>2</sub> at 3 K to produce materials which will yield visible optical emissions upon warm up, i.e., thermoluminescence (TL). These materials constitute prototypical High Energy Density Matter (HEDM) samples and will be used in laboratory-scale experiments to develop the new techniques required for producing, storing, and handling this new class of advanced propellants. As such, this study is part of a greater in-house effort at the Phillips Laboratory to adapt HEDM basic research<sup>1</sup> to applied research by coordinating it with the engineering aspects inherent in rocket propellant studies.

The interest in this area stems from the need for chemical propellants capable of surpassing the performance of the systems currently used. One HEDM concept is to use atomic and molecular radicals as high energy additives to cryogenic solid molecular hydrogen (SMH) propellants. These new advanced propellants will improve upon the performance of the current state of the art liquid oxygen/liquid hydrogen (LOX/H<sub>2</sub>) system. This effort is an extension of a program conducted by the National Bureau of Standards (NBS) in the late 1950's by Broida and his co-workers<sup>2</sup>. This program on the emission and absorption spectra of free radicals trapped in solids at low temperatures led to the conclusion that these additives would theoretically improve fuel performance.

The gases which are favorable candidates as precursors for high energy additives are evaluated experimentally in this study using standard matrix isolation spectroscopy (MIS) techniques. These systems will then be used in the scale-up experiment where they will be deposited directly onto a super-fluid helium surface. This experiment will produce a laboratory quantity of approximately one gram (ten cubic centimeters) of the doped SMH. By taking what is learned from the MIS experiments and expanding upon it, this research will

## THERMOLUMINESCENCE OF SIMPLE GASES IN MOLECULAR HYDROGEN MATRICES

Janet Petroski

help determine the relevant physical and chemical properties of the HEDM cryosolid prototypical fuel, especially its energy content and thermal properties and assist in resolving the issues of how to make, store, and handle the fuel.

The performance of a propellant system is characterized by the specific impulse,  $I_{sp}$ , which is a measure of the momentum transferred to the vehicle per mass of propellant expelled from the rocket engine, and is proportional to the mean velocity of the exhaust<sup>5</sup>. The specific impulse is related to the specific enthalpy of the chemical reactions taking place in the engine,  $\Delta H_{sp}$ , and to the mean molecular mass of the expelled propellant,  $m$ , by:

$$I_{sp} \propto \frac{(\Delta H_{sp})}{m}$$

Because of this relationship, the lowest molecular mass propellant is desired as well as those additives which increase the  $\Delta H_{sp}$ . Hence,  $H_2$  is ideal in the capacity as the matrix host. A survey of combustion energies of atoms and molecules with oxygen was conducted and indicates which gases will theoretically lead to significant improvements in the specific impulse when doped in SMH<sup>6</sup>.

These energetic species have been studied extensively for many years. The earliest experiments known on the spectra of radicals trapped in the solid state were performed independently by Vegard<sup>3</sup> and by McLennan and Shrum<sup>4</sup> in 1924. Their findings caused a considerable interest in this area and became the subject of many studies by these groups. After this initial attention, not much more work was done on radicals until the NBS Free Radical Program from 1956 to 1959<sup>2</sup>.

The advent of the MIS technique again led to further studies conducted on these radicals at low temperatures with the emphasis on various rare gas matrices<sup>7</sup>. Hydrogens as matrix hosts have not been frequently studied because of their high vapor pressure at the liquid helium boiling temperature<sup>8</sup>. But, this deterrent can be overcome by pumping on the liquid helium cryogen which lowers the temperature sufficiently to work in SMH matrices. Another problem of

## THERMOLUMINESCENCE OF SIMPLE GASES IN MOLECULAR HYDROGEN MATRICES

Janet Petroski

working with SMH not incurred with the rare gas matrices is the possibility of the SMH host reacting with the guest radicals. By insuring the reactions of the energetic species with molecular hydrogens are endothermic or have at least a slight activation barrier, this is no longer an obstacle. To date, many atoms including: Al, B, N, and O have been successfully trapped in the matrix<sup>9-12</sup>.

Although more information is being amassed on this subject all the time, there are still many questions which remain unanswered. Among the questions we hope to address in this work include: which radical species can be trapped in D<sub>2</sub>?; which species will react with the matrix host?; which species will yield TL?; and how does TL work (i.e. its mechanism)?.

The following section of this work presents a summary of the experimental apparatus, including schematic diagrams and descriptions of the data acquisition system and the vacuum and gas handling system. The results section depicts the TL emission spectra, glowcurves (the total TL intensity recorded during the warm up) and histograms of the data collected, as well as the spectral assignments of the emissions observed. The discussion consists of a detailed look at the excitation mechanism for the N/D<sub>2</sub> system and the data analysis completed to date. Lastly, the conclusions and recommendations section outlines further work to be done, including data analysis and other gases to try.

### Experimental

The experimental set-up is depicted in Figures 1 and 2. Figure 1 is a schematic diagram of the vacuum and gas handling system employed in the experiments. Figure 2 represents the data acquisition and sample area of the cryostat.

A liquid helium transfer cryostat (RG Hansen High Tran) can normally achieve cold tip temperatures as low as 4.2 K. A mechanical pump (Leybold Model

THERMOLUMINESCENCE OF SIMPLE GASES IN MOLECULAR HYDROGEN MATRICES

Janet Petroski

D40B) lowered the temperature to approximately 3 K by pumping on the liquid helium flow. Temperature readings were made with a temperature controller (Scientific Instruments Model 5500-1-25) connected to two sensors inside the cryostat. One of the sensors was mounted directly on the cold tip and the other on the far end of the sample substrate holder. An average was taken from these two readings for the reported matrix temperature.

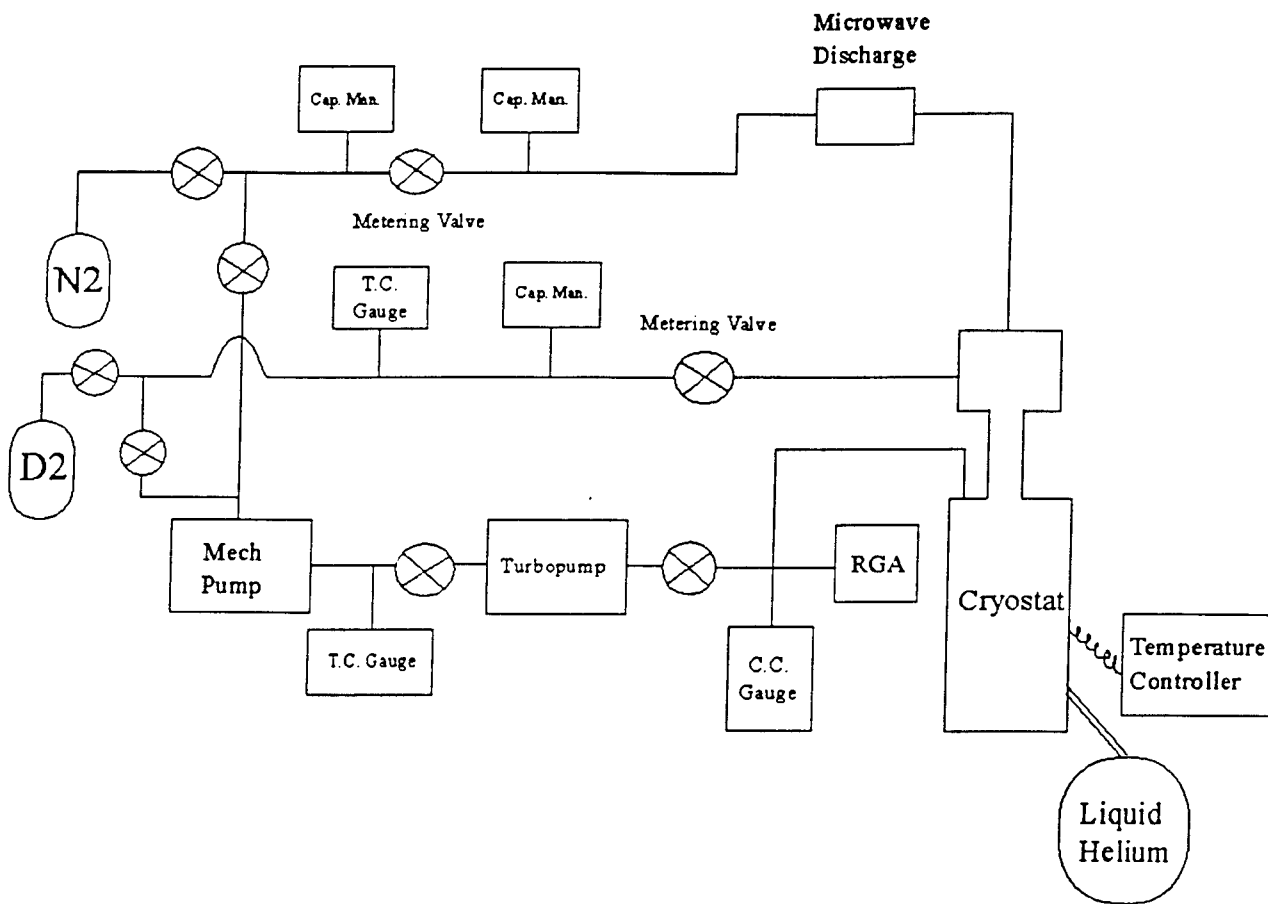


Figure 1. Schematic diagram of the vacuum and gas handling system used in these experiments. @ represents the valves in the vacuum line, RGA represents the Residual Gas Analyzer, C.C. Gauge is the cold cathode ionization gauge, T.C. Gauge is the thermocouple gauges, Mech Pump stands for the mechanical pump, and Cap. Man. is the capacitance manometers. See text for further explanation.

## THERMOLUMINESCENCE OF SIMPLE GASES IN MOLECULAR HYDROGEN MATRICES

Janet Petroski

Pressures as low as  $10^{-8}$  torr which are necessary for this cold temperature work were obtained using a turbo pump (Leybold NT 150/360) connected to a mechanical pump (Varian SD-200) and thermocouple gauge (Varian 801) (see Figure 1). A cold cathode ionization gauge (Varian 860A) and a Residual Gas Analyzer (RGA) (Spectra Vacscan) were used to determine the total pressure in the lines, and identify of the gases present from the mass spectrum. The RGA showed the main residual gases to have charge-to-mass ratios of 28, 18, 32, 17, 44, and 1 and were attributed to air ( $N_2$ ,  $O_2$ ,  $CO_2$ ) and water ( $H_2O$ ,  $OH^-$ , and  $H^+$ ) impurities.

The experiments were conducted using research grade gases (Air Products for  $D_2$  (99.0% purity) and  $CH_4$  (99.0% purity); Matheson for CO (99.5% purity); and Alphagaz for  $N_2$  (99.995% purity),  $O_2$  (99.999% purity), and  $CO_2$  (99.995% purity)). Mixtures of two gases were made directly in the vacuum lines by alternately adding the gases and the letting stand between 30 to 90 minutes to encourage mixing. The oxygen impurity occurred from a leak in the vacuum line above the microwave discharge.

The gases were deposited onto a cold sapphire plate fixed at a  $45^\circ$  angle from the base (see Figure 2). The guest matrix gas flowed through a microwave discharge (OPTHOS) set at a power level between 40 and 100 W (OPTHOS Power Supply). The microwave discharge consisted of a 12 mm diameter quartz tube surrounding a 6 mm diameter quartz tube with a 0.1 mm diameter pinhole opening. The outer tube was cooled by  $N_2$  gas during the discharge. A Tesla coil "ignited" the gas in the microwave discharge chamber. The discharge formed radicals from the sample gas which flowed through the pinhole opening and deposited onto the matrix window. The host  $D_2$  gas was deposited perpendicular to the window.

The matrix consisted of about 5% of the sample gas in the  $D_2$  host matrix. The composition was controlled by the flow rates of the gases. These flow rates were established by filling the two separate vacuum lines with the guest and host gases. The pressures of these lines were kept over atmospheric to minimize the

THERMOLUMINESCENCE OF SIMPLE GASES IN MOLECULAR HYDROGEN MATRICES

Janet Petroski

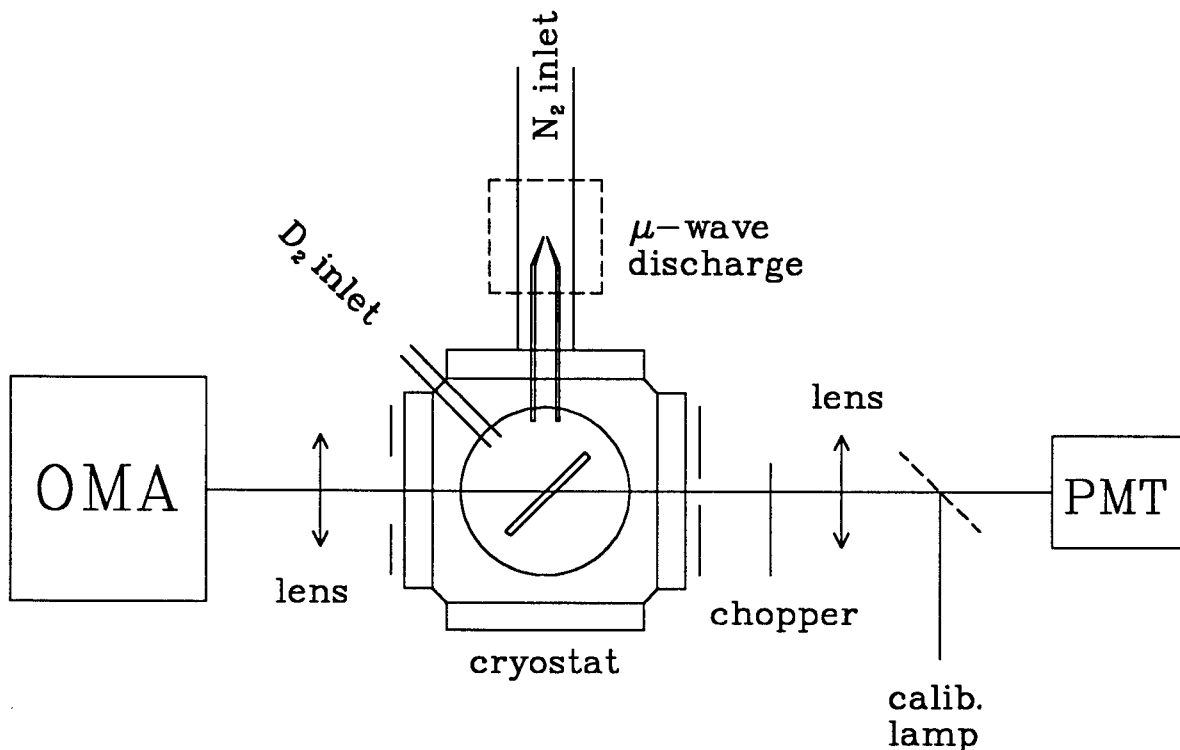


Figure 2. Schematic representation of the data acquisition system and sample region. See text for further explanation.

effects of any leaks which may have been in the lines (Baratron Capacitance Manometer for the sample gas and a Varian 801 Thermocouple gauge for D<sub>2</sub>). By adjusting the needle valves using the pressure readings from the two manifolds (PDR-C-2C Power Supply Readout for D<sub>2</sub> and a Datametrics 1500 Power Supply Readout for the microwave flow rate), the mixture composition of the matrix was controlled during the deposition. The flow rates were maintained at approximately 0.1 mmol/hr for the guest and 2.0 mmol/hr for D<sub>2</sub> gas. The microwave discharge pressure was kept between 100 and 150 mtorr.

After a 30 minute deposition, the microwave discharge power was shut off and the gas flow was stopped by closing the needle valves. The matrix was warmed

## THERMOLUMINESCENCE OF SIMPLE GASES IN MOLECULAR HYDROGEN MATRICES

Janet Petroski

up by shutting off the flow of liquid helium through the cryostat or by applying heat with the temperature controller. The latter allowed for a slower and steadier warm up of the matrix, but only gave a maximum temperature of about 25 K. The temperature was recorded simultaneously from the temperature controller by the Optical Multichannel Analyzer (OMA) (EG&G Model 1460) and an analog input on the lock-in amplifier with a buffer preamp (Stanford Research Systems SRS Analog Processor SR235) to increase the temperature voltage by 10. The OMA, monochromator (EG&G Model 1234) with a low resolution grating (150 grooves/mm), and a detector with a wavelength range of 230 to 830 nm (EG&G IR 1421 Array Detector) were used to record the TL emission spectrum at 1 sec/scan.

The light from the TL first passed through a mechanical rotating chopping wheel attached to a controller set at 408 Hz (Stanford Research Systems SR540 Chopper Controller). The chopper controller was connected to a lock-in amplifier (Stanford Research Systems SR530), a synchronous rectifier which acts like a switch that is opened and closed in sync with the chopper and cancels the averaged random noise. The chopper and lock-in amplifier combination improved the signal-to-noise ratio.

The emission was focused point-to-point by a 2 inch focal lens placed 4 inches from the detector to the matrix. The light then passed through a 80  $\mu\text{m}$  slit in the shutter to a photomultiplier tube (PMT) (EMI 1P28A) using a bias voltage of 600 V (Stanford Research Systems Model PS 325 High Voltage Power Supply). The PMT converts the light into an electrical signal. The bias voltage value was chosen so the signal from a strong TL would not be too intense and damage the PMT. A bipolar preamp (Stanford Research Model SR552) connected to the lock-in amplifier increased this signal by a factor of 10. An oscilloscope (Tektronix 2440) was used to visually monitor the intensity of the signal.

This signal was finally transferred from the lock-in amplifier to a PC via a GPIB interface. A BASIC program was used to record the intensity of the

## THERMOLUMINESCENCE OF SIMPLE GASES IN MOLECULAR HYDROGEN MATRICES

Janet Petroski

inphase signal of the TL glowcurve as well as the outphase signal, the time, and the temperature.

### Results

The gases which we trapped in the matrix were N<sub>2</sub>, O<sub>2</sub>, CO, CH<sub>4</sub>, CO<sub>2</sub> and mixtures of N<sub>2</sub> in varying dilutions with each of the other gases. We were able to detect intense TL from the nitrogen matrices, but no strong TL from the other pure gases. All the transitions evident in the TL emission spectrum have been previously assigned.

We performed these experiments in solid nitrogen matrices and in SMH matrices to compare with other experiments performed previously<sup>11</sup>. Figure 3 depicts TL from N/D<sub>2</sub> and N/N<sub>2</sub> matrices and the results match these prior experiments. The observed intensity of the TL was much less in the D<sub>2</sub> matrix than the N<sub>2</sub> matrix. Figure 3a shows two molecular transitions in this emission spectrum, the first is the more intense of the two known as the Vegard-Kaplan bands<sup>3</sup> and is the A<sup>3</sup>Σ<sub>u</sub><sup>+</sup> → X<sup>1</sup>Σ<sub>g</sub><sup>+</sup> transition which occurs in the range of 300 nm to 460 nm. The second weaker set from 600 nm to 760 nm is due to the B<sup>3</sup>Π<sub>g</sub> → A<sup>3</sup>Σ<sub>u</sub><sup>+</sup> transition. Figure 3b shows TL from a discharged 10% O<sub>2</sub>/N<sub>2</sub> sample co-deposited in a D<sub>2</sub> matrix. A feature previously assigned to the O atom appears at 556.6 nm and was interpreted by Broida and Peyron<sup>13</sup> as the 2p<sup>4</sup> (<sup>1</sup>S) → 2p<sup>4</sup> (<sup>1</sup>D) transition. Figure 3c exhibits TL from a N/N<sub>2</sub> matrix deposition. The most intense peak at 521.4 nm is the N atom emission and has been interpreted by Bass and Broida<sup>2</sup> as the parity forbidden 2p<sup>3</sup> (<sup>2</sup>D) → 2p<sup>3</sup> (<sup>4</sup>S) transition. The weaker peak at 793.0 nm is also assigned to this transition. Figure 3d depicts TL from another N/N<sub>2</sub> matrix deposition which we believe had an air impurity of an unspecified composition. Here the N<sub>2</sub> transition bands are absent.

Figure 4 shows the dependence of the TL intensity upon the warm up time for

THERMOLUMINESCENCE OF SIMPLE GASES IN MOLECULAR HYDROGEN MATRICES

Janet Petroski

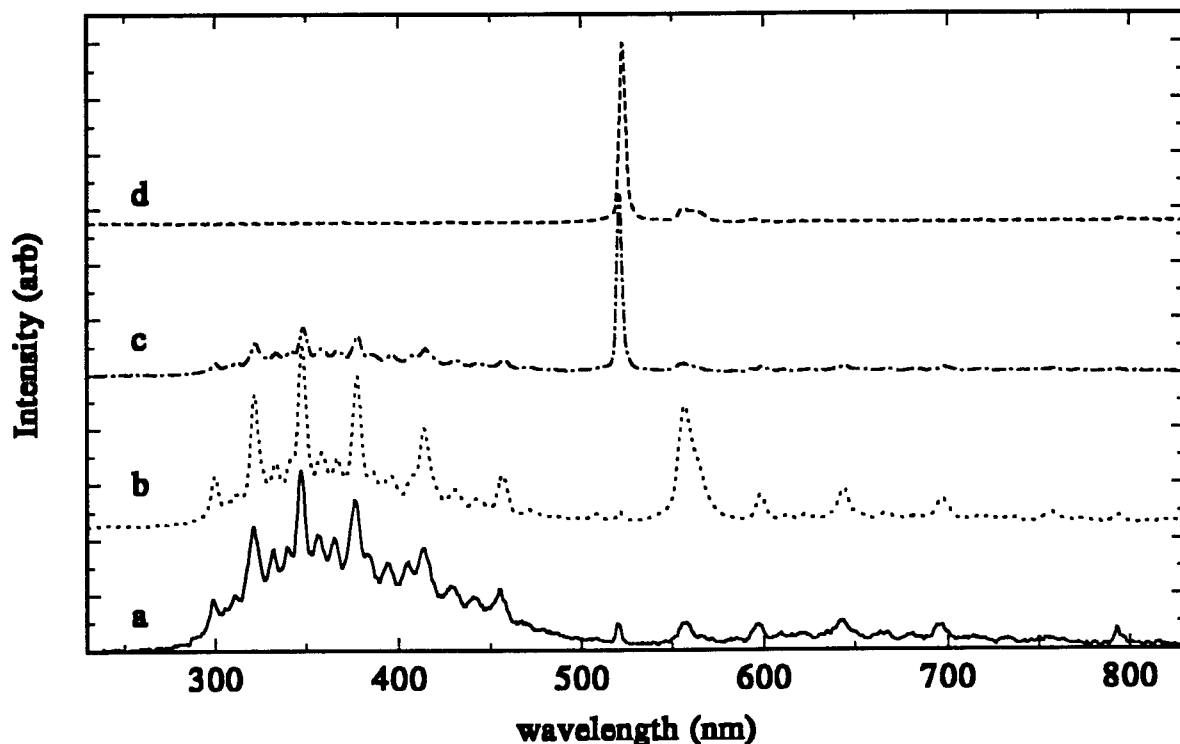


Figure 3. Thermoluminescence from  $\text{N}/\text{N}_2$  and  $\text{N}/\text{D}_2$  matrices. Trace (a) is from a  $\text{N}_2/\text{D}_2$  sample produced with:  $T = 3.6 \text{ K}$ ,  $P_{\text{microwave}} = 125 \text{ mtorr N}_2$ , discharge power = 60 W, a 1.9 mmol/hr  $\text{D}_2$  flow rate, and a 0.10 mmol/hr  $\text{N}_2$  flow rate for the 30 minute deposition; the emission was recorded during warm up from 4 to 24 K. Trace (b) is from a 10%  $\text{O}_2/\text{N}_2/\text{D}_2$  sample produced with:  $T = 3.6 \text{ K}$ ,  $P_{\text{microwave}} = 125 \text{ mtorr N}_2$ , discharge power = 60 W, a 1.8 mmol/hr  $\text{D}_2$  flow rate, and a 0.10 mmol/hr  $\text{N}_2$  flow rate for the 30 minute deposition; the emission was recorded during warm up from 4 to 24 K. Trace (c) is from a  $\text{N}/\text{N}_2$  sample produced with:  $T = 3.8 \text{ K}$ ,  $P_{\text{microwave}} = 125 \text{ mtorr N}_2$ , discharge power = 50 W, and a 0.09 mmol/hr  $\text{N}_2$  flow rate for the 30 minute deposition; the emission was recorded during warm up from 4 to 41 K. Trace (d) is from a  $\text{N}/\text{N}_2$  sample with an air impurity produced with:  $T = 4.7 \text{ K}$ ,  $P_{\text{microwave}} = 400 \text{ mtorr N}_2$ , discharge power = 50 W, and a 0.57 mmol/hr  $\text{N}_2$  flow rate for the 20 minute deposition; the emission was recorded during warm up from 4 to 41 K. The spectra were recorded with an optical multichannel analyzer equipped with an intensified array detector. They have not been corrected for the wavelength dependent detector response, and have been arbitrarily normalized for ease of presentation.

the  $\text{N}/\text{D}_2$  matrix. Figure 4a depicts the TL intensity and the associated temperature ramp for the  $\text{N}/\text{D}_2$  experiment of figure 3a. The temperatures of the three peaks are 5, 7, and 8 K. Figure 4b is a histogram computed from the data

THERMOLUMINESCENCE OF SIMPLE GASES IN MOLECULAR HYDROGEN MATRICES

Janet Petroski

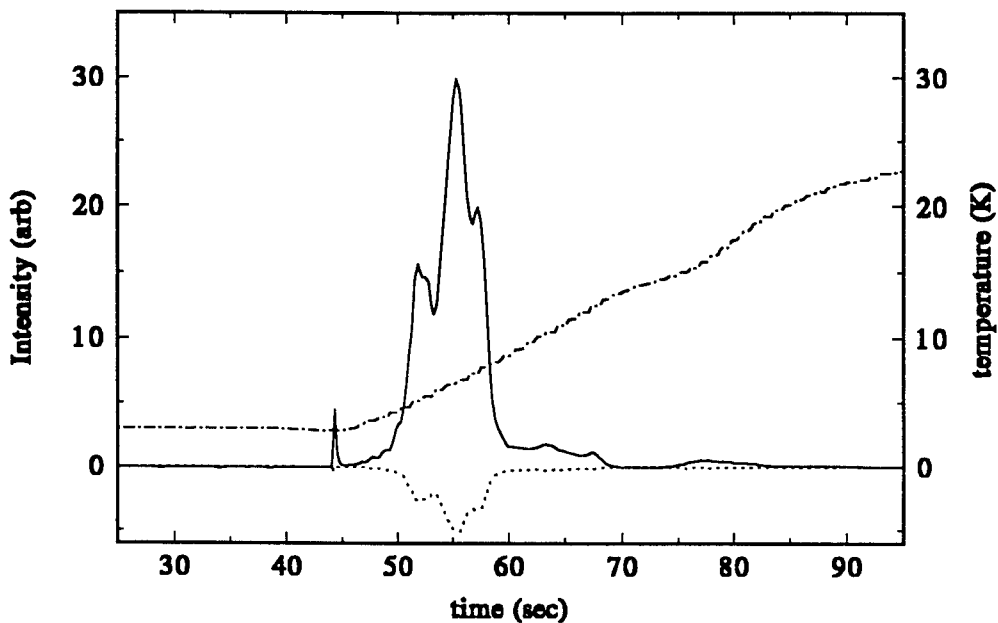


Figure 4a. Thermoluminescence glowcurve from N/D<sub>2</sub> matrix of Fig. 3a. The solid curve is the total TL intensity (inphase signal), the dotted curve is the outphase signal, and the dashed line is the temperature ramp.

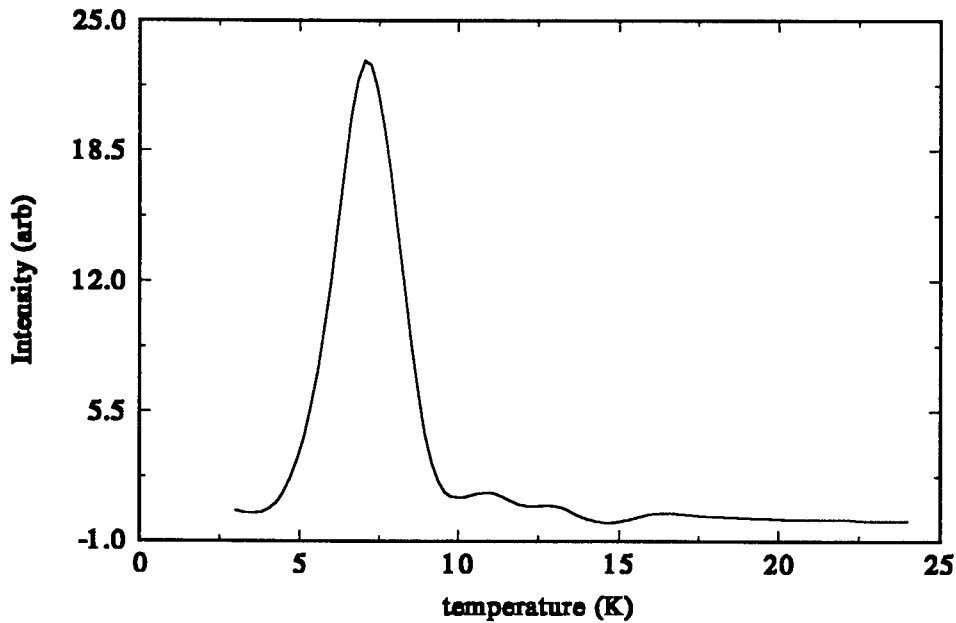


Figure 4b. Histogram of thermoluminescence glowcurve fo N/D<sub>2</sub> matrix of Fig. 4a.

## THERMOLUMINESCENCE OF SIMPLE GASES IN MOLECULAR HYDROGEN MATRICES

Janet Petroski

in figure 4a using 1 K wide bins. The primary emission occurs from 4 to 8 K with the major peak being at 7 K and minor peaks at 11 and 13 K. The intensities were then plotted against the temperature. There were also other peaks which were not always reproducible in the glowcurves and were attributed to thermal explosions.

Figure 5 is evidence of the dependence on the TL upon the warm up for N/N<sub>2</sub> matrix. Figure 5a shows depicts the TL intensity and the associated temperature ramp for the N//N<sub>2</sub> experiment of figure 5a. The temperature of the peak at the maximum point is 17 K. Figure 5b shows the histogram computed from figure 5a. The histogram was calculated the same as for figure 4. The emission occurred from 7 to 23 K with the highest peak at 20 K. There were other peaks not always reproducible and were attributed to thermal explosions.

In the other gases attempted, no other species were trapped that thermoluminesced or chemiluminesced or accepted energy transfer from N<sub>2</sub><sup>+</sup> or N<sup>+</sup> individually in the D<sub>2</sub> matrix. When O<sub>2</sub> was mixed with varying amounts of N<sub>2</sub> (at least 50% N<sub>2</sub> was needed), O atom emission was observed in addition to the N<sub>2</sub> molecule, but N atom was not detected. CO/N<sub>2</sub> mixtures also yielded TL (in a 50/50 ratio) and the same emission spectra as for O<sub>2</sub>/N<sub>2</sub>/D<sub>2</sub> was evident. Carbon emission (the C<sub>2</sub> Swann bands) was not observed. CH<sub>4</sub> and CO<sub>2</sub> did not give any signal, though CH<sub>4</sub> did show N<sub>2</sub> molecule emission exclusively with a 90% N<sub>2</sub>/CH<sub>4</sub> mixture. In the cases where TL emission was detected with the mixtures, the intensity of the bands was greatly diminished as compared to the N/D<sub>2</sub> matrices.

Thermal explosions were observed in the experiments as flashes of green light emitted during the warm up process. These were especially prevalent in the N/N<sub>2</sub> matrix experiments. Also noted was the discoloration of the microwave discharge chamber when CH<sub>4</sub> or CO experiments were run. The chamber would turn black by the end of a 30 minute deposition of CO which was attributed to a carbon build-up on the quartz tube. The CH<sub>4</sub> experiments yielded a brown layer primarily on the top section of the chamber tube which was thought to be a hydrocarbon

THERMOLUMINESCENCE OF SIMPLE GASES IN MOLECULAR HYDROGEN MATRICES

Janet Petroski

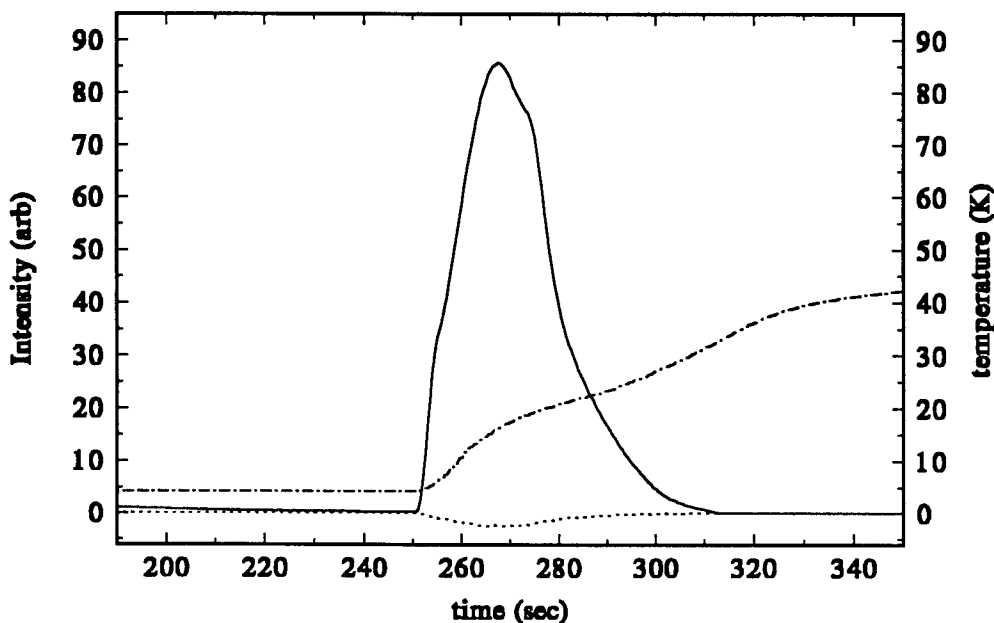


Figure 5a. Thermoluminescence glowcurve from  $N/N_2$  matrix of Fig. 3b. The solid curve is the total TL intensity (inphase signal), the dotted curve is the outphase signal, and the dashed line is the temperature ramp.

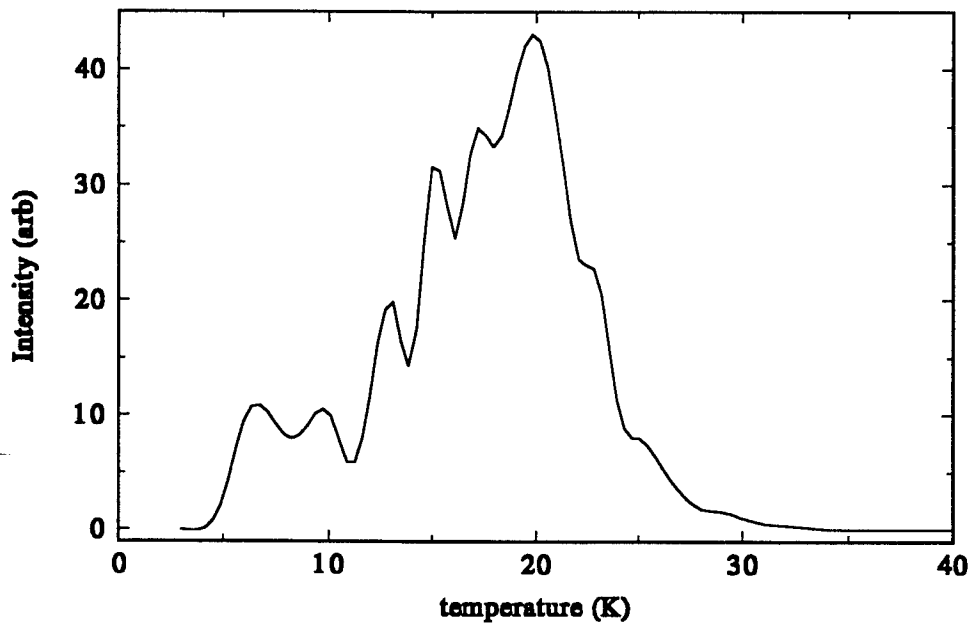


Figure 5b. Histogram of thermoluminescence glowcurve of  $N/N_2$  matrix of Fig. 5a.

# THERMOLUMINESCENCE OF SIMPLE GASES IN MOLECULAR HYDROGEN MATRICES

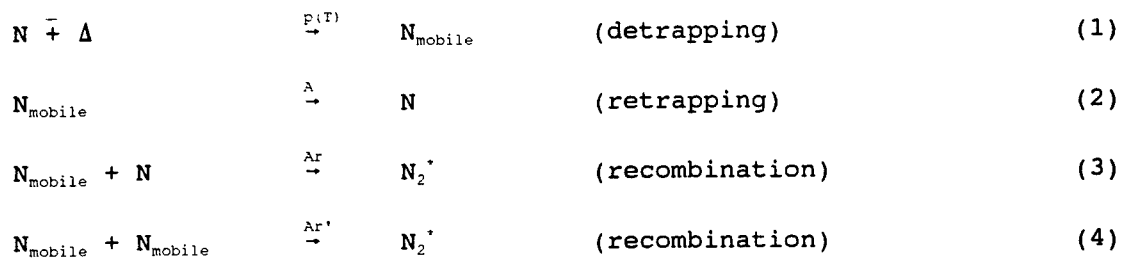
Janet Petroski

polymer. Also, the microwave power level setting was extremely difficult to maintain for the entire deposition time during the CH<sub>4</sub> runs and had to be watched carefully or the microwave discharge would extinguish.

## Discussion

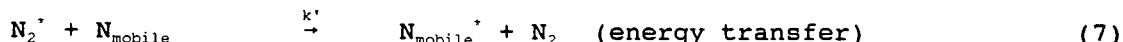
The spectra we observed in our experiments of the N/N<sub>2</sub> and N/D<sub>2</sub> samples reproduced previous work<sup>11</sup>. The spectroscopic assignments we made also agree with this previous work and the prior transition assignments<sup>2,3,13</sup>. The major emitters evident in the spectra are N<sup>+</sup>, N<sub>2</sub><sup>+</sup>, and O<sup>+</sup>. From our data, we can see that N atoms are trapped in the D<sub>2</sub> matrix and are needed in order that TL occurs.

Much information can be obtained from the kinetic analysis of the TL curves. Here we used a first order recombination mechanism for the observed TL of nitrogen<sup>14</sup>. This model assumes that the N atoms in the matrix are thermally activated to a mobile state. From this state they can recombine with another mobile N atom or another N atom trapped in the matrix. We assume that the detrapping of the N atom is the rate determining step in this process. These mobile N atoms can also retrap into the matrix prior to recombination. This recombined N<sub>2</sub><sup>+</sup> molecule is in an excited state which can then luminesce. In the case where the N atom TL is observed, there are the additional steps for the transfer of energy from the N<sub>2</sub><sup>+</sup> molecule to the atom and its subsequent emission. The process is represented by the following mechanism:



THERMOLUMINESCENCE OF SIMPLE GASES IN MOLECULAR HYDROGEN MATRICES

Janet Petroski



in which  $\Delta$  represents heat,  $p(T)$  is the temperature dependent detrapping rate constant given by the Arrhenius equation  $p(T) = ve^{-E/kT}$  where  $v$  is the frequency factor,  $E$  is the activation energy for detrapping,  $k$  is Boltzmann's constant, and  $T$  is the absolute temperature;  $A$  is the rate constant for the retrapping of the  $N$  atom,  $A_r$  is the rate constant for the recombination of the mobile  $N$  atom with one from the matrix while  $A_{r'}$  is the rate constant for the recombination of two mobile  $N$  atoms. The rate constant for the emission of  $N_2$  is given by  $1/\tau_{rad}$  and for  $N$  atom by  $1/\tau_{rad}'$ . The excited state energy transfer rate constants from a  $N_2$  molecule to a matrix  $N$  atom and a mobile  $N$  atom are  $k$  and  $k'$ , respectively.

For the  $N/D_2$  TL, only the first five reactions are necessary since the  $N$  atom emission was extremely weak in the spectrum. The following system of first-order, non-linear, coupled differential equations were derived from the above mechanism:

$$\frac{dN}{dt} = -p(T)N + AN_{\text{mobile}} - ArNN_{\text{mobile}} \quad (9)$$

$$\frac{dN_{\text{mobile}}}{dt} = p(T)N - AN_{\text{mobile}} - A_rNN_{\text{mobile}} - A_{r'}N_{\text{mobile}}^2 \quad (10)$$

$$\frac{dN_2^+}{dt} = A_rNN_{\text{mobile}} + \frac{1}{2}A_{r'}N_{\text{mobile}}^2 - 1/\tau_{rad}N_2^+ \quad (11)$$

$$\frac{dN_2^-}{dt} = 1/\tau_{rad}N_2^+ \quad (12)$$

The experimental data was matched with the best (least-squares) fits to the first order expression derived for the intensity which is proportional to the rate of disappearance of  $N_2^+$ . This expression was evaluated using numerical

## THERMOLUMINESCENCE OF SIMPLE GASES IN MOLECULAR HYDROGEN MATRICES

Janet Petroski

integration and the temperature ramps obtained from the experiments. The fits were performed for each peak by iteration of the  $\nu$  and  $E$  to minimize the mean square errors. This first attempt model produced very good fits between the experimental and theoretical TL glowcurves, but the fits yielded unphysical values for the detrapping frequency factor and activation energy. This error may be due to several of the assumptions we made in the kinetic model. The kinetic model assumes a homogeneous matrix (uniform temperature and concentration throughout the sample). But, we know that the recombination and emission processes release heat into the matrix causing the flashes of green light which were observed during the warm up. These thermal explosions may cause the local temperature in the matrix to rise for short periods of time. This could effect the TL intensity even though the temperature ramp is still rising smoothly since this would cause more N atoms to detrap from the matrix and become mobile. We also attempted to fit the peaks with only a single detrapping energy. Instead, the system may have a distribution of energies or several detrapping energies, as evident from the multiple peaks in the TL glowcurves. We are in the process of re-evaluating this model and reanalyzing the data.

The TL glowcurves in figures 4 and 5 demonstrate the differences in the temperature ranges for the emissions in the different matrices. This is because the detrapping and recombination rates in the N/D<sub>2</sub> samples are different from the N/N<sub>2</sub> samples. The higher temperature emissions ( $T > 8$  K) may be due to solid nitrogen regions emitting inside the D<sub>2</sub> sample which formed as the D<sub>2</sub> left the matrix.

### Conclusion and Recommendations

N and O atoms can be trapped in D<sub>2</sub> solids below 4 K. There must be N atoms present in order to see TL. The main emitters we observed were N<sub>2</sub><sup>+</sup>, N<sup>+</sup>,

## THERMOLUMINESCENCE OF SIMPLE GASES IN MOLECULAR HYDROGEN MATRICES

Janet Petroski

and O<sup>+</sup>. When the D<sub>2</sub> temperature rose above 4 K, recombination occurred rapidly and over a short temperature range (4 to 8 K) and was accompanied by atomic and molecular emission. No emissions from reaction products of the matrix host with the guest radicals were observed.

The N/D<sub>2</sub> matrix is a favorable candidate to be tested in the next phase scale-up experiment. The TL will serve as an internal thermometer for the doped D<sub>2</sub> solids since the temperatures from their visible emission is a valid temperature probe.

Further work is required in the analysis of the data gathered to date in order to understand the kinetic model and to quantify the frequency factors and activation energies for the TL glowcurves we observed. An explanation is needed for the emission spectra obtained when there was an air leak in the vacuum line and no molecular emission was observed for nitrogen. Further information can be gathered by infrared (IR) spectroscopic studies of the matrix which would give additional insight in what is happening in the matrix before and after TL.

Other gases to be studied in the D<sub>2</sub> matrix include: N<sub>2</sub>O, B<sub>2</sub>H<sub>6</sub>, NO, and mixtures of air with N<sub>2</sub>. Air and O<sub>2</sub> mixtures are to be studied in the N<sub>2</sub> matrix as well. These results should further elucidate the studies done to date.

### Acknowledgments

I would like to thank the Air Force Office of Scientific Research, Bolling Air Force Base, DC and Phillips Laboratory at Edwards Air Force Base, CA, especially the HEDM Group, for this research opportunity. In particular, I would like to express my gratitude to Dr. Mario Fajardo for his knowledge, patience, and guidance in this project, as well as Michelle DeRose for all her assistance. Lastly, I would like to thank Dr. Patrick Carrick and Dr. Susan Collins, CSU, Northridge, for helping to make this opportunity possible.

THERMOLUMINESCENCE OF SIMPLE GASES IN MOLECULAR HYDROGEN MATRICES

Janet Petroski

References

1. T.L. Thompson, ed., *Proceedings of the high energy density matter (HEDM) contractors' conference held 6-8 June 1993 in Woods Hole, MA*, PL-TR-93-3041, (USAF Phillips Laboratory, Edwards AFB, CA 93524-5000, 1993).
2. A.M. Bass and H.P. Broida, eds., *Formation and Trapping of Free Radicals*, (Academic, New York, 1960).
3. L. Vegard, *Nature* **113** (1924), 716. *The auroral spectrum and the upper atmosphere.*
4. J.C. McLennan and G.M. Shrum, *Proc. Roy. Soc. A106* (1924), 138. *On the luminescence of nitrogen, argon, and other condensed gases at very low temperatures.*
5. G.P. Sutton and D.M. Ross, *Rocket Propulsion Elements*, 4th edition, (Wiley, New York, 1976).
6. P.G. Carrick, *Specific impulse calculations of high energy density solid cryogenic rocket propellants 1: atoms in solid H<sub>2</sub>*, PL-TR-93-3014, (USAF Phillips Laboratory, Edwards AFB, CA, 93524-5000, 1993)
7. E. Whittle, D.A. Dows, and G.C. Pimentel, *J. Chem. Phys.* **22** (1954), 1943L. *Matrix isolation method for the experimental study of unstable species.*
8. S. Cradock and A.J. Hinchcliffe, *Matrix Isolation*, (Cambridge University Press, Cambridge, 1975).
9. S. Tam and M.E. Fajardo, to be published.
10. M.E. Fajardo, S. Tam, and M. Macler, *Trapping of light metal atoms in hydrogen matrices*, in ref 1.
11. T.L. Thompson, M.E. Cordonnier, and M.E. Fajardo, to be published.
12. R.L. Brooks, *J. Chem. Phys.* **85** (1986), 1247. *The UV-visible emission spectra of oxygen and nitrogen in solid hydrogen and deuterium hosts.*
13. M. Peyron and H.P. Broida, *J. Chem. Phys.* (1959). *Emission spectra of N<sub>2</sub>,*

THERMOLUMINESCENCE OF SIMPLE GASES IN MOLECULAR HYDROGEN MATRICES

Janet Petroski

*O<sub>2</sub>, and NO<sub>2</sub> molecules trapped in solid matrices.*

14. M.E. Fajardo and V.A. Apkarian, J. Chem. Phys. 89 (1988), 4124. *Energy storage and thermoluminescence in halogen doped solid xenon. III. Photodynamics of charge separation, self-trapping, and ion-hole recombination.*

**THE DYNAMIC CONVECTION REVERSAL BOUNDARY**

Aaron Ridley

Department of Atmospheric, Oceanic and Space Sciences

University of Michigan  
Space Physics Research Building  
Hayward St.  
Ann Arbor, MI 48109

C.R. Clauer, Robert Sitar, Volodya Papitashvili  
Department of Atmospheric, Oceanic and Space Sciences  
University of Michigan

William Denig  
Phillips Laboratory  
Hanscom Air Force Base

Egil Friis-Christensen  
Danish Meteorological Institute

Final Report For  
Graduate Student Research Program  
Phillips Laboratory

Sponsored by:  
Air Force Office of Scientific Research  
Bolling Air Force Base, DC

and

National Science Foundation grants ATM-9106958 and ATM-9204520

September 1994

---

## THE DYNAMIC CONVECTION REVERSAL BOUNDARY

Aaron Ridley

Department of Atmospheric, Oceanic and Space Sciences  
University of Michigan

### Abstract

Convection reversal boundaries which occur near the border of the northern summer polar cap ionosphere were observed by the radar at Sondre Stromfjord, Greenland, DMSP F9, F10 and F11 satellites, and the Greenland and MAGIC chains of magnetometers. The reversals observed were categorized into three different classes, Stationary and Uniform, Nonstationary, and Oscillating. A stationary and uniform boundary remains at the same invariant latitude for long periods of time and demonstrates no observable motion. A nonstationary boundary remains parallel to a line of invariant latitude, but will propagate northward or southward. The oscillating boundary will have wave-like motions on the reversal. A number of different boundaries were classified and then further studied to determine the causes for the different types of reversals. The flow across the reversal was also analyzed and found to be greater than the tangential flows in some cases and weak to nonexistent in other cases.

## THE DYNAMIC CONVECTION REVERSAL BOUNDARY

Aaron Ridley

### Introduction

Using the radar facilities at Sondre Stromfjord, Greenland and the DMSP F9, F10 and F11 satellites, we have located many convection reversal boundaries. With the radar, we have observed the spatial and temporal changes in the reversal boundaries and have begun grouping the reversals into different categories based upon these changes. Trends between the reversals in each category are searched for. The categories for our groupings are as follows:

- The Stationary and Uniform Boundary - This is a boundary which remains on a fixed invariant latitude, with no perturbations from this position.
- The Nonstationary Boundary - The entire boundary is observed to shift in position for this category. The motion of the boundary may be fast or slow, as long as it is observed to be a large scale motion and not a localized perturbation.
- The Oscillating Reversal Boundary - These boundaries have localized perturbations which resemble wave-like structures.

Convection reversal boundaries are not limited to simply one of the three classifications. The oscillating reversal boundary and the nonstationary boundary may combine to form a reversal which has large scale motions of the boundary and perturbations in the overall flow. One type of reversal may evolve into another type. The stationary and uniform boundary may make a sudden large scale motion, at which point it becomes a nonstationary boundary.

The DMSP satellites have helped to locate the reversals and give a picture of the field line mapping near the reversal boundary. An understanding of these mappings to the magnetosphere from the ionosphere may be important in determining the causes of the different reversals, and the DMSP satellites help to do this.

The Greenland and MAGIC chains of magnetometers can measure changes in the CRB. By analyzing perturbations measured by magnetometers, the wave-like motions on the oscillating reversal boundary can be studied in a more complete manner.

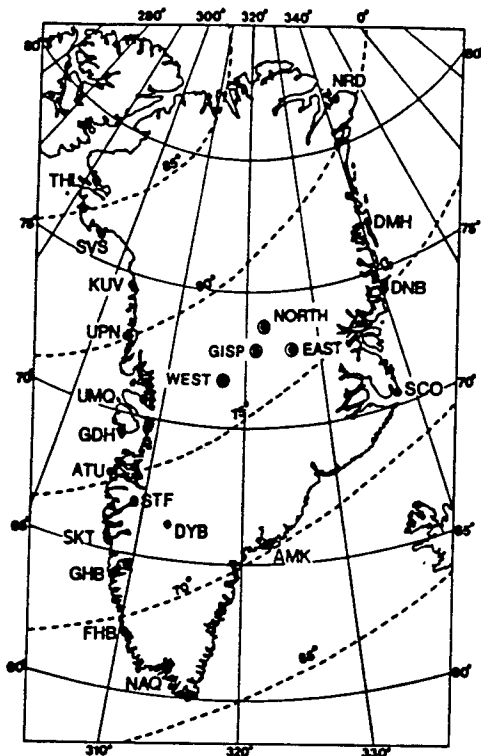


**Figure 1**  
Locations of the Greenland magnetometer chain and the MAGIC stations

types of reversals have been represented more than once. These periods were selected to show the time scales and the spatial scales which the radar was able to observe the boundary and to show the diversity in each of the different categories. The times for DMSP crossings over Sondre Stromfjord were also taken into consideration when selections were made. The time periods are as follows:

July 9, 1992:

For the first time period studied, the radar dwelled on the convection reversal boundary from 16:30 to 17:18 UT (Figure 2). North of 76.4 degrees invariant latitude, the flow was antisunward and south of 76.4 degrees, it was sunward. This is an example of a stationary and uniform CRB. The boundary remained at the same invariant latitude through almost the entire dwell, making only one small movement at 17:00 UT. Since the radar was looking close to orthogonal to the flows, the flow speeds measured seem very small. Since the flow was measured in one direction during

and ion electrostatic detectors, which measure the energy flux and the number flux for 20 different energy bands in the above energy range (see *Hardy et. al.*, 1984 for a complete description of the detectors), were used to map regions of the ionosphere to the magnetosphere.

The Greenland chain of magnetometers, combined with the MAGIC chain, is displayed in figure 1. The magnetometers in the Greenland chain are located on the western and eastern coasts, measuring perturbations from the background magnetic field once every 15 seconds. The MAGIC stations are in the center of Greenland, measuring perturbations once every 20 seconds. The separation between the stations allow spatial scales to be analyzed. Phase delays measured between the stations allows propagating events to be observed, and their velocities measured.

### Results and Discussion

Eight time periods were studied. Each of the different types of reversals have been represented more than once. These periods were selected to show the time scales and the spatial scales which the radar was able to observe the boundary and to show the diversity in each of the different categories. The times for DMSP crossings over Sondre Stromfjord were also taken into consideration when selections were made. The time periods are as follows:

the dwell, we can not estimate the actual velocity of the flows. However, azimuth scans from before the dwell indicate small flow speeds.

There were DMSP satellite crossings before, during and after the radar observed the boundary. These crossings, although they were not close to Sondre Stromfjord, did help to determine the size of the polar cap at these times.

Figure 3 shows the DMSP

F9, F10 and F11 passes and

the regions of the magnetosphere the field lines map to. The location of the edge of the polar rain/mantle can indicate the amount of solar activity and reconnection. In these passes, it is clear there is little activity, since the location of the edge is above 80 degrees invariant latitude in every pass.

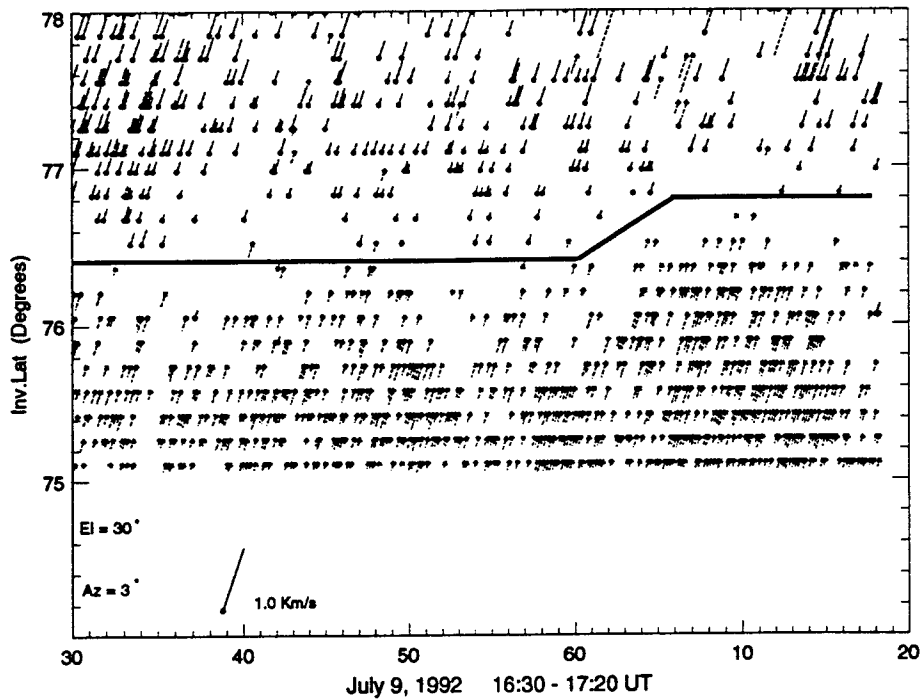


**Figure 2**

A stationary and uniform convection reversal boundary. The reversal stayed motionless at  $76.4^{\circ}$  invariant latitude until 17:00 UT, when it made a small poleward motion to  $76.8^{\circ}$ .

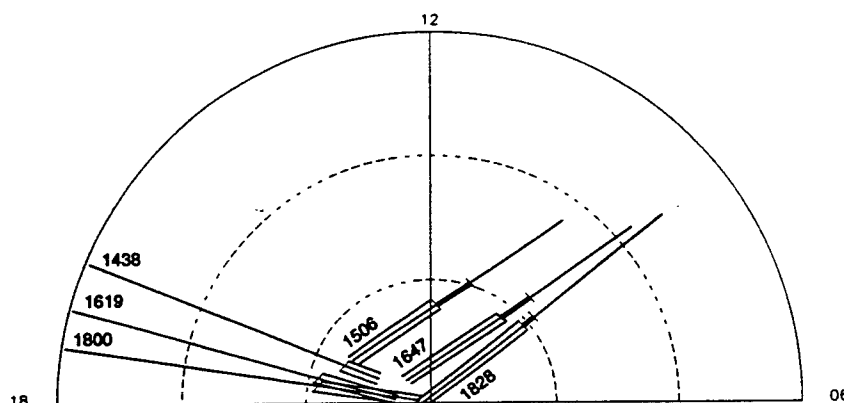


**Figure 3**

Six DMSP crossings before, during and after the radar observed the convection reversal boundary on July 9, 1992. The times displayed show the beginning of each crossing in Universal Time. The different line styles indicate which region of the magnetosphere the field lines which the DMSP satellite is passing through map to. The thin lines are central and boundary plasma sheet. The bold lines are low latitude boundary layer. The triple lines are mantle and polar rain. The passes which start near dusk are DMSP F11 passes and the others are DMSP F10 passes.

During this time, the IMF was very small ( $B_z$  approximately -2 nT,  $B_y$  between -4 nT and -2 nT). This is another indication that there could be low magnetospheric activity.

July 6, 1992:

At approximately 11:50 UT, the radar observed the CRB making a sudden

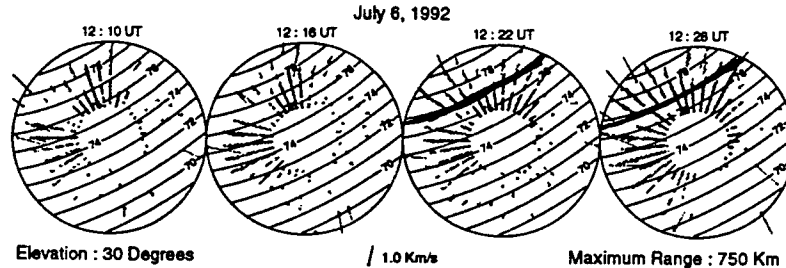
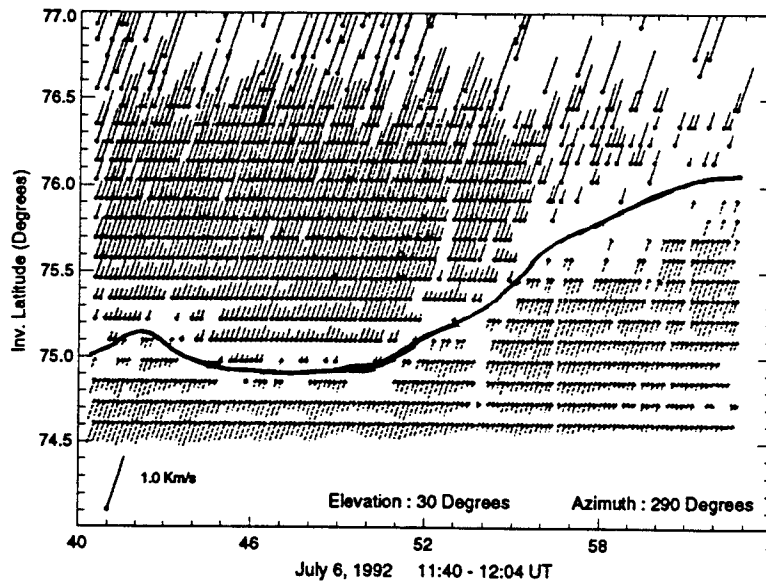


**Figure 4**

A dwell plot, showing 10 second resolution of the convection reversal boundary on July 6, 1992. The boundary starts to move northward, away from the radar, at about 11:51 UT. The next plot shows azimuth scans after the reversal moves out of the radar's field of view. The reversal is visible again at 12:22 UT.

also moved back to approximately the same position after a similar time delay.

The DMSP satellites indicated that the polar cap may have become smaller during the first boundary movement. The DMSP F10 satellite flew across the northern polar cap minutes before the movement of the boundary. The DMSP F11 satellite flew almost orthogonal to the DMSP F10 satellite path a few minutes later, just after the boundary movement. Figure 5 displays the two passes and the mappings of the different regions. It can be seen from the figure that the field lines which mapped out to the low latitude boundary layer (LLBL) on the latter pass were poleward of the field lines which mapped out to the LLBL on the earlier pass. This may imply a shrinking of the polar cap. Since there was no pass after the boundary moved back to the lower latitude, no conclusion can be made concerning the second boundary motion.

poleward motion. This type of motion is classified as a nonstationary boundary. The radar was in a dwell mode from 11:40 to 12:03 UT to observe the boundary with a ten second time resolution. Once the CRB moved far enough north, the radar was switched to azimuth scans in an attempt to locate it again. It was not in the radar's field of view for the first few scans, but came back into view shortly thereafter. Figure 4 shows the dwell of the boundary and a few azimuth scans after the dwell.

During this time period, the IMF changed twice. The first change was from  $B_z$  south to  $B_z$  north and  $B_y$  positive to  $B_y$  negative. The IMP-8 satellite observed these changes 15 to 20 minute before the CRB started to move. The second change occurred a few minutes later and was a return to the original IMF conditions. The CRB

August 4, 1991:

The radar was in a 360 degree azimuth scan mode during the majority of the time investigated, with each scan taking approximately six minutes. The CRB was in the radar's field of view from 11:05 to 14:00 UT and can be seen oscillating throughout many of the scans (figure 6 shows eight consecutive scans). The base line stays between  $74^\circ$  and  $80^\circ$  invariant latitude. During this time, the DMSP F9 and F10 satellites both traversed the northern hemisphere through the radar's field of view. The DMSP F9 satellite flew by Sondrestrom at 11:03 UT and the DMSP F10 at 12:59 UT. We have compared the drift meter measurements of the DMSP satellites with the radar's measurements, and the CRB location, as observed by the driftmeters, are in excellent agreement with the CRB location observed by the radar.

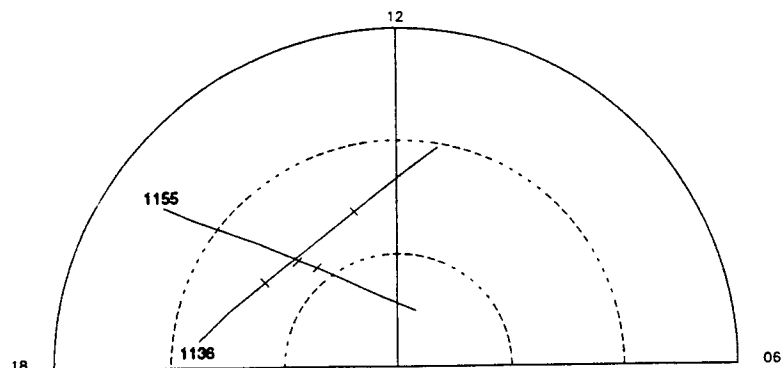


**Figure 5**

Two DMSP crossings on July 6, 1992. The region bracketed on each of the passes is low latitude boundary layer. The first crossing, DMSP F10, at 11:36 UT, shows the LLBL to be further south than the next crossing, DMSP F11, at 11:55 UT shows it to be.

AUG 04, 1991

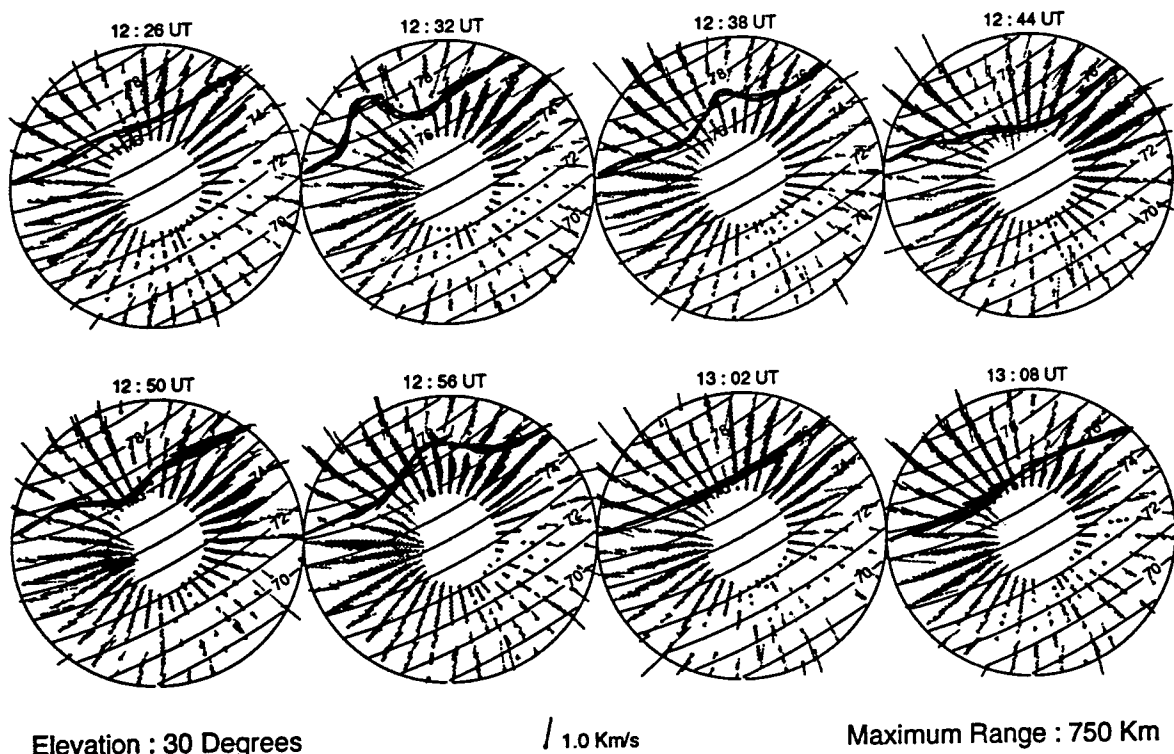


**Figure 6**

A series of 360 degree azimuth scans observing an oscillating reversal boundary on August 4, 1991.

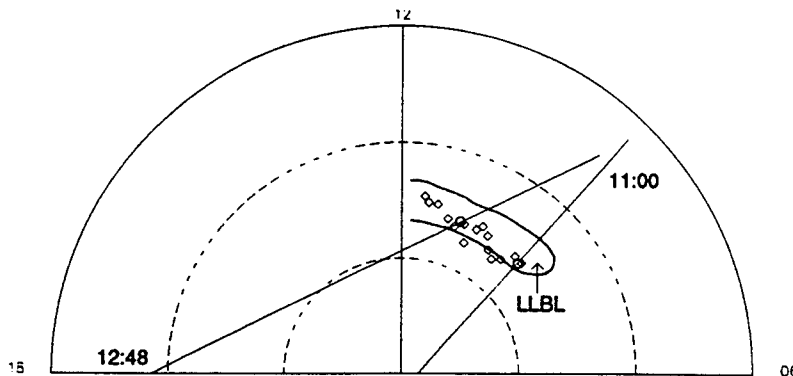


**Figure 7**

A diagram showing two DMSP crossings near Sondre Stromfjord, Greenland, along with mappings of regions of the magnetosphere to the ionosphere and the locations of the convection reversal boundary, as observed by both the radar and the DMSP satellites. The locations of the boundary observed by the radar are marked by squares and the DMSP observed locations are marked by circles.

located within the low latitude boundary layer.

The Greenland chain of magnetometers was also used in the analysis of this oscillating reversal. By high pass filtering the data, the oscillations become clear. Stations which are on approximately the same invariant latitudes were compared to see if there was a phase delay between them, which would imply a propagating perturbation. The phase delay and the distance between the stations indicate a velocity of approximately 1.3 km/s westward, or antisunward. The horizontal perturbations were plotted in a manner which displays the drift of the plasma and are shown in figure 8. Clear pulsations northward and then southward were seen. These pulsations repeated often during the time period considered, and have a strong resemblance to the perturbations discussed by *McHenry et. al.* These wave-like structures observed by the radar and the magnetometers were concluded to be continuous trains of ionospheric traveling convection vortices.

*McHenry et al* found that the propagating groups of vortices he observed were located on the equatorward edge of the low latitude boundary layer. This is very close to the location we are seeing the CRB, although it lies more towards the center of the LLBL. This difference may be due to the identification processes used in determining the mapped regions. Taking this and the similarities in the magnetometer into consideration, it is likely that the phenomena that *McHenry et. al.* observed with only magnetometers is the same sort of phenomena that was observed in this example.

August 1, 1991:

Using the electron and ion energy data from the DMSP satellites, a field line mapping from the ionosphere to the magnetosphere was constructed (see Figure 7). This picture is not comprehensive, since only two passes have been used to construct it. It does, however, provide useful information in the regions near the intersection of the two passes, which is quite close to the regions discussed. If we superimpose the diagram of the mapped regions with a diagram showing the position of the CRB observed by the radar, we can see that the reversal is

Several different categories of convection reversal boundaries were observed on this date. The first reversal could be seen from 11:02 until 11:19 UT. During this time, it slowly propagated northward from approximately 75° invariant latitude until it could no longer be seen by the radar. This reversal is not as clearly defined as others. On the equatorward edge of the reversal there is sunward flow, tangential to the boundary, but on the poleward side of the reversal, the flow is almost perpendicular to the boundary, towards the pole. Since this study is very basic at this point, this reversal will not be considered until a later time.

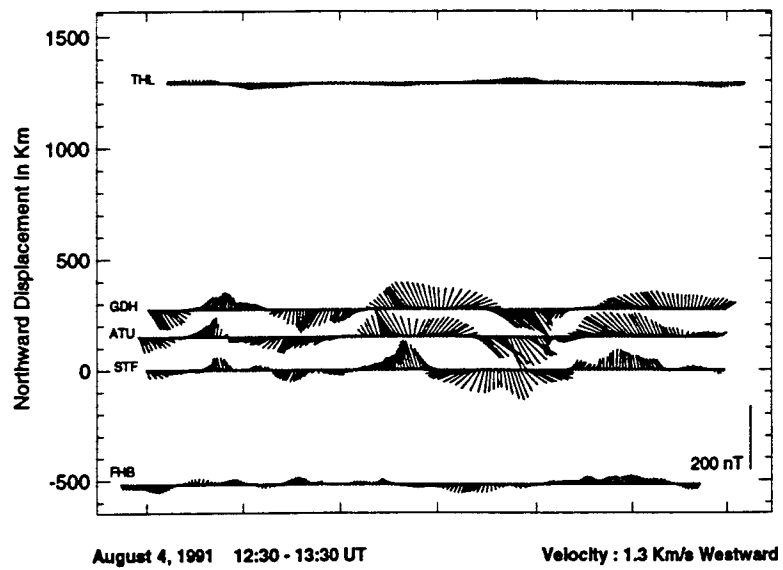


**Figure 8**  
A time series plot of horizontal magnetometer perturbations, rotated to show the equivalent plasma convection. A series of vortex like patterns is observed when the appropriate velocity is used when offsetting the vectors.

The next reversal the radar observes stays fixed in the same location from 11:41 UT until 12:43 UT, at which time it begins oscillating. The stationary and uniform reversal will be discussed first.

The IMF during this time period remains relatively small and steady. The IMF  $B_z$  was approximately -5 nT the entire time and the IMF  $B_y$  slowly increased from about 0 nT to about 5 nT. There was only one DMSP crossing while the radar observed this reversal, at 12:04 UT. The next crossing, after the stationary and uniform reversal, occurred at 12:51 UT, so it was used as a comparison to the previous crossing. There were earlier crossings at 10:23 UT and 10:58 UT, which were also used to compare conditions in the ionosphere.

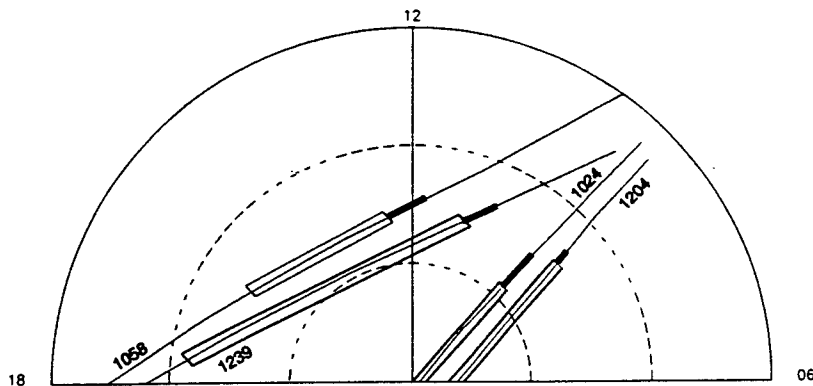


**Figure 9**  
DMSP F9 and F10 crossings before, during and after a stationary and uniform convection reversal boundary on August 1, 1991. The line styles are the same as in figure 3. The three passes after the 10:24 DMSP F9 pass all show agreement on the size of the polar cap.

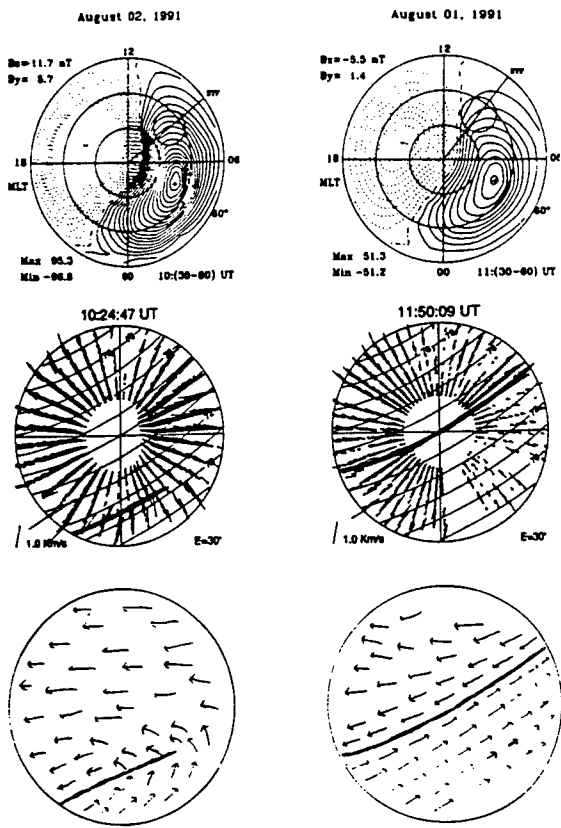


**Figure 10**

In the first column, and IZMEM run for August 2, 1991 10:(30-60) UT is shown, along with radar observations during that time and a two dimensional description of the flow field for the above radar observations. The second column shows the same, but for August 1, 1991 11:(30-60) UT. The first column shows flow across the boundary, as the IZMEM model shows. The second shows little to no flow across the boundary, which is contrary to the IZMEM model. The dark lines represent the convection reversal boundary.

convection reversal boundary, or is it an equipotential line, possibly spanning many hours of magnetic local time? With the help of the IZMEM model, some DMSP passes and the radar, that question might be answered.

Figure 10 shows some typical two cell convection patterns output from the IZMEM model with Sondre Stromfjord's field of view displayed as a circle. These patterns indicate that the radar should observe only a slight turning of a uniform flow. In the first figure, taken from August 2, 1991, the IZMEM model is very close what was observed, although the turning was exaggerated. The flow came from the south west and curved around to leave in the northwest. This reinforces the speculation that there is indeed flow across the boundary. In the next example, however, there is a typical two cell convection pattern, but the radar shows no indication of the steady, curved flow. There is a

As figure 9 shows, the size of the polar cap increases between 10:24 and 10:58 UT. It then remains fairly constant the remainder of the time. There are no indications in the DMSP passes as to why the reversal starts to oscillate at 12:43 UT. During the time period of the stationary and uniform reversal, the polar cap seems to be an average size, with very little to no change over an hour and a half. This is similar to the example discussed above.

The rest of the CRBs during this day will be left for later analysis.

August 2, 1991:

On this day, the flow patterns observed by the Sondre Stromfjord radar did not indicate a reversal, although the DMSP passes, which were within the radar's field of view, do. This difference between the flows brings up a long standing debate about the convection reversal boundary; is there flow across the

very narrow space separating two strong, tangential flows. This implies that the flow across the boundary is very small, or nonexistent, with respect to the tangential flow. These flows have been observed for many consecutive hours.

On other days, the convection reversal boundary may be observed to have both tangential and normal flow (such as the example sited above on August 1, 1991). This leads to the speculation that there are clear, tangential reversals, which stretch for many hours of magnetic local time at some times. There are also reversals which can not adequately be described as reversals, since the radar is observing a strong bending of the flow, like a U shape. Further study into these different types of reversals is necessary to make any definite statement, though.

March 31, 1993:

Most of this day, from 12:40 UT to the end of the observations (approximately 18:00 UT), a reversal was visible. The reversal was only out of the field of view once from 13:45 - 14:30 UT. The first time period analyzed was from 15:50 - 16:51 UT. During this time period, the CRB moved three times, implying a nonstationary boundary. The reversal started at  $75.1^\circ$  invariant latitude at 15:50 UT. It began moving northward to  $75.6^\circ$ , where it stayed until 16:21 UT. At this point, the CRB moved southward to  $75^\circ$ , where it remained until 16:35 UT. The reversal then moved northward above  $76^\circ$ .

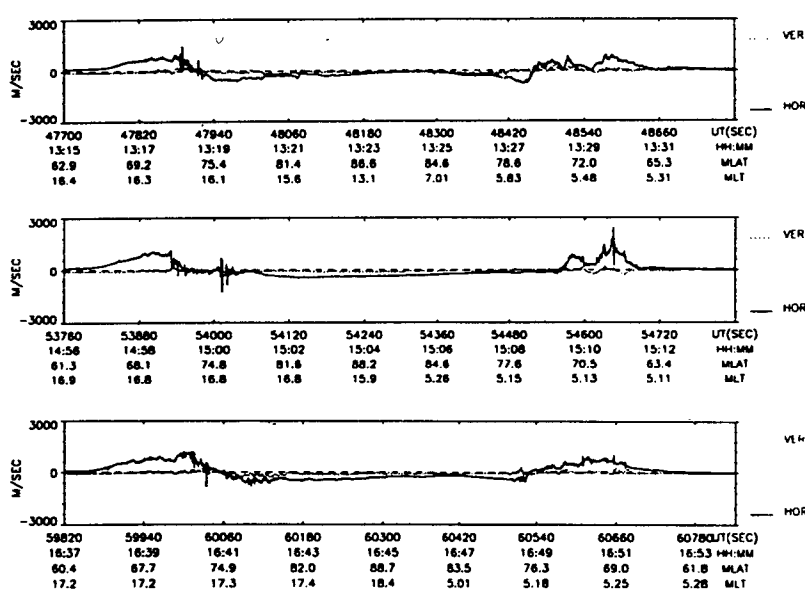


Figure 11

Three DMSP F11 crossings on March 31, 1993, showing only the driftmeter data. Perturbations in the flow around the convection reversal boundary can be seen in the 13:15 UT and 14:56 UT passes, but not in the 16:37 UT pass.

During this time, the IMF was average in magnitude, about 6 nT. The  $B_y$  component remained negative for the entire time, while the  $B_z$  component oscillated between north and south. The oscillations in the IMF coordinated with the motions of the CRB, but with a 15 - 20 minute time delay between the measurements of the IMF changes and the motions of the reversal. The magnitude of the  $B_z$  component was about 0-4 nT for the entire time. The sign of  $B_z$  determined the position of the CRB, northward  $B_z$  implying

higher latitudes and southward, lower latitudes.

There was only one DMSP pass during this time, so no comparisons can be made for the different times, as done in the previous example of a nonstationary boundary. There is good indication, however, from the radar and IMF conditions, that the polar cap was growing and shrinking during the large scale motions of the boundaries, but this can not be confirmed at this time.

Before becoming nonstationary, the boundary oscillated significantly (12:40 - 13:45 UT). There were no DMSP crossings over Sondre Stromfjord, making a mapping analysis impossible. But the driftmeters on the DMSP F11, during the observed oscillating reversal boundary, show perturbations in the uniform flow around the CRB, as shown by figure 11. The DMSP F11 satellite makes an almost perpendicular flight across each of the reversals, so it is measuring close to the true flow values. Two of the three passes (13:15 UT and 14:56 UT) show clear perturbations in the flows. The other pass (16:37 UT), indicates very small flow speed and is crossing the reversal just as it is beginning to oscillate (as explained above). The idea that the DMSP satellites can observe the nonuniform flow in the CRB is something that has not been looked into thoroughly and will be done at a later date.

The magnetometer data was not analyzed as of this time.

June 11, 1993:

From 10:23 until 12:05 UT, the radar dwelled on an oscillating reversal boundary (Figure 12). Unfortunately, there were no DMSP passes near Sondre Stromfjord in this time period, so no mapping can be done. However, the DMSP F11 satellite did observe the same sort of perturbations in the reversal boundary. The IMF  $B_y$  was strongly positive (8 nT), while the  $B_z$  component was approximately 0 the entire time.

The magnetometer data for this day was not analyzed at this time.

### Conclusions

The reversals discussed give some insight into the dynamics of the convection reversal boundaries. Three basic types of reversals were found, stationary and uniform, nonstationary and oscillating. Each of these type of reversals were studied and some conclusions can be made about each:

Stationary and uniform boundaries exist when the IMF is steady for a long period of time. For the examples

which were discussed, the magnitude of the IMF was below 6 nT, indicating that the magnitude may play a role in the lack of motion in these reversals. No solar wind data was available for this study, and it is unknown what conditions existed during these times. The apparent lack of solar activity is the striking feature of these reversals.

The nonstationary boundary is the most common form of reversal. Any time the CRB moves from its previous position it is classified as a nonstationary boundary. These types of reversals seem to be associated with changes in the IMF. A decrease in the amount of reconnection on the dayside may be caused by the IMF  $B_z$  switching from south to north. This decrease will lead to the shrinking of the polar cap and cause the convection reversal boundary to move poleward. The opposite is also true. A change in the  $B_y$  component will cause changes in the convection patterns in the magnetosphere and in the ionosphere. These changes may cause movements of the CRB, but no nonstationary boundary associated with a change in the IMF  $B_y$  was discussed in this paper.

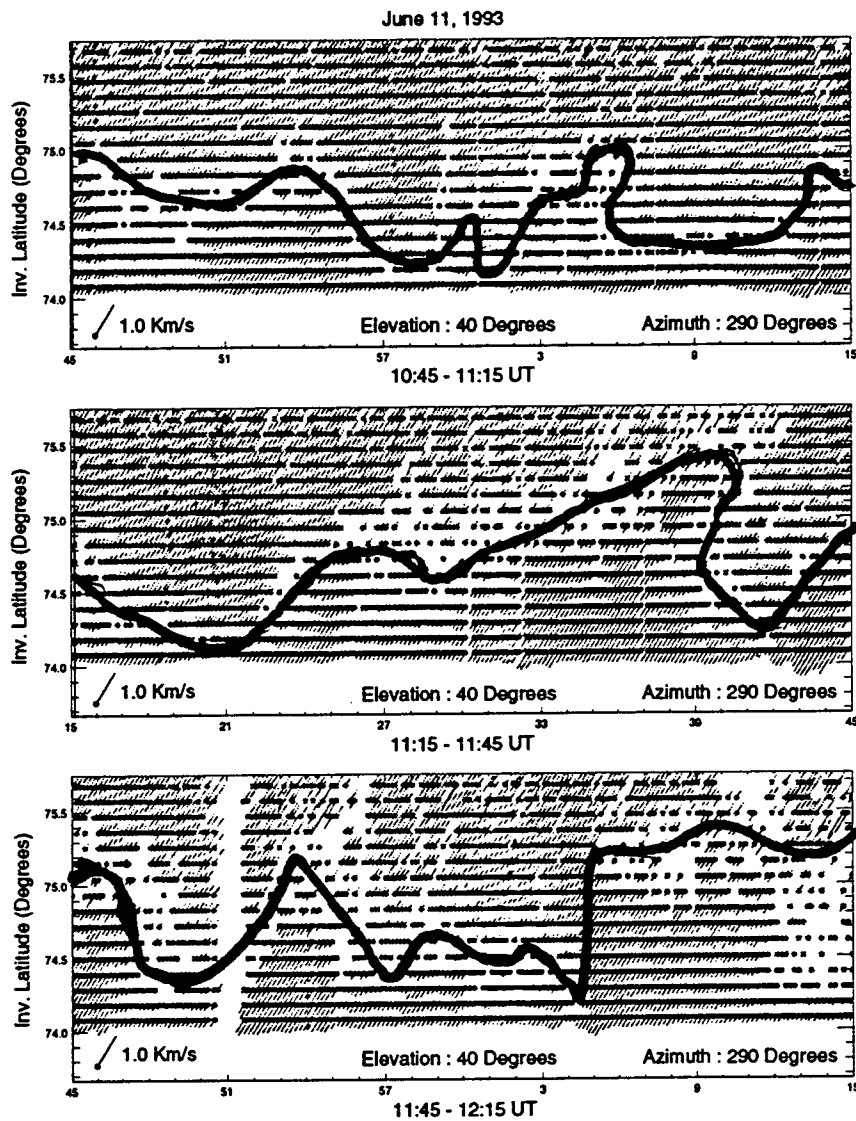


**Figure 12**  
A long dwell of an oscillating reversal boundary on July 11, 1993. The reversal was actually dwelled upon for more than 2 hours in total.

The oscillating reversal boundaries may reflect phenomena familiar to the continuous ionospheric traveling vortices discussed by *McHenry et. al.* The single event which was studied in detail in this paper has many features which are similar to the traveling vortices; they map to approximately the same place in the magnetosphere as the vortices and

they have similar magnetic perturbations as measured by magnetometers as the vortices. If indeed they are these types of propagating perturbations, then the nature of these vortices needs to be studied more. They appear to be a Kelvin Helmholtz instability, caused by the strong shear in the flow. Perturbations in the flow patterns were observed by the DMSP 11 satellite during some passes, but further studies are needed to form any speculation on whether the phenomena are linked.

The amount of flow across the boundary was also discussed. Although more studies need to be done on this topic, strong flows across the boundary can be observed occasionally and very little to no flow across the boundary other times. This observation stems from the radar data alone. Other types of data must be studied, such as DMSP drift meters, to reinforce these observations.

#### References

Hardy, D.A., M. S. Gussenhoven, and E. Holeman, A Statistical Model of Auroral Electron Precipitation, *J. Geophys. Res.* 90, 4229, 1985.

Hardy, D. A., H. C. Yeh, L. K. Schmitt, T. L. Schumaker, M. S. Gussenhoven, A. Huber, F. J. Marshall, J. Pantazis, Precipitating Electron and Ion Detectors (SSJ/4) for Block 5D/ Flights 6-10 DMSP Satellites : Calibration and Data Presentation, *Environmental Research Papers, No. 902*, November, 1984.

Heppner J. P., and N. C. Maynard, Empirical High-Latitude Electric Field Models, *J. Geophys. Res.* 92, 4467, 1987.

McHenry, M. A., C. R. Clauer, E. Friis-Christensen, P. T. Newell, and J. D. Kelly, Ground Observations of Magnetospheric Boundary Layer Phenomena, *J. Geophys. Res.* 95, 14995, 1990a.

McHenry, M. A., C. R. Clauer, E. Friis-Christensen, Relationship of Solar Wind Parameters to Continuous Dayside, High Latitude, Traveling Ionospheric Vortices, *J. Geophys. Res.* 95, 15007, 1990b.

Newll, P. T., W. J. Burke, C.-I. Meng, E. R. Sanchez, and M. E. Greenspan, Identification and Observations of the Plasma Mantle at Low Altitude, *J. Geophys. Res.* 96, 35, 1991.

Newll, P. T., W. J. Burke, E. R. Sanchez, C.-I. Meng, M. E. Greenspan, C. R. Clauer, The Low Latitude Boundary Layer and the Boundary Plasma Sheet at Low Altitude: Prenoon Precipitation Regions and Convection Reversal Boundaries, *J. Geophys. Res.* 96, 21013, 1991.

Newell, P. T. and C.-I. Meng, Cusp Width and  $B_z$ : Observations and a Conceptual Model, *J. Geophys. Res.* 92, 13673, 1987.

Newell, P. T. and C.-I. Meng, 'On Quantifying the Distinctions Between the Cusp and the Cleft/LLBL', in Electromagnetic Coupling in the Polar Clefts and Caps, P. E. Sandholt and A. Egeland (Eds.), pp. 87-101, Kluwer Academic Publishers, 1989.

Newell, P. T. and C.-I. Meng, Mapping the Dayside Ionosphere to the Magnetosphere According to Particle Precipitation Characteristics, *Geophys. Res. Lett.*, 19, 609, 1992.

Rich, F. J. and M. A. Hairton, Large-scale Convection Patterns Observed by DMSP, *J. Geophys. Res.* 99, 3827, 1994.

Riehl, K. B., and D. A. Hardy, Average Characteristics of the Polar Rain and Their Relationship to the Solar Wind and Interplanetary Magnetic Field, *J. Geophys. Res.* 91, 1557, 1986.

Wickwar, V. B., J. D. Kelly, O. de la Beaujardiere, C. A. Leger, F. Steenstrup, and C. H. Dawson, *Geophys. Res. Lett.*, 11, 883, 1984.

**FABRICATION AND MECHANICAL TESTING  
OF MIXED-MATRIX CARBON-CARBON COMPOSITES**

Richard M. Salasovich  
Graduate Student  
Department Of Aerospace Engineering  
& Engineering Mechanics

University Of Cincinnati  
Cincinnati, OH 45221

Final Report For:  
Graduate Student Research Program  
Phillips Laboratory

Sponsored By:  
Air Force Office Of Scientific Research  
Bolling Air Force Base, DC

And

Phillips Laboratory

August 1994

**FABRICATION AND MECHANICAL TESTING  
OF MIXED-MATRIX CARBON-CARBON COMPOSITES**

Richard M. Salasovich  
Graduate Student  
Department Of Aerospace Engineering  
& Engineering Mechanics  
University Of Cincinnati

Abstract

The high specific strength, stiffness, and thermal conductivity and low coefficient of thermal expansion of carbon-carbon composite makes it an ideal material for a passive spacecraft radiator. In support of the Carbon-Carbon Spacecraft Radiator Project at the Phillips Laboratory, a study was conducted to determine the potential to improve the specific mechanical properties of carbon-carbon composite by a final infiltration of toughened polycyanate resin. At the expense of the material's high temperature capability, filling the carbon matrix microcracks with resin promises to improve the mechanical properties of the composite without severely degrading its thermal properties. Samples were prepared with four different matrix structures: undensified carbon-carbon; undensified carbon-carbon impregnated with toughened polycyanate resin; pitch densified carbon-carbon; and pitch densified carbon-carbon impregnated with toughened polycyanate resin. Three types of mechanical tests were performed on each of these samples: longitudinal tension; interlaminar tension; and flexure. The results indicate that the mechanical properties of carbon-carbon composite can be improved by up to 61.9% with this final resin infiltration.

## FABRICATION AND MECHANICAL TESTING OF MIXED-MATRIX CARBON-CARBON COMPOSITES

Richard M. Salasovich  
Graduate Student  
Department Of Aerospace Engineering  
& Engineering Mechanics  
University Of Cincinnati

### Introduction

Carbon-carbon composites are produced by pyrolyzing an organic matrix composite. This pyrolyzation cycle drives off all volatiles from the organic matrix, leaving a low modulus amorphous char matrix. Microcracks in this matrix develop due to thermal stresses during cooling. In the fabrication of pitch-matrix carbon-carbon composites, these microcracks are filled with petroleum tar pitch which is then recarbonized with multiple iterations until the composite is fully densified. Since each pyrolyzation and pitch infiltration cycle takes an average of two weeks to complete, this process is slow and expensive. Also, the amorphous matrix has relatively low thermal conductivity, even with a final high-temperature graphitization heat treatment. However, the final composite has a high modulus, is extremely thermally stable, and retains its strength at higher operating temperatures than any material known.

In support of the Carbon-Carbon Spacecraft Radiator Project at the Applied Composites Laboratory, a study was conducted to determine whether a final resin infiltration could increase the material's mechanical properties while retaining its high thermal conductivity and thermal stability. To accomplish this, the material's high temperature capability had to be sacrificed. But this was considered an acceptable compromise for low-temperature spacecraft radiator applications.

The approach taken consisted of infiltrating the microcracks of the carbon matrix with a toughened polycyanate resin. An RS-14 low viscosity toughened polycyanate resin from YLA, Incorporated was chosen for the study. According to the company, the resin was developed to provide a good balance between toughness and high temperature / wet performance. It was chosen for its low microcracking during thermocycling, low moisture absorption, low volume change during cure, low outgassing, and low modulus after radiation exposure. Both undensified and pitch densified carbon-carbon composites were infiltrated with this resin. Then longitudinal tension, interlaminar tension, and flexure properties of each sample were evaluated.

### Material Processing

To expedite this initial feasibility assessment study, available material was used to the maximum extent possible. The chosen prepreg was manufactured with HITEM 35-7 (PAN-precursor) fibers woven into a five-harness-satin fabric with 6000 fibers / tow and impregnated

with F-064 phenolic resin. This HI-TEX 35-7/F-064 prepreg had been purchased previously from U.S. Polymeric.

The prepreg was laid-up into thirty-two, two-ply plates, 17.78 cm x 22.86 cm with the warp aligned with the 17.78 cm dimension. These two-ply plates were autoclave cured using standard vacuum bag procedures. The cure cycle is shown in Figure 1. The cured plates were stacked between two graphite caul plates, packed in lamp black, and pyrolyzed under nitrogen purge at 5.55°C/hr up to 871°C with a 10 hour hold at peak temperature. The pyrolyzation cycle is given in Figure 2. Because of time constraints, the high-temperature graphitization heat treatment could not be conducted on any of the material samples. The mean density of the undensified carbonized plates was 1.184 g/cc with a standard deviation of 0.006.

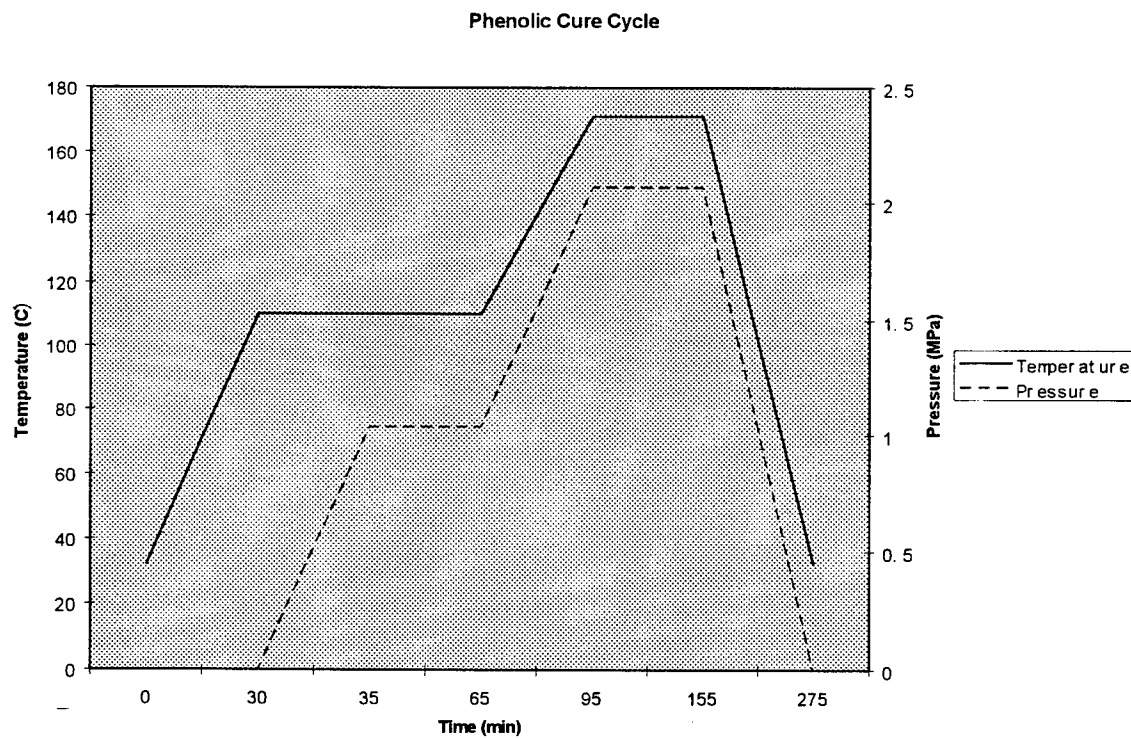


Figure 1

After pyrolyzation, sixteen of the plates were densified with A240 petroleum tar pitch. The composites were placed in a stainless steel foil pitch pot, buried in granulated pitch, and held under a 635 torr vacuum for two hours. Then, they were heated to 316°C in one hour and 1.03 MPa of nitrogen was applied at temperature to infiltrate the matrix microcracks of the composite.

After a three hour hold the parts were cooled, packed in lamp black under a nitrogen purge, and pyrolyzed a second time as shown in Figure 2. Again, the high-temperature graphitization heat-treatment of the composites had to be abandoned because of time constraints. The density of the pitch infiltrated parts was 1.282 g/cc with a standard deviation of 0.024. The densification process gave a 7.6% weight gain over the plain, undensified carbon-carbon plates.

At this point in the process, the thirty-two 17.78 cm x 22.86 cm plates (sixteen undensified and sixteen pitch densified) were cut on a diamond blade table saw into sixty-four 11.43 cm x 17.78 cm plates (thirty-two undensified and thirty-two pitch densified). This was done so that the plates could be accommodated by other processing apparatus. Sixteen undensified and sixteen pitch densified plates were left as processed for control specimens. The other sixteen of each treatment were impregnated with RS-14 toughened polycyanate resin. The plates were stacked in a Pyrex impregnation chamber with spacing to ensure resin exposure and they were subjected to a 635 torr vacuum for 2 hours. The impregnation apparatus is given in Figure 3. The toughened polycyanate resin was heated to its minimum viscosity temperature before the isolation valve was opened, introducing the resin into the impregnation chamber. After infiltration, the chamber was opened, the plates were removed and autoclave cured using standard vacuum bagging procedures. The resin cure cycle is shown in Figure 4.

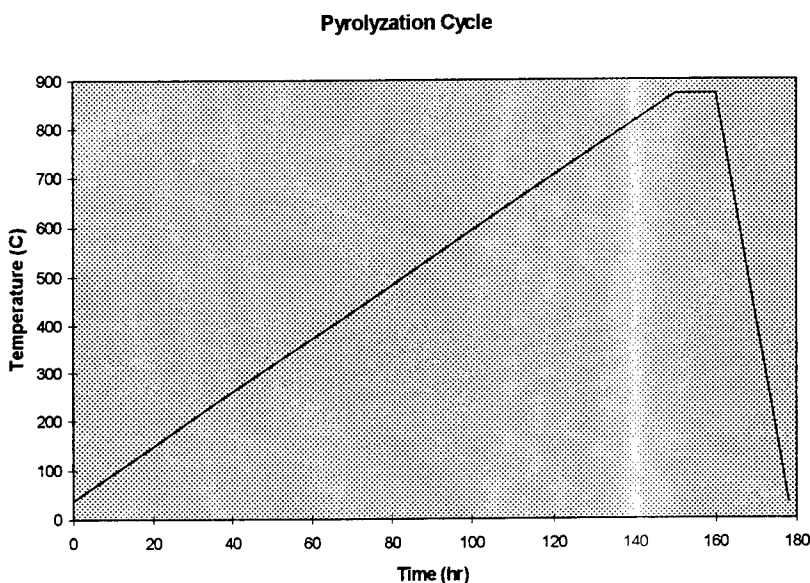


Figure 2. Pyrolyzation Cycle

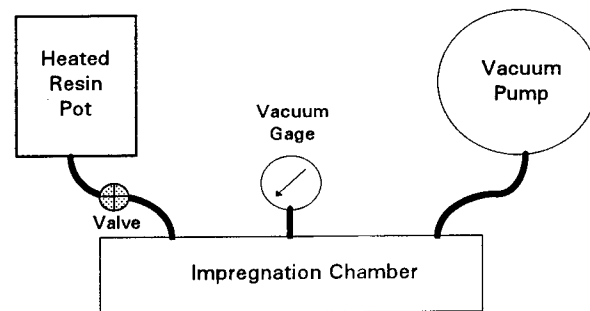


Figure 3. Impregnation Apparatus

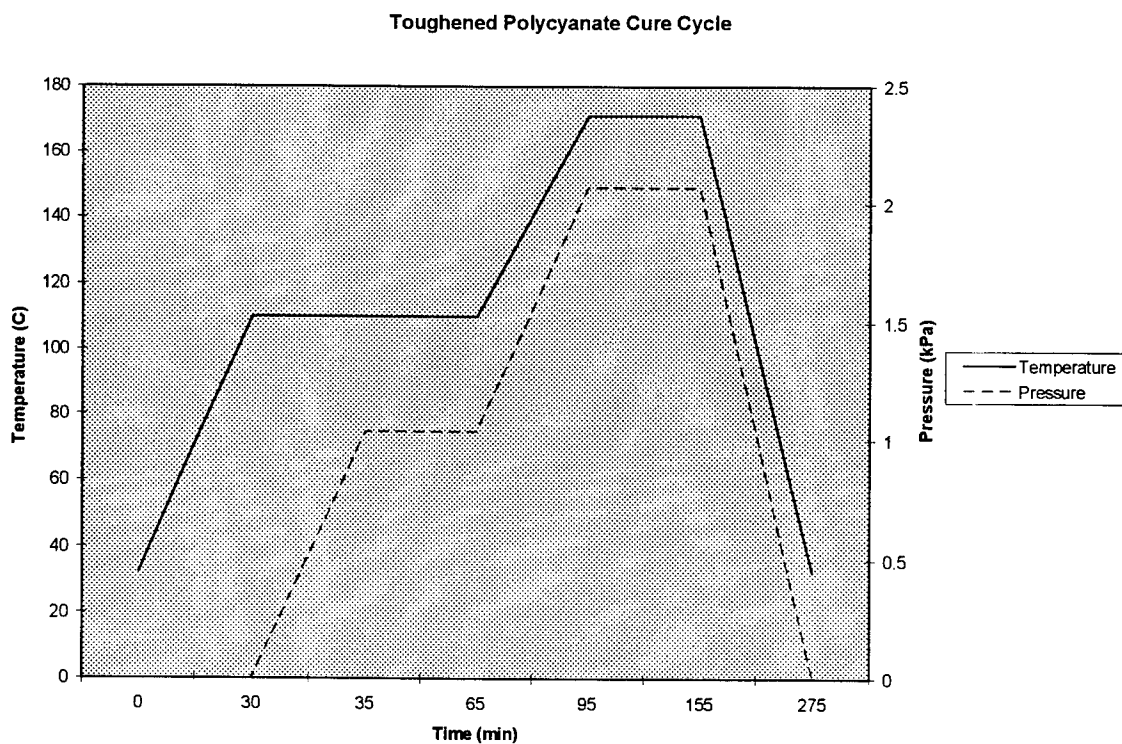


Figure 4. Toughened Polycyanate Cure Cycle

After infiltration with the toughened polycyanate resin, the mean density of carbon-carbon increased from 1.184 g/cc to 1.333 g/cc with a standard deviation of 0.005 (11.2% weight gain). The mean density of pitch densified carbon-carbon increased from 1.282 g/cc to 1.399 g/cc with a standard deviation of 0.026 (8.4% weight gain) due to resin impregnation. Density data throughout the process history are given in Table 1.

Density Data Throughout Process History			
Process	Density (g/cc)	Standard Deviation	Remarks
Undensified Carbon-Carbon	1.184	0.006	None
Undensified Carbon-Carbon With Resin Impreg	1.333	0.005	11.2% Weight Gain Over Undensified Carbon-Carbon
Pitch Densified Carbon-Carbon	1.282	0.024	7.6% Weight Gain Over Undensified Carbon-Carbon
Pitch Densified Carbon-Carbon With Resin Impreg	1.399	0.026	8.4% Weight Gain Over Pitch Densified Carbon-Carbon

Table 1

## Testing

The test matrix consisted of four types of material samples: undensified carbon-carbon; undensified carbon-carbon impregnated with toughened polycyanate resin; pitch densified carbon-carbon; and pitch densified carbon-carbon impregnated with toughened polycyanate resin. Three types of mechanical tests were conducted on each sample: longitudinal tension (warp aligned); interlaminar tension; and flexure of a flat sandwich construction.

The longitudinal tension test was conducted on a Sintech-1 servo-electric computerized test system with a 2224 N load cell. Data acquisition was controlled with a 286 PC equipped with MTS TestWorks v2.1. Strain was measured with a MTS 632.13B-20 knife-edged extensometer with a 1.27 cm gage section. Ten specimens per sample type were cut into 12.7 cm x 1.6 cm x 0.84 mm rectangular coupons with aluminum tabs, as shown in Figure 5. The specimens were pulled to ultimate stress using a standard method developed on-site for longitudinal tensile testing of carbon-carbon composites. 95% of all specimens failed catastrophically in the test section. One specimen in forty broke at the tab, and one failed due to fixture misalignment.

The interlaminar tension test was conducted on a MTS-880 servo-hydraulic computerized test system with a 22240 N load cell. Data acquisition was controlled with a 486 PC equipped with MTS TestWorks v2.1. Ten specimens per sample were cut into 2.54 cm diameter x 0.84 mm thick buttons and mounted on 2.54 cm diameter steel fixtures with EpiSeal 20-20 epoxy, as shown in Figure 6. The specimens were pulled to ultimate stress using a standard method developed on-site for interlaminar tensile testing of carbon-carbon composites. 98% of all specimens failed catastrophically at the interface between plies, with one specimen in forty exhibiting an adhesive failure.

The flexure test (three point bend) was conducted on a MTS-880 servo-hydraulic computerized test system with a 22240 N load cell. Data acquisition was controlled with a 486 PC equipped with MTS TestWorks v2.1. Displacement was measured with a MTS 632.06B-83 extensometer with a 1.27 cm gage section mounted directly below the center roller on the underside of the sandwich.



Figure 5. Longitudinal Tensile Specimen



Figure 6. Interlaminar Tensile Specimen

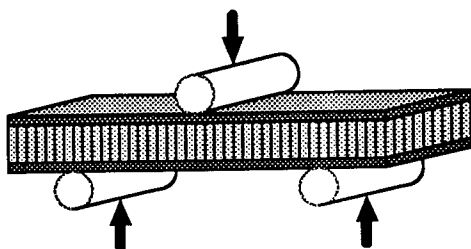


Figure 7. Flexure Specimen

Crosshead displacement was also measured. The flat sandwich structure was constructed with plates from each material sample adhesively bonded with Hysol EA9394 structural adhesive to 1.27 cm thick aluminum honeycomb supplied by Composite Optics (3/16 in cell, 5056 Al, 0.0007 gage, 2.0 pcf). Ten specimens per sample were cut into 17.78 x 3.24 cm x 1.42 cm sandwich structures as shown in Figure 7. The coupons were tested through ultimate load in accordance with ASTM C393. 93% of all specimens reached ultimate load when the compressive face sheet buckled from roller damage. These specimens continued to yield as the core honeycomb crushed when the test was stopped. Three coupons in forty failed catastrophically in the tensile region directly below the center roller.

## Results

The raw test data for each sample and specimen are given in Tables 2, 3, and 4. Stress-strain curves for the longitudinal tension tests are given in Figures 8, 9, 10, and 11. Figure 10 exhibits considerable scatter in strain data. This behavior is not well understood, but could be due to a combination of individual tow failure and the seating of the extensometer knife edges on the surface of the composite. Load-displacement curves for the flexure tests are given in Figures 14, 15, 16, and 17. For each test, the density-normalized mean values per sample are given in Figures 12, 13, and 18. From Figure 12, undensified carbon-carbon showed a 34.9% increase in longitudinal ultimate stress per unit density upon impregnation with toughened polycyanate resin. The results for the longitudinal tension test of the pitch densified composite are suspect, i.e. a decrease in specific strength should not occur due to pitch infiltration. The modulus per unit density of each sample was unaffected. From Figure 13, the interlaminar ultimate stress per unit density of undensified carbon-carbon increased 61.9% upon impregnation with toughened polycyanate resin. The interlaminar ultimate stress per unit density of pitch densified carbon-carbon increased 18.4% upon resin impregnation. However, whether the original carbon-carbon composite was densified with resin alone or the combination of pyrolyzed-pitch and resin, the resulting increase in interlaminar ultimate stress per unit density remained the same. This implied that the pitch densification step could be eliminated, saving at least ten days of processing time without significant penalty to the interlaminar ultimate stress per unit density. From Figure 18, the ultimate load per unit density of undensified carbon-carbon increased 16.8% and that of pitch densified carbon-carbon increased 5.1% upon impregnation with toughened polycyanate resin. Considering statistical error, the stiffness per unit density of each sample was unaffected.

Specimen Number	Longitudinal Tensile Test Results							
	Undensified C-C		Undensified C-C With Resin Impreg		Pitch Densified C-C		Pitch Densified C-C With Resin Impreg	
	Ultimate Stress (MPa)	Modulus (GPa)	Ultimate Stress (MPa)	Modulus (GPa)	Ultimate Stress (MPa)	Modulus (GPa)	Ultimate Stress (MPa)	Modulus (GPa)
1	48.5	4.19	69.2	4.56	33.8	4.11	45.9	4.89
	54.7	4.31	74.9	4.36	40.1	4.63	28.2	4.87
	41.8	2.48	74.1	5.79	41.8	4.55	53	5.20
	40.4	4.69	75.2	5.04	35.3	4.44	39.8	5.90
	52.8	4.59	77.5	4.24	42.5*	2.895*	44.3	5.18
	32.4	4.50	71.8	4.64	40	5.45	36.4	5.21
	55.7	4.08	73	5.07	53.4	4.56	25.6	4.98
	49	3.76	51.2	4.00	40.7	5.03	35.3	5.38
	38.2	3.99	58.8	5.87	19.0**	4.337**	38.8	5.34
	48.8	4.57	68	4.90	37.8	4.38	33.8	4.79
Minimum Value		32.4	2.48	51.2	4.00	33.8	4.11	25.6
Mean Value		46.2	4.12	69.4	4.85	40.4	4.64	38.1
Maximum Value		55.7	4.69	77.5	5.87	53.4	5.45	53
Standard Deviation		7.7	0.65	8.3	0.62	6	0.42	8.2
								0.33

Table 2

#### Longitudinal Tension Of Undensified Carbon-Carbon

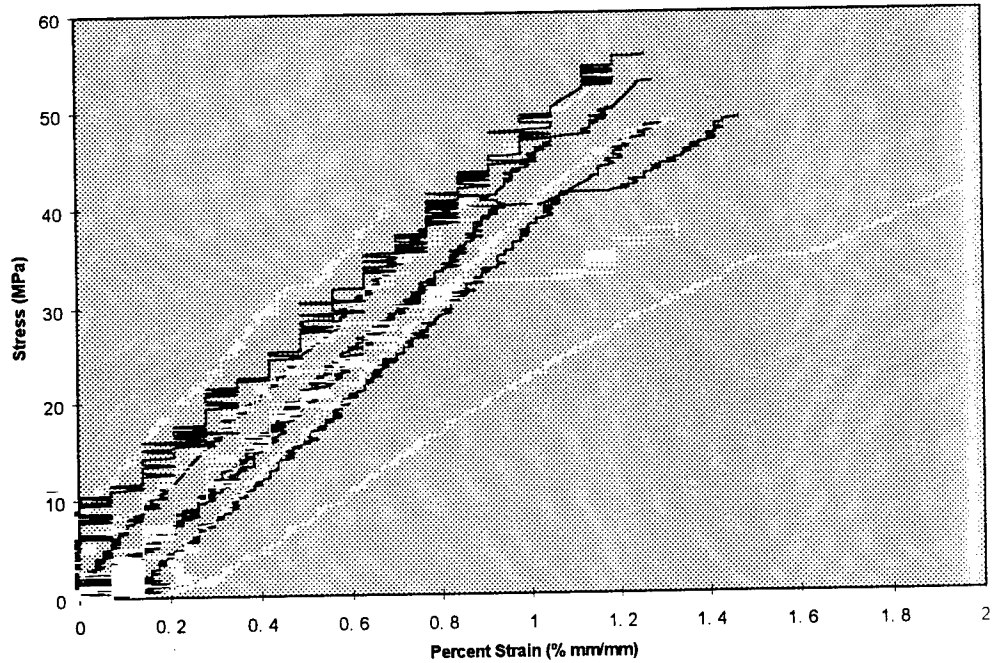


Figure 8

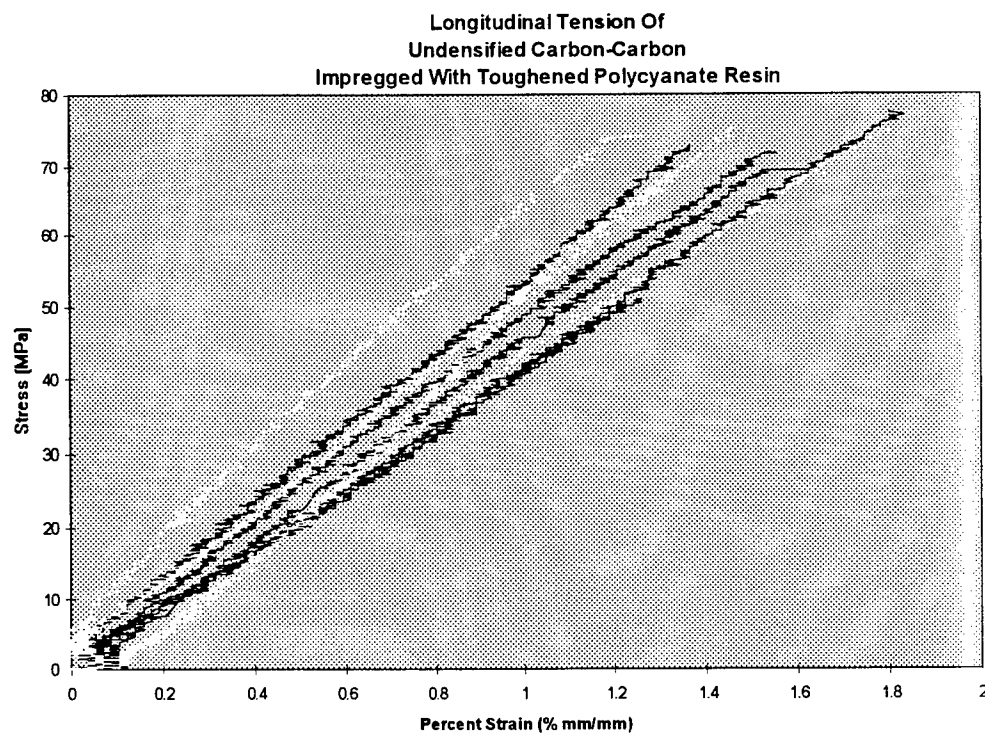


Figure 9

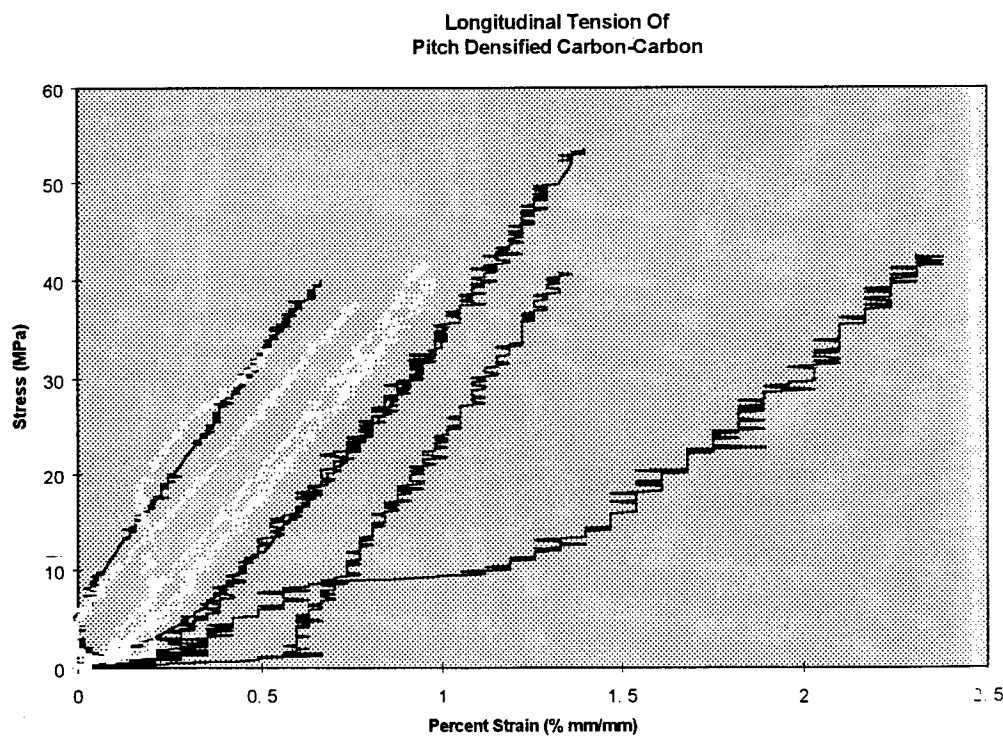
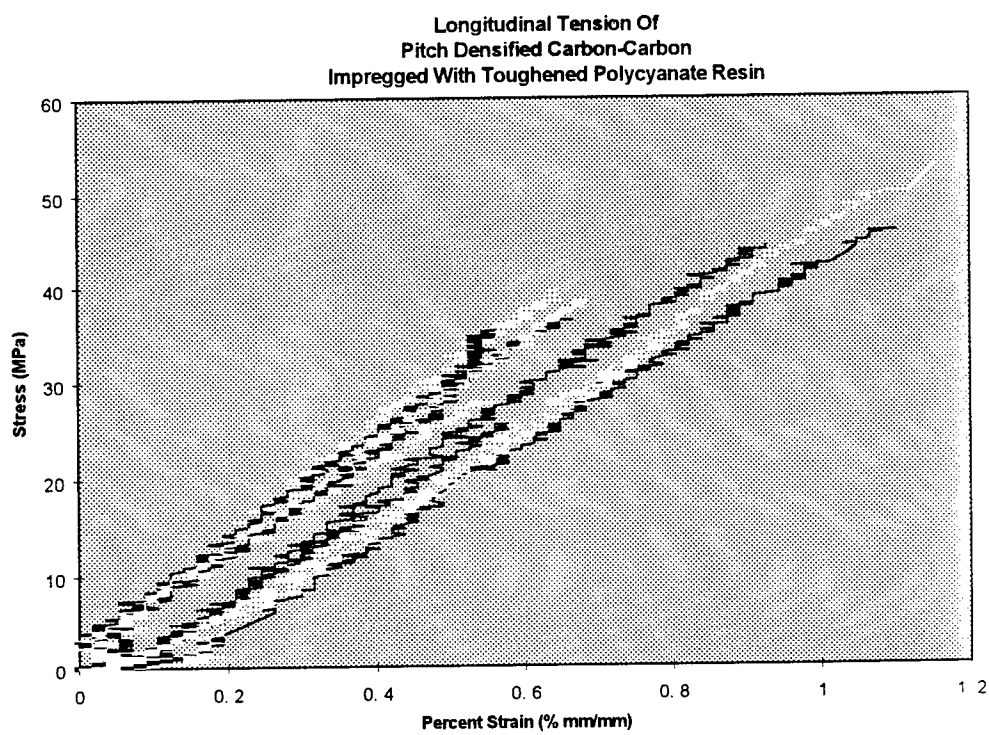
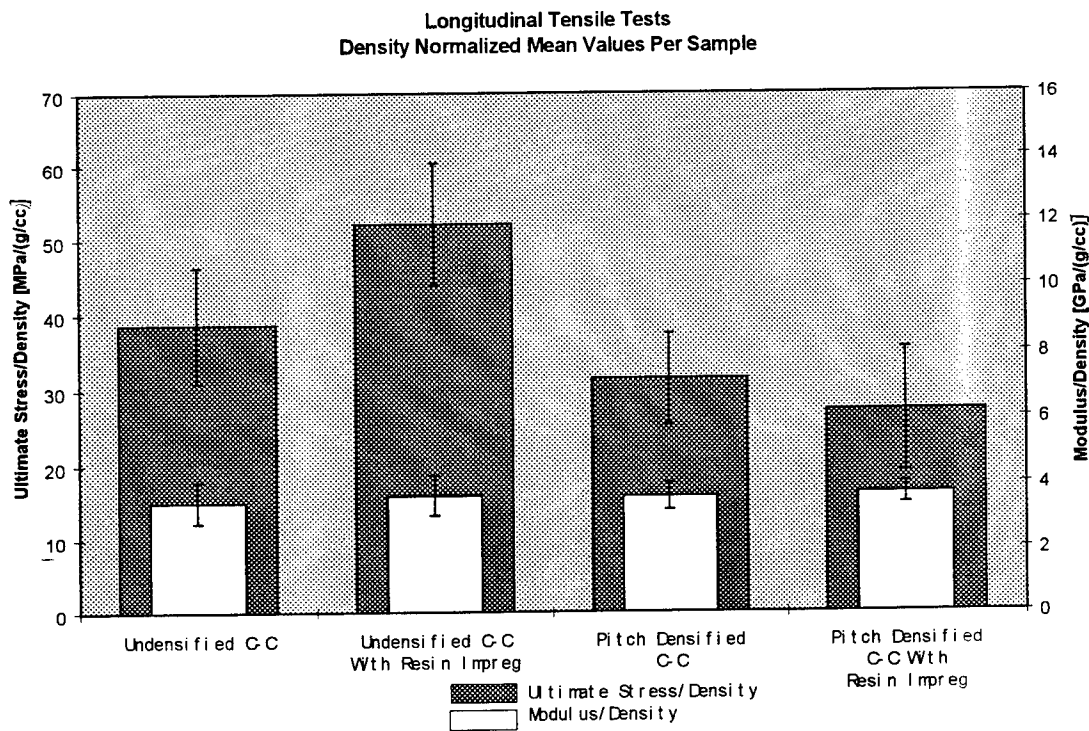


Figure 10



**Figure 11**



**Figure 12**

Interlaminar Tensile Test Results				
Specimen Number	Undensified C-C	Undensified C-C With Resin Impreg	Pitch Densified C-C	Pitch Densified C-C With Resin Impreg
	Ultimate Stress (MPa)	Ultimate Stress (MPa)	Ultimate Stress (MPa)	Ultimate Stress (MPa)
1 2 3 4 5 6 7 8 9 10	6.1	13.95	13.71	15.52
	5.98	14.67	10.82	15.46
	5.65	14.3	10.66	14.3
	5.47	15	12.78	15.62
	4.15	13.99	11.11	15.21
	3.04	13.47	9.03	14.88
	3.41	14.82	12.9	7.97*
	2.66	14.12	11.7	15.93
	7.09	14.13	12.9	14.09
	5.48	14.41	12.79	16.09
Minimum Value	2.66	13.47	9.03	14.09
Mean Value	4.9	14.29	11.84	15.23
Maximum Value	7.09	15	13.71	16.09
Standard Deviation	1.49	0.46	1.43	0.69

Table 3

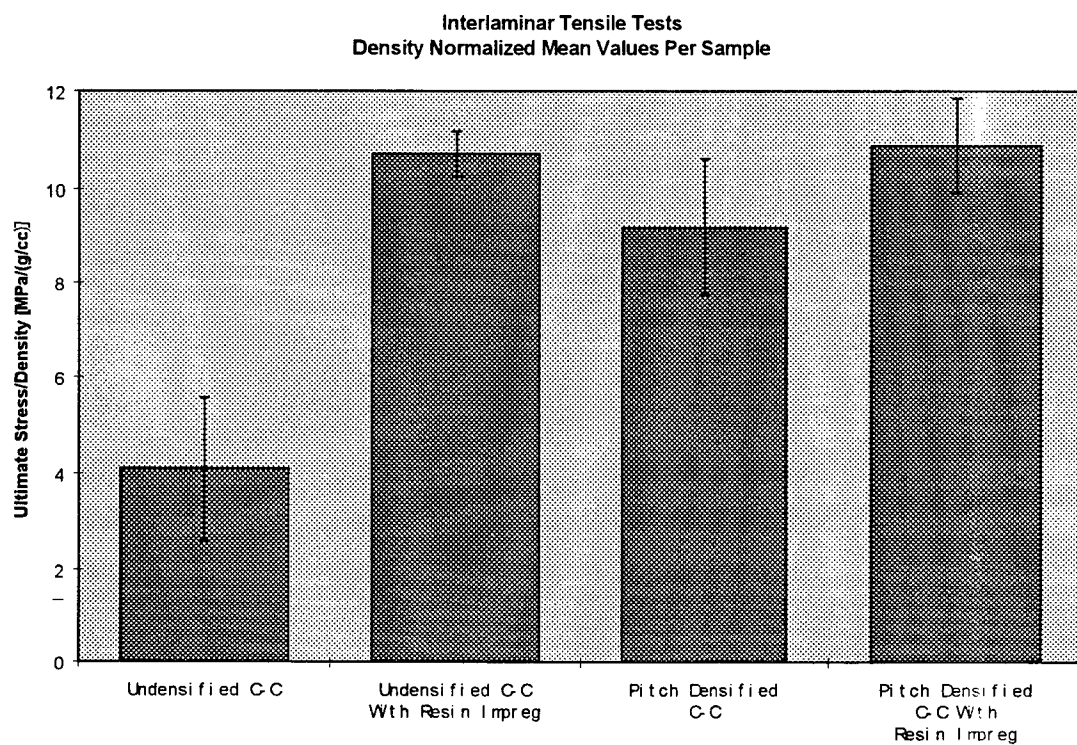


Figure 13

Flexure Test Results								
Specimen Number	Undensified C-C		Undensified C-C With Resin Impreg		Pitch Densified C-C		Pitch Densified C-C With Resin Impreg	
	Ultimate Load (N)	Stiffness (N/mm)	Ultimate Load (N)	Stiffness (N/mm)	Ultimate Load (N)	Stiffness (N/mm)	Ultimate Load (N)	Stiffness (N/mm)
1	464.3	957.3	593.2	914.0	422.9	722.9	569.5	4885.0
2	443.9	909.6	542.3	1118.1	429.7	1030.5	556.6	4874.0
3	416.1	937.2	572.9	1074.9	504.3	1138.4	555.9	5202.0
4	448.0	989.0	602.7	961.2	473.8	1048.2	534.9	940.1
5	453.4	958.6	646.9	1009.2	442.6	1167.8	539.6	1053.9
6	478.5	1061.0	571.5	1190.6	501.6	944.6	609.5	1299.6
7	400.5	743.0	509.1	745.4	492.1	1086.3	532.8	984.8
8	506.4	808.9	579.7	743.2	496.2	843.9	528.8	844.7
9	428.3	901.7	617.0	1018.2	546.4	1150.3	587.1	1208.0
10	424.2	765.7	572.2	964.9	513.8	924.1	524.0	1011.6
Minimum Value	400.5	743.0	509.1	743.2	422.9	722.9	524.0	844.7
Mean Value	446.4	903.2	580.8	974.0	482.3	1005.7	551.0	1049.0
Maximum Value	506.4	1061.0	646.9	1190.6	546.4	1167.8	609.5	1299.6
Standard Deviation	31.4	101.6	38.2	145.5	39.7	145.4	33.3	156.6

Table 3

**Flexure Of  
Undensified Carbon-Carbon**

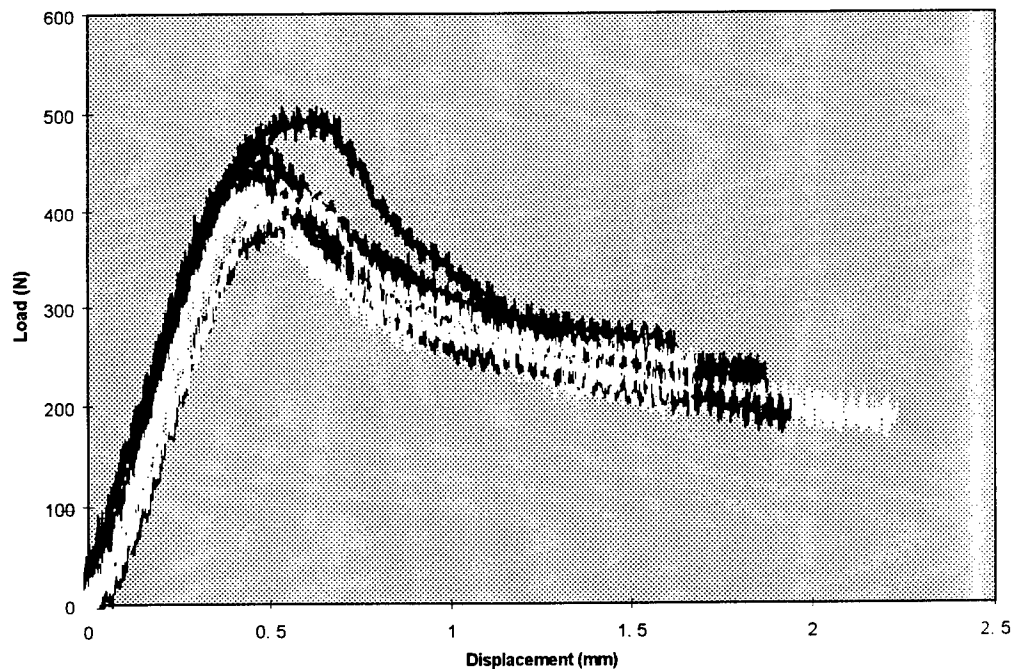


Figure 14

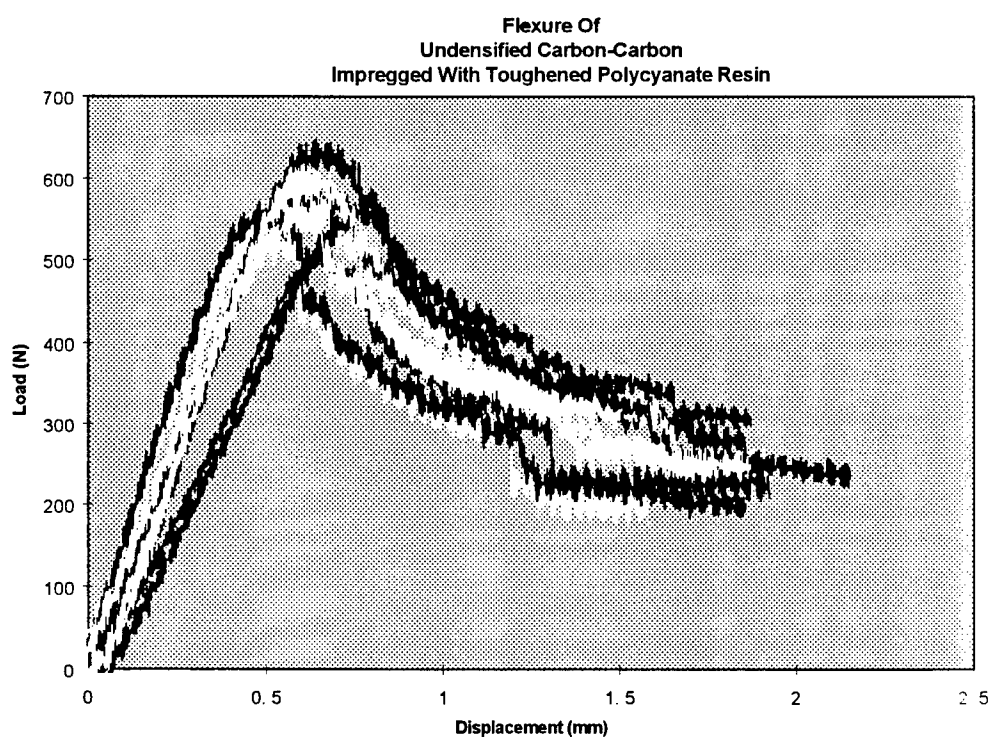


Figure 15

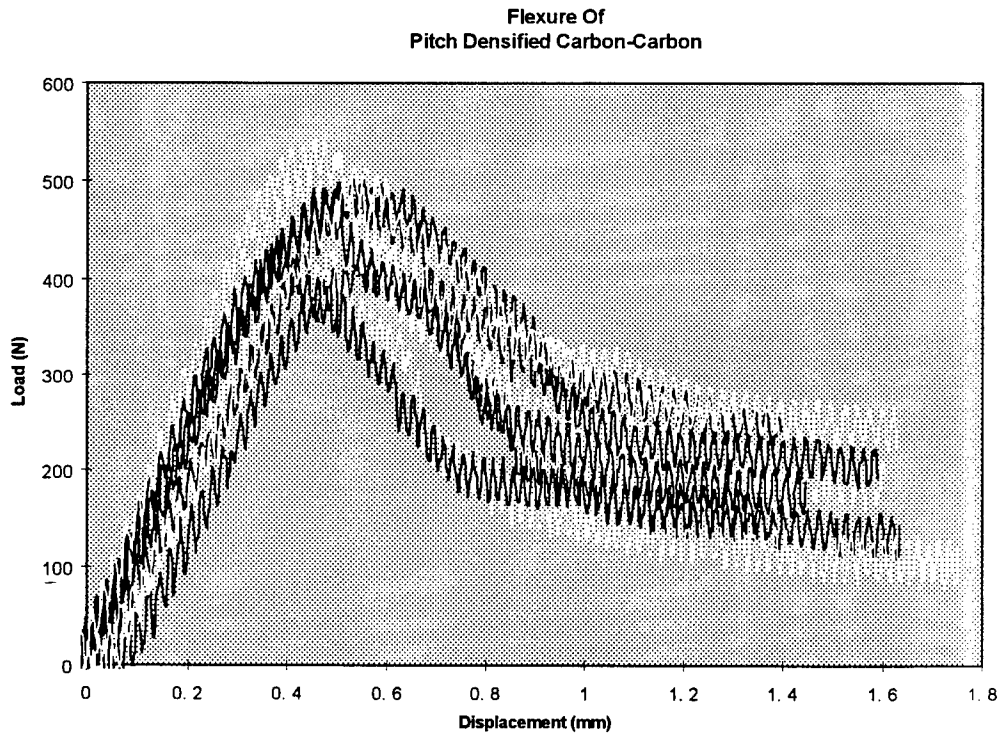


Figure 16

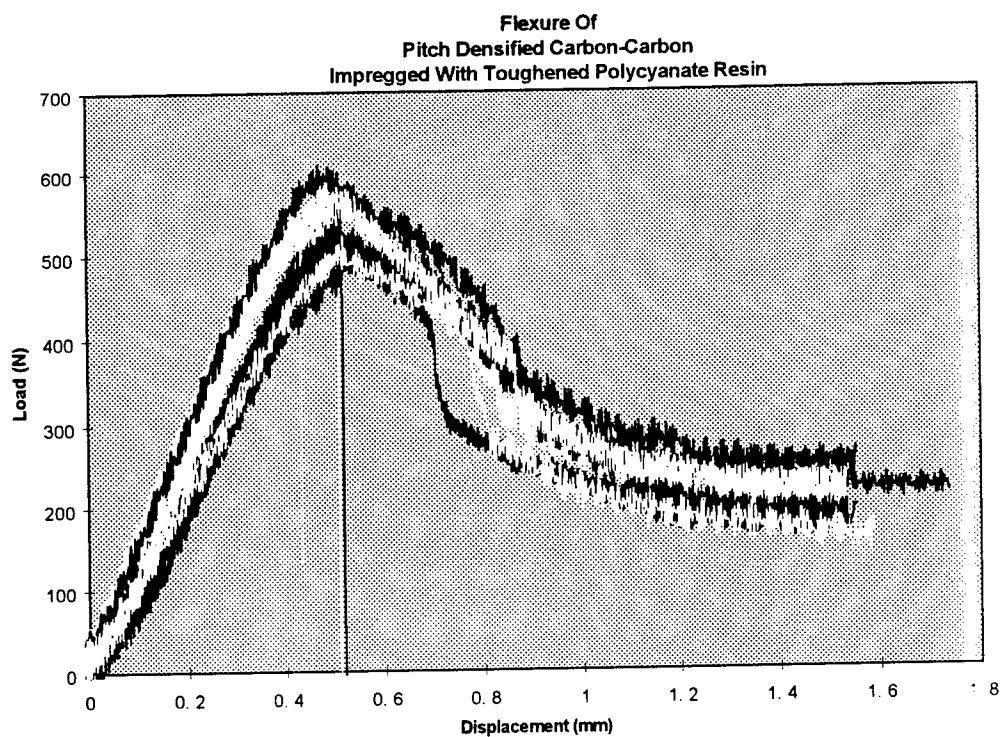


Figure 17

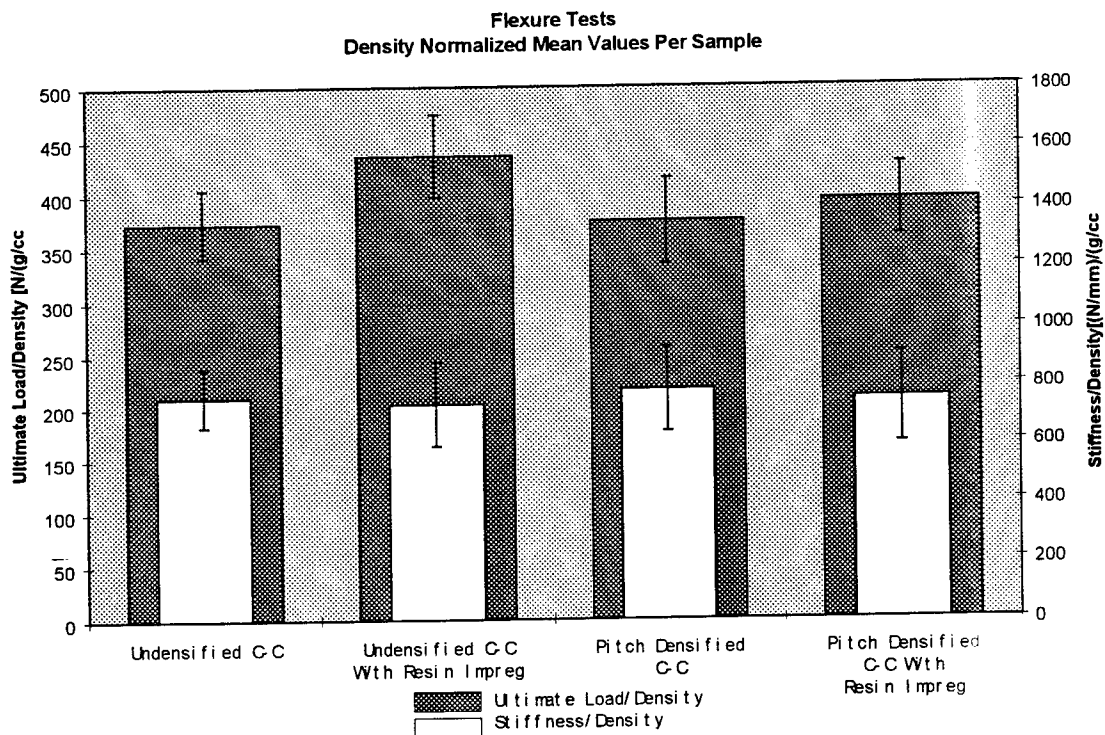


Figure 18

## **Conclusion**

The mechanical properties of carbon-carbon composites can be improved with a final infiltration of toughened polycyanate resin. Also, the long and costly pitch densification procedure can be eliminated without suffering any significant strength penalty. Resin impregnation improved the longitudinal ultimate stress per unit density of undensified carbon-carbon by 34.9%. Unexpectedly low ultimate stress values were recorded for the pitch densified carbon-carbon. The interlaminar ultimate stress per unit density increased 61.9% for undensified carbon-carbon, and 18.4% for pitch densified carbon-carbon. The ultimate load per unit density of flexure specimens increased 16.8% for undensified carbon-carbon, and 5.1% for pitch densified carbon-carbon upon impregnation with toughened polycyanate resin. The improvement in mechanical properties was apparent, but this occurred at the expense of the high temperature capability of the composite. However, for the spacecraft radiator application this sacrifice was justified.

## **Recommendations**

In the continuation of this study, much characterization and data analysis will need to be accomplished. Samples should be characterized with an optical microscope and with a scanning electron microscope to determine the extent and morphology of resin infiltration. Flexural data can be processed to give information on the strength of the tensile and compressive face sheets of the sandwich structure (please see ASTM C393). Data and failure modes should be investigated for an explanation as to why pitch densification did not improve the mechanical properties of the composite. Further testing of the pitch densified carbon-carbon should be initiated. The high-temperature graphitization heat treatment of the composite had to be eliminated because of time constraints. This processing step should be implemented in any further work. The material properties of a competitive organic matrix composite should be quantified to ensure that the use of carbon-carbon is justified. Finally, a separate study of the thermal properties of mixed-matrix carbon-carbon composites should be initiated to determine whether this processing technique is truly a viable option for a high performance passive spacecraft radiator.

## **References**

1. Buckley, John D. and D.D. Edie, ed., Carbon-Carbon Materials And Composites, NASA RP-1254, 1992.
2. Jensen, G, "Application Of High Conductivity Graphite/Epoxy For A Spacecraft Thermal/Structural Radiator", International SAMPE Technical Conference, 23rd, Kiamesha Lake, NY, Oct 21-24, 1991.
3. Rawal, S., B. Cullimore, and M. Misra, "Carbon-Carbon Radiators For Space Applications", Martin Marietta Astronautics Group, Denver, CO, 1993.

## **Acknowledgments**

This work was supported by the Air Force Office Of Scientific Research, Bolling Air Force Base, DC and the Applied Composites Branch of the Division of Structures and Controls, Space and Missile Technology Directorate, the Phillips Laboratory on location at Edwards Air Force Base, CA. I gratefully acknowledge the assistance I received from the following companies: Wyle Laboratories, Inc.; YLA, Inc.; Composite Optics, Inc.; and Research Opportunities, Inc. I sincerely thank Mike Powell, Tim Naughton, and Major Jay Galbraith, USAF for many helpful technical discussions and for the opportunity to work on an exciting and fun research project.

**A Study of Numerical Methods in  
Atmospheric Light Propagation**

Kevin Scales  
Graduate Student  
Department of Physics

University of New Mexico  
800 Yale NE  
Albuquerque, NM 87131

Final Report for:  
Graduate Student Research Program  
Phillips Laboratory

Sponsored by:  
Air Force Office of Scientific Research  
Bolling Air Force Base, DC

and

Phillips Laboratory

August 1994

---

## **A Study of Numerical Methods in Atmospheric Light Propagation**

Kevin Scales  
Graduate Student  
Department of Physics  
University of New Mexico

### *Abstract*

The use of numerical methods to study the propagation of a wavefront through the atmosphere was studied. Many frames of Zernike polynomial coefficients were used to generate eighty term polynomials representing a degraded wavefront. Wavefronts were numerically propagated through a lens to obtain intensity distributions. The Strehl ratios for different magnitudes of phase aberration were computed.

# A study of Numerical Methods in Atmospheric Light Propagation

Kevin Scales

## Introduction

The project for the summer was to explore the feasibility of coupling images from a 7 element interferometer into a fiber bundle consisting of 7 fiber cores embedded in a single cladding and arranged hexagonally. The hypothesis is that for a degraded wavefront, coupling into a fiber bundle would be more efficient than coupling into a single fiber.

For my own part of the project, I studied the propagation of a wavefront through the atmosphere. In theory, any wavefront can be represented by an infinite zernike polynomial. For our data, we used a finite sum. Using Zernike coefficients collected over an aperture, we had 80 terms collected from 128 data frames. Furthermore, I worked out a numerical integration for propagation of an arbitrary wavefront through a converging lens and focused onto a focal plane.

Finally, I investigated the Strehl ratio for varying levels of atmospheric aberration

## Zernike Polynomials

Zernike polynomials are commonly used to describe the aberration of an optical system. By evaluating the polynomials of a Zernike expansion out to a certain number of terms for as many points on the aperture as desired, An accurate representation of the phase of the wavefront can be determined. Their properties are described in detail in Noll, and in Born and Wolf [1],[2]. I will review the important features here.

In polar coordinates, the terms are defined as:

$$Z_{evenj} = R_n^m(r) \cos(m\theta)$$

$$Z_{oddj} = R_n^m(r) \sin(m\theta)$$

for  $m \neq 0$  and

$$Z_j = \frac{R_n^0(r)}{\sqrt{2}}$$

for  $m = 0$ ,

where

$$R_n^m(r) = \sum_{s=0}^{(n-m)/2} \frac{(-1)^s (n-s)!}{s![(n+m)/2-s]![(n-m)/2-s]!} r^{n-2s}.$$

Using these, we can form zernike polynomials in the form:

$$\psi(x, y) \approx \sum_{n=3}^{82} a_n Z_n(x, y)$$

where  $a_n$  are given coefficients.

The first term, representing the piston phase, and the second and third terms representing tilt were not included. They were removed during data collection. The coefficients are ordered according to figure 1.

An explanation should be made for figure 1. Increasing orders of Zernike polynomial terms are found by following the line, starting at the  $m=0, n=1$  position. For  $m \neq 0$ , two terms are associated with each point. For  $m=0$ , one term is associated with each point. Since the piston and tilt have been removed, the first three terms are not included in the data. Thus, the first included term would be at  $n=2, m=0$ . Also note that the cosine term (for even  $j$ ) always comes first in this setup.

The program has a few important features. The coefficients read in are automatically normalized to have a mean of zero. The user may specify the removal of as many lower order aberrations as desired.

We found that sufficient accuracy was achieved by evaluating, in polar coordinates, one hundred radial points and five hundred angular points over a given aperture. In addition to the center point, this allowed over fifty thousand phase aberrations to be calculated over an aperture.

I found that the average phase aberration was very close to zero, indicating that the aberated wave was very close to a plane wave.

## **Propagation through a lens**

The next step, after achieving a numerical representation of the wavefront, is to numerically propagate it through a converging lens. This can be done by evaluating the real part of the propagation integral:

$$\int_0^{2\pi} \int_0^a e^{i\phi} \exp\left[\frac{ik}{2}\left(\frac{|(\rho - \rho')|^2}{z} - \frac{\rho'^2}{f}\right)\right] \rho' d\rho' d\theta'$$

Because there were 128 frames to work with, It was only possible to plot the intensity distribution relative to that of a plane wave for many different phase aberration distributions over the aperture. A plot for the first frame of data is included as figure 2. Note that the on-axis intensity is about sixty seven percent that of the plane wave case.

The form of the intensity distribution is very close to the known Bessel function distribution for the plane wave case.

To further explore wavefront degradation, The phase at each position on the aperture was multiplied by a constant factor and re-evaluated the propagation through the lens. A plot for a factor of ten is included in figure 2.

## **Strehl Ratio**

The final step is to investigate the effect of using varying phases on the Strehl ration of an optical system. [3] To review, the Strehl ratio is defined as the on axis intensity of an aberrated wavefront divided by the on axis intensity of an unaberrated wavefront for the same optical system. By varying the magnitude of the phase aberrations, the Strehl ratio can be made to vary likewise.

Multiplicative factors ranging from one tenth to three were used. With increasingly large phases, the Strehl ratio was found to decline sharply at first, and then gradually leveling off. The Strehl ratios for three frames of data are included in figure 4.

In addition, the Maréchal approximations for a single frame of data are plotted on the same graph. [4] Here:

$$S_1 \approx (1 - \sigma_\phi^2)^2$$

$$S_2 \approx 1 - \sigma_\phi^2$$

$S_3 \approx \exp(-\sigma_\phi^2)$ .

$\sigma_\phi^2$  is simply  $\langle \phi^2 \rangle - \langle \phi \rangle^2$ .

Since  $\langle \phi \rangle$  is zero over the entire aperture, we only have  $\langle \phi^2 \rangle$  which is defined by:

$$\langle \phi^n \rangle = \pi^{-1} \int_0^1 \int_0^{2\pi} \phi^n(\rho, \theta) \rho d\rho d\theta.$$

As the graph shows, the Strehl ratio closely matches the approximations for small values of  $\sigma_\phi^2$ . Because the approximations are made by ignoring higher order terms in the expansion of  $\sigma_\phi$ , the approximate expressions will always be lower than the exactly computed Strehl ratio.

## Conclusions

Zernike polynomials have been shown to be useful to accurately represent an aberrated wavefront, even for cases in which the aberrations are highly random, such as in the case of atmospheric turbulence. Using a moderately powerful workstation, Zernike polynomials expansions can be evaluated to an arbitrary number of terms provided coefficients are given, and the calculations can be done in a reasonable time (less than thirty seconds per frame of data).

The validity of the process is shown by propagating the aberrated wavefront through a lens and investigating its intensity distribution in the focal plane. As we have seen, the intensity distribution matches the theoretical pattern for a randomly aberrated wave.

Finally, the Strehl ratio for varying phase aberration magnitudes follows the theoretical values, and provides a close match to commonly used approximations at low values of  $\sigma_\phi^2$ . As expected, the common approximations were slightly lower than the actually computed Strehl ratio, as they should be according to the expansions.

## Bibliography

1. R.J. Noll, *J. Opt. Soc. Am.* **66**, 3, 1976
2. M. Born, E. Wolf, *Principles of Optics*, 5<sup>th</sup> ed., Pergamon Press, Oxford, 1975
3. R. Tyson, *Principles of Adaptive Optics*, Academic Press, San Diego, 1991
4. V. Mahajan, *Aberration Theory Made Simple*, SPIE Optical Engineering Press, Bellingham, 1991

Fig. 1

Zernike Polynomials

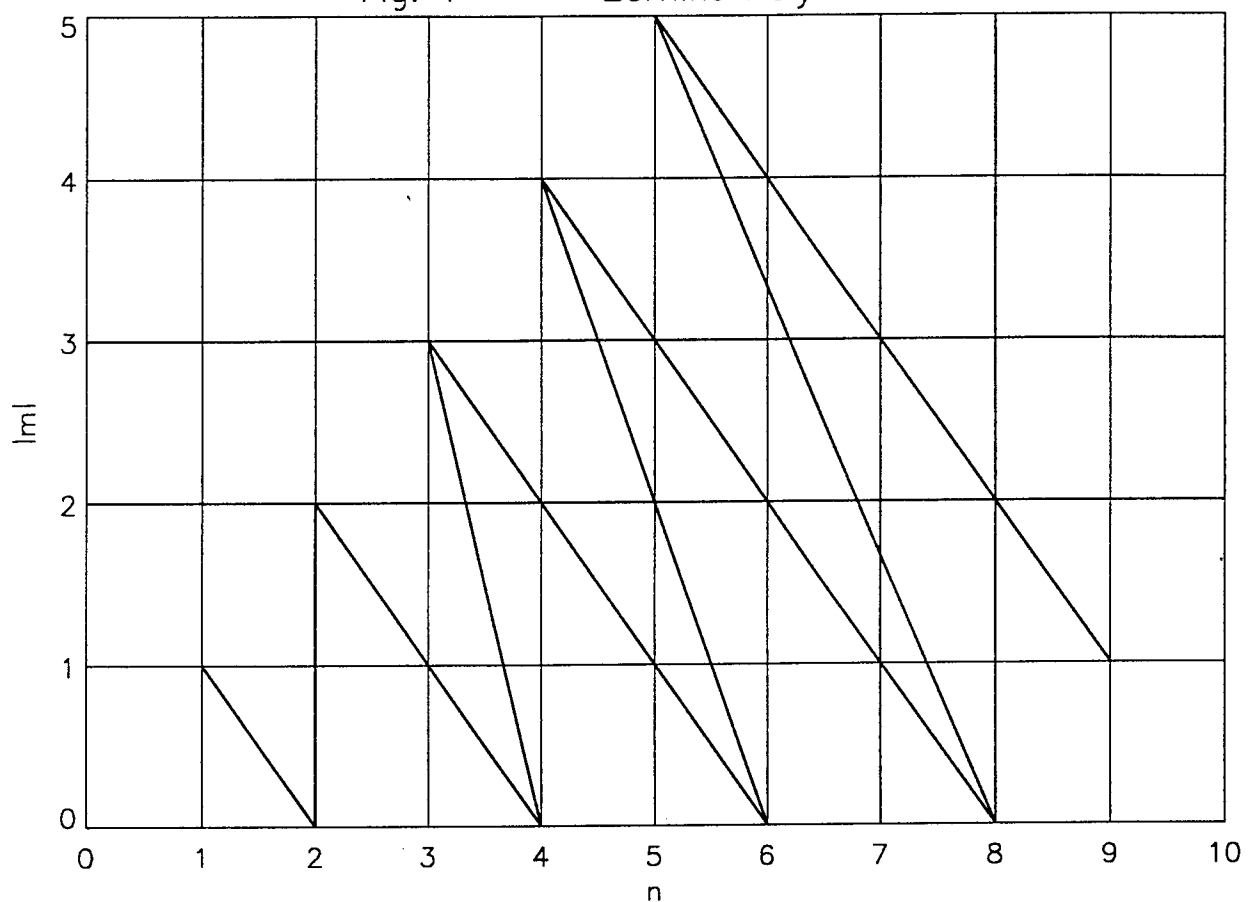


Fig. 2

relative intensity distribution

for mult. factor 1

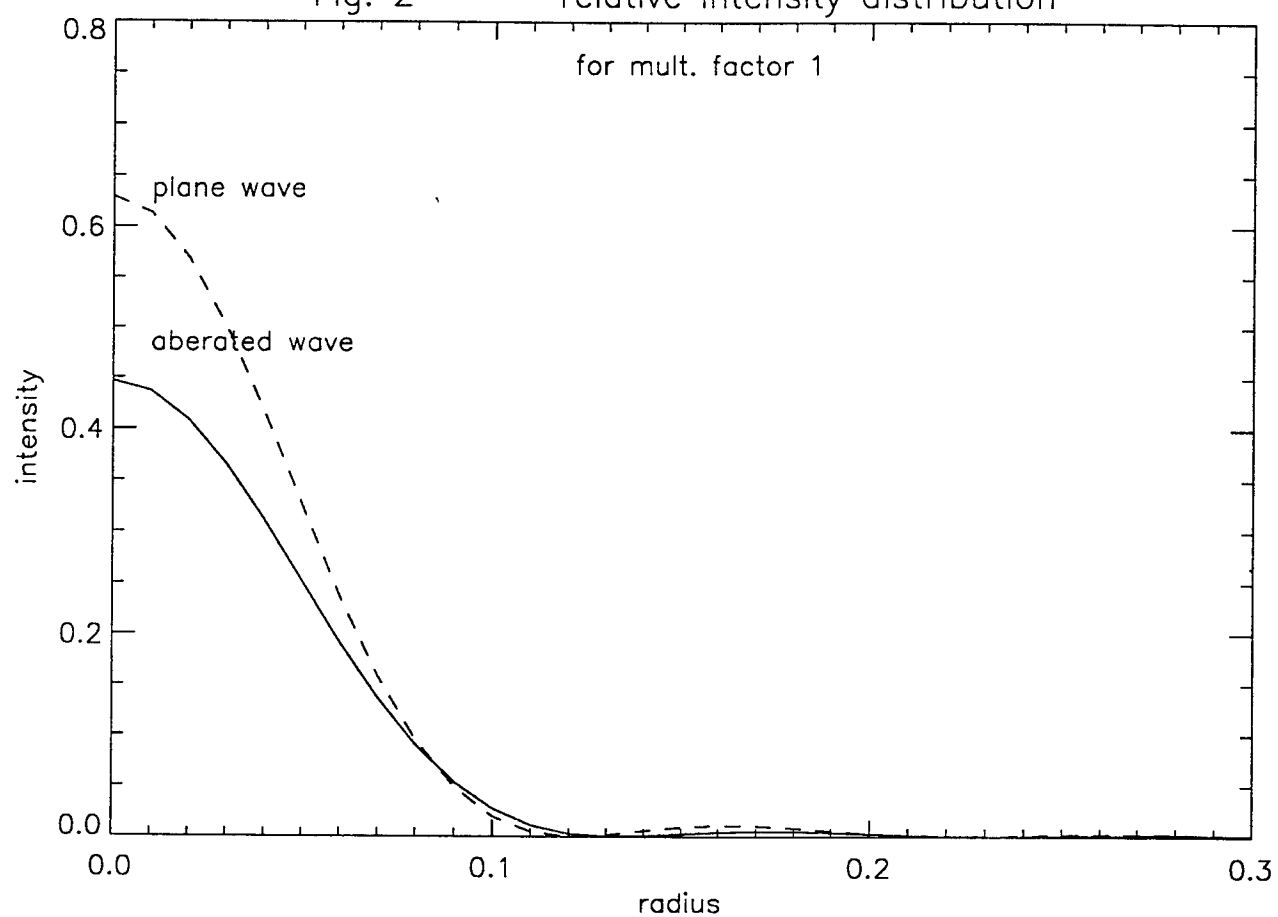


Fig. 3

relative intensity distribution

for mult. factor 10

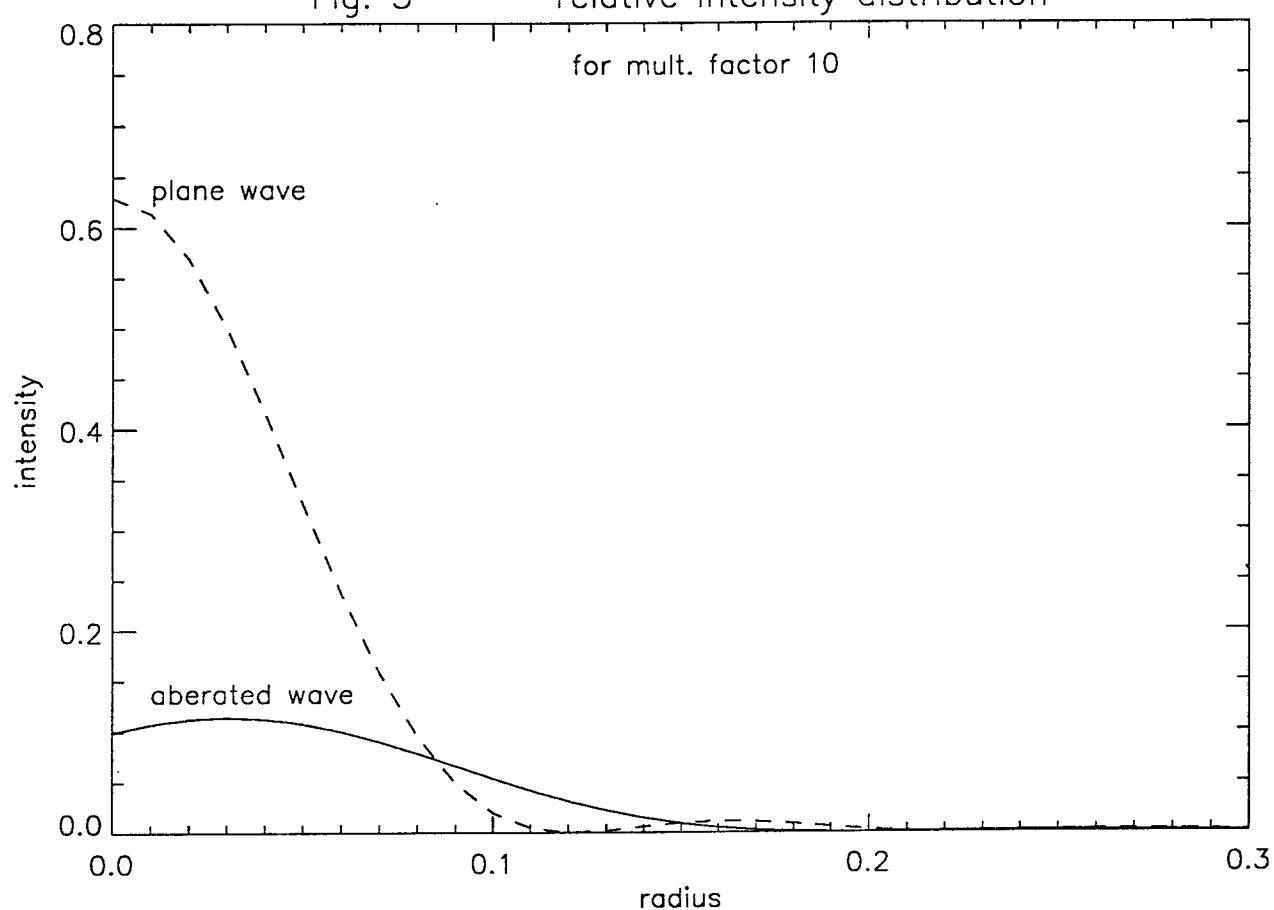
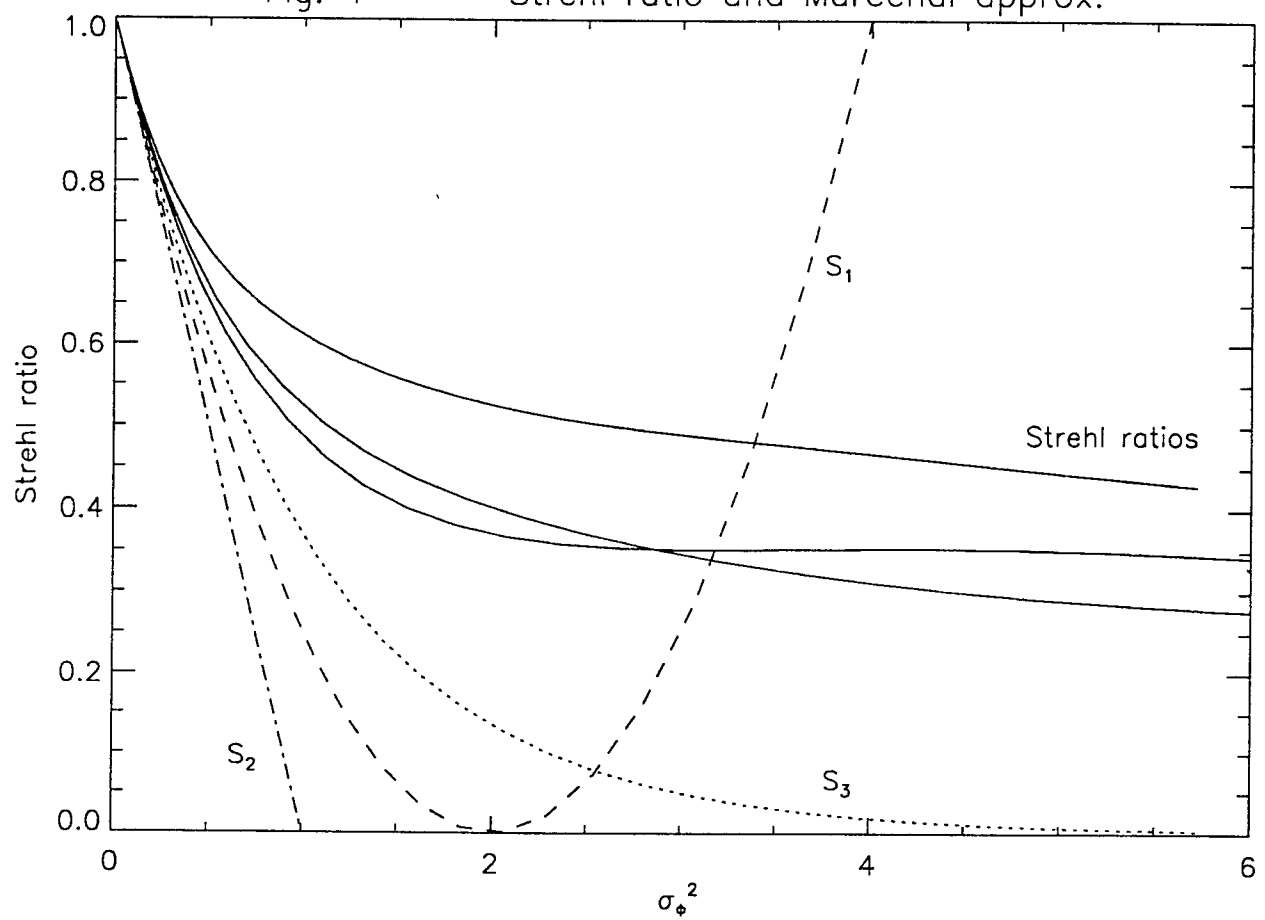


Fig. 4

Strehl ratio and Marechal approx.



FURTHER STUDIES OF A HIGH TEMPERATURE CESIUM-BARIUM TACITRON, WITH  
APPLICATION TO LOW VOLTAGE-HIGH CURRENT INVERSION

Greg T. Sharp  
Department of Electrical Engineering

University of New Mexico  
Rm. 110 EECE  
Albuquerque, New Mexico 87131

Final Report for:  
Graduate Student Research Program  
Phillips Laboratory

Sponsored by:  
Air Force Office of Scientific Research  
Bolling Air Force Base, DC

and

Phillips Laboratory

August 1994

FURTHER STUDIES OF A HIGH TEMPERATURE CESIUM-BARIUM TACITRON, WITH  
APPLICATION TO LOW VOLTAGE-HIGH CURRENT INVERSION

Greg T. Sharp  
Department of Electrical Engineering  
University of New Mexico

**Abstract**

In an effort to improve the performance and understanding of the cesium-barium (Cs-Ba) tacitron device, several upgrades in the device hardware and software have been undertaken. The present intended application for this device is for dc to ac power conversion as part of a power conditioning unit aboard a nuclear fueled satellite. Several other possible applications have been identified such as high temperature batteries, circuit breakers, electroplating, and metallurgical extrusion. The most immediate extension is for use as an inverter mounted near or directly on the end of a thermionic device. As many of the individual device parameters fall within the testing range of the current cylindrical cs-ba tacitron device, it is desirable to upgrade the device in the areas of temperature range, cesium and barium vapor pressure, component material and tolerances, data acquisition, control circuit speed, and understanding of the range of work functions for cesium and barium in relation to device forward voltage drop.

# FURTHER STUDIES OF A HIGH TEMPERATURE CESIUM-BARIUM TACITRON, WITH APPLICATION TO LOW VOLTAGE-HIGH CURRENT INVERSION

Greg T. Sharp

## Introduction

Space nuclear power systems are being designed to supply electrical power ranging from tens to hundreds of kilowatts to provide power to a variety of civilian and military space payloads. A radioisotope or nuclear reactor provide the heat source for power generation. In static conversion systems this heat is converted to dc electrical energy using thermoelectric generators or thermionic converters. Several design parameters are of critical importance when used in nuclear space power applications. Reliability, low mass, and tolerance to elevated temperatures and radiation, are some of the most important. The Cesium-Barium (Cs-Ba) vapor thermionic switch called "tacitron" is a triode device that is turned on by applying a positive voltage pulse to the grid and is turned off by supplying a negative pulse to the grid. The (Cs-Ba) tacitron is a tube-type device designed to be used to convert dc reactor output power to ac transmission and payload power as part of the power conditioning unit (PCU) located between the reactor and payload. Unlike semiconductor based PCU's that cease to function at high temperatures ( $>250^{\circ}\text{C}$ ) and are vulnerable to nuclear radiation [1, 2], the ability of the tacitron to operate under the harsh temperature and radiation conditions in close proximity to the nuclear heat source makes it a very promising candidate for use in the PCU [3]. This heat and radiation tolerance also mean that the tacitron can be mounted near the power source resulting in a mass savings (reduction in boom size), and much higher power transmission efficiencies due to reduced  $I^2R$  losses when transmitting low current vs. high current power [4-6]. With no moving parts involved in the static vs. dynamic heat to electrical energy conversion as well as the lack of moving parts in the tacitron, the possibility of a "reliable" PCU system using this device combination is much higher than with other methods.

Currently experimentation using a planar tacitron is underway at the University of New Mexico's Institute for Space Nuclear Power Studies (ISNPS) as well as the operation of a cylindrical device located

at the Phillips Laboratory's Space Power Laboratory (SPL) at Kirtland Air Force Base both in Albuquerque, New Mexico. Both facilities are investigating the operation characteristics of a single triode device. The tacitron uses molybdenum electrodes with a mixture of low pressure ( $\approx 10^{-3}$  Torr) cesium and barium which functions as the conduction medium. The cesium is used to increase the space charge limit (reducing the forward voltage drop) and the barium reduces the work function at the electrode surface (increasing conduction current). The device can conduct relatively high currents at repetition rates near 20 kHz with forward voltage drops less than 3 V.

Some of the other applications that have been identified for tacitron use are high temperature batteries, circuit breakers, electroplating, and metallurgical extrusion [7], as well as with fuel cells and thermionic devices.

### Motivation

The changing politics in military and space research funding dictate that many current projects will fall out of favor for a variety of reasons as an ongoing prioritizing process. Nuclear power of any kind is particularly vulnerable due to public opinion in regards to safety and waste processing. Commercially viable products that demonstrate an ability to show a return on investment in a reasonable amount of time tend to be high on the list of funded projects. For these reasons it is desirable to pursue the already identified commercial applications for the low voltage-high current tacitron switching device.

### Discussion of Problem

The current cylindrical tacitron device is of Russian design and construction. Many pieces have been hand finished prior to final assembly. Some of the pieces, the boron nitride insulators in particular, vary in dimension by more than  $10 / 1000^{\text{ths}}$  of an inch. These insulators separate the molybdenum components and seal the device as well. The loose fit of individual components allows leakage of the cesium and barium vapors making it difficult to control and monitor vapor pressure. The difference in gap spacing makes it impossible to determine how much voltage drop is occurring across each individual

section of the device as current flow in a plasma is spatially dependent. To remedy these problems, new boron nitride insulators have been machined and installed. The cylindrical device has been operated in inversion mode in 1993 at the ISNPS facility but the driver circuitry does not exist at it's present location. The present driver system which is capable of driving only one triode at a time incorporates a TTL controlled SCR relay system which is limited in switching speed due to the relatively slow rise times in the SCR's. A new push-pull, TTL actuated driver circuit designed by Gordon Masten, another project member, has been modeled using PSPICE and demonstrates significantly improved rise times and resulting switching speed. Upon assembly and testing of this new driver circuit, a complementary circuit will be constructed to power the second triode for use in the inversion mode. Since the cylindrical tacitron has a parallel configuration, with the addition of the second driver circuit, it will also be possible to determine if two triodes in parallel conduct twice the current. When the device was previously operated in inversion mode it was found that the cesium vapor pressure differed between the top and bottom triode sections most probably due to the location of the cesium orifice input at the base of the device in conjunction with the temperature gradient across the device. This difference in vapor pressure caused the bottom triode to operate near the top of it's vapor pressure range while the top triode operated near the bottom of it's vapor pressure range. The overlap allowed for a very narrow device operating range. Since vapor pressure is a function of temperature and distance in a static system, to compensate for this pressure imbalance a second cesium feed line of equal length entering the device at the top will be installed. Both lines will be held at the same temperature using heat tape. In addition to the second cesium line, particular attention will be paid to the installation of radiation shielding to minimize radiative losses which cause the temperature gradient across the device. These two changes should allow the tacitron a much wider range of operation in relation to the variability of cesium pressure. Premature failure of the base heater has restricted the variability of cesium vapor pressure also. The previous system consisted of a tungsten wire strung with ceramic fishbone insulators and was electrically connected using in-line set-screw connectors. This wire was wrapped around the base flange and shrouded under a radiation shield. The tungsten proved to be extremely brittle and would fracture due to thermal cycling or whenever the

electrical connectors were handled. The failure of this heater did not allow the temperature of the cesium reservoir to be raised above it's lower operating level as everything else in contact with the cesium vapor must be at a higher temperature than the reservoir or the cesium will plate out on the cooler surface. This problem was corrected using a tantalum heater wire installed similarly to the tungsten wire with the addition of a MACOR junction block at the electrical connection site to prevent bending strain on the heater wire during service. Data acquisition and device control have been substantially improved with the addition of Lab Windows software programmed by Yuri Djashiashvili a visiting Russian scientist from the Kurchatov Institute of Atomic Energy in Moscow, Russia.

### Conclusions

The need to maintain closer control over temperatures in the cesium and barium reservoirs as well as the device itself to more fully characterize the electrical properties of the tacitron has been addressed. Component spacing has been equalized removing another variable in the generation of a good working model. The cesium delivery system resulting in a more constant cesium pressure across the device has been designed and will soon be implemented. Software upgrades will enable faster, more accurate control and data acquisition. Upon completion of these modifications the cylindrical tacitron will be ready to begin characterization of the parameters for proposed commercial devices as well as to further characterize it's application in space nuclear power.

### References

- [1] Frasca, A.J. and G.E. Schwarze (1992), "Neutron, Gamma Ray, and Temperature Effects on the Electrical Characteristics of Thyristors," in Proc. 27<sup>th</sup> Intersociety Energy Conversion Engineering Conference, San Diego, CA.
- [2] Schwarze, G.E., J.M. Niedra, A.J. Frasca, and W.R. Wieserman (1993), "Radiation and Temperature Effects on Electronic Components Investigated Under the CSTI High Capacity

Power Project," in Proc. 10<sup>th</sup> Symp. on Space Nuclear Power and Propulsion, AIP, 599.

- [3] Murray, C.S. (1993), "Experimental and Theoretical Studies of a High Temperature Cesium-Barium Tacitron, With Application to Low Voltage-High Current Inversion," Ph.D. Dissertation, University of New Mexico, Albuquerque, New Mexico.
- [4] Tabisz, W.A., M.M. Jovanovic, and F.C. Lee (1992), "Present and Future of Distributed Power Systems," IEEE Modulator Symposium, 11.
- [5] Tsai, F.S. and F.C. Lee (1987), "Computer Modeling and Simulation of a 20 kHz AC Distribution System for Space Station," Proc. 22<sup>nd</sup> Intersociety Energy Conversion Engineering Conference, 338.
- [6] Hansen, I.G. and G.R. Sundburg (1986), "Space Station 20 kHz Power Management and Distribution System," IEEE Power Electronics Specialists Conf. Rec., 676.
- [7] Piper, A.K. (1991), "Market Survey for Thermionic Devices," Kiser Research Inc., Company Report.

A STUDY OF LOW FREQUENCY WEAK TURBULENCE  
IN A HOLLOW CATHODE DISCHARGE PLASMA

Joseph M. Sorci  
Graduate Student  
Department of Nuclear Engineering

Massachusetts Institute of Technology  
77 Mass. Ave.  
Cambridge, MA 02139

Final Report for:  
Summer Research Program  
Phillips Laboratory

Sponsored by:  
Air Force Office of Summer Research  
Culver City, CA

and

Phillips Laboratory

August 1994

A STUDY OF LOW FREQUENCY WEAK TURBULENCE  
IN A HOLLOW CATHODE DISCHARGE PLASMA

Joseph M. Sorci  
Graduate Student  
Department of Nuclear Engineering  
MIT

Abstract

Work was performed on a Hollow Cathode Discharge in the Nuclear Engineering Plasma Teaching Laboratory to characterize low frequency plasma oscillations and the drift wave turbulence associated with such oscillations for possible application to ionospheric plasma physics. Robust weak turbulence whose spectral characteristics depended reproducibly on the operating point of the discharge, most particularly on the axial magnetic field and on the plasma current, was measured in argon plasmas. The onset of this turbulence was found to occur at a critical value of axial magnetic field. The number of modes present as well as their amplitudes depended sensitively on axial magnetic field values above this critical value. The amplitude of the oscillations depended on the value of the plasma current.

A STUDY OF LOW FREQUENCY WEAK TURBULENCE  
IN A HOLLOW CATHODE DISCHARGE PLASMA

Joseph M. Sorci

Introduction

Work was performed on a Hollow Cathode Discharge in the Nuclear Engineering Plasma Teaching Laboratory to characterize low frequency plasma oscillations and the drift wave turbulence associated with such oscillations for possible application to ionospheric plasma physics. Of special interest were the concomitant transport processes that might contribute to the formation of large scale structure in the ionosphere and magnetosphere that duct whistler waves. The Hollow Cathode Discharge or HCD is an ideal platform for such studies because it can simulate a range of ionospheric conditions including disparate electron and ion temperatures ranging from 1-10 ev and .1-1 ev respectively, varying degrees of fractional ionization ranging from 50% to 99%, axial magnetic fields ranging from 300 Gauss to 650 Gauss, and a strong permeating radial electrostatic field on the order of 4 V/cm that gives rise to large  $\mathbf{E} \times \mathbf{B}$  drifts. Densities are high, on the order of  $10^{13}\text{-}10^{14} \text{ cm}^{-3}$ . An axial current on the order of 30-60A is carried by two distinct types of electrons: those drifting collisionally along the magnetic field driven by the DC voltage that sustain the arc and those streaming along the magnetic field at energies of about 20ev created by thermionic and secondary emissions at the hot spot of the cathode. More information on the principals of HCD operation is available in Lidsky<sup>1</sup>.

Best of all is that all of these phenomena are easily measurable in a linear device where the geometry is uncomplicated and uncomplicating. Operation is steady state and can be maintained for hours at a time. Here, emphasis has been placed on exploring the feasibility of drift wave turbulence studies on the HCD and possible applications to ionospheric physics. A robust, weakly turbulent argon plasma was found to be created easily, reproducibly, and with the added feature that the oscillations that characterized the weak turbulence present were to a great degree tunable by adjusting various operating parameters such as

magnetic field, gas feed and hence neutral density, and plasma current. Having such a workbench of low frequency (6-10 KHz) weak turbulence that is tunable would be of great use in transport studies as well as wave scattering experiments. The HCD is capable of producing other species of plasmas as well including hydrogen plasmas, oxygen and hydrogen plasmas, oxygen and argon plasmas, and argon and oxygen plasmas. None of these other combinations were explored in this work because time did not permit and because the presence of oxygen in the device degrades its useful lifetime.

### Methodology

Considerable effort was required to bring the HCD back into operation. Used primarily as a teaching device and no longer as a research tool, the HCD was in a deplorable state of disrepair, used only for the most basic measurements of electron temperature and density of quiescent argon plasmas for about two weeks every year. Cathode material was procured, circuits troubleshooted and repaired, and numerous other sundries attended to before operation could begin.

Next, a simple electrostatic probe or Langmuir probe was built by affixing tungsten wire into an alumina tube with vacuum epoxy. This arrangement was then fitted into a stainless steel tube that acted as a ground for the probe signal and a shield for the coax cable that brought the signal out from the probe to a 20MHz digitizing oscilloscope. The probe was then mounted via a vacuum feed through a port on the side of the HCD, leaving the probe tip free to scan in radius on the mid plane of the central region of the discharge. For signal processing, a simple wave form storage routine and subsequent FFT decomposition into normal modes was implemented on a PC.

Two sets of experiments were performed, both aiming at measuring floating potential fluctuation spectra of argon discharges under different conditions. The first set of experiments consisted of repeated scans with the tip of the Langmuir probe 1 cm from the center of the discharge for varying values of axial magnetic field from 300 Gauss to 650 Gauss. The second set of experiments consisted of repeated scans with the tip of the Langmuir probe 1 cm from the center of the discharge, axial magnetic field fixed at 500 Gauss, for varying values of the plasma current from 21A to 36A.

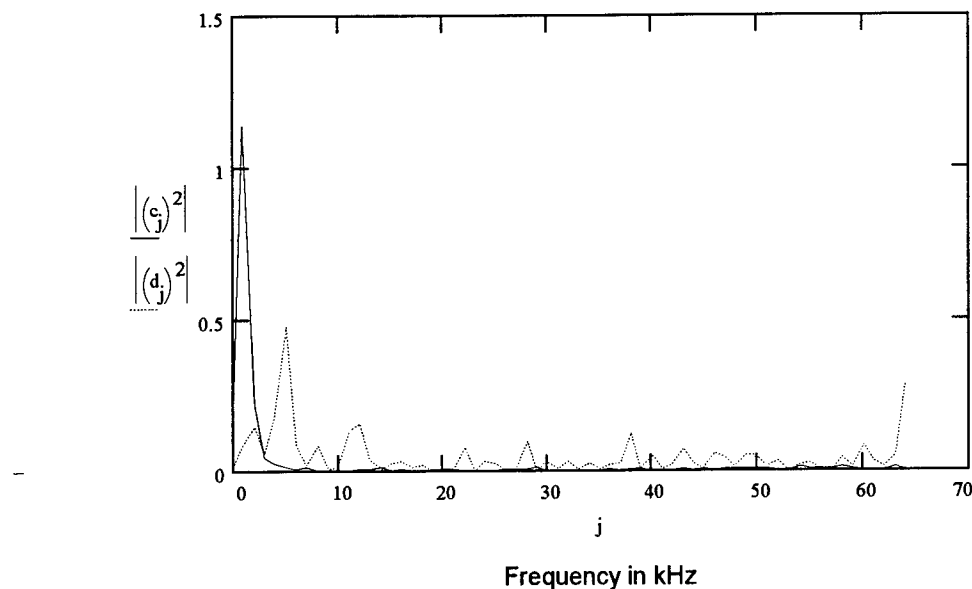
Other types of experiments were planned, but owing to time constraints and equipment failure, are not included in the present work. Amongst these are keeping both plasma current and axial magnetic field fixed while scanning in radius, keeping position, plasma current, and axial magnetic field fixed while varying gas feed rate through the cathode, and conducting heating/wave scattering experiments by mounting a microwave launcher on the machine for ECRH experiments. In fact a 2.45 GHz , 600 W source was successfully mounted on a port downstream of the probe; however ECRH experiments are not possible yet because the magnet power supplies can only create a field on the mid plane ahead of the launcher of about 650 Gauss while 875 Gauss is required to have this particular resonance in the machine.

### Discussion and Results

Plasma floating potential fluctuations first identified by Chung and Rose<sup>2</sup> were measured in the HCD.

They identified these fluctuations as drift wave instabilities and weak turbulence.

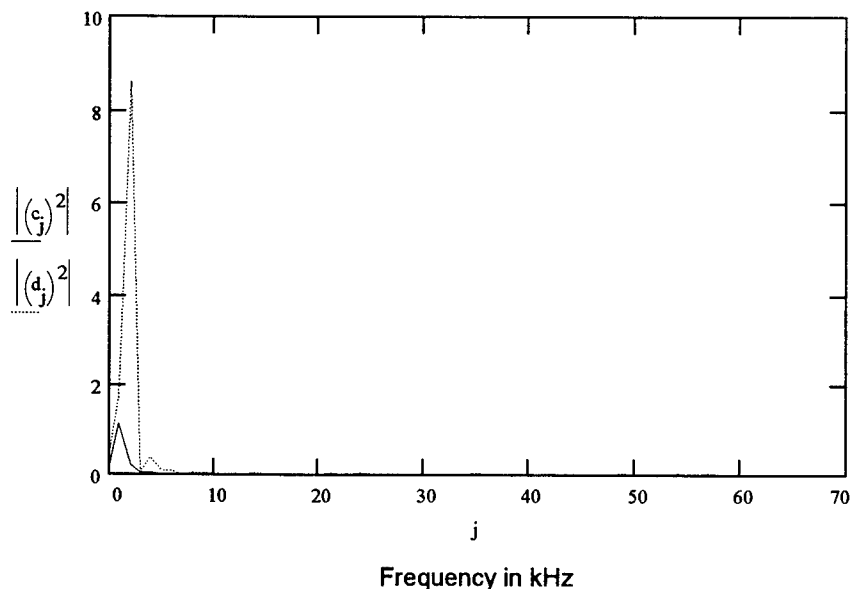
Figure 1: Power Spectrum from FFT for B=400 Gauss (solid line) and for B=650 Gauss (dashed line)



Y-axis: Normalized to Volts-squared

Figure 1 shows the results from the first set of experiments where the Langmuir probe was positioned 1 cm from the center of the plasma, the plasma current fixed at 21 A, and the magnetic field on axis scanned from 300-650 Gauss. The spectra plotted represent typical spectra for these operating conditions at 400 and 650 Gauss respectively. At low values of magnetic field, one normal mode at 2 KHz dominates an otherwise barren spectrum. As the magnetic field on axis is increased, the fundamental mode's amplitude decreases and shifts upward in frequency as additional modes grow up. The underlying mechanisms that populate the spectrum have not been identified , but the phenomenon is real and reproducible. An even more dramatic transition occurs at B=350 Gauss. Below this value, no coherent fluctuations in the frequency range shown above were detectable, only noise. At B=350 Gauss, the 2KHz oscillation suddenly appears indicating a threshold of some sort.

**Figure 2: Power Spectrum from FFT for I<sub>plasma</sub>=21A (solid line) and for I<sub>plasma</sub>=36A (dashed line)**



Y-axis: Normalized to Volts-squared

In figure 2 the results from the second set of experiments is displayed. In these experiments the probe was located at a fixed position 1 cm from the center of the discharge, the magnetic field was held fixed at 500 Gauss, and the plasma current was scanned from 21A to 36 A. The frequency shifts upward as the current is increased, but only slightly, and a tiny second harmonic grows up. Otherwise no other modes are seen in this frequency range. What is dramatic is that the amplitude of the fundamental mode increases by an order of magnitude as the current is ramped up 15 A. This suggest that underlying mechanisms are very sensitively dependent on the current as well as the density gradient.

#### Conclusions and Suggestions for Future Work

More careful measurements and analyses are needed to understand these HCD fluctuations and their possible applications to ionospheric plasma physics and the transport processes involved in forming large scale structure in the ionosphere that might be capable of ducting whistler waves. Fast scanning langmuir probes that generate radial  $T_e$  and  $N_e$  profiles as well as a magnet supply that could raise the axial field to 875 Gauss are essential to further characterizing this weak turbulence and its effect on transport and microwave scattering. Correlation measurements of floating potential fluctuations from strategically placed arrays of langmuir probes would be necessary to identify appropriate wave numbers and hence positively identify various modes through their dispersion relationships.

#### References

1. Lidsky, L. M., et. al., J. Appl. Phys. 33, pp.2490 (1962).
2. Chung, K., Rose, D.J., *Low Frequency Fluctuations in a Weakly Turbulent Hollow Cathode Discharge Plasma*, Symposium on Turbulence of Fluids and Plasmas, Polytechnic Institute of Brooklyn, pp.311 (1968).

# RADIATION EXPOSURE OF PHOTONIC DEVICES

Jonathan Stohs  
Graduate Student  
Department of Physics

University of New Mexico  
Albuquerque, New Mexico 87131

Final Report for:  
Summer Graduate Student Research Program  
Phillips Laboratory

Sponsored by:  
Air Force Office of Scientific Research  
Bolling Air Force Base, DC

and

Phillips Laboratory

August, 1994

## RADIATION EXPOSURE OF PHOTONIC DEVICES

Jonathan Stohs  
Graduate Student  
Department of Physics  
University of New Mexico

### Abstract

A brief explanation of some of the radiation experiments done recently by the Photonics Research Group at the Phillips Lab is given. The radiation studies were performed in order to assess the radiation hardness of key photonic technologies that are aimed at space applications. Three devices that were irradiated by high energy protons and electrons are described. Some of the techniques for measuring the temperature rise in an acousto-optic crystal caused by radiation exposure are listed, and a suggestion is given regarding temperature measurement of a region too small for conventional thermal sensors.

## RADIATION EXPOSURE OF PHOTONIC DEVICES

Jonathan Stohs

### INTRODUCTION

As the technology used in electrical systems improves, more applications for electro-optical or photonic devices are found. These are devices that involve the use of light to transmit signals instead of electrical current. New uses for optical components in satellites and other space vehicles continually present themselves, and knowledge must be gained about how they behave in the space environment.

An important factor influencing device performance is radiation exposure. In space an element of an electrical or optical system may be exposed to high energy electrons, protons, gamma rays, and neutrons. Its performance during and after irradiation can be determined in the laboratory by testing it in the presence of these types of radiation from appropriate sources.

This summer the Photonics Research Group at the Phillips Laboratory at Kirtland Air Force Base studied the performance of acousto-optic deflectors and a directional coupler for optical fibers in the presence of a beam of high energy protons. It also tested the directional coupler and components of a liquid crystal light valve in the presence of a beam of high energy electrons.

One of the main influences upon device performance is the heating caused by irradiation. It is useful to know how much the temperature has risen in a specific part of the device because the optical properties of the material, mainly the index of refraction, change with temperature.

### DISCUSSION

This group has been assessing various ways to sense the temperature of photonic components in order to study how their performance is affected by radiation-induced heating. The device studied most so far is the acousto-optic deflector (AOD). An AOD is comprised of a crystalline block with a transducer bonded to one end. The transducer creates an acoustic wave within the

crystal which in turn alters the index of refraction in a periodic manner. This is because the sound involves vibrations of the molecules about their equilibrium positions, which alter the optical polarizability and consequently the refractive index [1]. The simplest form of interaction of light and sound is the partial reflection of an optical plane wave from the stratified parallel planes representing the refractive-index variations created by an acoustic plane wave.

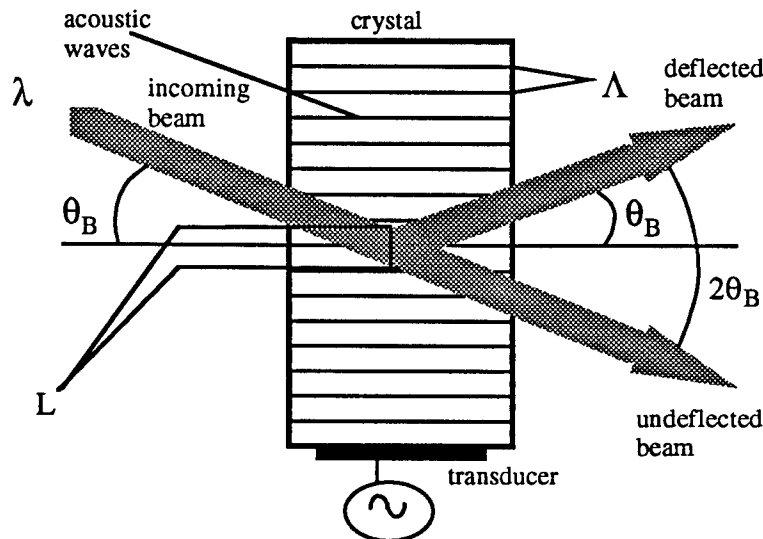


**Figure 1** Acousto-optic Deflector

A set of parallel reflectors separated by the wavelength of sound,  $\Lambda$ , will reflect light if the angle of incidence,  $\theta$ , satisfies the Bragg condition for constructive interference,

$$\sin \theta_B = \frac{\lambda}{2\Lambda} \quad (1)$$

where  $\lambda$  is the wavelength of light in air. This form of light-sound interaction is known as Bragg diffraction, Bragg reflection, or Bragg scattering [2].

Another important parameter in the performance of an AOD is the diffraction efficiency. This is a measure of how intense the deflected (diffracted) beam is. The diffraction efficiency is given as,

$$\eta = \frac{\pi^2}{2\lambda^2} \left( \frac{L}{\sin \theta_B} \right)^2 MI_s \quad (2)$$

where L is a length in the vertical direction related to the interaction length of the beam with the acoustic waves (see Figure 1),  $I_S$  is the intensity of the acoustic wave and M is a material parameter representing the effectiveness of sound in altering the refractive index. M is a figure of merit for the strength of the acousto-optic effect in the material [3].

An AOD will be influenced by exposure to radiation, such as a beam of high energy electrons or protons. The angle of the deflected beam and the diffraction efficiency may change while irradiation takes place. It is thought that the heating from the irradiation may play a large role in changing these parameters.

As can be seen from Figure 1, the AOD is mostly a crystalline block. In order to study the role of heating in this crystal it is necessary accurately to sense the temperature at various points on its surface. Two methods have been tried. In one method thermistors have been glued to the surfaces of the crystal and the temperature recorded during and after irradiation. The thermistors seemed to be slower in their response time than what was needed, and they did not seem accurate enough. In the second method non-contact infrared thermocouples were used to attempt to obtain surface temperatures of the crystal. However, they have a relatively large field of view. The crystal was small enough so that the infrared thermocouple saw both the crystal and its mounting. Consequently, the temperature it read was not that of the crystal surface. One thing that was tried was decreasing the field of view of the infrared thermocouple with a metal tube attachment. It was hoped the tube would act as an aperture. Instead, the thermocouple sensed the temperature mainly of the tube wall and not of the object.

In order to measure accurately the temperature at some point on a crystal surface, which is about a square centimeter in area, a small enough probe is needed. Conventional temperature sensors such as thermistors and thermocouples are too large. In the future a possible solution may be an optical fiber temperature sensor. Such a device is constructed using an optical fiber with a thin film of semiconductor material attached to its end. The semiconductor material's light-transmitting properties depend strongly on temperature. If light travels through the fiber and the

semiconductor, the amount reflected will depend on the temperature [4]. The film of material can also be constructed as a Fabry-Perot etalon resulting in temperature sensing using interferometric methods [5]-[8]. The small cross-sectional area of the fiber and the attached semiconductor film make this a good probe for sensing the temperature at a point on a crystal surface.

Two major elements of this summer's activities were trips to the University of California at Davis, California (UCD) and White Sands Missile Range, near Las Cruces, New Mexico, for experiments on photonic devices. Crocker Nuclear Laboratory at UCD operates a cyclotron which can accelerate protons up to energies of about 67 MeV. For two weeks we tested the performance of some AODs as they were exposed to the beam of protons. Experiments were conducted for various exposure times and proton energies. Some thermal sensors such as thermistors and thermocouples were set up for taking temperature measurements of the AOD crystal as it was irradiated by the proton beam. Data was collected, and it was found that the protons did not cause the temperature of an AOD crystal to rise very much at all. However, the AODs were observed to respond to the radiation.

The main experiments involved determining how the deflection angle and the diffraction efficiency were affected by proton irradiation. Another study involved checking for changes, caused by the protons, in the polarization of the deflected laser beam.

Another photonic device tested was a four-port proton-exchanged directional coupler (see Figure 2). It is constructed by implanting protons into an  $\text{LiNbO}_3$  substrate in a strip pattern in order to raise the index of refraction. The strips are then waveguides, and in the region where they are close to each other the optical wave from one strip can couple to the other. An input (usually made by coupling an optical fiber to a waveguide port) at either port 1 or 2 will end up as output at both ports 3 and 4.

Other types of couplers are used as optical switches by applying an electric field across the region where the waveguides are closer together. When this is done an input in port 1 can end up at port 3 or 4 depending on whether the field is on or off. Likewise an input at port 2 can result in

output at either ports 3 or 4. Usually the two states of the switch are ports 1 to 3 and 2 to 4 or ports 1 to 4 and 2 to 3. Reference [9] has more details.

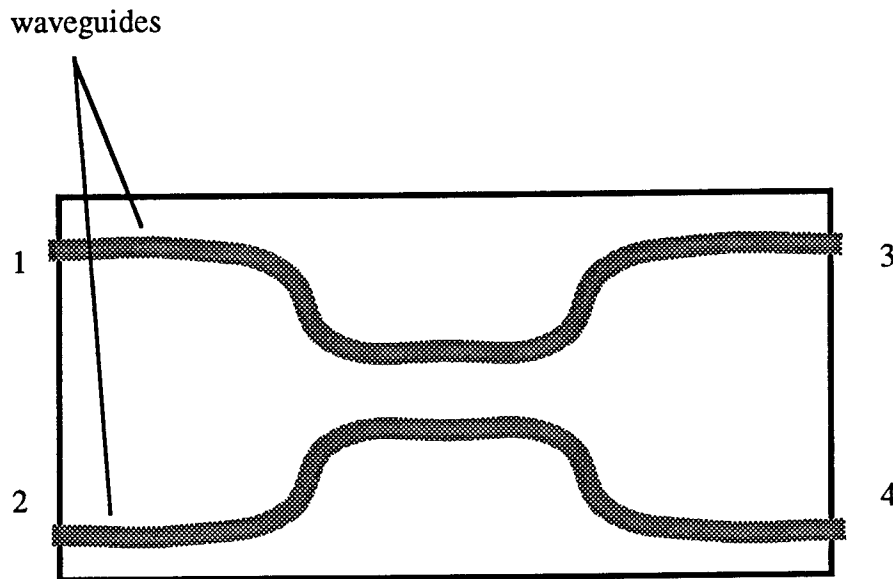


**Figure 2** Four-port directional coupler

The experiment involving exposure of the directional coupler to radiation was conducted according to a protocol developed by Edward Taylor [10]. A brief, preliminary viewing of the data suggested that the directional coupler's performance was not seriously degraded by proton beam exposure when the intensity of the optical beam through it was relatively high, but the proton radiation did affect its performance significantly when the intensity of the optical beam was much lower.

The second trip made this summer was to the electron linear accelerator at White Sands Missile Range (WSMR) for a week. This machine is capable of accelerating electrons up to energies of about 30 Mev, however, studies were performed at 15 Mev since previous studies ([11] and [12]) revealed this energy range to be optimum for the materials studied.

Two experiments were undertaken. The first was to expose the windows of a liquid crystal light valve to the electron beam and determine if their light-transmitting characteristics were altered. A liquid crystal light valve is a device that can modulate the phase or intensity of a light beam passing through it by controlling the way the liquid crystal molecules are aligned using an applied electric field [13]. The windows are the optical flats between which the liquid crystal cell is sandwiched. The exposure to the electron beam seriously degraded the windows of the liquid crystal light valve. Both uncoated and indium-tin-oxide-coated windows were irradiated.

The second experiment involved evaluating the performance of the proton-exchanged directional coupler in the presence of electron radiation. Data from this experiment will be evaluated in the future with other international laboratories that are participating in a “round robin” experiment for this device. There were no thermal measurements taken in the course of these two experiments at WSMR.

## CONCLUSION

As these optical components become more frequently used in satellites and other space-environment platforms, their performance in the presence of radiation will constantly need to be studied. The Photonics Research Group at the Phillips Lab provides these necessary services, and I am grateful for the opportunity to spend the summer with the members of this group participating in radiation experiments on photonic devices.

## References

- [1] Saleh, Bahaa E. and Teich, Malvin Carl, Fundamentals of Photonics; John Wiley and Sons Inc., New York 1991, chapter 20.
- [2] Saleh and Teich, chapter 20.
- [3] Saleh and Teich, chapter 20.
- [4] Berthold, J. W., Reed, S. E., and Sarkis, R. G., “*Simple, repeatable, fiber-optic intensity sensor for temperature measurement*”; SPIE Proceedings vol. 1169, September, 1989.
- [5] Beheim, Glenn, Fritsch, Klaus, and Anthan, Donald J., “*Fiber-optic temperature sensor using a spectrum-modulating semiconductor etalon*”; SPIE Proceedings vol. 838, August, 1987.
- [6] Hartl, J. C., Saaski, E. W., and Mitchell, G. L., “*Fiber optic temperature sensor using spectral modulation*”; SPIE Proceedings vol. 838, August, 1987.
- [7] Beheim, Glenn, Fritsch, Klaus, Flatico, Joseph M. and Azar, Massood Tabib, “*Silicon-etalon fiber-optic temperature sensor*”; SPIE Proceedings vol. 1169, September, 1989.
- [8] He, Gang and Wlodarczyk, Marek T., “*Dual wavelength fiber-optic temperature sensor*”; SPIE Proceedings vol. 2070, September, 1993
- [9] Saleh and Teich, chapters 7, 21, and 22.
- [10] Taylor, E. W., “*Experimental protocol for measuring the effects of nuclear radiation of proton exchanged LiNbO<sub>3</sub> directional coupler waveguides*”; Phillips Lab report TR 94 1102.
- [11] Taylor, E. W., “*Radiation effects in guided wave devices*”; SPIE Proceedings vol. 1794, September, 1992.
- [12] Taylor, E. W., “*Ionization-induced refractive index and polarization effects in LiNbO<sub>3</sub>:Ti directional coupler waveguides*”; IEEE Journal of Lightwave Technology, vol. 9, no. 3, March, 1991.
- [13] Saleh and Teich, chapter 18.

METEOROID AND ORBITAL DEBRIS COLLISION HAZARD ANALYSIS  
FOR SUN-SYNCHRONOUS ORBITS

José Suárez  
Graduate Research Assistant  
Mechanical and Aerospace Engineering Department

University of Alabama in Huntsville  
Sparkman Drive  
Huntsville, AL 35899

Final Report for:  
Graduate Student Research Program  
Phillips Laboratory

Sponsored by:  
Air Force Office of Scientific Research  
Bolling Air Force Base, DC

and

Phillips Laboratory

August, 1994

## METEOROID AND ORBITAL DEBRIS COLLISION HAZARD ANALYSIS FOR SUN-SYNCHRONOUS ORBITS

José Suárez

Graduate Research Assistant

Mechanical and Aerospace Engineering Department  
University of Alabama in Huntsville

### ABSTRACT

The Sun-synchronous orbit has historically been and continues to be commonly used in Air Force space missions. Due to its usage throughout the space age, Sun-synchronous orbits are heavily laden with space debris. Since the orbit is still in demand, there is a potential collision hazard for current space vehicles. For this analysis, an orbit of 700 km altitude and 98.2° inclination is chosen among all possible Sun-synchronous orbits. This paper presents an analysis of the collision hazard for spacecraft in this orbit by application of NASA-recommended orbital debris and meteoroid models. The flux on a randomly tumbling surface is calculated directly from the models. The directional distribution of collisions with orbital debris is estimated by assuming all debris objects are in circular orbits. Further analysis is provided to determine the flux on spacecraft surfaces orbiting with a fixed orientation.

# METEOROID AND ORBITAL DEBRIS COLLISION HAZARD ANALYSIS FOR SUN-SYNCHRONOUS ORBITS

José Suárez

## INTRODUCTION

The Earth is not a perfect sphere, rather, it is somewhat flattened at the poles and has a bulge along the equator. This bulge causes a gravitational pull on a satellite as shown in Figure 1 (after Bate, Meuller, and White, 1971). These forces create a torque on the satellite about the center of the Earth, and there is, therefore, a time rate of change of the angular momentum vector of the satellite. The result is that the angular momentum vector will rotate at a constant rate. If the rate of rotation matches the rate at which the Earth orbits the Sun, then the satellite will be Sun-synchronous.

A typical Earth orbit is shown in Figure 2 (after Bate, Meuller, and White, 1971). For an orbit to be Sun-synchronous, the line of nodes must rotate at the same rate that the Earth revolves around the Sun. For this to occur in a circular orbit, the following relation among the right ascension of ascending node  $\Omega$ , equatorial Earth radius  $R$ , orbital altitude  $h$  and inclination  $i$  must hold (Chobotov, 1991):

$$\frac{d\Omega}{dt} = -9.965 \left[ \frac{R}{R+h} \right]^{3.5} \cos i = 0.9856 \frac{\text{degrees}}{\text{day}}$$

An altitude of 700 km is selected at random, and to assure Sun-synchronicity, its corresponding inclination must be  $98.2^\circ$ .

Meteoroids and orbital debris pose a collision threat to space vehicles. In the orbital velocity regime, collisions are referred to as hypervelocity impacts. Such an impact, for example, by a 90 g particle, will impart over 1 MJ of energy to the vehicle. Within 2000 km of the Earth's surface, there exists about 200 kg of meteoroids and 1.5-3 million kg of orbital debris (Space Station Control Board (S.S.C.B.), 1991). Clearly, design and operational measures must be taken to ensure space vehicle survivability against the meteoroid and orbital debris environments.

The meteoroid population consists primarily of the remnants of comets (Zeilik and Smith, 1987). As a comet approaches perihelion, the gravitational force and solar wind pressure on it are increased, resulting in a trail of particles in nearly the same orbit as the comet. When the Earth intersects a comet's orbit, there is a meteor shower, and this occurs several times per year. Occasionally, when the progenitor comet has made a recent perihelion

passage, the next few times the Earth encounters that path the number of particles encountered may be greatly enhanced. Many comets, however, have not made a recent perihelion passage since they are of long orbital period, or they may not make another perihelion passage. In these cases, the particles are more evenly distributed along the parent comet's orbital path, and the yearly encounter yields constant numbers.

The Earth encounters many sporadic particles on a daily basis. These particles originate in the asteroid belt, and are themselves the smallest asteroids (Zeilik and Smith, 1987). Radiation pressure from the Sun causes a substantial drag force on the smallest particles in the asteroid belt. In time, these particles lose their orbital energy and spiral into the Sun. As they intersect the Earth's orbit and enter the atmosphere with no apparent pattern, they become sporadic meteors. (While in space, a particle is a meteoroid. When it enters the atmosphere, the visible trail it leaves is a meteor. If any pieces survive the fall to the ground, those particles are meteorites. This applies for shower as well as sporadic particles.)

Ever since there has been human activity in space, there has been a growing amount of matter left in orbit. In addition to operational payloads, there exist spent rocket stages, inactive payloads, fragments of rockets and satellites, and other hardware and ejecta, many of which will remain in orbit for many hundreds of years. Orbital debris is observed and tracked by the U.S. Space Command. However, since those facilities were designed primarily to distinguish between satellites and reentering ballistic missile warheads, the current facilities are not ideally suited for tracking orbital debris. For this reason, several efforts are underway at NASA and the U.S. Air Force to count and track, respectively, orbital debris with more sensitive and accurate radio and optical telescopes.

Most orbital debris exists in high inclination orbits where they sweep past each other at an average relative speed of 10 km/s. Recent observations indicate a total mass of about 1000 kg of orbital debris with diameters of 1 cm or smaller and about 300 kg of orbital debris with diameters smaller than 1 mm (S.S.C.B., 1991). This mass distribution make the orbital debris environment more hazardous than the meteoroid environment for most spacecraft applications below 2000 km altitude. Since the orbital debris population continually grows, it will be an increasing concern for any future space operations.

## SPACECRAFT EFFECTS

Practically all spacecraft systems will suffer catastrophic damage or decompression from a hypervelocity impact. Therefore, protective shielding is necessary to minimize this threat. The common double-wall protective shield serves to spread the initial impact into a cloud of secondary debris between the walls of the shield. If the impact on the outer wall is of sufficiently low energy, there could be enough energy dissipation such that the impact

on the rear wall is of little concern. However, the cloud may contain particles which posses enough energy to either penetrate the rear wall or induce spallation. In either case, a pressure wave may form with sufficient energy to cause further damage. The following is a summary list of the main effects of hypervelocity impact which may be of concern to the various spacecraft systems:

- catastrophic rupture
- internal fragments
- deflagration
- propagating failure
- pressure pulse
- reduced structural strength
- light flash
- leakage
- detonation
- degraded performance
- cyclical loading
- electrical short

Of particular concern to any mission is damage to systems which cannot be shielded, such as antenna surfaces or telescope optics. To reduce the damage on these systems, operational procedures such as pointing restrictions and strategic design locations onboard the spacecraft may be imposed to increase survivability.

## METEOROID ENVIRONMENT

The average total meteoroid environment presented below (Grun, *et. al.*, 1985) is comprised of the average sporadic meteoroids and a yearly average of shower, or stream, meteoroids. The meteoroid model calculates meteoroid flux as a function of mass, therefore, the size distribution will be dependent on density. Uncertainties in meteoroid density do not contribute greatly to uncertainties in damage estimates because the model was derived from curve fits to crater and impact data. Recommended values for density  $\rho$  for various meteoroid sizes  $d$  are (S.S.C.B., 1991)

$$\rho = 2.0 \text{ g/cm}^3, \quad d < 10^{-6} \text{ g},$$

$$\rho = 1.0 \text{ g/cm}^3, \quad 10^{-6} < d < 0.01 \text{ g},$$

$$\rho = 0.5 \text{ g/cm}^3, \quad d > 0.01 \text{ g}.$$

Because of the nodal regression of a satellite's orbit and the obliquity of the ecliptic, the meteoroid environment can be assumed to be omnidirectional relative to the Earth when averaged over mission lifetimes. The normalized meteoroid velocity distribution  $n(v)$ , in number per km/s, with respect to Earth is given by

$$n(v) = 0.112, \quad 11.1 \leq v < 16.3 \text{ km/s},$$

$$n(v) = 3.328 \times 10^5 v^{-5.34}, \quad 16.3 \leq v < 55.0 \text{ km/s},$$

$$n(v) = 1.695 \times 10^{-4}, \quad 55.0 \leq v < 72.2 \text{ km/s},$$

and is shown in Figure 3.

For historical reasons related to the measurement method, the meteoroid environment is specified as a time-averaged flux,  $F_r$ , against a single-sided, randomly tumbling surface. Flux is defined as the number of intercepted objects per unit time per unit area. The interplanetary meteoroid flux  $F_r^{ip}$  at any point at 1 A.U. (astronomical unit, the mean distance between the Sun and the Earth) is given for  $m \leq 10$  g by

$$F_r^{ip}(m) = c_0 \left\{ \left( c_1 m^{0.306} + c_2 \right)^{-4.38} + c_3 \left( m + c_4 m^2 + c_5 m^4 \right)^{-0.36} + c_6 \left( m + c_7 m^2 \right)^{-0.85} \right\}$$

where  $c_0 = 3.156 \times 10^7$ ,  $c_1 = 2.2 \times 10^3$ ,  
 $c_2 = 15$ ,  $c_3 = 1.3 \times 10^{-9}$ ,  
 $c_4 = 10^{11}$ ,  $c_5 = 10^{27}$ ,  
 $c_6 = 1.3 \times 10^{-16}$ ,  $c_7 = 10^6$ .

The Earth blocks a particular solid angle from contributing to the meteoroid flux on a orbiting satellite. This angle divided by  $4\pi$  steradians gives the fraction of the meteoroid flux blocked out by the Earth. This fraction, known as the shielding factor  $s_f$ , ranges from 0.5 just above the atmosphere to 1.0 in deep space. It is given by

$$s_f = \frac{1}{2} \left[ 1 + \sqrt{1 - \left( \frac{R_E}{R_E + H} \right)^2} \right],$$

where  $R_E$  = Earth radius + 100 km atmosphere (6478 km),

$H$  = height above Earth's atmosphere (Earth's atmosphere height is 100 km for this purpose).

The Earth's gravitational field attracts meteoroids and increases their flux. This effect, gravitational focusing,  $G_E$ , ranges from a maximum of 2.0 just above the atmosphere to 1.0 in deep space, and is given by

$$G_E = 1 + \frac{R_E}{r}$$

where  $R_E$  = Earth radius + 100 km atmosphere (6478 km),

$r$  = orbit radius.

The meteoroid flux, then, in Earth orbit, is given by

$$F_r = s_j G_E F_r^{ip},$$

and for the Sun-synchronous orbit is shown in Figure 4.

## METEOROID ENVIRONMENT UNCERTAINTIES

The physical properties of meteoroids must be determined by indirect means such as impact craters and meteor spectra. Their origin can be comets, which are made of ices and dust, or asteroids, which are like rocks. Therefore, there is considerable uncertainty in their properties. In particular, the uncertainty in mass tends to dominate the uncertainties in the flux measurement. For meteoroids less than  $10^{-6}$  g, the mass is uncertain to within a factor from about 0.2 to 5 times the estimated value, which implies the flux is uncertain to within a factor of 0.33 to 3 at a given mass. For meteoroids above this size, the flux is well defined but the associated mass is even more uncertain. This implies an effective uncertainty in the flux of a particular mass within a factor from 0.1 to 10.

## ORBITAL DEBRIS ENVIRONMENT

To account for the irregularities in shape and that orbital debris may impact with any orientation of the debris particles, the recommended values for mass density of debris size  $d$  is

$$\rho = 2.8 d^{0.74} \text{ g/cm}^3 \quad (d \text{ in cm}), \quad d \geq 0.62 \text{ cm},$$

$$\rho = 4.0 \text{ g/cm}^3, \quad d < 0.62 \text{ cm}.$$

Averaged over all altitudes, the non-normalized collision velocity distribution, i.e., the number of impacts with velocities between  $v$  and  $v+dv$ , relative to a spacecraft with orbital inclination  $i$ , is given by the following equation (Kessler, Reynolds, and Anz-Meador, 1989):

$$f(v) = [2vv_0 - v^2] \left[ G \exp\left(-\frac{v-Av_0}{Bv_0}\right)^2 + F \exp\left(-\frac{v-Dv_0}{Ev_0}\right)^2 \right] + HC(4vv_0 - v^2)$$

where  $v$  is the collision velocity in km/s, and

$$A = 2.5$$

$$B = \begin{cases} 0.5 & i < 60 \\ 0.5 - 0.01(i - 60) & 60 < i < 80 \\ 0.3 & i > 80 \end{cases}$$

$$C = \begin{cases} 0.0125 & i < 100 \\ 0.0125 + 0.00125(i - 100) & i > 100 \end{cases}$$

$$D = 1.3 - 0.01(i - 30)$$

$$E = 0.55 + 0.005(i - 30)$$

$$F = \begin{cases} 0.3 + 0.0008(i - 50)^2 & i < 50 \\ 0.3 - 0.01(i - 50) & 50 < i < 80 \\ 0.0 & i > 80 \end{cases}$$

$$G = \begin{cases} 18.7 & i < 60 \\ 18.7 + 0.0289(i - 60)^2 & 60 < i < 80 \\ 250.0 & i > 80 \end{cases}$$

$$H = 1.0 - 0.0000757(i - 60)^2$$

$$v_0 = \begin{cases} 7.25 + 0.015(i - 30) & i < 60 \\ 7.7 & i > 60 \end{cases}$$

When  $f(v)$  is less than zero, the function is to be reset to zero. It is convenient to normalize  $f(v)$  so that

$$f'(v) = \frac{f(v)}{\int_0^\infty f(v)dv}$$

When normalized in this manner,  $f'(v)$  over any velocity interval in km/s becomes the fraction of debris impacts within that velocity interval. This function is calculated for the Sun-synchronous orbit in Figure 5.

Frequency of impact from a given direction can be estimated by using this velocity distribution. It is assumed that the direction of impact is specified by the intersection of the spacecraft velocity vector and the debris velocity vector in a circular orbit. Referring to Figure 6 and applying the law of cosines gives

$$V_{deb}^2 = V_{spa}^2 + V_{rel}^2 - 2V_{spa}V_{rel} \cos\alpha.$$

Since the debris particle and the spacecraft must be at the same altitude for a collision to occur, the magnitudes of their velocity vectors are equal, and so

$$V_{rel}^2 = 2V_{spa}V_{rel} \cos\alpha$$

Although the orbital velocity of a spacecraft in low Earth orbit varies with its altitude, an average spacecraft velocity of 7.7 km/s is used in the model, and so the direction of the relative velocity vector is given by

$$\cos\alpha = \frac{V_{rel}}{2V_{spa}} = \frac{v}{15.4}$$

where  $v$  is as used above, and the results are shown for the Sun-synchronous orbit in Figure 7. This distribution is symmetric about the ram direction in two lobes as shown in polar format in Figure 8.

For historical reasons related to the measurement method, the orbital debris environment is specified as a time-averaged flux,  $F_r$ , against a single-sided, randomly tumbling surface. Flux is defined as the number of intercepted objects per unit time per unit area. The cumulative flux of orbital debris of diameter  $d$  and larger is given by the following equation (S.S.C.B., 1991):

$$F_r(d, h, i, t, S) = H(d)\Phi(h, S)\Psi(i)[F_1(d)g_1(t) + F_2(d)g_2(t)]$$

where  $F_r$  = flux, impacts per square meter of surface per year,

$d$  = orbital debris diameter in cm,

$t$  = date (year),

$h$  = spacecraft orbital altitude in km ( $h \leq 2000$  km),

$S$  = 13-month smoothed solar radio flux  $F_{10.7}$  for year  $(t - 1)$  in  $10^4$  Jy,

$i$  = spacecraft orbital inclination in degrees,

and

$$H(d) = \left[ 10^{\exp -((\log_{10} d - 0.78)/0.637)^2} \right]^k$$

$$\Phi(h, S) = \Phi_1(h, S) / (\Phi_1(h, S) + 1)$$

$$\Phi_1(h, S) = 10^{((h/200) - (S/140) - 1.5)}$$

$$F_1(d) = 1.22 \times 10^{-5} d^{-2.5}$$

$$F_2(d) = 8.1 \times 10^{10} (d + 700)^{-6}$$

$p$  = assumed annual growth rate of mass in orbit = 0.05

$q$  = estimated growth rate of fragment mass;  $q = 0.02$ ,  $q' = 0.04$

$$g_1(t) = (1+q)^{(t-1988)} \quad \text{for } t < 2011$$

$$g_1(t) = (1+q)^{23} (1+q')^{(t-2011)} \quad \text{for } t \geq 2011$$

$$g_2(t) = 1 + p(t - 1988)$$

The inclination-dependent function  $\Psi(i)$  defines the relationship between the flux on a spacecraft in an orbit of inclination  $i$  and the flux incident on a spacecraft in the current population's average inclination of  $50^\circ$  (Kessler, Reynolds, and Anz-Meador, 1989), and is shown in Figure 9. The orbital debris flux for the Sun-synchronous orbit during the year 2006 is shown in Figure 10. This year is selected to reflect the flux encountered, averaged over a ten-year mission lifetime, beginning in the year 2001.

## ORBITAL DEBRIS ENVIRONMENT UNCERTAINTIES

The debris model presented here has been recommended for most, if not all, NASA engineering applications since mid-1990. Preliminary comparisons to data from the Long Duration Exposure Facility and the Haystack radar appear to be consistent within the uncertainty of the model. Table 1 (after S.S.C.B., 1991) summarizes the uncertainties and estimates of uncertainty for the various parameters which comprise the model.

## ANALYSIS FOR FIXED-ORIENTATION SURFACES

For  $F_r$ , the relevant area is the actual surface area of the satellite. One may also define a cross-sectional area flux,  $F_c$ , for a randomly tumbling satellite, where the relevant area is the time-averaged cross sectional area. A useful theorem which is obvious for a tumbling sphere but which holds for objects of arbitrary shape, assuming no concave surfaces, is that  $F_c = 4F_r$ .

For spacecraft which fly with a fixed orientation, the meteoroid and orbital debris fluxes,  $F$ , are treated somewhat like a vector quantity and the effects of directionality must be carefully evaluated. Some effects of impact will be direction-dependent. To evaluate the expected number of impacts,  $N$ , between times  $t_1$  and  $t_2$ , from meteoroids, one may use a "k factor" method and the appropriate  $F_r$ , such that

$$N = \int_{t_1}^{t_2} \sum_i k_i F_r A_i dt,$$

where the summation is over the  $i$  surfaces of the spacecraft, each of area  $A_i$ .

The parameter  $k$  is defined as the ratio of the flux against an oriented surface to the flux against a randomly tumbling surface. The value of  $k$  can theoretically range from 0 to 4; a value of 4 can only be achieved when a surface normal is oriented in the direction of a monodirectional flux. If the surface is randomly oriented, then  $k = 1$ . Referring again to Figure 6, let the flux from each lobe be

$$f_1(v, \theta) = \begin{cases} f'(v) & \alpha(v) - \phi > -\frac{\pi}{2} \\ 0 & \text{otherwise} \end{cases}$$

$$f_2(v, \theta) = \begin{cases} f'(v) & \alpha(v) + \phi < \frac{\pi}{2} \\ 0 & \text{otherwise} \end{cases}$$

where  $\phi$  is the azimuth angle in the orbital plane, and  $\theta$  is the zenith angle measured out of the orbital plane, for each oriented surface. However, since the surface may be oriented in such a way as to block part of one or both lobes, the flux contribution actually reaching the surface is different in each lobe, and is given by

$$F_1(\phi) = \int_0^{15.4} f_1(v, \phi) \cos(\alpha(v) - \phi) dv$$

$$F_2(\phi) = \int_0^{15.4} f_2(v, \phi) \cos(\alpha(v) + \phi) dv.$$

The  $k$  value for each orientation  $(\phi, \theta)$  along the spacecraft is hence given below, and is shown in Figure 11.

$$k(\phi, \theta) = 2(F_1(\phi) + F_2(\phi)) \sin \theta.$$

Since  $N$  can then be determined explicitly, the probability of exactly  $n$  impacts occurring on a surface in the corresponding time interval is found from Poisson statistics, thus

$$P_n = \frac{N^n}{n!} e^{-N}.$$

Caution:  $k$  factor analysis provides only the expected number of impacts on each surface. Since damage depends strongly on the collision angle of the particle with the spacecraft surface, the angular distribution on each surface must be considered separately.

## ACKNOWLEDGMENTS

The author is grateful to the Air Force Office of Scientific Research and Research and Development Laboratories for selecting him as a Research Associate. Lt. Scott Maethner, Space Debris Program Manager, suggested the topic of this study and provided useful direction for which the author is grateful.

## REFERENCES

- R. R. Bate, D. D. Mueller, and J. E. White, *Fundamentals of Astrodynamics*, Dover Publications, Inc., New York, NY, 1971.
- V. A. Chobotov (editor), *Orbital Mechanics*, American Institute of Aeronautics and Astronautics, Inc., Washington, DC, 1991.
- Space Station Control Board, *Space Station Program Natural Environments Definition for Design*, NASA SSP 30425 Revision A, 1991.
- M. Zeilik and E. v. P. Smith, *Introductory Astronomy and Astrophysics 2nd Edition*, Saunders College Publishing, Philadelphia, PA, 1987.
- E. Grun, et. al., *Collisional Balance of the Meteoritic Complex*, Icarus **62**, 244, 1985.
- D. J. Kessler, R. C. Reynolds, and P. D. Anz-Meador, *Orbital Debris Environment for Spacecraft Designed to Operate in Low Earth Orbit*, NASA TM 100 471, 1989.

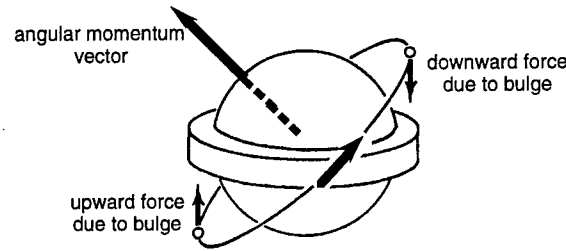


Figure 1. The torque exerted on a satellite by the Earth's equatorial bulge.

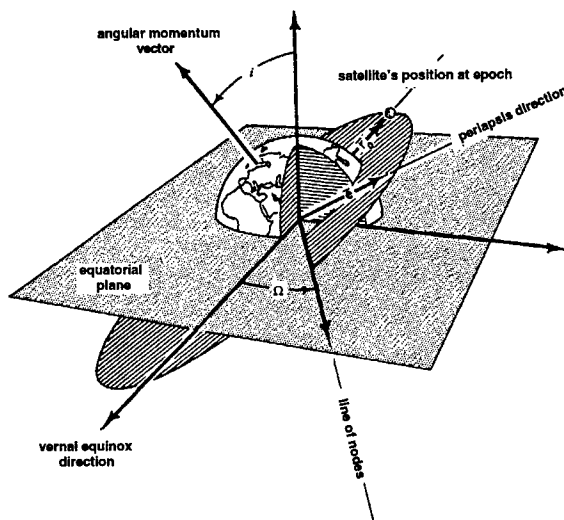


Figure 2. Schematic description of orbital elements for a typical satellite orbit.

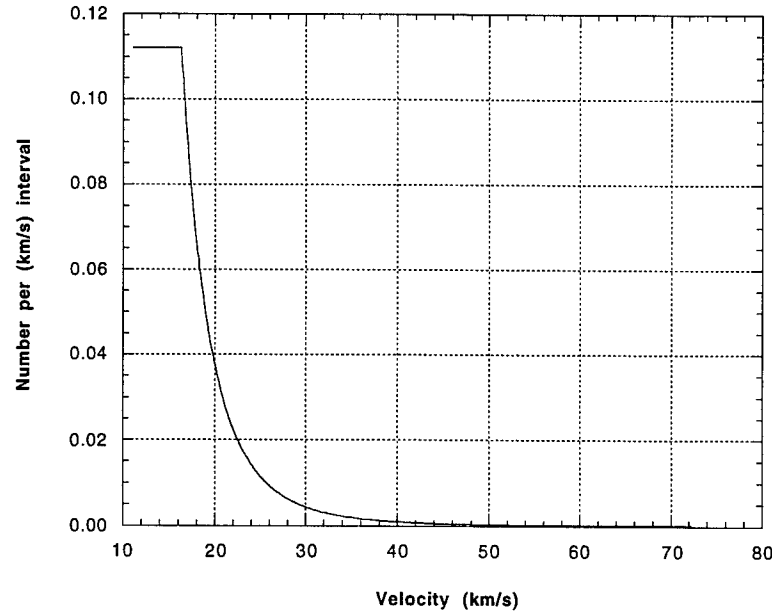


Figure 3. The meteoroid velocity distribution (normalized to velocity in km/s).

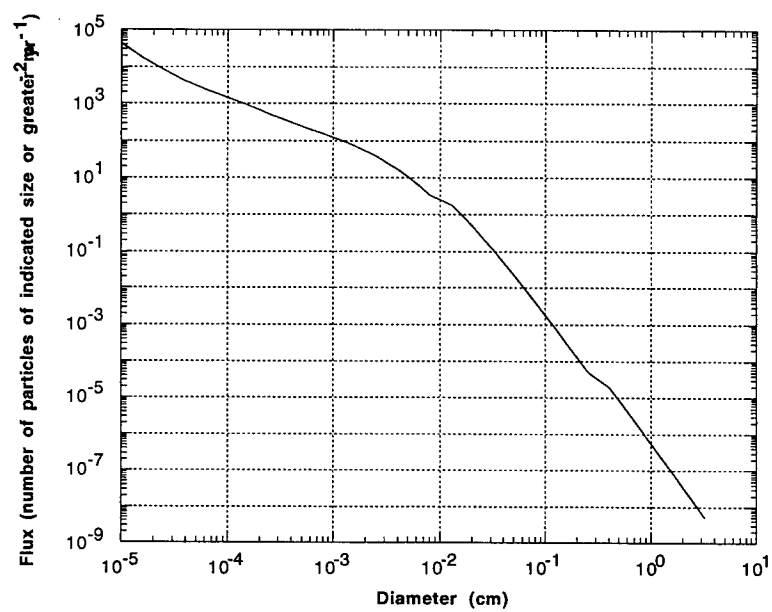


Figure 4. The meteoroid flux for the Sun-synchronous orbit.

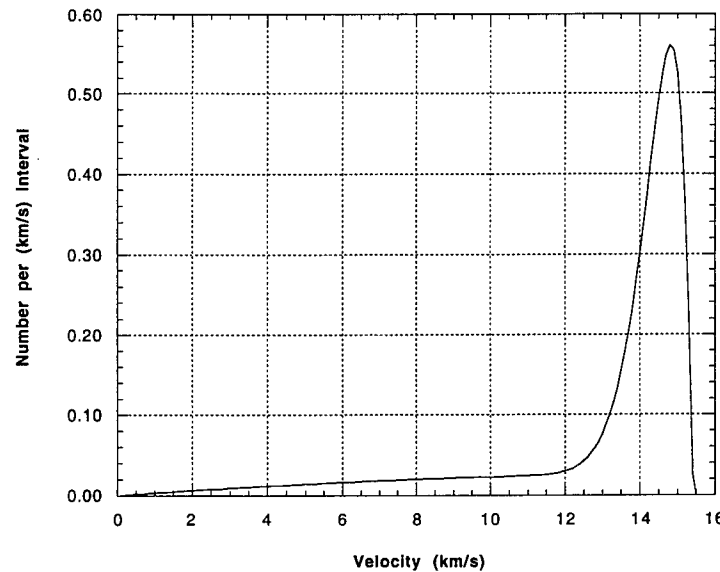
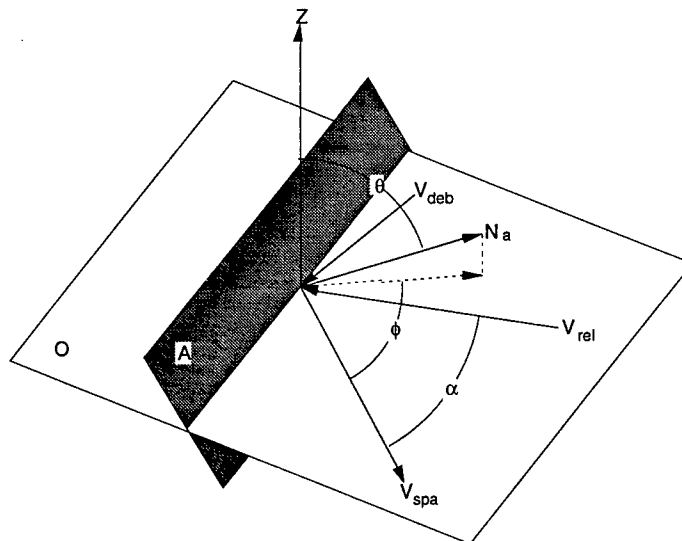


Figure 5. The orbital debris velocity distribution (normalized to velocity in km/s).



Plane A represents a surface of the spacecraft.

$N_a$  is the unit vector normal to the plane A.

$V_{spa}$  is the spacecraft velocity vector, or the ram direction.

$V_{deb}$  is the debris velocity vector (inertial).

$V_{rel}$  is the collision velocity relative to the spacecraft.

$\alpha$  is the angle between  $V_{spa}$  and  $V_{deb}$ .

$\theta$  is the zenith angle of  $N_a$ , or (90 – degrees out of horizontal).

$\phi$  is the azimuth of  $N_a$ , or degrees off ram.

Z is the Earth's and spacecraft's vertical.

O is the spacecraft's local horizontal plane.

Figure 6. Directionality and  $k$  factor reference frame.

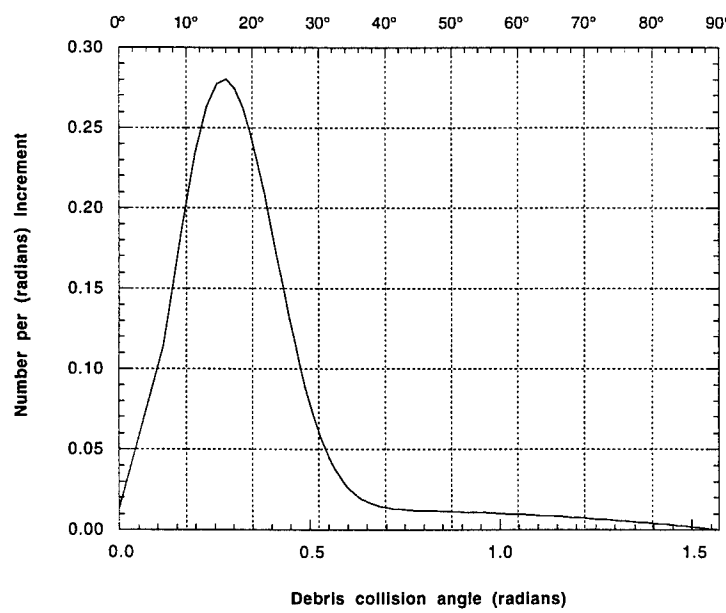


Figure 7. Orbital debris collision angle distribution (normalized to angle in radians).

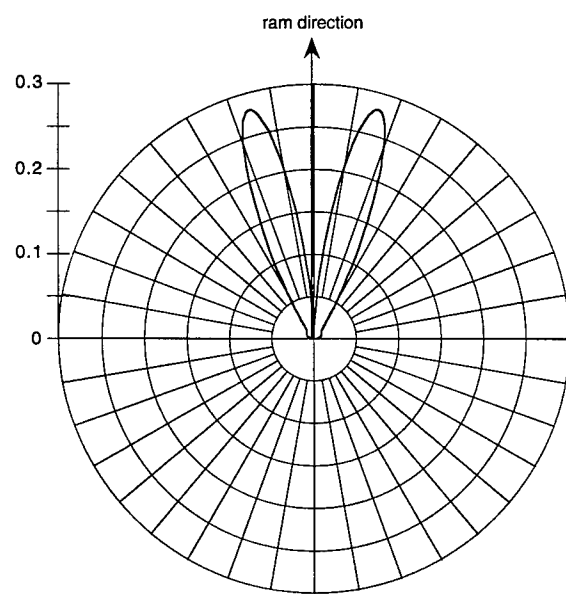


Figure 8. Orbital debris collision angle distribution (normalized to angle in radians).

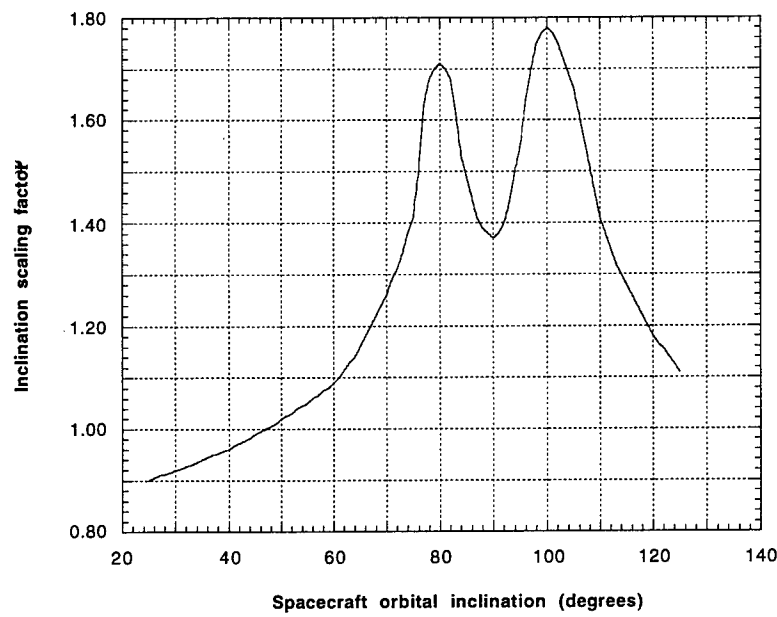


Figure 9. Inclination scaling factor  $\Psi$  for any orbit.

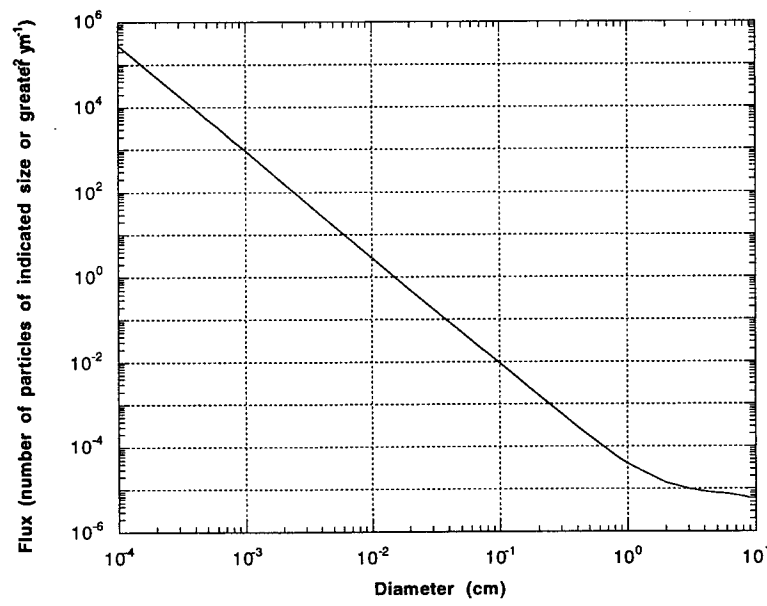


Figure 10. The orbital debris flux for the Sun-synchronous orbit in the year 2006.

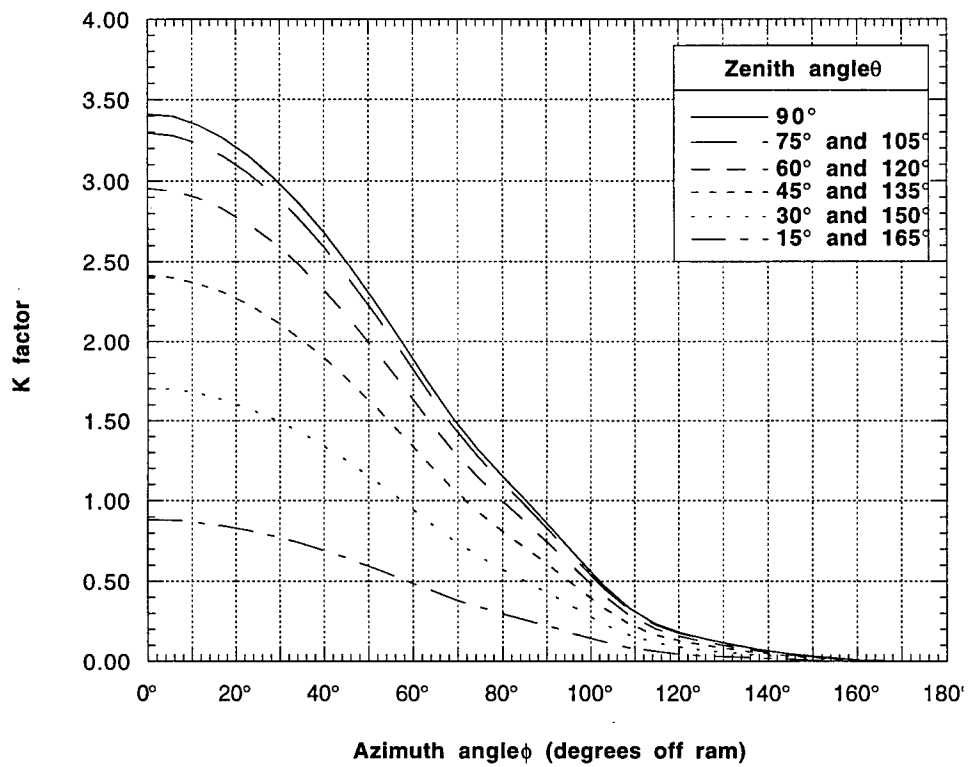


Figure 11. The  $k$  factors for single-sided flat plates.

Uncertainty in Current Environment			
	Treatment	90% confidence	Notes
Flux measurements (d > 10 cm)	Best estimate	1.5 to 0.5 X (1988 flux)	
Flux measurements (0.05 cm < d < 10 cm)	Best estimate	3 to 0.33 X (1988 flux)	Due to statistical and measurement limitations in portions of range, data missing (interpolation used) in rest of range
Flux measurements (d < 0.05 cm)	Best estimate	2 to 0.5 X (1988 flux)	
Altitude distribution (d < 10 cm)	Best estimate	5 to 0.2 X (1988 flux) per 200 km past 500 km	Due to difficulty in determining flux in highly elliptical orbits
Altitude distribution (d > 10 cm)	Smoothed best estimate	2 to 0.5 X (1988 flux)	Uncertainty is somewhat worse in 800 and 1000 km regions
Debris density (d < 1 cm)	Simplified best estimate	0.1 @ 1.8, 0.5 @ 2.8, 0.1 @ 4.5, 0.3 @ 8.9	Estimated typical "heavy" distribution. Insufficient data to develop a true uncertainty limit estimate.
Debris density (d > 1 cm)	Best estimate, non-conservative	2 to 0.5 mean density	Mean values are fairly well defined, but number vs. density distribution is broad.
Debris shape	Best estimate		Spherical shape is assumed, actual debris will be irregular.
Velocity distribution, fraction < 5 km/s	Best estimate	0.5 3 X (Slow fraction)	Distribution of orbital inclinations could be in error and changes in time.
Uncertainty in Trend Projection			
Launch rate and orbit use profile	Best estimate	p = 0.04 to "comp p" = 0.1 q = 0 to 2p	"comp p" implies $g_2 = (1 \pm p)^{(t-1988)}$ . Worst case assumes combined effect of increased traffic and increased use of LEO above 400 km.
Fragmentation rate, fragmentation mechanics	Best estimate	q = 0 to 0.10	Assuming no changes in projected launch rate and orbit use profile.
Statistical variation of fragmentations	Best estimate	0.5 to 1.5 X (current flux)	
Solar activity	Best estimate	Substitute "max" and "min" S values from solar forecasts	Model tends to overestimate variation with solar cycle, so these would be extreme limits.
"Local" fragmentation events	Non-conservative	2 to 0.5 X (1988 flux)	Difficult to assess, depends strongly on type of event and proximity to orbit. Ignored in current model.

Table 1. Uncertainties and accuracy limits for the orbital debris environment.

**PICLL: A PORTABLE PARALLEL 3D PIC CODE  
IMPLEMENTATION NOTES**

Tony von Sadovszky  
Graduate Research Associate  
Department of Physics  
University of Nevada, Reno  
Reno, NV 89557 - 0058

Final Report for:  
Graduate Student Research Program  
Phillips Laboratory

Sponsored by:  
Air Force Office of Scientific Research  
Bolling Air Force Base, DC

and

Phillips Laboratory

August 1994

PICLL: A PORTABLE PARALLEL 3D PIC CODE  
IMPLEMENTATION NOTES

Tony von Sadovszky  
Graduate Research Associate  
Department of Physics  
University of Nevada, Reno

Abstract

PICLL (Particle In Cell Linked List) is a three dimensional relativistic PIC code for the investigation of non-collisional plasmas and new PIC methodologies. PICLL is implemented in portable ANSI C, and has been ported to a variety of serial and parallel high performance computing systems. The overall goal of the PICLL development effort has been the production of an efficient parallel code, which is easy to use and maintain. One of the novel features of PICLL is its use of linked lists as the code's primary data structures. This report details the overall structure of the code, and some of the considerations that have gone into the early development of PICLL.

## PICLL: A PORTABLE PARALLEL 3D PIC CODE IMPLEMENTATION NOTES

Tony von Sadovszky

### Introduction

PICLL (Particle In Cell Linked List) is a three-dimensional relativistic particle in cell code. The code is currently used to model non-collisional plasmas with several million particles and spatial cells. It is portable to any MIMD architecture that supports ANSI C and the functionality of the Message Passing Interface (MPI) standard. The code's design takes advantage of linked list data structures. Grids used by the code are composed of Cartesian cells, but the only restriction on the mesh is a one-to-one face mapping of the spatial cells. PICLL's physics algorithm is designed with parallel efficiency in mind. The amount of data sent between nodes is minimized. Also the time interval between asynchronously sending data and its use is maximized.

The physics algorithm used by PICLL makes no assumptions about the method of walking through the spatial grid, or the locality of specific particle and field data values. All the necessary data to perform the required physics calculations are stored and referenced through linked list data structures. Storing data values in this manner allows complex problems to be solved with a minimum number of spatial cells. The added overhead resulting from linked list structures is more than compensated for by the smaller number of cell's required to model complex geometries, and the ease of manipulating these data structures. Also, the data structures used for this Cartesian cell case are an excellent starting point for further evolution to spatial meshes composed of arbitrary geometry cells.

### Overview of PICLL Structure

In order to insure the portability and the maintainability of PICLL, the code was designed to be highly modular. Currently, the PICLL code is composed of three separate, standalone modules:

1. input preprocessor
2. PICLL engine
3. post processor

These three modules are isolated from each other via a series of interface routines. This prevents alterations made to one routine from critically impacting the other modules.

The input preprocessor requires user input, defining the problem parameters, and a geometry definition file. With these, it sets up the problem to be solved by the PICLL engine. Currently, the preprocessor supports geometry input in the form of an IBM CAEDS mesh definition file. Using this, the preprocessor constructs a computational mesh composed of physical and ghost cell layers. The ghost cells mirror adjacent physical cells. This computational mesh is then properly initialized with current, field and particle data, according to the additional user inputs. The need for two additional ghost cell layers arises from PICLL's parallel implementation. These mirror layers provide a buffer between computational nodes. This allows the problem to be distributed across several nodes, while ensuring that communication between these nodes can be performed asynchronously. Once the preprocessor has prepared the problem file, the PICLL engine "solves" the problem.

The PICLL engine performs the physics calculations based upon the input files prepared by the preprocessor. The engine advances particle positions within the cells

defined by the mesh, and computes the current components (x, y, z,) across the mesh. These are used to solve Maxwell's equations (Ampere's and Faraday's Laws) via a second order center differencing scheme throughout the computational mesh. The resulting fields are used to determine the forces on the particles and advance the particles through the next time step. This process is iterated, until the requested number of time steps is completed. The Courant condition provides a limit on the size of the time step based upon the cell size and the particle velocity. No particle is allowed to traverse more than one cell width in a single time step.

This simplified discussion of the PICLL computational process is complicated by the need to minimize communication bottlenecks between processing nodes. The various current, field and particle push calculations are performed at different times at various places (groups) in the computational mesh. Only one asynchronous communication is necessary to complete a time step. All other communications between nodes are not required until the next time step. This is required to minimize the bottleneck introduced in the calculations, by the need for data, not yet available from other parts of the physical mesh. These computational mesh groupings are designed to allow the maximum time between a calculation and the time that the result is needed at some other point in the problem. This minimizes the bottleneck resulting from the need to halt computations due to data still enroute from another node, and thus allows maximization of the computation to communication ratio.

Additional parts of the PICLL engine provide particle injection and summary output information for later analysis by the post processing module. The resulting 3D data sets produced from these computations are huge. To analyze the data, a number of

different graphical post processing tools are used. These include Interactive Data Language (IDL) by Research Systems Inc., IBM's Visualization Data Explorer and Mathematica by Wolfram Research Inc.

### Field Data Structures

The use of linked lists as the primary data structure throughout the code is one of PICLL's innovations. Cell information is divided into a series of lists containing, cell properties, particle specie's properties (charge, mass, etc.), and particles (position, velocity, etc.). Similarly, the current and field data is divided into a series of lists. A list is maintained for each component (x, y, z) of each field, for each computational group. Since the electric field and the current are collocated on the computational mesh, a single list entry contains both electric field and current data. Magnetic field component data is maintained on another similar series of lists.

Each list entry contains the magnitude of the current or field component, its position in space, a series of pointers to associated fields, and a pointer to the next element in the list. The associated fields are the corresponding neighboring fields. Elements of the magnetic field list, corresponding to a field mesh location, point to electric field list elements, corresponding to the physically surrounding points. This high degree of interconnectivity via pointers, maintains a minimal overhead when sharing information between cells, as well as computational nodes. Furthermore, the arbitrary structure of the list gives PICLL great flexibility when dealing with problems of complex geometries. As so often occurs when arrays are used, there is no structure imposed on the problem by the form of the data structures employed in PICLL. The use of dynamic memory allocation, in conjunction with the linked lists, and the power of pointers, provides an

avenue for dynamic mesh alteration during the execution of the problem. The use of linked lists as the primary data structure, however, raises certain performance issues that will be discussed below.

#### Structure of E & M Routines

Contained within the PICLL engine is a module for manipulating the data in the field and current lists. These routines, provide an interface between the data structures and the physics routines. When a computation requires a piece of field data, the request is serviced, and a copy of the data is returned. After a calculation, a call is made, and the appropriate field data is updated. This isolation of the physics modules from the data, makes it easy to maintain the code. This module also contains routines for the creation and maintenance of the lists themselves. This task is simplified by the use of dynamic memory allocation, and the ability to quickly and easily, insert and delete list elements via pointer manipulation.

#### Linked List Efficiency

The use of linked lists as the primary data structures in PICLL, while providing novel strengths to the PIC code, raises certain performance issues. Since PICLL is intended to be a production code as well as a research tool, it is important that these performance issues be addressed. Unfortunately, much of the information relating to the issue concerning the use of linked lists versus arrays is based more on folklore than on anything else. In order to address these issues, a series of low level test were performed.

These tests consisted of benchmarks to determine the added cost in linked list usage relative to the use of arrays. These test were performed on two separate platforms (IBM RISC 6000 25 T and a SUN Microsystems SPARC 10) at all levels of optimization. Clock cycles were measured for the traversal of linked lists and arrays, and the results of several runs were averaged. These times did not include the time required to initialize the data structures.

As expected there was a substantial degree of variation between different optimization levels. At similar levels of optimization, on average, there was a consistent 20% additional overhead associated with the use of linked lists. This was true for lists created via calls to CALLOC, which allocates a contiguous block of memory. Lists created via calls to MALLOC proved substantially less efficient in both speed and memory usage. The lists created with CALLOC, displayed the same memory usage as the array implementations, as expected, due to the nature of compiler memory allocation methods. The ~20% cost was also maintained when the lists and arrays were accessed randomly instead of sequentially. When compared with similar array based routines implemented in FORTRAN, there was no difference in the results. Thus the use of linked lists comes at a price: ~20% loss in performance.

There are, however, compensating factors. The manipulation of the list elements is exceptionally more efficient than the manipulation of similar array based data. To insert a new element into a list is trivial in comparison to the same task implemented via arrays. Ultimately, one must consider whether the costs entailed in the use of lists is justified by the resulting gains in convenience, simplicity, and generality. The answer to the question depends on the problem to be solved. If a substantial portion of

the code is spent manipulating the lists, as in dynamic load balancing, then the answer favors a linked list implementation. However, if a more pedestrian problem, with a simple geometry, is to be solved, then a more traditional array based approach may be justified. As a platform for PIC code research, linked lists are the best data structure to use due to their inherent generality.

One last issue, concerning the performance associated with the use of linked lists, is vectorization. The code arising from the use of linked lists is not inherently vectorizable. The vector pipelines cannot be easily filled, and as a result when running on a vector machine, PICLL will take a substantial performance hit. The cost of this overhead was not determined, however, various ways to overcome this problem should be addressed in the future.

#### Code Implementation & Validation

Currently, the serial version of PICLL has been tested on a number of platforms:

- IBM RISC 6000 25 T (PLK/WSP)
- SUN Microsystems SPARC 10 (PLK/WSP, both CC and GCC)
- IBM SP1 (MHPCC)
- INTEL PARAGON (WPAFB)
- TMC CM-5 (Minnesota Supercomputing Center)
- CRAY T3D (Arctic Region Supercomputing Center)

The code has been debugged using LINT on several of the above platforms, in order to insure portability. PICLL breaks the ANSI C convention by supporting both old style and new style functions declarations, through the use of C Preprocessor macros. From

the list of systems above, it is apparent that the code is capable of running on a wide range of high performance computing assets.

The physics of the code has been validated, thus far, via a set of simple test cases:

- stationary particle
- two particle repulsion and attraction
- particle in a static electric field
- particle in a static magnetic field
- particle in static combined fields
- $\vec{E} \times \vec{B}$  drift at both classical and relativistic velocities
- electric and magnetic fields resulting from a line of current

A combination of periodic and metallic boundary conditions were investigated.

Additionally, all permutations of velocity and field components were tested. The resulting output was correct and consistent across all platforms.

#### Utility of PICLL & Future Work

PICLL was written to be a research tool as well as a production code. As a production code, it is planned to combine the three main PICLL modules into a single code, linked via a user friendly graphical interface. This interface would include both a simplified problem definition path, as well as rudimentary post processing capabilities. Also, a continued emphasis will be placed on increasing PICLL's computational efficiency without sacrificing its flexibility. One direct avenue is the vectorization of the code.

Currently, PICLL is used to model relativistic electron beams, beam extractors, resonance cavities and RF generators. The code's flexible treatment of complex geometries allows complex three-dimensional problems to be solved easily and efficiently. The promise of parallel computing ensures that the solutions are arrived at quickly. PICLL may find future use in modeling interplanetary astrophysical processes. An example being, the recently observed infrared "foot" of the Io flux tube impinging on the Jovian atmosphere (Connerney, John E. P., Science, November 12, 1994) While predicted over a quarter of century ago by theorists Peter Goldreich and Donald Lynden-Bell, the system has yet to be modeled adequately in its entirety.

PICLL is well suited as a tool for research into new PIC methodologies. Current codes, based on non-cubic cells, rely upon a remapping of the cells to logical cubes, and back again to cells. This methodology has its own inherent weaknesses, that have yet to be fully explored. An adaptive non-Cartesian based code, similar to those used in computational fluid dynamics and finite element analysis is currently beyond the state of the art for PIC codes. The use of flexible data structures in PICLL makes it perfectly suited for exploration and research in these areas. Additionally, this flexibility, combined with PICLL's parallelism, provides an avenue for the investigation of novel dynamic load balancing methodologies. In PICLL, the computational cell is the fundamental unit. This allows for fine control of the problem distribution across nodes.

The PICLL Team

Dr. Leon J. Chandler

Capt. Bryan M. Minor, Ph.D.

Dr. John S. Wagner

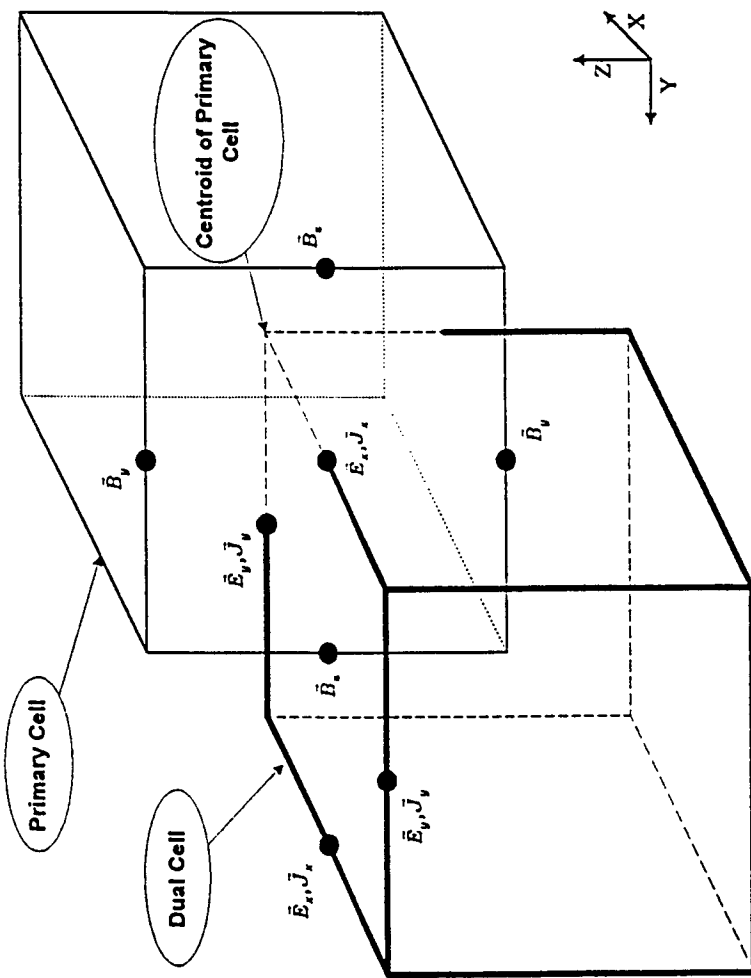
Tony von Sadovszky

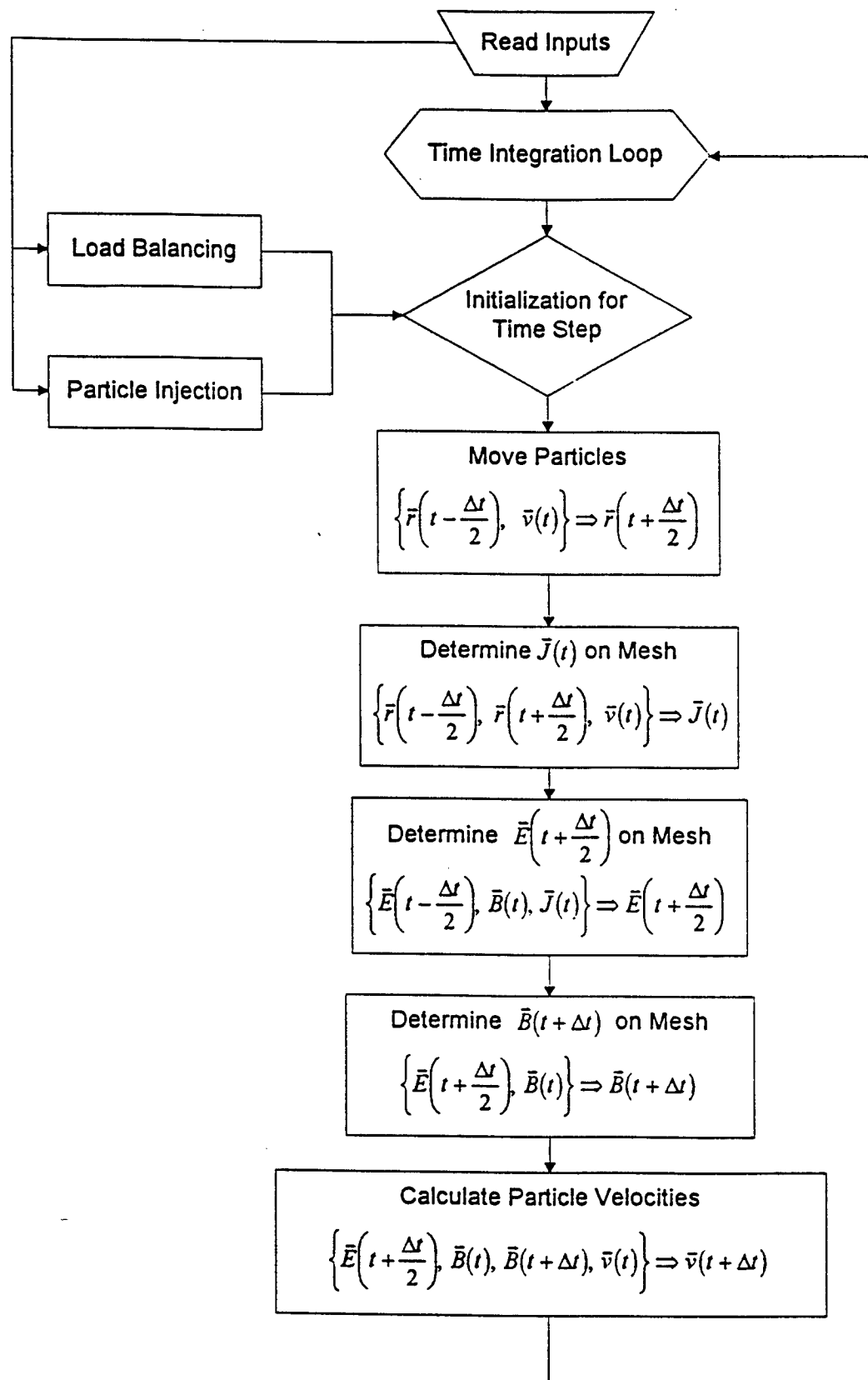
Mike Trahan

Nicholas Mitchell

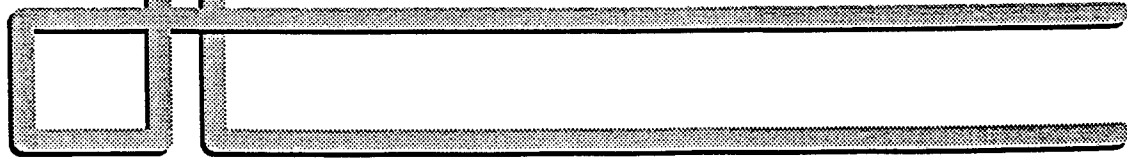
Pat Helles

# Primary/Dual Cell Mesh





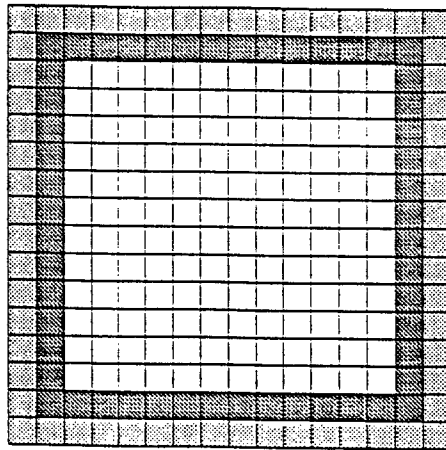
## Ghost Cells for each Node



- Primary Node Mesh
- First Layer of Ghost Cells
- Second Layer of Ghost Cells

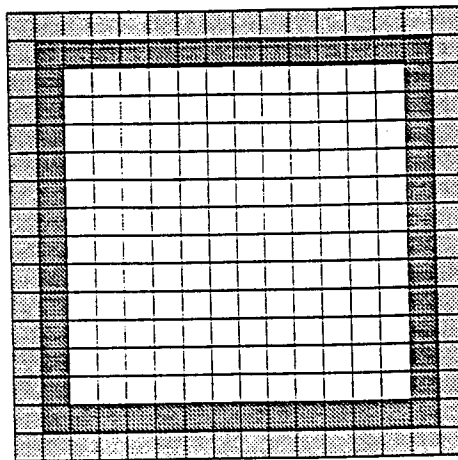
## B Field Groups

- Group 0  
→ Values on Faces of
- Group 1  
→ Values on Faces of
- Group 2  
→ Values on Interior  
Faces of



## E Field and J Current Groups

- Group 0  
→ Values on Edges of  $\square$
- Group 1  
→ Values on Edges of  $\blacksquare$



# Data Structures

## ● Field Data

► Field Type

→ Group

→ Component

→ Field Values